Design and Evaluation of a Novel Lens-Based SPECT System Based on Laue Lens Gamma Diffraction: GEANT4/GAMOS Monte Carlo Study

Author:
Barhoum, Ala'

Publication Date:
2023

DOI:
https://doi.org/10.26190/unsworks/25330

Design and Evaluation of a Novel Lens-Based SPECT System Based on Laue Lens Gamma Diffraction: GEANT4/GAMOS Monte Carlo Study

Alaa Hamdan Barhoum

A thesis in fulfilment of the requirements for the degree of

Doctor of Philosophy

School Engineering and Information Technology
Faculty of Engineering

The University of New South Wales

Canberra, Australia

June 2023

ORIGINALITY STATEMENT

☑ I hereby declare that this submission is my own work and to the best of my knowledge it contains no materials previously published or written by another person, or substantial proportions of material which have been accepted for the award of any other degree or diploma at UNSW or any other educational institution, except where due acknowledgement is made in the thesis. Any contribution made to the research by others, with whom I have worked at UNSW or elsewhere, is explicitly acknowledged in the thesis. I also declare that the intellectual content of this thesis is the product of my own work, except to the extent that assistance from others in the project's design and conception or in style, presentation and linguistic expression is acknowledged.

COPYRIGHT STATEMENT

AUTHENTICITY STATEMENT

☑ I certify that the Library deposit digital copy is a direct equivalent of the final officially approved version of my thesis.

UNSW is supportive of candidates publishing their research results during their candidature as detailed in the UNSW Thesis Examination Procedure.

Publications can be used in the candidate's thesis in lieu of a Chapter provided:

- The candidate contributed **greater than 50%** of the content in the publication and are the "primary author", i.e. they were responsible primarily for the planning, execution and preparation of the work for publication.
- The candidate has obtained approval to include the publication in their thesis in lieu of a Chapter from their Supervisor and Postgraduate Coordinator.
- The publication is not subject to any obligations or contractual agreements with a third party that would constrain its inclusion in the thesis.

☑ The candidate has declared that **some of the work described in their thesis has been published and has been documented in the relevant Chapters with acknowledgement**.

Candidate's Declaration

I declare that I have complied with the Thesis Examination Procedure.

The University of New South Wales

Thesis/Dissertation Sheet

Surname or Family name: **Barhoum**

First name: **Alaa** Other name/s: **N/A**

Abbreviation for degree as given in the University calendar: **PhD**

School: **School of Engineering and Information Technology** Faculty: **UNSW Canberra, ADFA.**

Title: Design and Evaluation of a Novel Lens-Based SPECT System Based on Laue Lens Gamma Diffraction: GEANT4/GAMOS Monte Carlo Study

Abstract While improvements in SPECT imaging techniques constitute a significant advance in biomedical science and cancer diagnosis, their limited spatial resolution has hindered their application to small animal research and early tumour detection. Using recent breakthroughs established by the high-energy astrophysics community, focusing X-ray optics provides a method to overcome the paradigm of low resolution and presents the possibility of imaging small objects with sub-millimetre resolution. This thesis aims to tackle the constraints associated with the current SPECT imaging designs by exploiting the notion of focusing high energy photons through Laue lens diffraction and developing a means of performing gamma rays imaging that would not rely on parallel or pinhole collimators. The gradual development of the novel system is discussed, starting from the single, modular, and multi-Laue lens-based SPECT. A customized 3D reconstruction algorithm was developed to reconstruct an accurate 3D radioactivity distribution from focused projections. A plug-in implementing the Laue diffraction concept was developed and used to model gamma rays focusing in the GEANT4 toolkit. The plug-in will be incorporated into GEANT4 upon final approval from its developers. The single lens-based, modular lens-based and multi lens-based SPECT models detected one hit per 42 source photons (sensitivity of $790\ cps/\mu Ci$), three hits per 42 source photons (sensitivity of $2{,}373\ cps/\mu Ci$), and one hit per 20 source photons (sensitivity of $1{,}670\ cps/\mu Ci$), respectively. Based on the generated 3D reconstructed images, the achievable spatial resolution was found to be $0.1\ mm$ full width at half maximum (FWHM). The proposed design's performance parameters were compared against the existing SIEMENS parallel LEHR and multi-pinhole (5-MWB-1.0) Inveon SPECT. The achievable spatial resolution is decoupled from the sensitivity of the system, which is in stark contrast with the existing collimators that suffer from the resolution-sensitivity trade-off and are limited to a resolution of $2\ mm$. The proposed system allows discrimination between adjacent volumes as small as $0.113\ nL$, which is substantially smaller than what can be imaged by any existing SPECT or PET system. The proposed design could lay the foundation for a new SPECT imaging technology akin to a combination of tomosynthesis and lightfield imaging.

Signature **Alaa Barhoum** Date June 2023

Signature Witness Date

FOR OFFICE USE ONLY Date of completion of requirements for Award

Originality Statement

I hereby declare that this submission is my own work and to the best of my knowledge it contains no materials previously published or written by another person, or substantial proportions of material which have been accepted for the award of any other degree or diploma at UNSW or any other educational institution, except where due acknowledgement is made in the thesis. Any contribution made to the research by others, with whom I have worked at UNSW or elsewhere, is explicitly acknowledged in the thesis. I also declare that the intellectual content of this thesis is the product of my own work, except to the extent that assistance from others in the project's design and conception or in style, presentation and linguistic expression is acknowledged.

Alaa Barhoum
University of New South Wales.
Canberra, Australia.
Date: June 13, 2023

Copyright Statement

Alaa Barhoum
University of New South Wales,
Canberra, Australia.
Date: June 13, 2023

Authenticity Statement

I certify that the library deposit digital copy is a direct equivalent of the final officially approved version of my thesis.

Alaa Barhoum
University of New South Wales,
Canberra, Australia.
Date: June 13, 2023

Abstract

Background: While the development of in vivo imaging techniques constitutes a significant advance in biomedical science and cancer diagnosis, their limited spatial resolution has limited their application to small animals and hindered early carcinogenic tumour detection. Numerous attempts were made to achieve high-quality SPECT imaging using the collimator and pinhole concepts; however, these concepts suffer from restricted sensitivity and poor resolution, requiring high radiological doses and longer acquisition times. Focusing X-rays optics, originally developed for high-energy astronomical imaging, is a way out to overcome the compromise between resolution and sensitivity for imaging small objects with submillimeter resolution.

Materials and Methods: This thesis aims to tackle the constraints associated with the current SPECT imaging designs by introducing the notion of x-ray focusing by diffraction and by developing a means of performing x-rays imaging of small objects that doesn't rely on parallel or pinhole absorptive collimators. This novel approach relies on the Laue lens as the focusing element. To thoroughly examine the behaviour of a SPECT system augmented with a Laue lens, I developed several case studies in MATLAB using one and three spherical point sources with a radius of $0.03\,mm$, where the radiation points were equivalent to $0.1\,mCi$ activity. Also, another spherical point source filled with Tc^{99} with $0.1\,mCi$ activity was modelled in the GAMOS and GEANT4 experiments for validation purposes. A significant contribution of this work is the design and optimisation of the first Laue lens for the intended application as being incorporated into a SPECT imaging system. Moreover, this work presents the implementation of a tracking Monte Carlo simulation, the first of its kind, in different toolkits for the envisioned system (in MATLAB, GAMOS, and GEANT4). The designed environments incorporate a realistic physical interaction that accounts for possible absorption and attenuation phenomena. The gradual development of the system is discussed. I first introduce the first realization of a novel ultra-high-resolution single lens-based SPECT and conduct its Monte Carlo simulation, then analysis. Aiming to boost sensitivity, I proposed a second geometry, a single lens-based SPECT system fitted with partially curved detector modules and Laue lens arrays. I call it modular lens-based SPECT. The Laue lenses are positioned in inclined planes in a modular fashion, forming the detector geometry. The multi lens-based SPECT is a more complicated geometry consisting of an array of diffraction

lenses placed at the pinhole centres of a multi-pinhole SPECT collimator. A customized 3D reconstruction algorithm was developed for the different configurations to calculate an accurate 3D radioactivity distribution from the acquired projections tailored to the focused Laue lens projections. To validate the 3D reconstruction algorithm, I conducted validation studies that addressed two essential parameters: the mapping of the depth and shift information in the 3D reconstructed images and the sensitivity mapping over the field of view (FOV).

To examine the authenticity of the argument stated throughout the thesis, it was necessary to study the designed system's behaviours with the complete diffraction process in a Monte Carlo simulation toolkit. In this work, I present the first attempt to model X-rays and gamma rays focusing based on Laue diffraction in the GEANT4 toolkit in the form of a plug-in that I developed, using an advanced example. It is expected that the Laue diffraction plug-in and the example will be made available as an open-source code in the GEANT4 toolkit after the GEANT4 developers' approval.

Results: The single lens-based SPECT simulation detected one hit per 42 source photons, corresponding to a sensitivity of $27\ cps/MBq$, equivalent to $790\ cps/\mu Ci$. The modular lens-based SPECT detected three hits per 42 source photons for a source placed at the centre, corresponding to a sensitivity of $81\ cps/MBq$, equivalent to $2{,}373\ cps/\mu Ci$. The array of Laue lenses placed in a planer fashion in the multi-Laue lens geometry detected one hit per 20 source photons, roughly comparable to a sensitivity of $57\ cps/MBq$, equivalent to $1{,}670\ cps/\mu Ci$. Based on the generated 3D reconstructed images, the reconstructed spatial resolution was found to be 0.1 mm at full width at half maximum (FWHM). The proposed system allows discrimination between adjacent volumes as small as $0.113\ nL$, which is substantially smaller than what can be imaged by any existing SPECT or PET system. For detailed comparison and rigorous evaluation, the 3D reconstructed images of the proposed design were compared against the existing parallel SIEMENS LEHR and multi-pinhole (5-MWB-1.0) Inveon SPECT. The achievable spatial resolution of the proposed system is decoupled from its sensitivity, which is in stark contrast to the existing collimators that suffer from the resolution-sensitivity trade-off. The proposed system achieved comparable sensitivity compared to the existing SPECT used in clinical applications. However, it outperformed the conventional SPECT in terms of system resolution, achieving 0.1 mm resolution compared to the 2 mm resolution of current clinical SPECT systems.

Implications: The research findings highlight the significant implications and practical applications of a lens-based SPECT imaging system. The introduction of a lens-based focusing technique has the potential to revolutionize SPECT imaging by combining elements of tomosynthesis and lightfield imaging. Applying a similar concept to SPECT imaging using a lens-based system allows for multiple projections of the radiotracer distribution within the body. Additionally, incorporating the concept of lightfield imaging enables capturing spatial and directional information about gamma rays, leading to more accurate localization and characterization of the radiotracer distribution.

The lens-based SPECT system also offers unparalleled sub-millimetre spatial resolution, which is crucial for studying small animal models and improving the accuracy of image interpretation. By overcoming the limitations of conventional SPECT, such as restricted resolution and sensitivity, the lens-based system has the potential to detect and visualize small, early-stage tumours, improving cancer detection at the most treatable and curable stage. Furthermore, the experiments with low activity phantoms demonstrate the system's ability to detect abnormalities with reduced doses of radiotracer, which could benefit patients by reducing the amount of injected radioactive substances. The development of an advanced example and plug-in in GEANT4 for the Laue diffraction process adds to the existing knowledge and provides researchers with a tool to simulate and study gamma diffraction phenomena for various applications. Overall, these findings contribute to the field of SPECT imaging and offer a foundation for further exploration and improvement of the lens-based SPECT system design.

Conclusion: A conceptual lens-based SPECT imaging system was designed and evaluated in industry-standard simulation environments; these are MATLAB, GAMOS, and GEANT4 toolkits. Physical principles governing the design of this system are also presented, along with a series of measurements analysing various characteristics of the generated projections and 3D reconstructed images. The proposed design could lay the foundation for a new SPECT imaging technology akin to a combination of tomosynthesis and lightfield imaging, not requiring moving parts. The system's novelty relies on the ability to view the data from every lens separately to capture a specific view of the object, or it can be integrated to generate a three-dimensional image from the three modules, including accurate information about the object's size and location. The achieved resolution is outstanding and would open SPECT to other applications like oncology, thyroid, breast, and infant SPECT imaging, with new possibilities for the sub-organ-level study and early detection of lesions.

Future Work: Fabricating a physical prototype of this miniature Laue lens should be a major source of future investigation. The scale of the 40 mm diameter lens falls outside the scope of conventional fabrication techniques, with 3D printing and micromachining being too coarse and lithography and nano-fabrication techniques too fine. A hybrid approach needs to be developed. The Monte Carlo model can be applied for further studies on the development and evaluation of the system and to optimize forward projection and 3D image reconstruction methods. Based on the achieved resolution, future work can be devoted to designing a dedicated Laue lens for thyroid and breast cancer detection by optimizing the lens for I^{123} radiation energy. Further bio-chemical applications can be in the imaging of proteins and viruses. Non-medical applications of the Laue lens, which are currently limited to astronomical imaging, can be envisioned when miniature versions can be manufactured, such as enhanced radiological detectors and surveying equipment.

The mind, once stretched by a new idea, never returns to its original dimensions."

Ralph Waldo Emerson

This quote resonates with me the most, expressing that when we come across novel concepts that broaden our comprehension of the universe, they permanently transform our thinking patterns and modify how we perceive and engage with the environment.

To Myself…..

Completing a PhD is a transformative and deeply personal journey, just like delivering a baby. It encompasses years of dedication, hard work, and emotional investment.

But, for me, the culmination of my PhD elicits a mix of emotions, including fear and apprehension about letting go……

Throughout the PhD journey, we pour our hearts and souls into our research, nurturing it with countless hours of work, intellectual exploration, and personal sacrifices. It becomes a part of us, intertwined with our identity and aspirations.

While the act of letting go is so scary to me, it is also an act of trust in ourselves and in the value of our work. We have honed our skills, expanded our intellectual horizons, and contributed to the body of knowledge in our respective fields. By sharing our research and findings with the world, we contribute to the collective growth of academia and society at large.

Alaa Barhoum

9th of June 2023

Acknowledgments

Gratitude fills every fibre of my being as I embark on expressing the profound depth of appreciation I have for my primary supervisor, **Dr. Murat Tahtali**. Words seem inadequate to capture the immense impact he has had on my academic journey.

Your dedication to my growth as a researcher and your mentorship have profoundly influenced both my academic and personal development. I still remember our initial meetings, where you patiently listened to my research ideas and answered my countless questions. The weekly meetings have been a cornerstone of my progress. They served as a platform for fruitful discussions, brainstorming and a space to express my thoughts and concerns freely. Beyond the academic realm, I am grateful for the personal support and understanding you have shown to me. You have been there to lend an ear during moments of stress and offer encouragement when I felt overwhelmed. Beyond the countless hours invested in advising and mentoring me, you consistently went above and beyond to nurture my intellectual curiosity, which also imparted valuable life lessons, which have become an integral part of who I am today. The transformative impact of your mentorship extends far beyond the completion of this thesis; I am now equipped with a lifelong toolkit of skills and knowledge thanks to your guidance.

Murat, I am forever grateful for your presence in my life, not just as a supervisor, but as a mentor and a friend, I will be immensely beholden to you till no life. And every word penned here falls short of capturing the depth of respect I hold for you.

To my co-supervisor and supervisor in the causal academic duty, **Prof. Andrey Miroshnichenko**, I am deeply humbled and overwhelmed with gratitude for the invaluable guidance and care for my wellbeing. Thanks for giving me the chance to tutor a course with you. Working closely with such a knowledgeable and inspiring mentor like you has been an honour. The trust you placed allowed me to contribute to the teaching process, and it has been an invaluable experience for my professional development.

To my external supervisor, **Dr. Riccardo Camattari**, your technical expertise, and dedication have been a tremendous asset to my research. I am grateful for your willingness to share your expertise and always ensuring that I had the necessary tools to tackle the technical aspects of my research, and I still remember all the professional, timely and accurate replies to my countless email, thanks for your patience.

I am deeply grateful for the invaluable guidance and mentorship provided by my esteemed mentor, **Professor Susanna Guatelli,** even amidst her own demanding commitments.

Prof. Michael Barlow (Spike), **Prof. Sean O'Byrne**, and **Dr. Ugur Turhan**, you showed genuine care for my wellbeing. Your kindness, empathy, and willingness to lend an ear during moments of personal difficulty meant the world to me.

A special thanks to my fellow colleague **Dr. Manu Francis** for his encouragement and guidance during this journey.

I am grateful to **UNSW Canberra** for providing the Postgraduate Research Scholarship to support my PhD. Special thanks to my fellows and colleagues in the **Optica student chapter members**, thanks for all the support I received during my role as the president.

I find solace in expressing my deepest gratitude to my **beloved father, Hamdan Barhoum**, who has passed away. Daddy, even when I doubted myself, you propelled me forward and instilled in me a love for learning, an unyielding work ethic, and the courage to pursue my dreams relentlessly. Daddy, you are not here to witness the completion of this thesis, but I am today as you always wanted me to be.

My mother, **Raghda AbuSaid**, her nerves mirrored my own. Her genuine concern for my wellbeing and success acted as a reminder of the significance of this undertaking. I owe my achievements to her unconditional love. Love you, Mom.

My Brothers, you are the best friend I ever had. Through the good and bad times, you have been my confidant and my rock.

To my **wonderful four children**, I love you to the moon and back. You have been my constant motivation and source of inspiration. As you continue to grow, I hope my dedication to my studies serves as an example for you to pursue your own passions and dreams. I want you to know that no matter what path you choose in life, I will always support and encourage you, just as you have done for me. Your patience during times when my attention was divided between my studies and family responsibilities have meant the world to me. You have shown remarkable resilience and maturity beyond your years, and I am immensely proud of each one of you.

To my loving husband, this thesis represents not only my academic achievements but also our entire family's collective efforts and sacrifices. It is a testament to the love and support we share. Thanks for being by my side through the highs and lows of life. Your patience, understanding, and willingness to take on added responsibilities at home have allowed me to dedicate the time and focus needed for my research. I am deeply grateful for your role in this journey, and your love.

List of Publications

The work presented in this thesis has produced the following publications and conference presentations.

Journal Papers

1. A. Barhoum, M. Tahtali and R. Camattari, " Review Article: Recent Advances in SPECT Design and the History of Laue Lens in Gamma Focusing: Recent Trends in SPECT Based on Light Field" *Medical physics (2022).* This article is under review.

2. A. Barhoum, M. Tahtali, R. Camattari, and Susanna Guatelli " Feasibility Study of Multi-Lens-Based SPECT with a Dedicated Laue Reconstruction Algorithm: A First Monte Carlo Study" *Scientific Reports* (2023). This article is under review.

3. A. Barhoum, M. Tahtali, R. Camattari, and Susanna Guatelli " Ultra-High-Resolution Lens-Based SPECT Based on Laue Gamma Diffraction: A First GAMOS/GEANT4-MATLAB Monte Carlo Study" *Physica Medica* (2023). This article is under review.

Conference Papers:

1. Barhoum, A., Francis, M., Camattari, R., & Tahtali, M. (2021, October). Design and Evaluation of a Novel Ultra High-Resolution Lens-Based SPECT: Insight to Light Field Imaging. In 2021 IEEE International Conference on Systems, Man, and Cybernetics (SMC) (pp. 1436-1442). IEEE.

2. Barhoum, A., Tahtali, M., & Camattari, R. (2022, October). Feasibility Study of a Lens-Based SPECT With a Tiled Lens and Detector Geometry for Animal

Research: Simulation Results. In *2022 IEEE International Conference on Systems, Man, and Cybernetics (SMC)* (pp. 3143-3149). IEEE.

3. A. Barhoum, M. Tahtali and R. Camattari and Susanna Guatelli. (2022, October). The GEANT4-Gamma Diffraction Code Based on Laue lens Modelling: Design Foundation and Implementation of the First Set of Models in GEANT4. In 2022 Fourth GEANT4 International User Conference at The Physics-Medicine-Biology Frontier.

Scientific Contributions

- Contributed to extending **GAMOS** functionality by developing a GAMOS based detector simulation example for Laue lens diffraction as a first attempt. The example is to be approved for ***GAMOS 6.3.*** version by Professor Pedro Arce, CERN.

- Contributed to extending **GEANT4** functionality by developing a GEANT4 based detector simulation as an advanced example for Laue lens diffraction as a first attempt. The extended example is to be approved by Prof. Susanna Guatelli, UOW academic director of the Bachelor of Medical and Radiation Physics.

- Invited to submit an abstract for the **26^{th} GEANT4 Collaboration Meeting** (24th to the 26th of October 2022).

List of Awards and Honors

- Faculty top three winners, 3MT UNSW Australia, 2022.

- The PhD research and Novel idea I proposed was nominated and selected as one of the top research projects to compete in the *Idea to Impact project*, as a competitive program for innovators managed by Canberra Innovation Network, Canberra, 2023.

- Based on the research outcome and the 3MT thesis competition, I have been selected as a mentor and a judge for the "*Responsible Development and innovation projects: rHACK*" workshop for the Australian National University engineering students, hosted by Canberra Innovation Network.

Table of Contents

List of Tables

List of Figures

Glossary

The following is a list of nomenclature and abbreviations used throughout this thesis; most symbols do not have exclusive definitions as they are re-defined in context when necessary.

Firstly, the Nomenclature:

Symbols in straight bold are vector or matrix quantities whereas scalars and functions are in italics. The symbols are listed in approximate order of appearance in the text.

Symbol	Description
$\boldsymbol{I^{123}}$	Iodine -123
$\boldsymbol{Tc^{99}}$	Technetium 99
$\boldsymbol{F^{18}}$	fluorine-18
$\boldsymbol{C^{11}}$	Carbon-11
$\boldsymbol{N^{13}}$	Nitrogen-13
$\boldsymbol{O^{15}}$	Oxygen-15
$\boldsymbol{NaI}(\boldsymbol{TI})$	Thallium-doped Sodium Iodide
$\boldsymbol{CsI}(\boldsymbol{TI})$	Thallium-doped Cesium Iodide
$\boldsymbol{d}$	Pinhole diameter
$\boldsymbol{h}$	The separation between the sensor plane and pinhole array
$\boldsymbol{R_g}$	Collimator's Geometrical resolution
$\boldsymbol{\mu Ci}$	Microcurie
$\boldsymbol{Bq}$	Becquerel
$\boldsymbol{keV}$	kiloelectronvolt, the unit of energy used in atomic and nuclear physics
$\boldsymbol{p}(\boldsymbol{\omega})$	Fourier transform
$\boldsymbol{\theta_B}$	Bragg's angle
$\boldsymbol{P}(\boldsymbol{s})$	The projection image
$\boldsymbol{f}(\boldsymbol{\omega_x}, \boldsymbol{\omega_y})$	2D Fourier transform
$\boldsymbol{f}$	Focal length of the lens
$\boldsymbol{Z_f}$	The depth
$\boldsymbol{L_s}$	The distance between the lens and the source
$\boldsymbol{L_d}$	The distance between the lens and the detector
$\boldsymbol{M}$	Magnification
$\boldsymbol{t}$	Thickness
$\boldsymbol{d_{hkl}}$	The distance between atomic planes
$\boldsymbol{\lambda}$	$\boldsymbol{\lambda}$ is the monochromatic light wavelength,
$\boldsymbol{h}$, $\boldsymbol{k}$, and $\boldsymbol{l}$	The planes' Miller indices of the Laue lens
$\boldsymbol{n}$	The diffraction order

$\boldsymbol{d}$	The distance between consecutive atomic layers
$\boldsymbol{\theta 2_{Incident}}$	The angle between the diffracted beam and the crystalline planes that cause diffraction
$\boldsymbol{Pixel\ Location_{Reconstructed}}$	The pixel location of the phantom in the reconstructed images
$\boldsymbol{x}$	The minimum resolvable distance between two points
$\boldsymbol{g}$	The recorded image
$\boldsymbol{G}$	The Fourier transform of image
$\boldsymbol{f}$	The input truth object
$\boldsymbol{F}$	Fourier transform of f.
$\boldsymbol{h}$	The PSF of the imaging instrument
$\boldsymbol{H}$	Fourier transform of h.
$\boldsymbol{N}$	The number of detector modules
$\boldsymbol{W}$	The width of each module
$\boldsymbol{F}$	The distance between the source's center and the Laue lens module
$\boldsymbol{dirX, dirY, dirZ}$	The initial direction of the photons. in X, Y, and Z directions
$\boldsymbol{az_S}$	The azimuthal angle in a spherical coordinate
$\boldsymbol{pol_S}$	The polar angle in a spherical coordinate
$\boldsymbol{xInter, yInter, zInter}$	The interaction points with the lens in X, Y, and Z coordinates

Next, the Abbreviations:

Abbreviation	Description
ADC	Analogue to Digital Conversion
CNR	Contrast-to-Noise Ratio
DNA	Deoxyribo Nucleic Acid
2D	Two Dimensional
3D	Three Dimensional
SPECT	Single Photon Emission Computed Tomography
LOR	Line of Response
CT	Computed Tomography
cc	Cubic centimeter
ROD	Rate of Dos
FBP	Filtered Back Projection
FOV	Field of View
FWHM	Full Width at Half Maximum
GAMOS	GEANT4-based Architecture for Medicine Oriented Simulations
GEANT	GEometry ANd Tracking
LEHR	Low-energy, High-resolution
MRI	Magnetic Resonance Imaging
MATLAB	MATrix LABoratory
NEMA	National Electrical Manufacturers Association
Na(TI)	Sodium Iodide
PMT	Photomultiplier Tubes
PSPMTS	Position sensitive Photomultiplier Tubes
PET	Particle Emission Tomography
PSF	Point Spread Function
ROR	Radius of Rotation
SNR	Signal to Noise Ratio
MPH	Multi-pinhole
MPI	Myocardial perfusion
ROI	Region of interest
MC	Monte Carlo
LM-OSEM	List-mode ordered-subsets expectation- maximisation
OSEM	Ordered subset expectation maximization
ART	Algebraic reconstruction technique
SAI	Small animal SPECT imaging
CZT	Cadmium Zinc Telluride) detector
CA	Coded aperture
ESA	European Space Agency
JDA	Japanese Space Agency
SARIS	Small animal radionuclide imaging system
TPS	Treatment planning systems
VRT	Variance reduction techniques
MLA	Micro Lens Array

ASCII	American Standard Code for Information Interchange
LSPECT	Lightfield SPECT
MFP	The mean free path of the photons
DRDC	Research and Development Committee
HEP	High energy physics
GPS	General particle source

1. Introduction

In today's technological environment, sophisticated instrumentation and imaging systems have evolved into formidable instruments. Technological advances, quick data processing, image reconstruction, and pattern recognition have permitted the introduction of advanced research techniques that are now utilised in numerous scientific disciplines and application sectors. A significant number of technical innovations were initially generated in particle physics but have now extended to astrophysics, medicine, biology, and materials science, amongst other application disciplines, and of course, nuclear imaging [1].

Imaging in nuclear medicine is a blend of numerous fields. These disciplines include chemistry, physics, mathematics, computer technology, and medicine. Nuclear medicine is a subspecialty of medicine in which radioactive chemicals are administered to patients for the purposes of diagnosis or treatment. Contrast this with the application of radiation in conventional radiology and radiotherapy, when it is often introduced from outside the body. Since its inception in the 1950s, it has progressed to the point where nuclear medicine departments can be found in most big and medium-sized hospitals [2]. In a nuclear medicine scan, a radiopharmaceutical is injected into the patient, and a radiation-detecting imaging device is used to detect biochemical changes inside the body. In contrast to imaging techniques that principally characterize anatomies like conventional ultrasound (US), computed tomography (CT), or magnetic resonance imaging (MRI); nuclear medicine imaging can provide crucial quantitative functional information about living subjects' normal tissues or disease conditions [3]. Nuclear imaging modalities such as positron emission tomography (PET) and single-photon emission computed tomography (SPECT) excel at depicting the biological function of the tissue. Unlike structural imaging techniques, they provide functional diagnostic information about brain tumours, stroke, neurodegenerative disorders, epilepsy, cortical vision loss, and migraine. SPECT and PET can measure a wide range of biological activities and is cost-effective to operate. SPECT has been utilized extensively in evaluating stroke, subarachnoid haemorrhage, and head trauma [4]. SPECT and PET imaging emerged around the same time in the late 1970s. SPECT cameras, which were based on modified gamma cameras that could gather $360°$ of data and spin around the patient, rapidly found a place in medical imaging [5].

SPECT is a constantly developing discipline, and in the past few years, both its hardware technology and image-processing techniques have evolved substantially. There have been advancements in scintillators, photon transducers, and the availability of semiconductor technology at the component level. These technologies allow the production of smaller, more compact systems that can be tailored to specific purposes [6]. Improved methods for detecting the intensity, position, and timing of counts emitted by injected radiopharmaceuticals invariably lead to further advancements in the accuracy, safety, and convenience of the SPECT modalities. However, the efficiency and performance parameters of SPECT imaging are limited by the reliance on mechanical parallel-hole collimators, which results in low sensitivity and poor resolution [7]. For this reason, developing and adopting new technologies is necessary to improve SPECT imaging performance [8, 9].

This chapter discusses the research challenges associated with conventional SPECT imaging systems. This is followed by a detailed introduction to nuclear medicine imaging, including the two most common modalities, SPECT and PET. A brief introduction to optical light-field imaging is also provided, as its X-ray counterpart would have implications for the future of SPECT with the availability of an X-ray focusing element. The statement of the problem and study motivation for addressing the current SPECT limitations is clearly identified. Finally, the research contributions to knowledge are presented.

This chapter is structured as follows: Section 1.1 introduces nuclear medical imaging and its history. Section 1.2 discusses the technical pitfalls and limitations of collimator-based SPECT. Section 1.3 presents the lightfield imaging concept and relates its association with new imaging trends in SPECT with this thesis' objective. Sections 1.4 and 1.5 state the research objectives and the study's contributions, respectively. Finally, Section 1.6 describes the thesis organization.

1.1 Nuclear Medical Imaging

Nuclear medicine is the study and use of radioactive materials in diagnosing and treating human diseases. In the early 1920s, Georg Karl von Hevesy was the first to formulate the "tracer principle". The tracer concept studies the in vivo disposition of chemicals utilising trace amounts of non-pharmacologically active radioactive tracers. Today, externally sensitive imaging equipment is utilised to research many facets of physiology, including cellular metabolism, DNA (deoxyribonucleic acid) proliferation, blood flow in organs, organ function, receptor expression, and aberrant physiology utilising the same approach [10, 11]. Nuclear medicine is function-based. Because of this, it is known as functional imaging. Unlike X-ray imaging in radiology, nuclear medicine scans usually show the whole-body distribution of the radioactive chemical by acquiring a series of images over time representing the spatiotemporal distribution of the radiotracer inside the body [10].

The scientific findings during extensive research and technology advancements over the past six decades have altered the practice of medicine and laid the groundwork for the future of nuclear medicine and molecular imaging [12, 13]. Moreover, they produced various nuclear medicine applications that have significantly enhanced patient care. Nuclear medicine has expanded to become a $1.7 billion industry as nuclear medicine technologies and therapies have become indispensable to numerous medical subspecialties [14]. Today, nuclear medicine offers diagnostic, prognostic, predictive, and intermediate endpoint biomarkers in oncology, cardiology, neurology, and infectious and inflammatory disorders [12, 15]. Single Photon Emission Computed Tomography (SPECT) scans, and Positron Emission Tomography (PET) scans, are the two most prevalent imaging modalities in nuclear medicine [16].

1.1.1 History of Nuclear Imaging

Blumgart and his colleague Otto C. Yens modified the cloud chamber to measure the arm-to-arm circulation time of blood in 1925, marking the beginning of nuclear medicine instrumentation [17]. They employed a blend of beta- and gamma-emitting radium decay products. Blumgart suggested several assumptions for constructing a detector or measuring technique that continue to hold in comparison to current requirements: the approach must be objective, non-invasive, and capable of automatically measuring the arrival of the drug [17, 18]. In 1951, Benedict Cassen created the rectilinear scanner to record the distribution of accumulated radioactivity in the human body [19].

In 1953, Hal Anger designed the first camera using a photographic X-ray film in contact with a NaI(Tl) intensifying screen. He projected the distribution of gamma rays onto the scintillation screen using pinhole collimation with a modest detector size. Initially, the camera was employed to scan patients who had ^{131}I therapy [20]. The limited field of vision of the imaging equipment was the drawback of this prototype. In addition, good image quality was difficult to achieve without high doses and lengthy exposure durations. In 1958, Anger devised the first effective scintillation camera, which he named after himself, the Anger camera. Using a NaI(Tl) crystal, photomultiplier tubes (PMTs), and a broader field of view, he was able to significantly improve the detection efficiency [21, 22]. While most modern and commercially available gamma cameras are primarily based on Anger's original concept of employing sodium iodide crystals, successful new imaging systems are emerging to meet specialised imaging requirements or to improve image quality and diagnostic accuracy [23, 24].

1.1.2 Positron Emission Tomography (PET)

Positron Emission Tomography (PET) is a fundamental imaging modality within the field of nuclear medicine. It quantitatively measures biochemical and physiological processes in vivo by employing radiopharmaceuticals labelled with positron-emitting radionuclides such as C^{11}, N^{13}, O^{15}, and F^{18} [25, 26]. PET employs a positron-emitting radionuclide tracer isotope that, on decay, emits a positron, the antiparticle to an electron, from its nucleus. This positron instantaneously collides with an electron in the medium, producing two gamma ray photons with opposite momentums [27], as depicted in Figure 1.1, which is called annihilation. It is the process by which particles and their corresponding antiparticles collide and are transformed into energy or other particles. When a particle collides with its antiparticle, it can mutually annihilate, converting its mass into energy, often in the form of high-energy photons (e.g., gamma rays) or other particles. The distance travelled by the positron is typically less than $2\ mm$, depending on the specific emission energy of the isotope and the tissue density. The annihilation generates two $511\ keV$ photons that travel in opposing directions at the speed of light and are nearly 180 degrees apart. The PET scanner captures these photons by their near simultaneous detection by the crystal array, thereby pinpointing the annihilation site. Therefore, PET scanners do not image the source of positron decay but rather the location of positron-electron annihilation [28, 29].

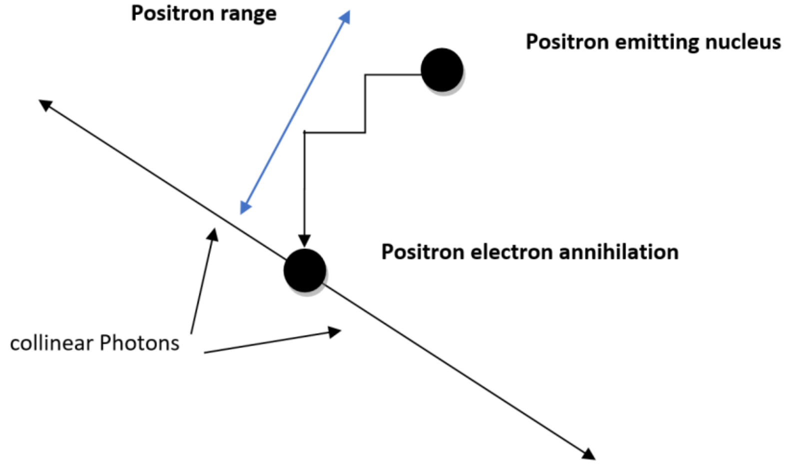

Figure 1.1 Basic PET imaging principle: radionuclide decay, positron emission, multiple scattering, electron annihilation, and the generation of two collinear 511 keV photons [28].

Figure 1.2a, Figure 1.2b, and Figure 1.2c depict the overall procedure of the PET technology. The positron-labelled tracers are typically injected intravenously into the patient and distributed throughout the body, exchanging between blood and tissue, then binding or participating in metabolic reactions, i.e., becoming localised under physiological conditions and decaying exponentially over time. The $511\ keV$ photons leave the annihilation site, travel through the body, and are detected by the scanner in an ideal scenario. The patient is surrounded by a ring of scintillation detectors in the scanner. When one photon enters a detector, it generates a small amount of light that is magnified into an electrical signal and detected as one count. After getting a single count from one detector, the system waits for a few nanoseconds for a second single count to occur in another detector. If two single counts occur inside this specified time interval, the system pairs these photons and saves them as a coincidental occurrence. This coincidence indicates that the antihalation event happened somewhere along the line connecting the two single detections. The line between two detectors is known as the line of response. (When time-of-flight detection is utilised, the difference in arrival times pinpoints the location of the annihilation event to within 10 cm) A single line-of-response effectively monitors the integral of annihilations along a single line through the patient after collecting many photons [30]. These lines in a single trans-axial plane are arranged according to their azimuthal and radial angles and recorded in a 2D matrix termed a sinogram (a single annihilation site will map a sine wave in the sinogram domain). The sinogram is the Radon transform of the object's annihilation distribution and is conceptually the same data space employed by all tomographic modalities [31, 32].

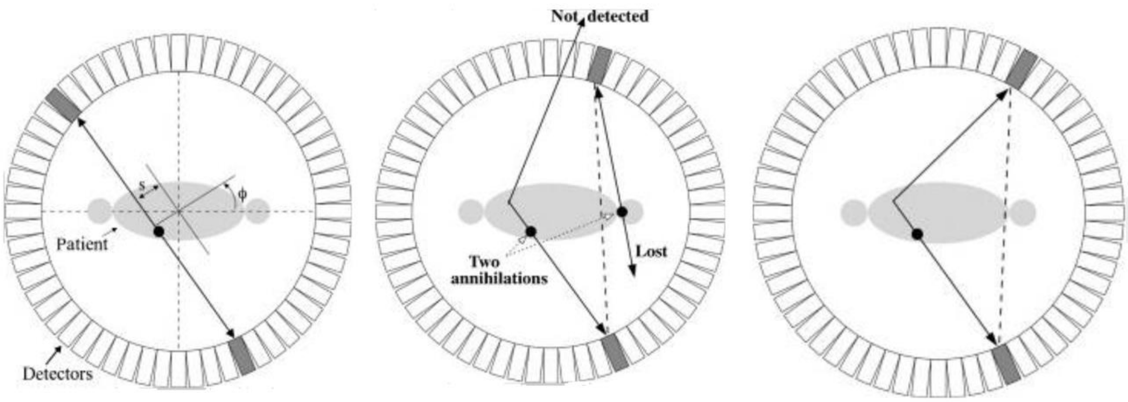

(a) (b) (c)

Figure 1.2 The trans-axial illustration of a patient and a ring of detectors illustrate the forms of coincidental incidents. (a) True coincidence, (b) Random (accidental) coincidence, (c) Scattered coincidence. In the second two situations, the annihilations represented with solid black dots do not occur along the identified line-of-response, resulting in increased systemic noise in the data [28].

The term pharmaceutical refers to any chemical compound intended for disease diagnosis, treatment, or prevention. *Radiopharmaceuticals* are medications that have been tagged with a radionuclide [33]. These radiopharmaceuticals are employed as tracers in nuclear imaging to diagnose and treat various diseases. Several tracers are utilised in various biochemical, pharmacological, and biophysical pharmacological processes in live organisms. Clinical applications of such tracers include neurology, cardiology, and cancer. Tracers utilised for PET imaging must meet particular characteristics, such as possessing a high specific activity. Specific activity refers to the activity per unit mass of a particular radionuclide. The most effective clinical PET radiopharmaceutical is the glucose analogue F^{18} Fluoro-2-deoxyglucose (F^{18}-FDG). F^{18} accumulates at high levels in metabolically active malignancies in the brain and myocardial tissue [34]. Even though the half-life of F^{18} is only 110 minutes, it is available in unit doses wherever one has access to a cyclotron facility. Other PET radiopharmaceuticals potentially having a substantial clinical impact include deoxy-F^{18} fluorothymidine (FLT) for tumour imaging, F^{18} fluorocholine for prostate cancer, F^{18} fluoradopa for brain receptor imaging, and N^{13} ammonia for cardiac perfusion imaging [28, 35-38].

PET neuroimaging is based on the mechanism in which a highly radioactive area is correlated with increased brain activity, and that activity is quantified indirectly by the blood flow to various sections of the brain, which is generally assumed to be correlated with the uptake of the radiotracer O^{15} [39, 40]. PET scanners are composed of multiple rings of detector elements, which may or may not be split by thin annular rings or septa of photon-absorptive material, often tungsten, which allow collimation. All data is collected in 2-dimensional slices between septa using collimation. This acquisition technique is referred to as 2D despite the fact that the reconstructed image stack provides 3-dimensional information about the tracer uptake throughout the patient [41].

One of the essential aspects of a PET scanner is its sensitivity. It is a measure of the proportion of the annihilation gamma rays identified and validated by the system during the scan. Consequently, it affects the amount of radiotracer that must be administered to the patient and the duration of the imaging operation to get a quantitative and qualitative image. In modern clinical PET scanners, the axial coverage is approximately $25\ cm$, while the diameter is about $70\ cm$ [42]. The scanner's field of view (FOV) is defined by the solid angle covered by the detector rings. As a result of the isotropic emission from the tracer, a significant number of gamma rays escape this restricted FOV and are therefore lost. Furthermore, due to the detection effectiveness of the scintillator and the photodetectors, not all photons that reach the detector rings are registered. Coincident events pose a source of ambiguity. In addition to actual coincidences, it is possible to measure scattered, random, and numerous coincidences [42, 43]. The decision of whether to accept or reject these events is based primarily on the system's coincidence time window (to eliminate randoms) and energy resolution (to dismiss scattered events). Still, these filters accept some dispersion and unintentional coincidences, resulting in inaccurate positioning information and a reasonably homogeneous background that contributes to a contrast reduction [43, 44]. Multiple coincidences involving the simultaneous detection of three or more photons are typically detected directly [45].

The operational cost of PET scanners is one of its major downsides [46]. Moreover, in terms of the limitations of these imaging methods, it is possible, albeit uncommon, for radiopharmaceutical-induced allergic reactions to develop, causing mild pain and redness that normally decrease rather quickly [47]. Moreover, PET scanners may not be widely available due to the need for a cyclotron facility nearby to create the short-lived radionuclides [48].

1.1.3 History of PET

In 1951, two independent reports on the potential medical applications of coincident detection of positron absorption were published. Wrenn et al. from Duke University recommended the use of coincidence detection [49]. At the same time, Sweet from Boston University mentioned it in a more general report on the use of nuclear disintegrations in the diagnosis and treatment of brain cancers [50]. Brownell and Sweet from Massachusetts General Hospital (MGH) published in 1953 a comprehensive article on implementing the coincidence detection method for localising brain tumours. A pair of sodium iodide detectors were positioned on either side of the head and scanned rectilinearly to determine the radioactivity distribution [51].

The objective was to scan the distribution of the positron emitter, which leaks through the blood-brain barrier disruption induced by the tumour. In 1961, a group at the Brookhaven National Laboratory created a head-encircling ring of 32 sodium iodide-based coincidence detectors [52]. Anger, who devised the gamma camera at the Donner Laboratory of the University of California, Berkeley, utilised it in conjunction with a reference detector. In the late 1960s, the MGH team led by Brownell created the hybrid scanner by building static two-dimensional (2-D) arrays of individual coincident detectors to image the brain [53, 54]. The image was captured with substantially greater sensitivity, albeit predominantly two-dimensional, compared to a single pair of scanning probes. In the early 1970s, the MGH team created a positron camera with a $27 - 30\ cm$ field of vision. Unique to the system created by Burnham and Brownell was a coding scheme that enabled smaller sodium iodide crystals to be encoded by fewer, larger photomultipliers, hence decreasing cost and enhancing spatial resolution [55].

Chesler rotated the MGH positron camera to acquire several views, which were subsequently filtered and back projected to generate trans axial tomographic images. Chesler also captured a transmission image using an external source of Ga^{68}, which provided an accurate attenuation correction for each line-of-response between coincidence detectors for each projection. This allowed us for avoiding distortion in the 3D reconstructed image and the derivation of quantitative tissue radioisotope concentration estimates. In 1971, he presented this method for the first time at the 18th annual meeting of the Society of Nuclear Medicine in Los Angeles, California [56]. And in 1972, at a meeting on tomographic imaging in nuclear medicine, the proceedings of which were published in 1973. He compared his computational method for eliminating out-of-plane activity with traditional tomography, in which the activity was blurred but not eliminated [57].

In St. Louis, Missouri, around 1974, TerPogossian, Phelps, Hoffman, and Mullani re-evaluated the physical properties of a positron tomograph to ensure the ability to quantify regional concentrations of the tracer in tissue. This was the next significant advancement in instrumentation. They concentrated on optimising the physical design of the scanner to limit the registration of unwanted coincidences and scattered events, as well as dead time losses caused by the high flux of incident gamma rays on the detectors. To overcome these obstacles, a hexagonal array of sodium iodide scintillation detectors was built around a single trans axial plane and shielded with substantial side shielding. Similar to the MGH positron camera, apertures made of lead were installed before each detector to improve spatial resolution. To ensure proper sample inside the plane, they also adopted the MGH group's technique of physically moving the detector heads one inter crystal distance in discrete stages and slowly rotating the assembly around the trans axial plane [58, 59].

The St. Louis team demonstrated the ability to conduct quantitative measurements of the restricted tissue content of a positron-emitting radionuclide by minimising the impact of scattered coincidences acquired in their scanner design [60, 61]. These quantitative measurements have proven to be a significant characteristic of PET, where tissue uptake obtained from image voxels can be measured in absolute units of radioactivity. This can be accomplished by cross calibrating a phantom filled with radioactive fluid that is scanned in the scanner and aliquot samples taken from the phantom that is quantified in a well-counter or dose calibrator.

The most significant advantage of PET imaging over SPECT is its substantially better sensitivity. In SPECT, physical collimators reject photons outside a narrow angular range to estimate the incidence angle [62]. Both techniques have seen setbacks in recent years due to radiopharmaceutical supply issues, and both have advantages and disadvantages. The question of which modality will dominate in the future remains unanswered. However, the operational costs of PET scanners are one of the major downsides [46]. In addition, PET's application is constrained by the expensive supporting infrastructure. This includes the requirement for an on-site cyclotron to produce positron emitters with a short half-life. Moreover, the imaging process is lengthy [47]. The benefit of SPECT is that it can conduct investigations over a more extended period due to more widely available equipment and routinely used radionuclides having a longer half-life [63].

1.1.4 Single Photon Emission Computed Tomography (SPECT)

Single Photon Emission Tomography (SPECT) is a well-established, non-invasive nuclear medicine imaging modality frequently used in hospital studies to diagnose diseases. Cardiology, cancer, and neurology are the most significant diagnostic applications of SPECT. SPECT can noninvasively visualise and analyse metabolic and functional processes prevailing in a particular organ [64, 65]. SPECT imaging has undergone significant transformations due to technological improvements and improved therapeutic alternatives. It has arisen not only as a diagnostic tool but also as a prognosis instrument that can provide information on myocardial perfusion, ventricular function, and viability from a single test. In contrast to PET, SPECT physics theoretically permits images with high spatial resolution and the capacity to track tracer uptake over extended time intervals, such as hours or days. Due to the short half-lives of most tracers, PET imaging lacks this quality. In contrast to PET scanners, dual tracer imaging is simply achievable using SPECT compounds and a gamma camera system combined with a multichannel analyser using SPECT compounds [64].

The administration of a modest amount of a radiolabelled tracer to a patient enables SPECT imaging to visualise both anatomical and physiological processes. Depending on its bio-kinetic qualities, this labelled tracer is dispersed throughout the body to reveal the functional status of the organ of interest [65, 66]. The acquisition period and the tracer dose influence the raw data count density, and the patient's body impacts attenuation and scatter. The detector and collimator characteristics influence the procedure's resolution and sensitivity. These physical and technical limitations degrade the obtained data, typically resulting in reconstructed images with pixel values that do not accurately represent the activity concentrations [64].

1.1.5 History of SPECT

The discovery of radioactive elements marks the beginning of SPECT's history. The French physicist Antoine-Henri Becquerel's ground-breaking innovation on X-ray and the discovery of radiation laid the groundwork for numerous early twentieth-century scientific studies. In 1896, he discovered hazy apparitions on a photographic plate held near non-phosphorescent uranium salts. Then, he discovered that this was the result of radiation emanating from uranium salts [67]. Nevertheless, the term radioactivity was coined by Becquerel's PhD student Marie Curie, who, along with her husband Pierre Curie, began researching this phenomenon. In 1903, due to their contributions to the discovery of radioactivity, the trio was awarded the Nobel Prize in Physics. Marie Curie was awarded the Nobel Prize in Chemistry in 1911 for her contributions to the study of radioactivity. The Hungarian physicist George de Hevesy established the concept of radioactive tracing. It is based on the theory that because the human body cannot discriminate between radioactive and nonradioactive isotopes of an element at the molecular level, the radioactive isotope can reach the same organs as the element itself [68, 69]. Hevesy's innovative test contains growing a plant in a radioactive solution and tracking the radioactive solution to examine the plant's progress. Following his ground-breaking work, he discovered that radioisotopes could pass through physiological processes like any other molecule. He also observed that the plant absorbed only the amount of lead it needed. He realised that absorption is highly selective as a result. His concluding observations from this experiment concerned the durability of lead, which did not last forever and deteriorated at a definite rate [45]. Irene and Frederic Joliet-Curie created the first synthetic radioisotopes in 1934 by blasting nuclei with high-energy atomic particles. In 1935, they received the Nobel Prize in Chemistry for this achievement. After discovering new radioactive elements, Hevesy's study revealed that radioisotopes could also be localised in specific animal organs. This unconventional research paved the way for current nuclear medicine applications, for which he was awarded the Nobel Prize in Chemistry in 1943 [70].

Ernest Lawrence, the American physicist who developed the cyclotron, who was awarded the 1939 Nobel Prize in Physics, conducted additional pioneering work in developing biologically relevant radiotracers at the University of California, Berkeley. A *cyclotron* is a particle accelerator that produces high-energy particles to bombard material to produce isotopes [71]. In pursuing this breakthrough, his colleagues produced many of the most prevalent radiotracers used in nuclear medicine today, including Technetium-99m (Tc^{99}). The discovery of Tc^{99} by Seaborg and Serge in 1938 inaugurated the age of SPECT imaging [72]. Radioisotopes were initially used for therapeutic purposes, but their use was limited by the unavailability of detecting methods for high-energy photons

[58]. During the golden period of nuclear medicine, the most prevalent and rudimentary technology was planar imaging. Hofstadter's 1948 discovery of the NaI(TI) scintillation crystal, the scintillator most commonly employed in SPECT systems today, was a significant event. In 1949, the first image using an isotope was captured by a CaWO4 scintillator [73, 74]. The first focused collimators were introduced in 1952, and the first positron annihilation image was published in 1956 [75, 76]. The development of an imaging device did not commence until 1951. American physicist Benedict Cassen's revolutionary invention of a scintillation scanner paved the way for imaging equipment, where he demonstrated the dispersion of iodine radioisotopes throughout the thyroid gland [77]. In 1953, physicist Gordon Brownell and physician William Sweet created a detector that could catch gamma ray photons that were captured in synchronicity. This finally paved the way for another imaging approach in nuclear medicine, PET, which was already discussed [51, 78]. In 1954, David Kuhl devised a photo-recording scanner to detect the radiotracers' distribution. He made the first of many contributions to the field of medical imaging through this breakthrough [79].

Kuhl was among the first to develop a SPECT system based on a stationary scanner location and patient rotation [80]. This system was equipped with a computer for data processing and revolving scanners, while the patient's position remained stationary. This method led to the development of the modern SPECT scanner. While there is no definite inventor of the first SPECT machine, Kuhl is undoubtedly credited for its invention [81]. Based on the collimator and scintillation detector advancements, modern SPECT scanners have come a long way since their invention in the late 1950s.

1.1.6 Physics of SPECT

SPECT acquisition of the projection images is accomplished by rotating a gamma camera around the patient while collecting information into the digital matrix of a computer from all sampled angles. According to CT theory, just 180° of arc of projection views are necessary for accurate reconstruction [82]. However, the nuclear medicine gamma camera is not an ideal imaging technology; competing viewpoints are not identical. First, as the distance between the gamma camera and the subject being imaged increases, the camera's resolution declines. Second, a portion of Compton scatter is interpreted as photopeak gamma rays due to the camera's limited energy resolution. Thirdly, a part of an object's produced gamma rays is attenuated (absorbed) when they pass through an attenuating medium, such as a patient.

This phenomenon varies based on the attenuating medium's depth between the item and the gamma camera. Opposing projection views in clinical SPECT will never be identical. Therefore, most SPECT investigations require a full 360° rotation for accurate reconstruction [83].

1.1.7 SPECT Radiotracers

Radioactive decay is the natural process through which the nucleus of an unstable nucleus loses energy by the spontaneous emission of ionising radiation [84]. Radioactive decay modes include alpha decay, beta decay (divided into beta-minus and beta-plus decay), gamma decay, electron capture, and isomeric transition decay. These phenomena are critical in nuclear science and have practical applications in fields such as radiotracer studies and medical imaging [85]. Radionuclides or radioisotopes are unstable atoms exhibiting the property of radioactive decay and can be naturally occurring or artificially produced. Technetium-99m is one of the most frequently used radioisotopes in SPECT. It decays to technetium-99 via the emission of gamma rays of $140\ keV$ of energy. Technetium-99m (Tc^{99}) is usually produced by the longer-lived molybdenum-99 permitting on-site availability of the isotope for medical use [86]. Table 1.1 shows the typical radiotracers used in diagnostic nuclear imaging.

Table 1.1 The radioisotopes used in Nuclear Imaging for Diagnostic purposes.

Nuclide	Radiotracer	Decay Mode	$T_{1/2}$	Energy keV	Modality	Function
Tc^{99}	NaTcO4	IT	6.02 h	140.5	SPECT	General purpose
Ga^{67}	Ga citrate, Ga nitrate	EC	78.3 h	93, 185, 300	SPECT	Tumour detection
In^{111}	I salt	EC	67.8 h	171, 245	SPECT	Brain study
I^{123}	NaI	EC	13.2 h	159	SPECT	Thyroid study
Ti^{201}	Tl salts	EC	73.1 h	135,167	SPECT	Diagnosis of coronary artery disease
F^{18}	FDG, F-DOPA	β^+	109 min	511	PET	Oncology
O^{15}	O2, CO2, CO	β^+	2 min	511	PET	Neurology
C^{11}	CO2, CO, HCN, CH3I	β^+	20.4 min	511	PET	Cardiology
N^{13}	NH3	β^+	10 min	511	PET	Cardiology

1.1.8 Single Photon Detection: Data Collection

A gamma camera with single or several detector heads is utilised to detect photons emitted by the radiotracer. The active component of the detector head is typically a scintillation crystal capable of capturing incident photons not absorbed by the material of the physical collimator placed in front of the crystal [84, 87]. A collimator is made from lead or tungsten with a high probability of photon contact and many holes to restrict photon access to the direction parallel to the holes. Photons arriving at the collimator from other directions have an extremely high possibility of being absorbed by the collimator's septa [88]. Figure 1.3 shows the process of photon detection [81]. X and Y represent the position signals and X_d and Y_d are the detected positions in the projection image as the output of PMTs. As photons are emitted from regions of radiopharmaceutical uptake at various depths within the body, they may experience a variety of interactions with matter. Consequently, photons will reach the gamma camera detector heads either unimpeded or after being deflected from their initial emission direction [84]. Only photons that reach the detector in directions parallel to the collimator's holes will interact with the crystal, resulting in the crystal's ionisation. An appropriate crystal material must have a high interaction probability with incident photons. Typically, sodium iodide doped with thallium, NaI(TI), is used in gamma cameras. As a scintillation crystal, NaI(TI) has suitable properties for high efficiency in detecting photons in the energy range used in conventional nuclear medicine. In contrast, other materials may be better suited for detecting higher energies, such as the 511 keV annihilation photons in PET [7, 89].

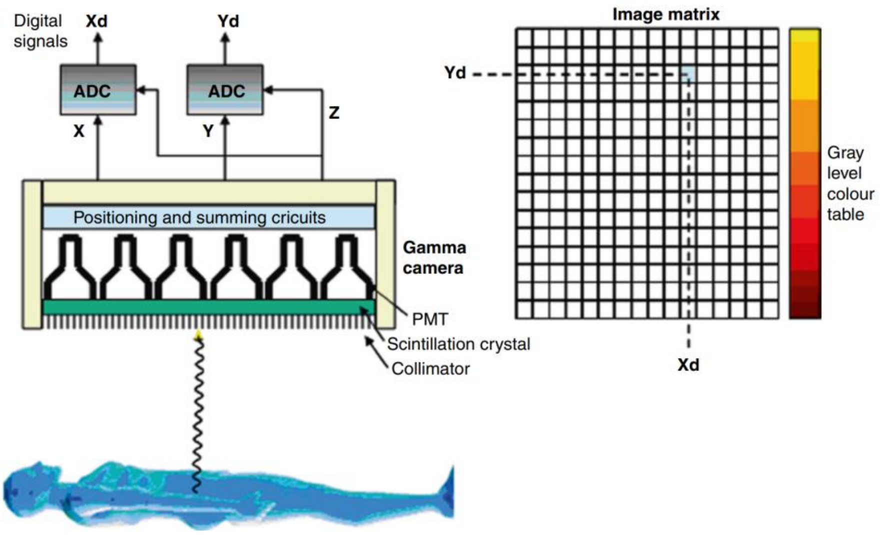

Figure 1.3 The gamma camera diagram and the process of photon detection [84].

De-excitation of the scintillation crystal happens by the emission of lower energy visible light photons, which can be detected by the photomultiplier tubes (PMTs) positioned behind the crystal. PMTs are devices that can transform scintillation light into an electrical pulse. The photocathode of the PMT converts the scintillation light from the crystal into electrons. These electrons will be accelerated by the electric potential between the metallic anodes of the PMT, causing gradually more electrons at each anode, thereby amplifying the initial signal into an electric pulse that the gamma camera's electronics can detect. The pulse processing by the system's electronics will determine the energy and position of the incident event, its acceptance within the predefined energy window and, following analogue to digital conversion (ADC), the event's coordinates inside the image matrix [7]. The calculation of the finer x, y coordinates from the coarser PMT array typically involves a technique known as "position reconstruction." In particle physics, PMT arrays are frequently utilized to detect and measure the energy and position of particles such as electrons, photons, and ions. When a particle passes through a material, the PMT array produces and detects a cascade of photons. Each PMT produces a signal proportional to the number of particles it detects [90]. The signals from all PMTs are then combined to create the aggregate signal. Using a mathematical algorithm, the signals from the PMTs are analysed to determine the position of the particle. A prevalent technique is known as ”centroiding”. This requires calculating the PMT signals' centre of mass in both the x and y directions. Consider the centre of mass to be the average location of all particles detected by the PMT’s. The mass centre can be determined using a weighted sum of the PMT signals. The weight ascribed to each PMT signal is proportional to its distance from the array's centre. PMTs closest to the array's centre are assigned a greater weight, while PMTs further away are assigned a smaller weight [91].

In Single Photon Emission Computed Tomography (SPECT), transverse images of the activity distribution within the body are derived from a series of planar projections acquired with the gamma camera from various angles around the patient [92]. Each planar image acquired at a specific camera rotation angle, known as a projection, provides all the details at each pixel regarding the integral of counts over the body. Typically, to create cross-sectional images of the activity distribution throughout the body, a sequence of projection data over the whole rotation of the camera around the subject is necessary. This is accomplished using image reconstruction methods [84, 87, 93].

1.1.9 SPECT Collimators

Comparable to the range of lenses available for reflex cameras, the design of SPECT collimators is highly variable and must be suited to the imaging challenge at hand [94].

Parallel Hole Collimators: The honeycomb is an ideal analogue for the most popular type of collimator, the parallel-hole collimator. Collimators are composed of several parallel channels that are generally long and narrow and arranged in a dense and regular lattice, as shown in Figure 1.4a. The channels are lengthy and narrow to confine the view of the imaged item from each detector element: Ideally, the detector should only observe the activity along a single straight line across the object through each channel. This is comparable to stating that activity in each portion of the object will only be imaged at a single position on the detector, as defined by how the collimator produces the object's projection. Scintigraphy (and, by extension, SPECT) derives its fundamental piece of information from the overall activity present along the line of response (LOR). This is quite similar to computed tomography, in which the essential data acquired is the total X-ray attenuation along the LOR formed by a detector element and the focal spot of the X-ray tube [92]. The collimator channels have a finite width and length; thus, photons from approximately parallel lines are detected. This has two consequences. First, because larger and shorter channels allow more photons to pass, sensitivity increases; this improvement enhances the counting statistics and, consequently, reduces image noise. Second, broader and shorter channels have a larger acceptance angle, meaning they loosely define the LORs, diminishing spatial resolution. This compromise leads to the initial design decision: high resolution or high sensitivity [94, 95].

Converging Collimators: Magnification is one of the most distinguishing characteristics of SPECT collimators. When all channels are parallel, the object is projected in parallel lines onto the detector. Therefore, the object's projection is the same size as the object. However, it is not the case if the collimator's holes converge, as shown in Figure 1.4b. The distance between the focal locus and the collimator is called the collimator's focal length. At the focal locus, magnification relies on the object's distance from the collimator and is greatest. Under typical circumstances, both fan and cone beam collimators amplify. In a fan-beam collimator, magnification occurs along only one of the collimator's two dimensions, often the transverse direction, whereas a cone-beam collimator also magnifies along the axial dimension.

Diverging Collimators: The diverging collimator is designed in such a way that the holes diverge away from the crystal, as shown in Figure 1.5a. This can potentially increase the field of view but, by default, also reduces the image size. Diverging collimators are used to image objects whose size exceeds the field of view of a detector equipped with a parallel hole collimator. As it is a collimator with variable-angle holes, the field of view increases as the object moves away from the collimator. Also, resolution (depth) suffers a minor degradation and worsens as the distance from the collimator's face increases. The diverging collimator is utilised on smaller field-of-view cameras and is beneficial for imaging the lungs, liver, and bones [96].

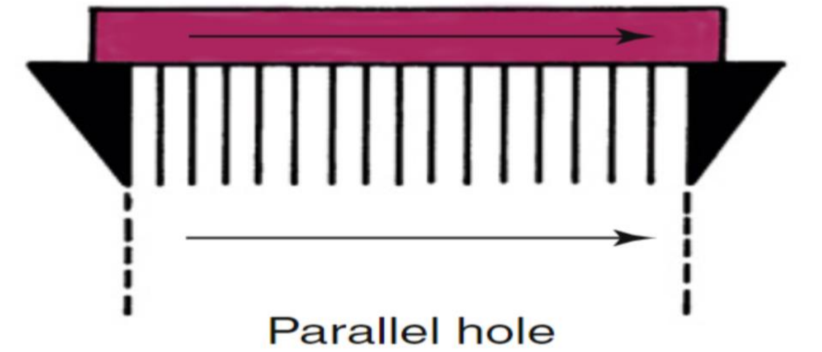

(a)

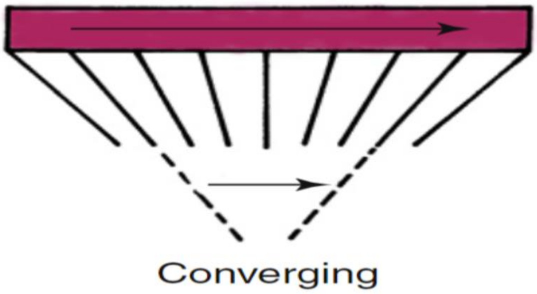

(b)

Figure 1.4 SPECT collimators. (a) Parallel hole, (b) Converging [97].

Pinhole Collimators: The pinholes function similarly to a pinhole camera (camera obscura). The pinhole produces a mirrored and inverted image of the object, which must be considered during image reconstruction. Only photons that can pass through the pinhole without being absorbed by the collimator are considered as incident. Pinhole collimators were the earliest designs; they are experiencing a resurgence because of the recent popularity of small animal imaging. Pinholes and cone-beam collimators share the same beam geometry, as shown in Figure 1.5b. A crucial distinction is that sensitivity is most remarkable, and the field of view is lowest next to the collimator. Because a modest FOV is sufficient, these features have made pinholes particularly useful in imaging small animals [98, 99]. But they have limited their utility in human investigations. A noteworthy exception is the imaging of therapeutic dosages of I^{131} for which pinholes are particularly appealing because they can be fabricated from specific materials, and their geometry is more resistant to penetration than collimators based on septa [100, 101].

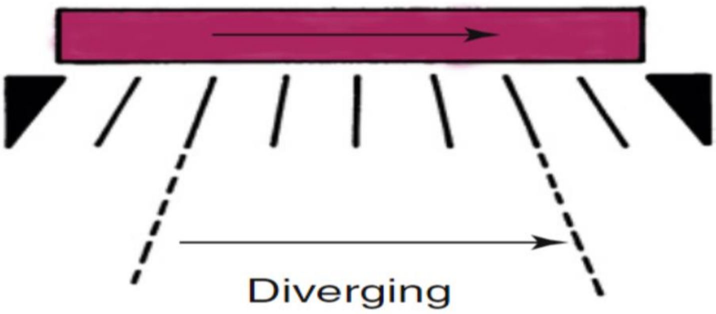

(a)

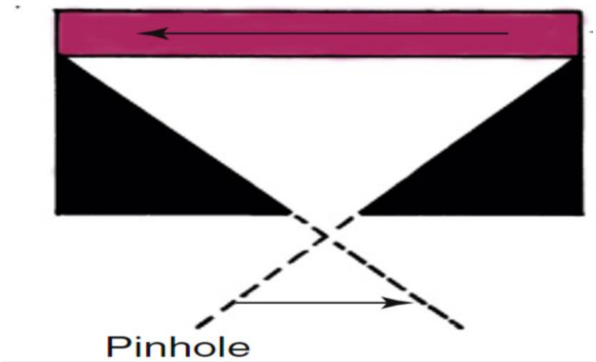

(b)

Figure 1.5 SPECT collimators. (a) Diverging collimator, (b) Pinhole collimator [97].

Multi-pinhole Collimators: Recently, this technology has been refined to include multi-pinhole collimators, resulting in sensitivity gains that scale linearly with the number of pinholes. In these setups, each pinhole forms a projection on the detector's plane. This method allows the acquisition of data with the exact resolution while increasing the overall sensitivity of the measurement. With multi-pinhole imaging, it is essential to ensure that the design of the collimator does not permit a considerable overlap of the projected data, or that processing software is available to compensate for the multiplexing effect of the overlapping images. Even with a sophisticated compensation algorithm, it is impossible to entirely eliminate all overlap artefacts for objects of all sizes inside the imaging field of view [102, 103].

1.2 Performance Parameters

Sensitivity and resolution are critical performance parameters that underpin imaging quality and reliability. Sensitivity assesses the system's ability to detect and capture signals accurately, while resolution determines its capacity to distinguish closely spaced objects, especially relevant in fields like microscopy and radiology. These parameters form the basis for quantitatively evaluating the imaging system's capabilities [104].

1.2.1 Sensitivity

In nuclear medicine or PET imaging, sensitivity can be defined as the ratio of true counts detected by the system to the actual number of emitted gamma-ray events from a radioactive source:

$$s = \frac{TP}{TP - FN}$$

where Sensitivity (S) represents the measure of the imaging system's ability to correctly detect and capture true positive cases. True Positives (TP) are the cases where the imaging system correctly identifies and captures the signal or target of interest. False Negatives (FN) are the cases where the signal or target is present but not detected by the imaging system.

1.2.2 Resolution

Resolution in imaging can be defined in different ways, depending on the specific application and modality. One common aspect of resolution is spatial resolution, which focuses on the ability to distinguish between two closely spaced objects. It is often characterized by the Full Width at Half Maximum (FWHM) of the Point Spread Function (PSF). The FWHM represents the width of the PSF at half of its maximum intensity and is related to the minimum resolvable distance. Mathematically, the spatial resolution can be described as:

$$R = FWHM = 2.355.\partial$$

where R is the resolution (spatial resolution), $FWHM$ is the Full Width at Half Maximum, and ∂ represents the standard deviation of the Gaussian function characterizing the PSF.

1.3 Technical Pitfalls and Limitations of Collimator-Based SPECT: SPECT in Animal Research

This section explores the technical pitfalls and limitations encountered when employing collimator-based SPECT in the context of animal research, which explicitly states the research's problems.

1.3.1 Statement of the Problem

Nuclear medicine techniques, PET and SPECT, offer a non-invasive alternative to studying biological processes in vivo. The same animal may be used for multiple longitudinal investigations before and after particular pharmacologic or experimental manipulations, few animals are used, and each animal can act as its control [82, 103]. Small laboratory animals have been given access to anatomic imaging technologies like ultrasonography, CT, and MRI [104].

Technical issues and limitations with spatial resolution arise due to the size of the animals involved. Therefore, if animal imaging studies match the quality of human research, the spatial resolution of the animal studies must be 10 times higher [63]. Despite the reduction in the size of volume resolution components from 1 cm to 1 m, the signal per voxel element should be roughly the same between experimental and human investigations so that the system's overall sensitivity remains appropriate. Increasing efforts have been made to adapt SPECT and PET methods for imaging small animals [63]. SPECT generally have 50-100 times less detection sensitivity and $3-4$ times less spatial resolution than PET [105]. Another significant disadvantage of SPECT is its temporal resolution or count rate capabilities [106]. This refers to the system's ability to respond quickly to changing physiologic events across time. The spatial resolution of small objects positioned at the collimator opening can be significantly enhanced using a pinhole collimator. Therefore, designing a pinhole SPECT imaging system for tiny animals might be beneficial. However, a significant downside is lower sensitivity or count efficiency, which necessitates more significant radioactivity or more extended acquisition periods [107].

The SPECT image is obtained by rotating the camera's head around the object or by rotating the animal in front of the camera. In order to boost spatial resolution, non-commercially accessible pinhole apertures as narrow as $1.0\, mm$ have been evaluated for research purposes, resulting in spatial resolution of $1 - 2\, mm$. The ensuing drop in sensitivity can be compensated by increasing the number of camera heads and employing larger quantities of radiopharmaceutical or higher specific radioactivity [108-110].

Human studies typically only require parallel hole collimators for clinical SPECT, as the resolution is not a relevant consideration. Clinical imaging technologies lack the required resolution and sensitivity to capture images of animals that are significantly smaller than humans. However, better-resolution images are essential in preclinical mouse studies to visualise minuscule structures and their physiological processes. To image objects of this scale, a different technology is necessary; pinhole collimation has become an absolute necessity. Although this technology applies to clinical systems, it is currently primarily used in preclinical SPECT imaging systems [111].

The rapidly advancing knowledge of molecular biology has encouraged the exploration of innovative therapeutics targeting specific sites in molecular pathways associated with cardiac illnesses, neurodegenerative disorders, cancer, and numerous other pathological processes [112]. Identifying the role of a molecule in an in vitro model of a disease process does not necessarily translate to knowledge of its interactions with other molecular processes in vivo. Furthermore, due to logistical and ethical considerations, few disease processes can be thoroughly researched in human patients [113].

Small-animal models provide a linkage between molecular discoveries and the implementation of clinically appropriate diagnostics or therapies. Increasing emphasis is placed on the necessity for these models to adequately represent the disease and the environment in which the critical molecular processes occur. Xenograft mice models of cancer, for instance, are simple to construct but are not regarded as very useful for understanding the molecular connections underlying carcinogenesis. Transgenic models employing oncogene activation or tumour suppressor inactivation have advanced to the point where tumours can be produced spatially and temporally by deleting specific genetic sequences [113-115]. Studies using small-animal models rely on tissue sectioning and microscopy or, in the case of radionuclide-based assays, tissue g-counting and autoradiography for a significant amount of time following euthanasia. These technologies restrict researchers' potential to investigate a single animal longitudinally and necessitate the laborious assembly of histologic or autoradiographic sections. In essence, it is considered that the compilation of several images from various animals adequately represents a continuous biochemical process [113].

Using molecular imaging to examine dynamic biological processes in small animal disease models is overcoming these constraints. SPECT and PET provide numerous benefits in these applications, including a variety of radionuclide half-lives, relatively simple radiolabelling chemistry, low cost, and wide availability. Nuclear imaging follows these tracers at nanomolar and picomolar concentrations to explain molecular interactions critical to the diseases' onset and progression and investigate the biological relevance of drug candidates and potential imaging agents in streamlined development methodologies [113, 116]. Over the past decade, the expansion of these nuclear imaging applications has further prompted the academic and corporate development of SPECT and PET systems tailored for small-animal imaging.

However, the spatial resolution of these approaches is restricted to 1-2 mm [117-119]. Due to the small size of rat subjects, spatial resolutions must be at least ten times greater than humans. In addition, the sensitivity must be sufficient to provide an acceptable image. Cancer is caused by a small number of cells undergoing malignant change. However, current nuclear imaging technology cannot detect such a small change. It would be impossible to investigate and prevent the crucial early phases of oncogenesis. As a result, there is a pressing need to improve spatial resolution, as most research interests require less than $0.1\ mm$ precision. An enhanced spatial resolution would improve the SNR and would be better at pinpointing the location of tiny lesions.

The amount of effort devoted to achieving high spatial resolution for brain SPECT is testament to its significance. It would benefit the clinical evaluation of brain lesions and physiological investigations to understand the functioning of the brain [120]. Several commercial multi-head devices were explicitly designed for SPECT brain imaging, and various research prototypes and commercial brain imagers have been introduced [121-123]. However, the need to minimize patient injections while generating diagnostically valuable SPECT images exceeds the requirements of conventional SPECT and necessitates unique concepts in both the diagnostic and therapeutic realms. Even when covering a large region, detectors with a higher resolution remain prohibitively expensive [118]. Multi-pinhole and pinhole SPECT mitigates the constraints of the detectors' resolution by substantially amplifying the object on the detector to project an adequately enlarged image of a broad region of the object. However, a large detector surface area is needed. To prevent projections from overlapping, a restricted number of pinhole cameras are used to encompass the object being imaged. The resulting cumbersome camera with a small number of pinholes is rotated around the object to obtain projections at an appropriate increment of angles. Recent developments in detector resolution have drastically altered the requirements for pinhole and multi-pinhole devices. High-resolution detection technologies necessitate a lower magnification [124-126]. Focusing the gamma rays through the pinholes is a realistic method for taking advantage of the most advanced detector technologies. This could be achieved by augmenting SPECT with a focusing element that focuses the radiation onto a focal point on the detector's crystals. However, gamma rays cannot be focused using traditional refractive optics [127]. Reflective grazing angle focusing is successfully used where there are no space constraints, such as the Chandra x-ray space telescope [128]. A refractive focusing lens, the Laue lens, originally developed for astronomical x-ray imaging, is a promising option.

1.4 Lightfield Imaging

The concept of lightfield imaging goes back to integral photography first introduced by Lippmann in 1903 [129]. In 1936, Arun Gershun defined the lightfield as the light intensity moving through every point in space in every direction [130]. In 1991, Adelson and Bergen explicitly developed the seven-dimensional "plenoptic function" to describe the visible light emitted by all objects in the universe to the human eye [131]. This function is characterized by the camera's three-dimensional coordinates, the two dimensions (angular or cartesian) of the view direction, the wavelength, and the time. Lightfield cameras offer advanced features in postprocessing, such as refocusing after the image is being captured and point of view shift [132]. In currently available SPECT systems, it is impossible to refocus images at different angles after the patient is scanned.

To apply the lightfield concept to current diagnostic SPECT imaging systems, there is a need for optics capable of focusing gamma rays. However, for high-energy photons focusing, the microlens array used in light field cameras cannot be used [133]. As a prospective insight to advanced SPECT imaging, I introduce a Laue lens SPECT based on gamma focusing by diffraction. The concept of lightfield imaging in the envisioned lens-based SPECT is discussed in more detail in Section 4.2. Lightfield imaging, in this context, involves capturing the intensity of the gamma rays and the direction from which they originate. This additional directional information can be utilized to extract depth or 3D information from the reconstructed images.

By incorporating the lightfield concept into SPECT imaging through a Laue lens, it is anticipated that the spatial resolution and depth information of reconstructed images could be enhanced, leading to improved diagnostic capabilities. However, it's important to note that the practical implementation of such a system would necessitate significant technological advancements and further research to address challenges related to the design, fabrication, and integration of Laue lenses into SPECT imaging systems.

1.5 Research Objectives and Motivation

The Laue lens is a likely contender to tackle the constraints of conventional SPECT systems, as a possible means of enhancing resolution and sensitivity, breaking the trade-off between the two. The distinctive characteristics of crystal diffraction make it possible to design monochromatic imaging lenses sensitive to only a small band of gamma rays' energy. The lens captures radiation from a relatively large solid angle and concentrates it on a small point on the sensor surface.

Two distinctive features of the Laue lens are that, unlike conventional pinholes used in imaging systems, its effectiveness does not decline with the source size, and it can focus on microscopic objects. This renders the focusing apparatus highly insensitive to background noise caused by the scattering of the primary gamma rays in the body and other gamma ray sources. This monochromatic characteristic thus improves the signal-to-background ratio and enhances the ability to detect minute sources. The sensitivity of a single lens system is comparable to that of traditional systems for large sources. Nonetheless, it has lower background noise. Moreover, the lens system maintains the same overall efficiency and is considerably more effective when imaging sub-millimetre sources.

Radionuclide imaging requires a paradigm shift due to the acknowledged limitations of current nuclear imaging techniques. In this current research, a unique system capable of imaging gamma rays without relying on absorbent collimation is developed to circumvent its primary effect on the resolution-sensitivity trade-off, which is a significant problem in existing nuclear imaging systems. A submillimeter resolution and exact source localization could be attained by mounting the imagined Laue lens collimator on a mechanical system/arm that adjusts the focal length based on the desired depth.

This dissertation aims to examine the proposed novel lens-based SPECT based on Laue lens gamma diffraction. The envisioned system has the potential to overcome the limitations of conventional SPECT for small animal imaging and tumour detection. The initial system design is demonstrated to be capable of detecting volumes in the nano-litre range at a substantially enhanced submillimeter resolution compared to the existing SPECT designs. For the proof of concept, several Monte Carlo SPECT simulations tailored to the application presented in this thesis were developed in stable and well-established platforms with realistic and high-fidelity physics. The three Monte Carlo toolkits are MATLAB, GAMOS and GEANT4. The performance characteristics of the novel lens-based SPECT augmented with a Laue lens and the associated problems for overcoming the inadequacies of the conventional SPECT are analysed. Based on the research findings, the proposed system has the potential to revolutionize SPECT imaging technology by combining tomosynthesis and lightfield imaging, eliminating the requirement for mechanical components. What makes this system unique is its ability to independently capture data from each lens, allowing for specific perspectives of the object to be obtained. Alternatively, by integrating the data from all three modules, a comprehensive three-dimensional image can be generated, providing precise details regarding the object's size and location. The achieved resolution is exceptional, leading to significant advancements in various SPECT applications such as oncology, thyroid, breast, and infant imaging. This innovation opens up new avenues for studying organs at a sub-organ level and enables the early detection of lesions.

1.6 Research Contributions to Knowledge

- A significant contribution of this thesis lies in investigating a novel lens-based SPECT design that incorporates a Laue lens instead of the pinhole. This research endeavour explicitly addresses the persistent challenge of reconciling the trade-off between resolution and sensitivity in conventional SPECT systems, focusing on their application in small-animal imaging and early tumour detection. By surpassing the limitations imposed by traditional in vivo imaging techniques, the findings of this study provide novel avenues for achieving enhanced spatial resolution and improved efficacy in identifying nano-volumes that represent tumours just at their early stages. Consequently, this innovative SPECT design holds substantial potential for redefining the forefront of small-animal and cancer SPECT, thereby substantially impacting the respective domains.

- One of this study's scholarly contributions involves identifying tailored parameters for the Laue lens, customized explicitly for medical imaging applications and specifically for SPECT imaging, specifically for the proposed novel lens-based SPECT system. While the design parameters of the envisioned lens bear similarities to those commonly employed in astrophysics applications, it is essential to note that the design process significantly diverges due to inherent differences between the two fields. In astrophysics, lens optimization primarily focuses polychromatic radiated hard X-rays originating from remote celestial sources, which are assumed to propagate in parallel. In contrast, nuclear imaging scenarios entail the emission of divergent monochromatic photons, exhibiting propagation in various directions. Consequently, the design of the lens for medical imaging necessitates a distinct set of considerations. In this study, the selection of materials for the lens elements was guided by applying a Monte Carlo simulation, enabling the evaluation of different single-crystal materials with preferable lattice plane orientations.

- Another notable contribution of this thesis involves the development of a tracking Monte Carlo simulation environment using MATLAB. This simulation environment serves as a tool for predicting the distribution of focused photons. It has been specifically tailored to align with a SPECT gamma camera’s setting, enabling precise photon behaviour estimation. Additionally, the thesis proposes a novel system design encompassing three different geometries: single, modular, and multi lens-based SPECT. These configurations incorporate an array of Laue lenses positioned at the centres of the pinholes on a multi-pinhole SPECT collimator. This innovative approach holds promise for advancing SPECT imaging techniques and provides valuable insights into the potential integration of Laue lenses in various system arrangements.

- It is crucial to develop the appropriate 3D image reconstruction algorithms to evaluate the performance of each new imaging system. To this end, this thesis' noteworthy contribution lies in developing 3D image reconstruction algorithms customized for the lens-based SPECT system. While the developed algorithms for the lens-based SPECT would unquestionably differ from those presently used for conventional SPECT or other tomographic modalities, it should be possible to adapt existing techniques to interpret images acquired with the Laue lens. In this study, I developed three different customized 3D reconstruction methodologies as a first attempt to reconstruct 3D images from the Laue lens projections. These 3D reconstruction algorithms demonstrate the first effort to reconstruct a meaningful 3D image from Laue lens projections. Using the proposed algorithms, significant results have been observed from the lens-based SPECT data.

- As a critical contribution of this thesis, the attained performance was critically evaluated compared to the SIEMENS parallel LEHR and Inveon multi-pinhole SPECT systems (which were modelled within the scope of this research), based on two figures of merit: resolution and sensitivity. Furthermore, the performance parameters were systematically assessed across the transverse and sagittal field-of-view (FOV) to enable comprehensive analysis and precise assessment. To validate the system's capacity for accurately mapping precise shifts and depths of on-axis and off-axis sources, the depth and shift observed in the 3D reconstructed images were meticulously compared to the experimental depth and shifts applied to the phantom. This rigorous evaluation enhances the understanding of the system's capabilities and provides valuable insights for future research and development in the field.

- The challenge in developing new conceptual metrics to characterize the proposed system as a "conventional one" and to demonstrate how this concept applies to practical/clinical use is essential. Moreover, it is important to have a precise model of its response to accurately assess its performance and repeatability. In this thesis, different simulation environments were developed for the proposed lens-based SPECT design. The first implementation was in MATLAB, the second was in the GAMOS toolkit, and the third was in the GEANT4 toolkit. The obtained projection and 3D reconstructed images in each of the environments were calibrated against each other for the proof of concept.

- Another contribution of this thesis involves addressing the challenge of developing novel conceptual metrics to characterize the proposed system as a "conventional one" and demonstrating its practical and clinical applicability. Moreover, it is important to have a precise model of its response to accurately assess its performance and repeatability. This thesis focuses on developing various simulation environments for the proposed lens-based SPECT design to accomplish these objectives. The first implementation was in MATLAB, the second was in the GAMOS toolkit, and the third was in the GEANT4 toolkit. The obtained projection and 3D reconstructed images from each environment were calibrated against each other for the proof of concept to ensure the reliability and consistency of the simulated results across the different platforms.

- A significant contribution of this thesis involves addressing the emerging interest in Laue gamma diffraction as a powerful technique for developing high-energy ray focusers. Conducting physical experiments on Laue lens behaviour presents itself as a fundamental tool for understanding physical issues and elucidating the main concept in gamma diffraction. However, Laue lens manufacture is quite challenging as it requires high precision in positioning and aligning diffractive crystals of various elements. Readily feasible alternatives to physical experiments are computer simulations of the Laue lens in a stable state-of-the-art high-energy physics simulation environment such as GEANT4. However, as of the start of this study, the Laue diffraction process was not implemented in any of the available Monte Carlo simulation platforms so far. To address this challenge, I contributed to extending GEANT4's functionality by developing a GEANT4 plugin function to simulate Laue lenses. I designed and implemented the first set of Monte Carlo simulations in GEANT4 for a gamma diffraction example. By bridging the gap between theoretical concepts and practical experimentation, this thesis significantly contributes to the understanding and exploration of gamma diffraction through the application of advanced simulation techniques, the developed example presents the first attempt to model X-ray and gamma rays focusing based on Laue diffraction in the GEANT4 toolkit using an advanced example in its early conception.

- Aspects of the newly proposed system are discussed, considering its possible clinical application as a tumour detection tool that takes maximum advantage of the unique properties of the Laue lens focusing capability. By placing the envisioned Laue collimator on a mechanical system/arm that adapts the focal length in response to the desired depth, a submillimeter resolution and precise source localization could be achieved.

- Based on the simulated experiments and the research findings, the proposed system allows discrimination between adjacent volumes as small as $0.113\,nL$, which is significantly smaller than any conventional SPECT or PET designs can currently detect or resolve. Moreover, the $0.1\,mm$ achievable spatial resolution is decoupled from sensitivity, which is in stark contrast to the existing collimators that suffer from the resolution-sensitivity trade-off and are limited to a resolution of $2\,mm$.

1.7 Thesis Organization

This dissertation is organized into nine chapters which are summarised briefly below.

Chapter 2 examines the research body of evidence on SPECT collimator and detector design optimization. Moreover, the emerging trends in SPECT imaging based on lightfield imaging are reviewed in light of the most recent technological advancements, and the applications of the Laue lens from astronomy to nuclear imaging and radiotherapy are explored. The methodology followed in this work, the simulation tools, and the designed environment set-up are discussed in Chapter 3.

Chapter 4 discusses the gradual development of the dedicated Mote Carlo simulation used for designing and optimizing the Laue lens tailored for the envisioned SPECT application. Moreover, it describes the initial design parameters and the tracking Monte Carlo models for the envisioned system. I started by proposing a single lens-based SPECT geometry.

In Chapter 5, I report and elaborate on the attempts to establish a high-resolution SPECT technique augmented with a Laue lens with further optimized geometries. For the purpose of boosting sensitivity, I proposed a single lens-based SPECT system fitted with partially curved detector modules and Laue lens arrays, called modular lens-based SPECT. The multi lens-based SPECT is a more complicated geometry consisting of an array of diffraction lenses placed at the pinhole centres of a multi-pinhole SPECT collimator. This chapter thoroughly examines the imaging capabilities of these two novel geometries.

In Chapters 4 and 5, the designed MATLAB environments incorporated realistic physical interactions, which count for the possible absorption and attenuation of the envisioned lens-based SPECT with three different geometries. However, it was running under ideal detector conditions. To ascertain the validity of the argument presented throughout this thesis, I started examining the possibility of designing a real detector design incorporated with the augmented collimator with a Laue lens.

Chapter 6 extends this research by proposing an alternative method to simulate the effect of focusing the gamma rays at the sensor plane and simulate detector response due to the focused photons projection in the GAMOS/GEANT4 toolkit. However, the study was limited because the simulation of waved-based properties as the diffraction process is not yet implemented in any of the available Monte Carlo toolkits. The methodology followed in this work is thoroughly discussed in this Chapter.

Chapter 7 discusses the design foundation and implementation of the first set of models in GEANT4 for Laue lens diffraction as the first attempt to model X-ray and gamma rays focusing based on Laue diffraction in the GEANT4 toolkit using an advanced example in its early conception. This chapter presents the conducted case studies for the lens-based SPECT incorporated in a well-known SPECT configuration which is the SIEMENS Inveon multi-modality system.

Chapter 8 presents the set of Monte Carlo models in GAMOS for the Laue lens diffraction. Several case studies are presented with the designed detector parameters. The first is a single lens in a pinhole with a one-point source. The second is a single lens in a pinhole with a three-point source. The third and fourth case studies are for multi Laue lens in multi-pinhole configuration with one and three-point sources, respectively. Moreover, for comparison purposes, I implemented the SIEMENS LEHR SPECT geometry currently used in clinical applications in GAMOS to compare the performance with the proposed lens-based SPECT based on the proposed detector configuration.

Finally, Chapter 9 presents a comprehensive summary of the study's key components. It provides an overview of the research findings and their significance, highlighting the implications and practical applications derived from the results. Each chapter's main points are summarized, and their contributions to the research are outlined. The concluding remarks encapsulate the main takeaways and insights gained from the study. Furthermore, this chapter proposes implications for future improvement work, suggesting further exploration and development areas based on the research outcomes.

2. Literature Review

Nuclear imaging is one of the leading medical imaging techniques. It is used for acquiring functional images of the body's internal structures. It examines the organs' physiological processes at the cellular and molecular levels. Nuclear imaging has been recognized as having a substantial impact on all medical fields, most prominently in detecting cancer in its early phases by identifying anomalies. Functional imaging is the backbone of particular disciplines, such as the early detection of heart illness and brain disorders.

Single Photon Emission Computed Tomography (SPECT) is a functional nuclear imaging modality capable of non-invasively reconstructing the three-dimensional distribution of the injected radiotracer. Optimizing the collimator geometry for a given number of pinholes in a multi-pinhole (MPH) SPECT has proven to be a challenging task and motivated a number of researchers to develop a variety of SPECT designs. Optimizing and increasing the number of pinholes in the SPECT imaging collimator would lead to significant advances in early cancer detection. However, existing nuclear imaging techniques are hampered by several limitations that hinder image reconstruction quality. Initiatives have been undertaken to develop a SPECT imaging system with higher resolution. Researchers continued to design new collimators by optimizing the number of pinholes, their pitch, and their radius [134-136]. Collimator-free gamma cameras for SPECT applications were proposed [137]. The primary objective of these systems is to circumvent the considerable collimator influence on the resolution-sensitivity trade-off. However, none of these solutions was evaluated for an actual SPECT application.

This chapter is structured as follows: Sections 2.1 and 2.2 thoroughly examine the corpus of research on SPECT collimator and detector design optimisation. It provides insights and expert comments on the direction and future of SPECT design research. Moreover, it investigates research that examines the impact of pinhole size, shape, material, and geometry on the performance and resolution of SPECT imaging in identifying the optimal collimator design and their effects on the final 3D reconstructed images. Section 2.3 discusses the proposed techniques to mitigate the impact of multiplexing, coded aperture SPECT imaging, system tailoring, and task-based imaging technologies that gave rise to adaptive SPECT. The recently demonstrated technologies and geometry for SPECT detectors and the approaches available to enhance the scintillator's light extraction are also investigated. Section 2.4 discusses the gamma focusing methods. The emerging trends in SPECT imaging based on lightfield imaging are reviewed in light of the most recent technological advancements, and the applications of the Laue lens from astronomy to nuclear imaging and radiotherapy are explored in Section 2.5. Sections 2.6 and 2.7 present the 3D image reconstruction concept and the chapter summary, respectively.

2.1 SPECT Collimator and Detector Optimization Methods

2.1.1 Collimator Optimization Methods

The collimator is principally responsible for the reconstructed images' low sensitivity and resolution in current SPECT systems. Parallel-hole and pinhole collimators are two prominent collimator designs. By adjusting the thickness of the septa and the diameter of the pinhole, it is possible to design parallel and multi-pinhole collimators with different geometries [138]. A crucial aspect of collimator design is that the spatial resolution drops dramatically as the object's distance increases. Nonetheless, the change in sensitivity is constant for parallel-hole collimators, which rises for converging collimators, and falls for pinhole and diverging collimators [139]. Thus, the collimator's design parameters significantly affect the imaging system's overall performance [140]. Particular attempts have utilized numerical ray-tracing techniques to analyse the penetration components in the collimator, including septal penetration and septal scatter, the penetration of photons through the collimator septa, and photon scattering in the collimator, respectively. Moreover, while designing the septal thickness, special care must be taken to ensure that the number of gamma photons that pass from one pinhole to the adjacent is negligible [141]. However, restricting photon penetration by increasing septal thickness would improve resolution at the expense of sensitivity. A parallel-hole collimator with cone-shaped holes was developed to combat photon penetration while retaining system sensitivity and resolution [142]. Figure 2.1a depicts the cone-shaped pinholes in a parallel-hole collimator with all the pinhole measurement and parameters presented, while Figure 2.1b shows Monte Carlo simulations for two-point sources with different source intensities and radiotracers positioned at various distances from the collimator. The performance of the developed collimator was compared to that of parallel-hole, high-energy, general-purpose collimators.

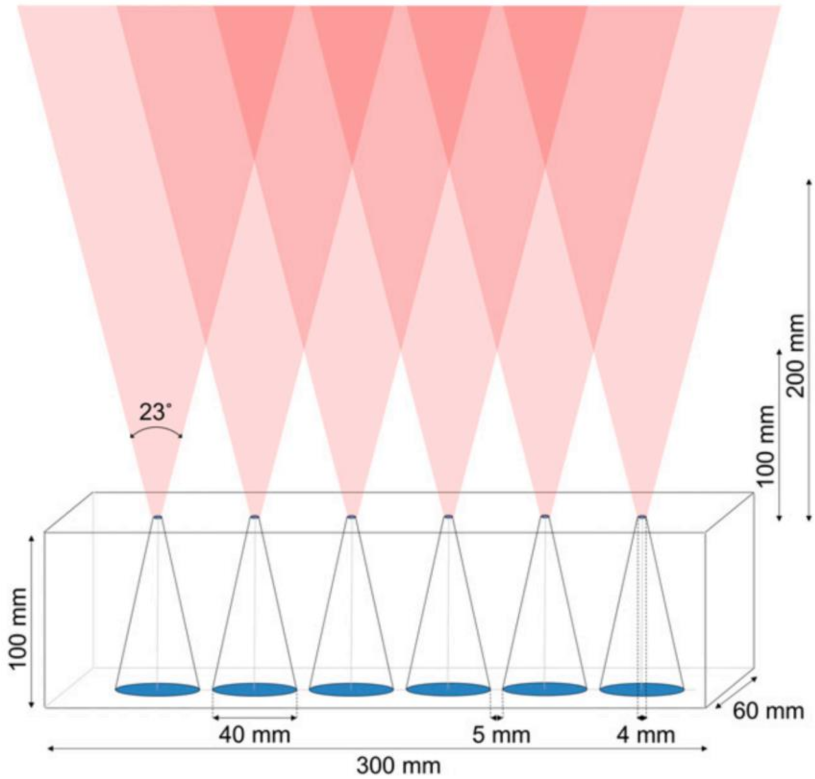

(a)

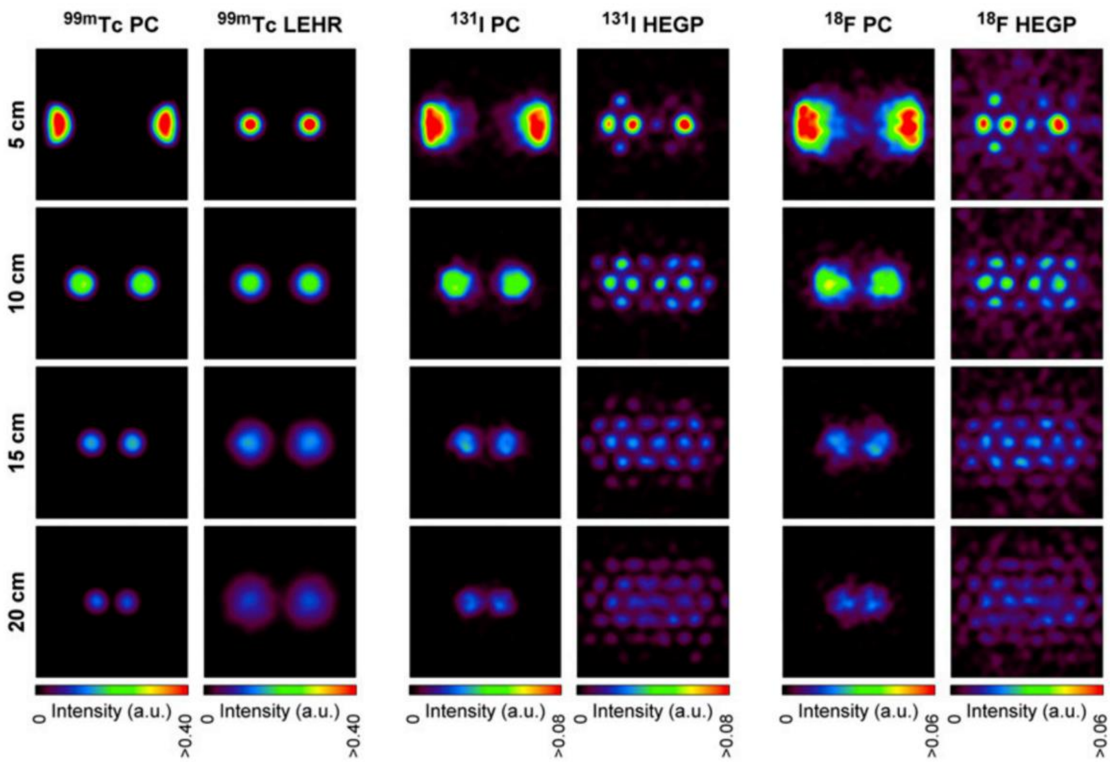

(b)

Figure 2.1 (a) Prototype of the cone-shaped pinholes in a parallel-hole collimator [9], (b) Monte Carlo simulations for parallel-hole collimator with cone shaped pinholes [142].

Due to the significant drop in photon penetration, the proposed pinhole design has resulted in a sharper PSF than conventional collimators while maintaining superior image quality compared to the parallel collimator. The concern of the small animal imaging has imposed restrictions on the minimum accepted system resolution while keeping the sensitivity unimproved due to the sensitivity-resolution trade-off. Ivashchenko et al. developed a SPECT collimator design for an ultra-high sensitivity SPECT while maintaining a high submillimeter resolution system for small-imaging animals [143]. This was accomplished by increasing the magnification factor. As depicted in Figure 2.2, the pinholes of the collimator were designed with varying opening angles, hence different field of view. The proposed method obtained a high submillimeter resolution while keeping the radiotracer dose to a minimum. The maximal sensitivity and resolution achieved were 1.3% and $0.85\ mm$, respectively [143].

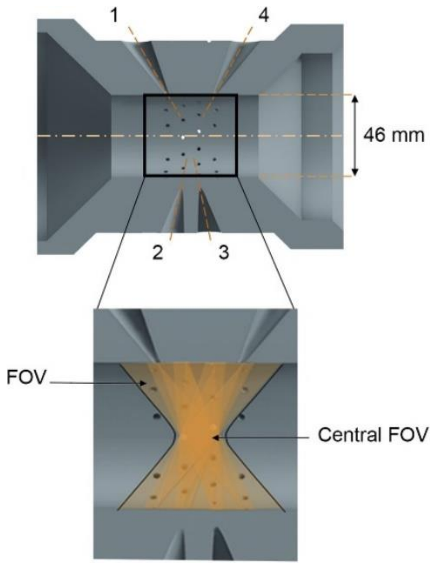

Figure 2.2 Ultra-High sensitivity collimator designed with different pinhole opening angles [143].

Telikani et al. evaluated the influence of pinhole shape, size, material, and geometry on the overall SPECT imaging performance and resolution to discover the optimal collimator design [144]. As demonstrated in this work, using a gamma camera would considerably increase the sensitivity due to the ability to align the pinholes with the active detector element instead of projecting onto the inactive detector area. Simulations with GEANT4 for a dual-head camera, hexagonal, square, and round pinholes revealed that the hexagonal hole outperformed the other pinhole geometries in maximising the imaging system's resolution and sensitivity [145]. This conclusion demonstrates the significant impact of the pinhole aperture’s compactness on enhancing system sensitivity. Figure 2.3 The simulation environment for the hexagonal-pinhole collimator and the initial prototype.

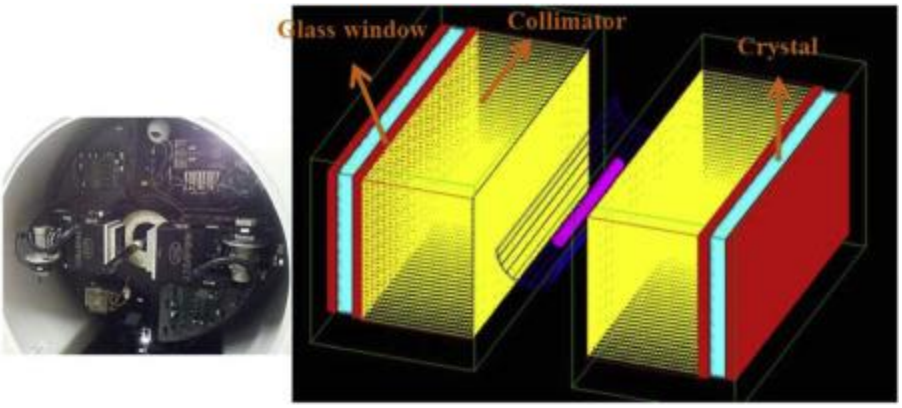

Figure 2.3 The simulation environment for the hexagonal-pinhole collimator and the initial prototype [144].

Research on investigating the collimator parameter design impact on SPECT reconstructed images was initiated using an multi-pinhole collimator system with a triple-head gamma camera [146]. Different pinhole diameters and projections were simulated for the system in three distinct scenarios. This design enables the acquisition of many projections at varying angles; Figure 2.4a shows the three head camera for SPECT acquisition, while Figure 2.4b illustrates the collimator's geometry featuring different configurations corresponding to the adjustments in pinhole diameters. The appealing aspect of this work is the ability to combine projections from different angular points to compensate for the artefacts of the reconstructed images during stationary data acquisition [146].

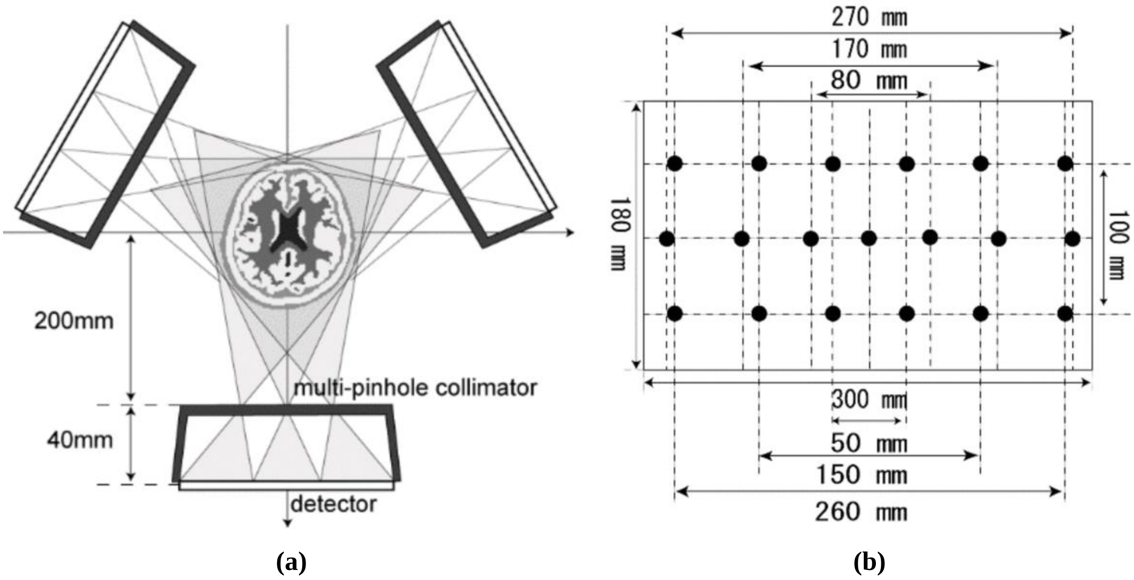

(a) **(b)**

Figure 2.4 (a) Geometry of SPECT acquisition, (b) simulated configurations with different pinhole diameters [146].

Due to the trade-off between resolution and sensitivity in collimator-based imaging systems, the investigation into the possibility of substituting the collimator in SPECT imaging systems continued. Akbari-Lalimi-et al. conducted exclusive simulation research for a collimator-less SPECT imaging system depicted in Figure 2.5, the row of detector are shown where A is the distance between two lead septa, B is the row of detectors, and C is the Speta between detector rows [137]. The primary goal of the design is to eliminate the need for a collimator by utilising a series of detectors with varied fields of view of the phantom. Using Monte Carlo software, 98 detectors in a zigzag geometry were simulated to conduct the study. Sixty projections were obtained by rotating sensors around the radioactive source emitting 140.5 keV. The obtained projections showed that most of the information contained in the source radiations was revealed on the detector side. This is demonstrated by the comparable sensitivity levels of the proposed device and a conventional gamma camera with a collimator. However, photon behaviour was not accounted for in the simulation.

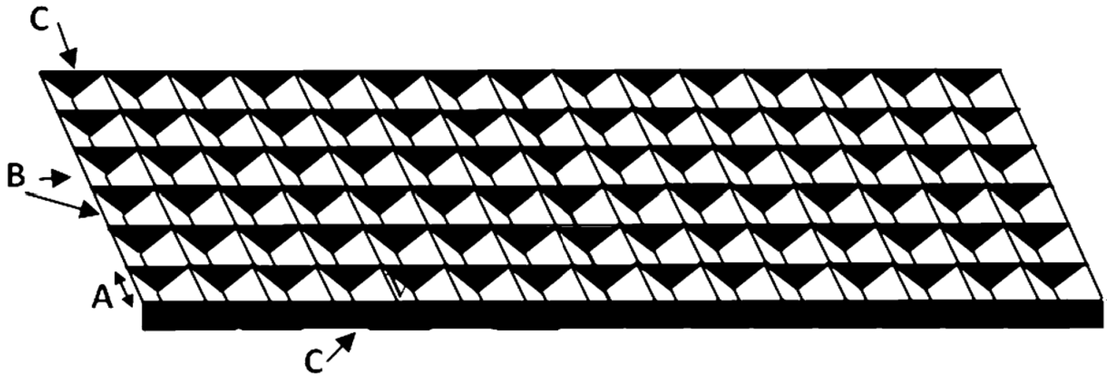

Figure 2.5 SPECT Collimator-less arrangement of detectors, where A is the distance between two lead septa, B is the row of detectors, and C is the Speta between detector rows.[137].

2.1.2 Adaptive SPECT

Investigating the benefits and drawbacks of adaptive SPECT was a concern that prompted several research studies. Hesterman designed the first adaptive SPECT imaging system; the suggested architecture kept the standard configuration of the four stationary gamma cameras [147]. However, slots were added to the pinhole apertures to allow a smooth transition between pinhole apertures in response to the study’s aim. The appropriate number of pinholes and geometry allowed for system optimization and task-based imaging systems. The study sparked empirical investigation towards adaptive SPECT. Freed et al. built a prototype for adaptive single-pinhole SPECT. The suggested SPECT allows for the selection of four distinct pinhole diameters. In addition, it enables the pinhole-object and pinhole-detector lengths to be altered [148]. By building numerous rings of detectors around customizable pinhole apertures, the prototypes for AdaptiSPECT and FastSPECT were developed. Multiple configurations of a one-step optimization for an adaptive SPECT system were designed [149]. Despite the system's capacity to acquire projection images for all viewing angles in a single frame, the insufficient number of angles had a significant impact on the estimation results. A unique variable pinhole SPECT collimator was developed in order to build a collimator capable of adjusting the acceptance angle based on the region of interest (ROI) being studied [150]. Having a minimal configurable distance between the collimator and the target will thereby increase the system's sensitivity.

In contrast, earlier adaptive SPECT systems varied the pinhole width, object-to-pinhole distance, and pinhole detector distance while keeping the pinhole acceptance angle constant [151, 152]. Figure 2.6a, Figure 2.6b, and Figure 2.6c show the tungsten sheet with the drilled pinholes, the motor-controlled sliding motion of the pinholes and a sketch of the variable pinhole collimator with various drilled apertures, respectively.

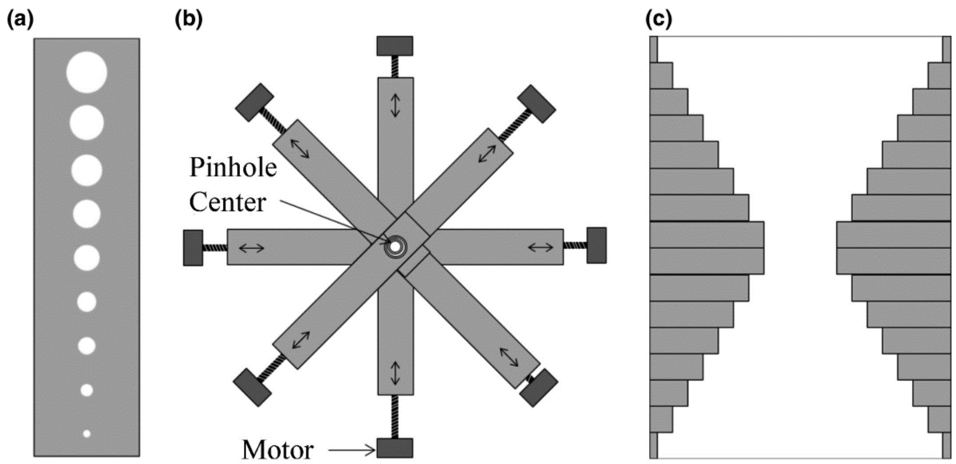

Figure 2.6 (a) Apertures were drilled into a tungsten sheet, (b) pinhole sliding movement is controlled by a motor, (c) a sketch of variable pinhole collimator with various drilled aperture sizes [150].

Figure 2.7a and Figure 2.7b show the conventional pinhole-detector movement and the early prototype of the collimator for different rotation angles , respectively.

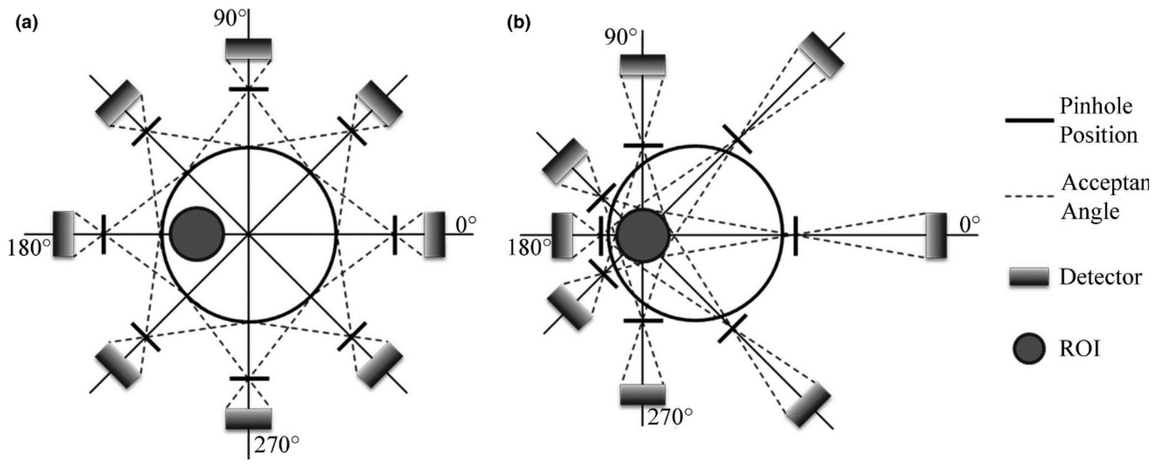

Figure 2.7 (a) Conventional pinhole-detector movement, (b) proposed variable pinhole SPECT movement [150].

Using the GEANT4 toolkit, the system was simulated by its authors, and the maximum-MLEM technique was utilized to reconstruct the projected images. Despite obtaining a significant gain in sensitivity compared to traditional SPECT, the suggested system is restricted to a pinhole design and must be expanded to allow multi-pinhole collimators. Moreover, the proposed technique is not cost-effective due to the requirement to develop and construct a complex actuation system, which, in turn, increases the device's cost relative to existing SPECT collimators. AdaptiSPECT-C SPECT for brain imaging is designed using a keel-edge with multiple pinholes [153]. The imaging system was modified in response to variations in the pinhole diameter and the height of the keel-edge. The initial prototype comprised 23 hexagonal detectors categorized into three distinct ring levels. The sensitivity and photon penetration of $159\,keV$ energy sources were examined. The projections were reconstructed using a custom-built MLEM reconstruction technique. The study concluded that the optimal keel-edge height for limiting penetration and maximizing sensitivity is between $0.375 - 0.75\,mm$.

According to the results obtained from the various simulated schemes, the keel-edge pinholes improved brain imaging with a high degree of separation between complicated structures. In 2018, an adaptive SPECT prototype with real-time adjustable pinhole geometry was disclosed. System resolution and sensitivity may vary based on the shape of each individual pinhole [154]. In addition, the multiplexing effect is modulated in the study by mixing several pinhole modules. Figure 2.8a, Figure 2.8b, and Figure 2.8c show the customized pinhole insertion in gear, the adjustment of the pinhole diameter is achieved by rotating the piece around the aperture and combining multiple modules into one multi-pinhole assembly, which allows for multiplexing, respectively. Developing a real-time customizable pinhole SPECT imaging system has made it possible to achieve customizable sensitivity and resolution for each acquisition instance. Despite resolving the optimal number of collimator pinholes for brain SPECT in Adaptive SPECT, the overlapping issue impaired the quality of the reconstructed images [155].

As shown in Figure 2.9, a dynamically adjustable SPECT was developed to facilitate dynamic imaging. This was accomplished by modifying the sensitivity and resolution in real time based on system needs. The apertures of the pinhole are fine-tuned using the Arduino microcontroller [156].

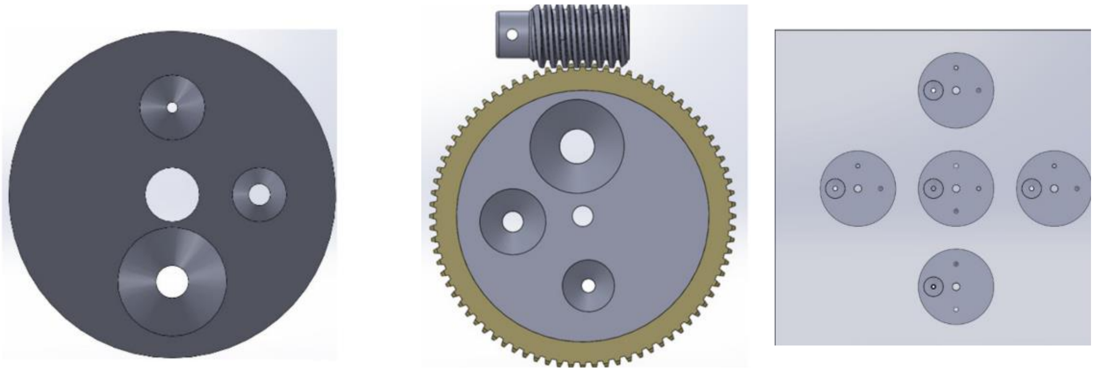

(a) **(b)** **(c)**

Figure 2.8 (a) Customized pinhole insertion in gear, (b)The adjustment of pinhole diameter is achieved by rotating the piece around the aperture, (c) Combining multiple modules into one multi-pinhole assembly allows for multiplexing, as well as single pinhole imaging to resolve multiplexing ambiguities [154].

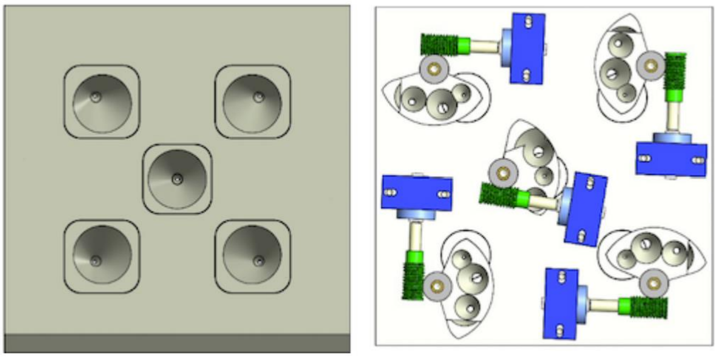

Figure 2.9 The aperture plate and the apertures ring with the rotating components [156].

2.1.3 Multiplexed SPECT Imaging

While multi-pinhole SPECT imaging improves sensitivity and range of view, the MPH design is constrained by the multiplexing. Multiplexing occurs when projections from distinct pinholes in a multi-pinhole collimator overlap on the detector plane [157]. It is regarded as the greatest constraint on the functionality and parameter design of multi-pinhole collimator SPECT [158]. This overlap causes confusion regarding the pinhole from which a photon comes, resulting in an artefact in image reconstruction [88].

Recent research has focused on incorporating two key features into traditional SPECT systems: SPECT adaptability and multiplexing in the projection plane. Permitting more pinholes would boost system sensitivity and, thus, the signal-to-noise ratio at the expense of increased projection multiplexing. This dilemma prompted researchers to devise various strategies to circumvent the multiplexing effect in MPH SPECT collimators. Mohammed et al. focused on reconstructing SPECT images by specifying overlapping and non-overlapping to varying degrees [159]. In several multiplexed projections, the acquired results revealed a decrease in noise level and, thus, an increase in SNR while maintaining spatial resolution. In a study for brain SPECT imaging with changeable multi-pinhole and multiple detectors, the size of the aperture opening, and the determination of which pinhole opens are implemented to accommodate various configurations and degrees of overlapping projections [88]. Based on simulation results, the original AdaptiSPECT-C with a high degree of multiplexing and five pinhole apertures for each detector produced a reconstructed image comparable to the standard image of the brain fusion phantom. However, photon scattering was not modelled for the investigation in that work. In addition, the study did not include a statistical analysis of the various simulated configurations.

According to research, multiplexing provides ambiguous data for reconstructions, resulting in non-unique image reconstruction solutions. Therefore, multiplexing systems require complicated algorithms to counteract the overlapping effect [160]. However, the researchers hypothesised that spatial resolution might be improved for highly multiplexing systems while noise is reduced. Ilisie et al. invented a multi-pinhole SPECT with a high degree of multiplexing and enhanced sensitivity [161]. This is accomplished by designing an active septum to detect the coordinates of the photons transmitted. The proposed septa concurrently function as a collimator and a scintillator to calculate the photons' x and y coordinates. Additionally, it prevents photons from entering the overlap. The problem of artefacts in reconstructed images due to multiplexing would presumably be eliminated by pinpointing the photon's real point of origin. It is determined through a Monte Carlo simulation what the septa and actual detector spatial resolutions are. The projection images were reconstructed with the LM-OSEM (list-mode ordered-subsets expectation-maximisation) technique. The presented novel multi-pinhole SPECT offered a one-of-a-kind solution to the highly multiplexed issue associated with multi-pinhole collimators. In addition, simulation studies have demonstrated a considerable increase in system sensitivity compared to conventional SPECT. Figure 2.10a and Figure 2.10b show the conventional multi-pinhole geometry with highly multiplexed regions on the detector plane and the design of the functional septa, respectively. The active septa acts like a septa and a detector simultaneously that prevents gamma rays from being detected by the radiation-sensitive material, thus preventing overlapped projections. Figure 2.10c shows the geometry of the collimators and detectors. The active radiotracer dose limitation and low SNR of the existing SPECT imaging system were the incentives for developing an adaptive and highly multiplexed SPECT design for an MPH collimator [162]. This concept is predicated on utilising both flexible and non-stationary pinhole modules.

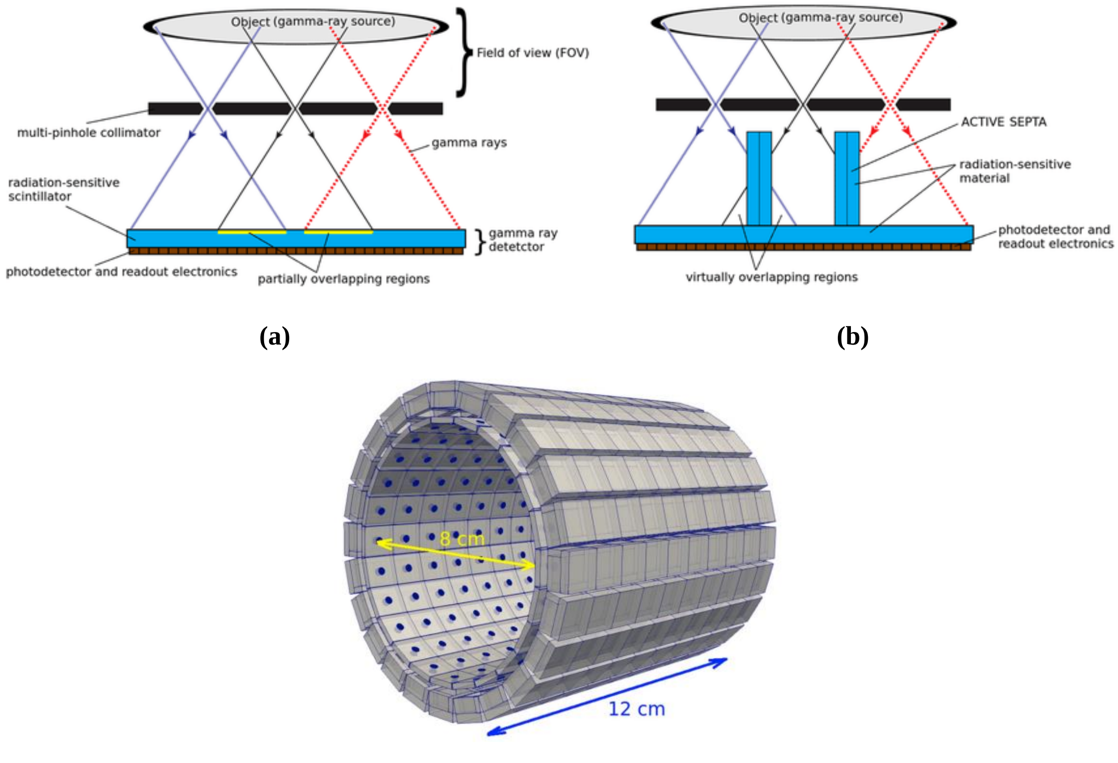

(a) **(b)**

(c)

Figure 2.10 (a) Multi-pinhole SPECT with highly multiplexed regions in the detector plane, (b) Representation of the active septa implemented in SPECT gamma camera, (c) Collimator-Detector geometry generated using GEANT4 [163].

These systems were simulated using MATLAB code and GEANT4 and tested with physical SPECT systems. Figure 2.11a shows the pinhole array design of the proposed system. Each array of pinholes has its own geometry, which results in a variable pitch. The distances between the collimator and the object and the collimator and the detector remain unchanged. Figure 2.11b shows the simulation that examined three setups. The projected images were reconstructed by altering the geometry of the pinhole arrays and considering the various degrees of multiplexing. The study demonstrated a significant increase in sensitivity. However, no comparable analysis using typical SPECT imaging equipment was provided. In addition, the simulated phantoms produced photons with energy of $40\ keV$, whereas the energy range of standard SPECT radiotracers is between $90 - 190\ keV$.

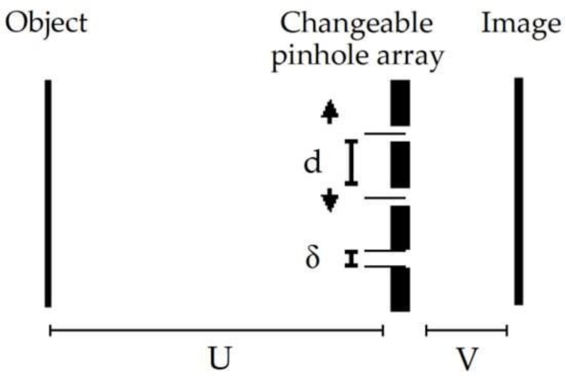

(a)

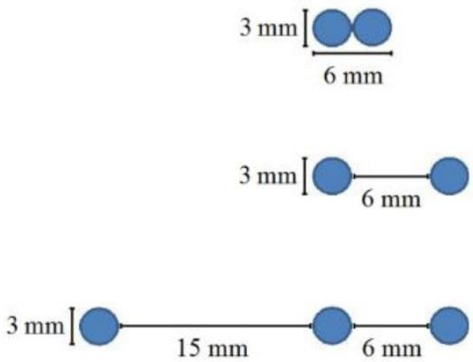

(b)

Figure 2.11 (a) Pinhole array for the proposed design having selectable pitch while keeping the U & V distances unchanged, (b) three simulated pinhole array configurations with different degrees of overlapping [162].

2.1.4 Synthetic SPECT

In response to concerns over the complexity of image reconstruction in multiplexed multi-pinhole SPECT imaging systems, researchers have sought potential approaches for resolving the ambiguity of photon origin. In a highly multiplexed SPECT system, synthetic collimation was the first technology capable of compromising the introduced artefact in the overlapped system and the quality of the reconstructed images. Wilson et al. introduced synthetic collimation to standard SPECT systems [164]. By introducing a revolutionary

SPECT imaging system with synthetic collimation-based three-dimensional reconstruction; obtaining projections through two distinct detectors provides novel insights for task-based imaging. In addition, it allows the acquisition of a tomographic image without using a stationary pinhole detector. As a result, the related artefacts in the reconstructed images of moving systems are avoided. This is accomplished by acquiring various projections with varying pinhole collimator distances. Lin et al. designed a synthetic SPECT collimation system with two detectors situated at two distinct distances from the multi-pinhole SPECT collimator in an effort to solve the multiplexing problem [165]. Figure 2.12 demonstrates that the first detector-pinhole layout prohibits overlapping (Silicon detector), whereas the second geometry supports a high degree of multiplexing (Germanium detector). Several computational strategies were employed to overcome the undesired effect of multiplexing by employing non-multiplexing detector information. Mean squared Wiener error was the desired measure of merit. Using various configurations, a comparison analysis is undertaken between the pinhole and multi-pinhole conventional SPECT systems. Those are acquired by adjusting the degree of multiplexing and the distance between the detector and the collimator. Results indicated that the synthetic collimator is superior to conventional SPECT collimation. Moreover, research demonstrated that synthetic collimation SPECT has the potential for task-based imaging due to its dual detectors and variable projection angles.

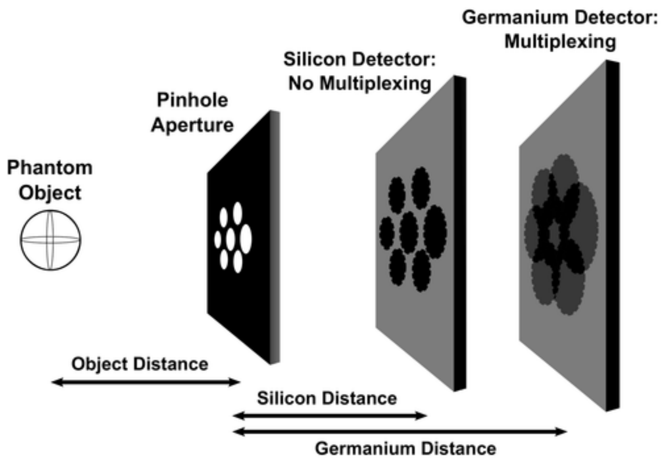

Figure 2.12 Synthetic SPECT [165].

2.1.5 Task Based SPECT

Several organ-specific designs were introduced by optimising the SPECT imaging settings based on the examined organ. A collimator design targeting the "striatum was proposed [166]. The intended resolution was $8\ mm$, and the field of view was $200\ mm$. Simulations demonstrated the capacity to resolve two rods measuring $7.9 - 6.4\ mm$ with the desired resolution and higher image quality than conventional parallel collimators. Figure 2.13 depicts the MPH collimator used for imaging the striatum.

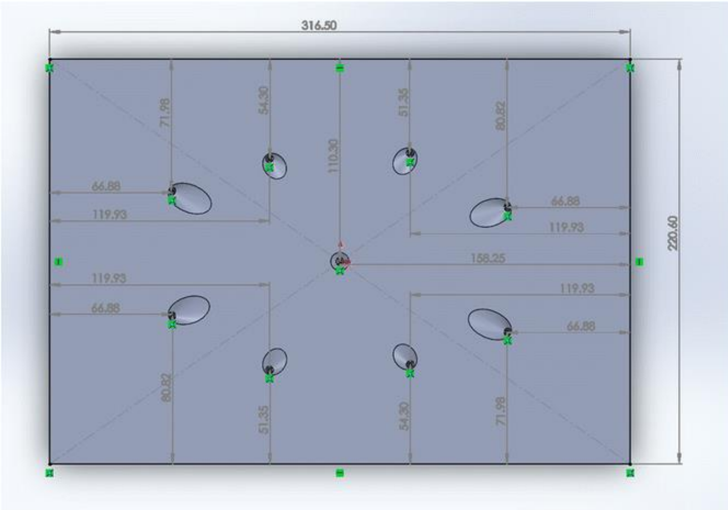

Figure 2.13 Multi-pinhole collimator designed specifically to striatum imaging [166].

Si et al. developed an MPH collimator optimised and adapted for myocardial perfusion (MPI) and small animal SPECT imaging (SAI). The pinhole geometry-imposed design constraints were applied to reduce truncation and multiplexing effects [167]. However, only one gamma camera was considered for the intended multi-pinhole collimator, unlike standard dual-head imaging systems. In this investigation, no photon scattering, nor attenuation were examined.

SPECT imaging dedicated to the brain employing a stationary parallel-hole collimator was presented to overcome image quality degradation caused by system rotation [168]. Using simulations based on Monte Carlo in one of the Monte Carlo toolkits called, the GEANT4 Application for Tomographic Emission (GATE), the system could reconstruct a sampling without artefacts. Nonetheless, the stated immobile design restricts the minimal size of the collimator required to cover the complete body. In addition, the simulations that were done only accounted for parallel-hole collimators with a more straightforward simulation.

2.2 Detector Optimization Methods

The detector technology of SPECT gamma cameras has drawn tremendous interest in the field of research. Several investigations examined novel detecting technologies. Others utilized traditional detector technology but emulated the system with several detectors instead of a single detector. The need for high-resolution SPECT imaging in a clinical study prompted the exploration/research of novel technologies and detector geometries. As depicted in Figure 2.14a and Figure 2.14b, the authors presented a stationary single-pinhole SPECT system for imaging small animal and brain with numerous pixelated CZT detector modules. Each pinhole-detector module is regarded as a gamma camera. As proof of concept, a resolution of $0.1\ mm$ and a sensitivity of 0.0009% were produced [169].

The system in [170] obtained a resolution of $1.1\ mm$ and a sensitivity of 0.09 percent without requiring any rotation of the collimator or detectors. The unique technology provided has shown promise and has the ability to return a system with great sensitivity and resolution. In addition, based on the simulation results, detecting the different fields of view without rotating the modules would necessitate further design consideration or implementation. A study targeted building a collimator adequate for use with radiotracers of varying energies while ensuring low penetration through the collimator's pinholes was proposed.

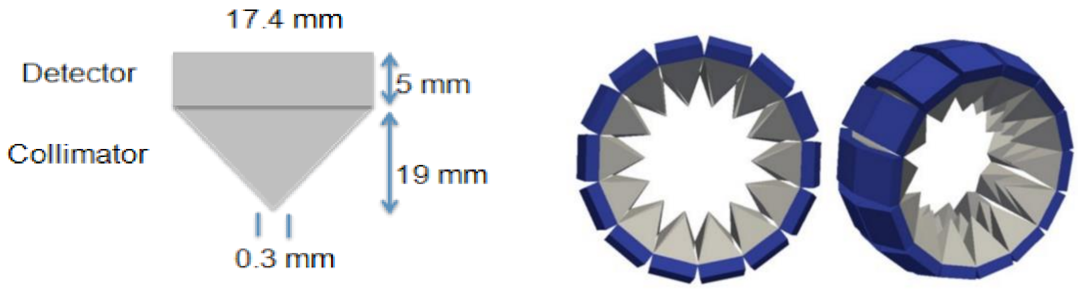

(a) **(b)**

Figure 2.14 (a) Side view of the stationary single pinhole-detector SPECT module, (b) Gate generated assembly of 42 pinhole-detector geometries arranged in three different rings [169].

The study simulated a parallel hole collimator with the perfect matching between the collimator pinhole and the CZT detector pixels for the case of circular, hexagonal, and square pinholes, as shown in Figure 2.15a, Figure 2.15b, and Figure 2.15c. The primary objective of the matching is to minimise the dead area on the detector plane generated by the septa. While maintaining the collimator's independence from photon energy, the system's simulations demonstrated a higher detection efficiency while retaining the collimator's independence. However, additional evaluation studies are required to test the system's ability to maintain the target efficiency at higher photon energies.

Researchers in [171-173] developed new detector technologies to enhance the performance of SPECT imaging systems by using newer scintillators, photomultipliers, and electronic circuits. Researchers in [174] proposed using pixelated detectors to restrict the spread of scintillation light. However, this technology demands a significant design constraint, especially when submillimeter pixel resolution is considered [169].

Focusing the radiation onto the scintillator could be one of the unique future solutions to the issue of light scattering on the detector plane. Massari et al. suggested a novel method for reconstructing the high-frequency content of various SPECT images [175]. The resolution of the parallel hole collimator SPECT imaging system has increased significantly due to the SSR technique. In addition, the method benefited from the independence and homogeneity of the field of view (FOV) in parallel hole collimators, as opposed to pinhole or multi-pinhole collimators. In [176], a SPECT system for imaging the brain was described using a square and hexagonal multidetector and a multi-pinhole system for each detector module. A method of shutters was devised to allow photons to flow through a series of several pinholes selectively. The multiplexing effect was considered by permitting overlapping projections on the detector module. Figure 2.16 shows the three hemispherical rings of detectors. The simulation results indicated the diameter of the detector module for performance and sensitivity optimisation. Despite a comparative investigation between the various detector modules and varied pinhole geometry through the shutters, a comparative study with a conventional SPECT imaging system is lacking.

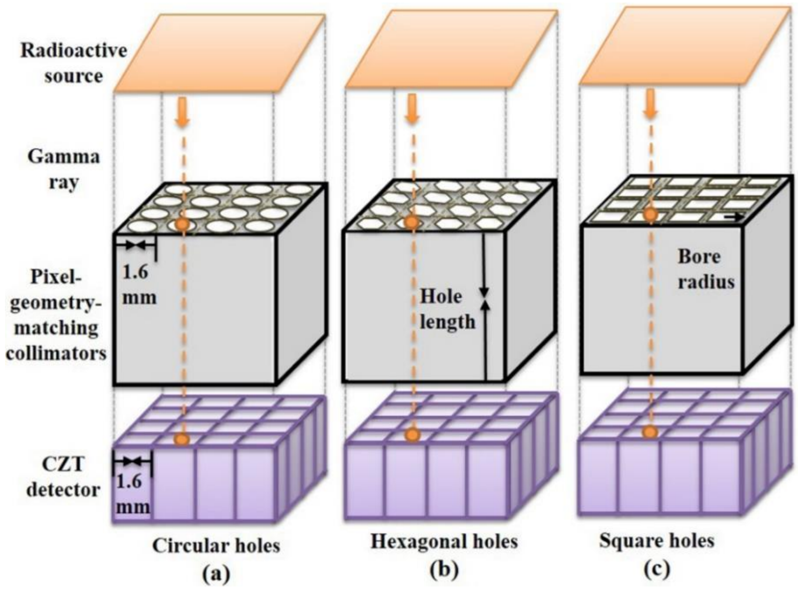

Figure 2.15 Collimator-pinhole CZT-pixel matching with (a) circular holes, (b) hexagonal holes, (c) square holes [170].

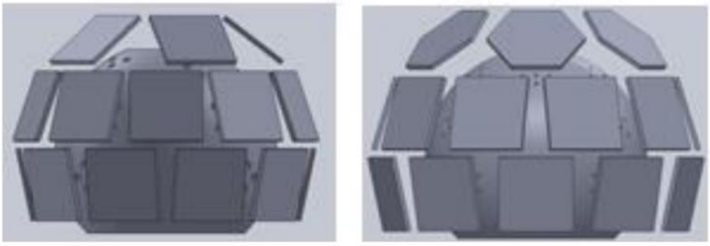

Figure 2.16 Three rings of hemi-spherical detectors surrounding patient head [176].

This study inspired/sparked further research into the squared and hexagonal detector rings, as shown in Figure 2.17. The fundamental objective of this suggestion is to modify the irradiation hexagonal and squared detector rings by applying the shuttering approach and enabling the rotation of the detector rings [177].

Several pixelated detectors proposed to develop a unique digital SPECT showed a significant improvement in image clarity and contrast compared to conventional SPECT imaging systems [178]. The small design of pixelated digital detectors makes it possible to effectively utilise the overall projection area on the detector plane [179].

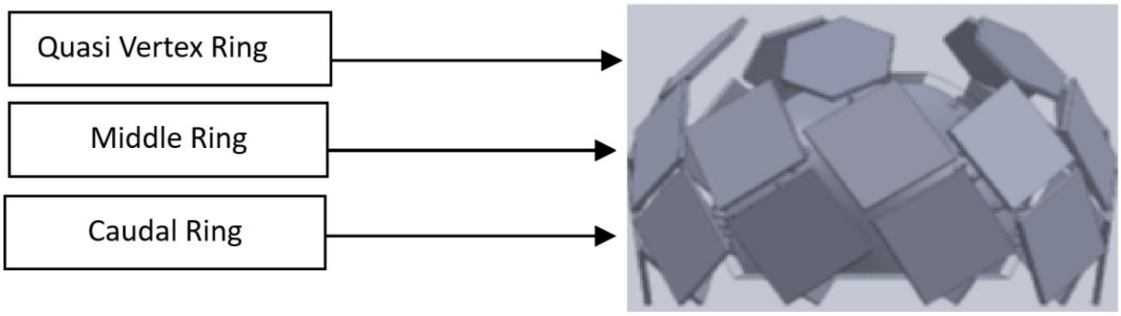

Figure 2.17 Three rings of hemi-spherical detectors surrounding patient head [177].

The proposed system is comprised of pixelated moving CZT detectors installed on the camera gantry with radial rotation to scan the target region. Figure 2.18 illustrates this proposed design configuration.

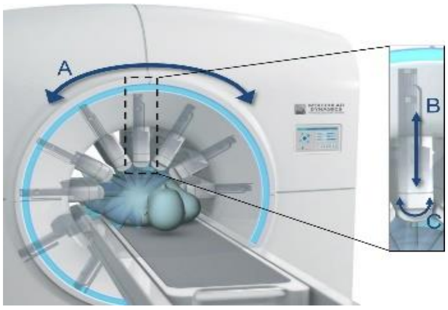

Figure 2.18 Pixelated moving CZT detectors [178].

Despite improvements to the imaging system's sharpness and sensitivity, additional work is required to address some of the study's limitations, such as the inability of the human eye to evaluate images and the difference in FOV size between the analogue and digital SPECT systems.

In SPECT imaging, detector technology is essential for extracting dynamic light from the scintillator. Nonetheless, several factors limit the light extraction effectiveness of the scintillator and result in complete internal reflection within the scintillator. Due to the internally reflected light absorption effect within the scintillator, this considerably reduces light output [180, 181]. Several solutions to this dilemma were offered, including plasmonic lattices [182] and photonic crystals [182, 183]. Despite the enhanced effectiveness of light extraction employing these approaches, its application in scintillators is limited by their reliance on the light's wavelength [184]. By presenting a scintillator design with micro-lens arrays at the top of the scintillator, a possible solution to the wavelength dependency challenge is provided. Employing microlenses to determine radiation directional information was examined, and the setup was tested using Monte Carlo ray-tracing techniques [185-187]. Figure 2.19a depicts the suggested system architecture, whereas Figure 2.19b illustrates the influence on the light path and directionality with and without the microlenses covering the scintillator. The system simulation demonstrated an increase in light output and SNR. The refractive index and form of each microlens substantially influence the enhancement of light extraction and impose design constraints on the intended microlens arrangement.

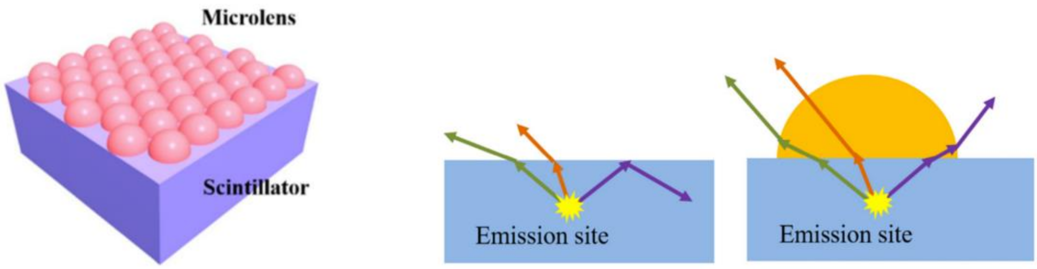

(a) (b)

Figure 2.19 (a) Scintillator with Micro-lens array, (b) Scintillation light path difference in scintillator with (left) and without (right) microlens array [187].

A full-ring SPECT system with eight large-area CZT cameras was proposed in [188]. Each detector is independently spun around its rotation axis. It has a radial motion for changing aperture sizes that may be matched to varying sizes of the image volume, as depicted in Figure 2.20. Compared to the typical scanning time, the system's acquisition time has been reduced by threefold.

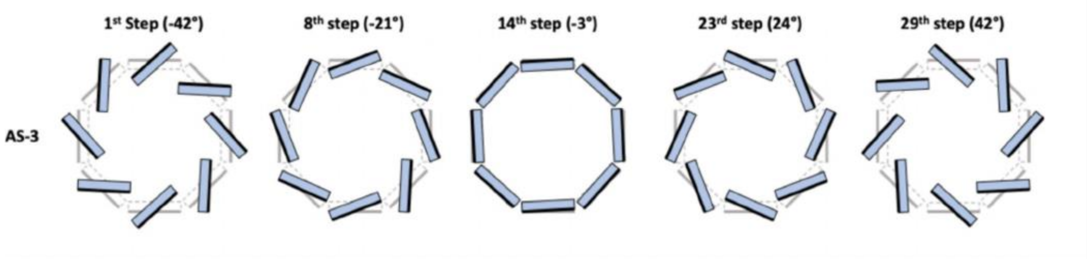

Figure 2.20 Eight ring CZT detector, each detector can rotate independently around the patient [188].

2.3 Coded Aperture: SPECT

Typically, imaging is accomplished via lenses and mirrors at optical wavelengths. In contrast, the energy level of hard X-rays and gamma rays is too high to be reflected or refracted. Therefore, they pass right through the lenses and mirrors of optical instruments. X-rays and gamma rays imaging systems use coded apertures (CA) because these high-energy rays cannot be focussed using lenses or mirrors designed for visible light [189]. The data obtained by the multi-pinhole coded aperture collimator must be post-processed to be decoded. Different images from multiple apertures will overlap on the detector array of a coded aperture camera, which is more advanced than a pinhole camera. Consequently, it is necessary to reconstruct the original image by a computer process. This way, acquiring a sharp image without a lens is possible.

In nuclear medicine, coded apertures were introduced as an alternative to traditional tomography in order to increase the sensitivity of gamma cameras while keeping the system's spatial resolution [189-195]. In these systems, the collimator is replaced with a mask containing a large number of holes, which acquire several copies of the object, some of which are distinct from one another and others which overlap. The data obtained by the multi-pinhole CA collimator must be post-processed in order to be decoded. For Nuclear medicine applications, where the object being studied should be placed as close to the detector plane as possible, the near-field artefacts created by such proximity pose significant challenges, necessitating the use of mask and anti-mask techniques to partially circumvent this issue [196]. Additionally, the projected image is deformed when a multiple-pinhole CA is used. The data is comprised of multiple overlapping projections, making it difficult to decode the overlaps. Mu et al. proposed an innovative CA SPECT reconstruction technique [197]. The imaging of hot sources and cold lesions was examined using near-field CA. With the 3D MLEM technique, the CA images were reconstructed. The generated images exhibit enhanced Contrast-to-Noise Ratio (CNR) and root-mean-square when compared to 5-pinhole images. In addition, the noise aberration was more prominent in pinhole images than in CA images. However, the resolution remained essentially unchanged. The comparisons were restricted to small-pinhole-count multi-pinhole images. In order to obtain more generalised conclusions, it is necessary to increase the pinholes and conduct additional research. A study published in 2020 revealed the capabilities of a system based on a coded aperture mask and a hybrid pixel Timepix detector with a CdTe sensor to monitor SPECT radiotracers with a resolution of 1 mm [198]. At higher energies, however, the image quality declines due to diminished detection efficiency and collimator absorption. This exacerbates the reconstruction artefacts that become obvious for gamma photons at approximately 180 keV. Figure 2.21 displays CA-reconstructed images for various sources of energy. Shadowgrams refer to the reconstructed images or patterns obtained through the process of decoding the information collected by the coded aperture. These shadowgrams are intermediate images that represent the distribution of radiation sources or objects in the field of view, before further processing to obtain the final image [199].

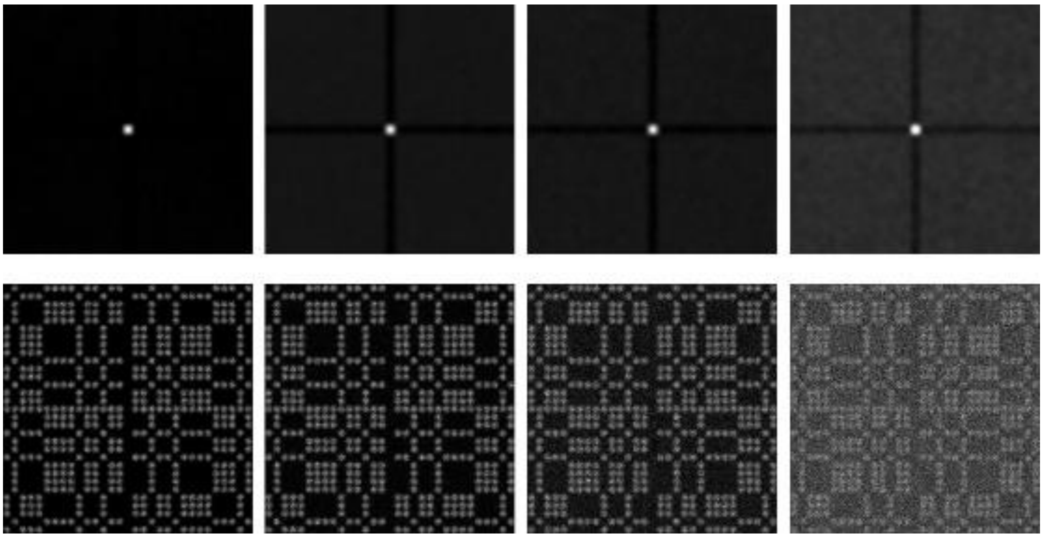

Figure 2.21 Simulated images of a source emitting gamma rays with energies of 30, 140, 180, and 350 keV. The top row shows the reconstructed images. The bottom row shows the corresponding shadowgrams [198].

The SPECT collimator and detector design poses a major concern in nuclear medicine; reviewing past studies in the literature reveals research gaps that have yet to be addressed.

2.4 Gamma Focusing Methods

Mirrors or lenses can be used to bend the pathways of photons and concentrate visible light to a single location. This makes the image sharper and brighter [200]. Gamma rays focusing is a challenging task. When a gamma ray collides with matter, the interaction destroys or drastically modifies the gamma energy. This means that conventional mirrors and lenses cannot be used to focus gamma radiations [201]. In the introduction to X-ray telescopes, X-rays were focused using "grazing incidence" mirrors, which cause incoming photons to skim across the mirror's surface. Gamma rays are more energetic than X-rays; hence they must enter at an even shallower angle, rendering grazing incidence mirrors unsuitable for gamma ray astronomy [202]. In reality, gamma rays telescopes lack adequate focusing lenses. Instead, scientists have developed alternative approaches to determine the source of gamma rays in the sky. Gamma ray astronomy commonly employs collimators, anti-coincidence shields, and coded aperture masks [203].

Low energy focusing telescopes up to 70–80 keV have been successfully constructed, but beyond $100\ keV$, crystal diffraction looks to be the most efficient way to concentrate photons [204]. Gamma rays focusing optics are also essential for enhancing the angular resolution, with the best results currently obtained with coded mask telescopes (about 15 arcmin) [205]. Today, focusing telescopes in the soft gamma rays band are crucial for overcoming the sensitivity limitations of the present generation of gamma rays telescopes that observe the sky [206]. Several attempts have been made to develop a diffraction lens, namely a Laue lens, with a broad energy passband $100 - 600\ keV$and a long focal length (up to $20\ m$ and beyond) for astrophysics [207].

2.4.1 History of Gamma Focusing Based on Laue Lens Diffraction

During World War II, many changes were instigated in daily living. The introduction of high-energy photon sources was one of them [208]. This is the result of the development of fission reactors for electrical generation and scientific study, which made available numerous radioactive isotopes that generated high-energy gamma rays and the advent of energetic X-ray sources increased the availability of photons of medium energy [208]. The applications were extensive in medicine and industry. These sources led to the development of techniques for detecting cancer in humans, monitoring production lines, testing welds for cavities or flaws, and an array of novel imaging technologies, ranging from chest X-rays to computerized axial tomography scans. These efforts led to the invention of numerous novel detectors for high energy photons. The demand for detecting tiny tumours and weaker sources prompted the design of detectors with improved sensitivity [209]. In most instances, this was addressed by increasing the size of the detector. The astrophysics community made its first flight of high-energy gamma rays detectors to observe gamma rays and energetic X-rays from distant astrophysical sources at the beginning of the space era. As the investigations progressed, astrophysicists began to examine gamma rays from sources in our galaxy and galaxies in the distant universe [210]. Due to their large distances, these sources are considerably weaker. Therefore, in perspective, they began to consider crystal diffraction lenses as a potential solution to the extremely low luminosity of these sources.

Substantial design considerations are required for X-rays detection with high efficiency. Some non-focusing techniques for X-rays detection utilizing collimators as geometric optics have been developed [211]. However, when background noise increases, the effectiveness of geometrical optics diminishes. Quantum optics is an additional non-focusing technique proposed in [212]. On the other hand, Laue lens-based focusing approaches have the potential to overcome the constraints of non-focusing detection methods. Examples include the Compton telescope [213], the gamma rays imager [214], and the hard X-ray telescope research [215].

A new interest in X-rays and gamma rays from astrophysical sources was sparked by the success of the Einstein Observatory satellite X-ray telescope [216-218]. This telescope comprises a series of concentric reflecting shells that focus X-rays with energy up to 5 keV. This introduced a new field of astrophysics and raised the question of how energetic photons could be focused. During the 1980s, the Argonne group investigated the types of crystals (mosaic and bent) that may be utilized in crystal lenses and the various forms of crystal lenses [219-225]. Moreover, they conducted several research projects for examining various Laue lens crystal designs for focusing intense photons in the realm of astrophysics [201, 208, 225, 226].

In the late 1980s, the Argonne group ended up producing a full-size lens for the Treaty Verification programme in the late 1980s. It consists of eight rings containing 600 germanium crystals [208]. The success of this lens led to a partnership with the Toulouse-based group led by Ballmoos to use the lens in balloon flight research [227]. A new lens based on the Argonne design was developed. The lens utilized novel mosaic crystals set to deflect 170 keV X-rays from the Crab Nebula and was utilized in two balloon flights to demonstrate that this technique could be used to see gamma rays from astrophysical sources [228].

2.4.2 Gamma Focusing in Medical Applications

The necessity to compensate for the resolution/sensitivity trade-off in conventional collimation SPECT systems by employing focusing optics for energetic gamma photons was the main purpose for studying the effects of X-rays focusing and reflective optics. Absorptive collimation is used in current SPECT imaging techniques, which sets efficiency against resolution. Conventional SPECT methods are effectively limited to a spatial resolution of less than 2 mm due to efficiency constraints, limiting the examination of several major areas of biomedical research [229].

Using recent breakthroughs pioneered by the high-energy astrophysics community for focusing X-rays and gamma rays optics provides a method to break the paradigm that sets resolution against efficiency and offers a path to imaging small animals with sub-millimetre resolution.

2.4.3 Grazing Mirrors: Medical Imaging

Wolter proposed the first symmetric X-rays optics designs just over fifty years ago [230]. He found that a practical optic could be made utilising pairs of conoids to build a short-wavelength microscope for biological research (i.e., hyperbolas, parabolas, and ellipses). The functioning angles for grazing incidence systems (also called Wolter optics) are typically a few degrees or fewer to achieve the critical angle needed for total external reflection of light [208]. Wolter's prospective microscopes were not realized due to limitations in optical production and coating procedures. His ideas went untested until the late 1960s, when the X-rays astronomy community embraced grazing incidence designs for the first generation of X-ray telescopes [231]. To boost efficiency by collecting light from a bigger aperture, a significant invention was to nest numerous pairs of mirrors inside, much like Russian dolls fit inside one another. Since the first X-ray telescope was launched onboard the Einstein Observatory in 1978, NASA, the European Space Agency (ESA), and the Japanese Space Agency (JSA) have constructed and launched 10 more X-rays astronomy satellites at the cost of several billion dollars ($US) [118].

Based on grazing incidence mirrors for the focusing of energetic photons, a small animal radionuclide imaging system (SARIS) was proposed [232-234]. The research developed a high-resolution imaging system for small animals based on reflecting optics. The shape of the stacked mirrors used to focus gamma rays is depicted in Figure 2.22 and Figure 2.23. The focal length f is indeed the sum of the distances between the middle of the optic and the mouse f_1 and the middle of the optic and the detector f_2:

$$f = f_1 + f_2 \qquad \mathbf{2.1}$$

And the magnification M of the optics is expressed as:

$$M = \frac{f_2}{f_1} \qquad \mathbf{2.2}$$

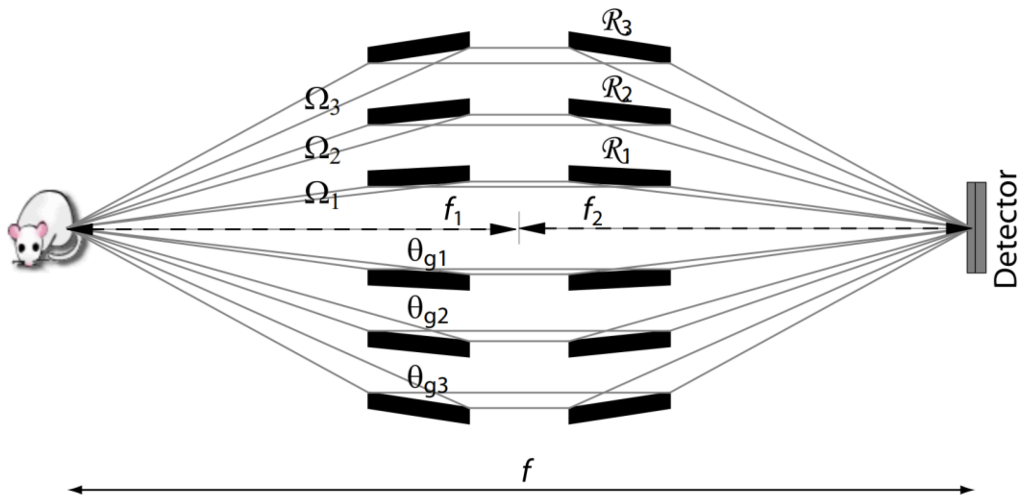

Figure 2.22 Geometry of the nested mirrors for focusing gamma rays in small animal imaging [232].

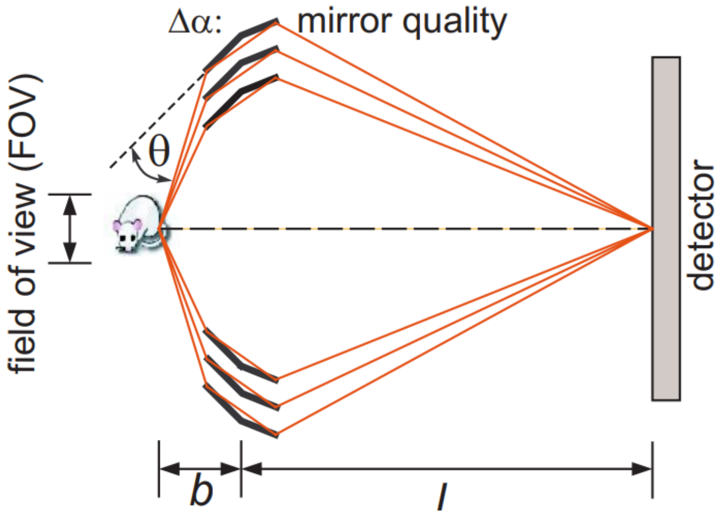

Figure 2.23 A schematic illustration of a gamma rays lens with three nested mirrors, the parameters that determine the system's resolution and field of view [232].

The prototype optics demonstrated the feasibility of X-rays optics for small animal imaging: a four-reflection symmetric prototype and a two-reflection asymmetric optic with unity magnification. The study couldn't fabricate substrates specifically for biomedical imaging due to financial restrictions. Instead, it employed thermally generated substrates initially designed for astronomical telescopes. Using a dedicated Monte Carlo simulation, the study demonstrated that practical optics have efficiencies of 10^{-5}, which is comparable to pinhole systems with $0.75\, mm$ resolution, and spatial resolution at least an order of magnitude better than state-of-the-art pinhole collimators, for gamma photons with an energy of $27.5\, keV$.

Another study was initiated to develop a small animal radionuclide imaging system that uses grazing incidence optics to focus the low-energy gamma rays in the energy range of $17 - 20\ keV$ or $27.5\ keV$ (the primary energy emitted by I^{125}) [118, 232]. With present detectors and a reasonable efficiency, the best spatial resolution feasible with a pinhole collimator is $1\ mm$. Given the limitations of absorptive collimation techniques, the focusing methods based on grazing incidence represent a potential solution for sub-millimetre resolution.

However, using reflecting gamma rays optics for small animal imaging has drawbacks. First, increasing the number of lenses is the only method to boost the system's sensitivity. Second, a single lens will consist of tens of nested mirror pairs, resulting in a far higher production cost than a single collimator element [232]. Moreover, this method is impractical for Tc^{99} radionuclide imaging that emits gamma rays in the energy range of $100 - 200\ keV$, due to the inverse relationship between the angle of reflection and photon energy. With separation distances between the small animal and the detector in the order of a few metres, a complete focusing system will require more laboratory space than an absorptive collimation system.

2.4.4 Laue Lens Application: Medical Imaging

Enhancing image resolution and sensitivity is imperative to detect cancers at their earliest stages. Focusing is the only option to increase sensitivity, as there is nothing more that can be done to detectors already capable of detecting single events. However, it is impossible to focus gamma rays using conventional refractive optics [235]. Consequently, bringing the concept of diffractive focusing to nuclear imaging via the Laue lens is a promising strategy for enhancing resolution. A Laue lens is a collection of crystals capable of focusing high-energy photons using diffraction [236]. Thus, the Laue lens could focus a large number of intense gamma photons into a small focal area on the detector plane, enabling high-resolution radionuclide imaging of small animals and the brain. The primary distinction between imaging with an array of crystals lens and a collimator is that the lens permits the decoupling of angular resolution and collection power or sensitivity. This is especially crucial for the astrophysics lens, where relatively large crystals can be used in a large lens without affecting its angular resolution.

In the 1990s, the Argonne crystal diffraction group took the initial step in investigating the potential application of Laue lens diffraction, focusing on nuclear imaging. A high SNR was attained due to the detector's small surface area [209]. In addition, the detection effectiveness remained high even when dealing with small radiation sources. Using the concept of diffraction, an imaging system for detecting gamma rays between $100 - 200\ keV$ was proposed later in 2005 [237, 238]. By constructing the first lens system capable of focusing $140.5\ keV$ gamma rays from Tc^{99}, the researchers began to investigate the viability of using diffracting lenses to scan radioactivity. In the study, a Laue lens with 13 rings comprised of 900 copper crystals was presented for nuclear imaging. Figure 2.24 shows a schematic of the designed Laue lens. The primary objective of this technique was to further investigate suspected tumour masses as small as $2 - 3\ mm$ after a body scan. On a purposely built stand, the designed Laue lenses were evaluated by placing the detector on top, the Laue lens in the middle, and the source at the bottom. The photo and the conceptual drawing of the experiment's stand are shown in Figure 2.25a and Figure 2.25b, respectively. Argonne researchers continued to investigate the use of Laue lenses in medical imaging. Using the notion of diffraction, an imaging system for detecting gamma rays in the range of $100 - 200\ keV$ was developed in 2006 [238].

The best achieved resolution using this lens was $3\ mm$, which is less or almost equivalent to the current pinhole collimators. Based on the Laue lens diffraction approach, Paterno et al. developed a gamma ray focusing investigation for gamma photons. The research's major objective was to produce a high-resolution image on the detector plane [78]. Even though the Laue lens design made its way into the nuclear medicine field, no evidence was found in the literature to support how to combine the Laue lens geometry with a typical gamma camera hardware system.

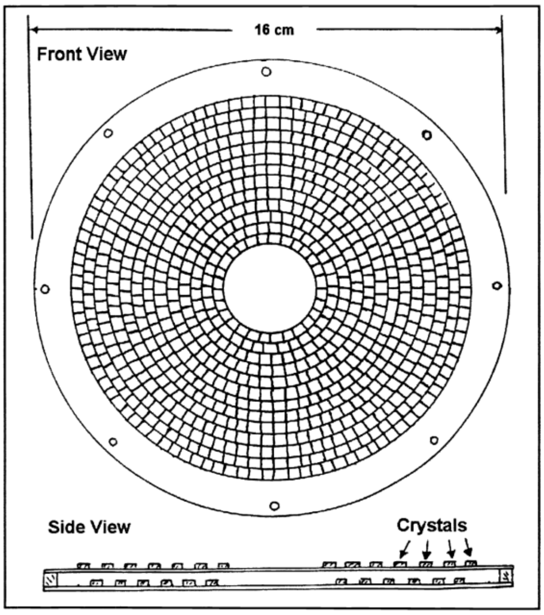

Figure 2.24 Front and side view of the Laue lens showing all 14 concentric rings of crystals. Each crystal is 4 mm by 4 mm and 2-4 mm thick [238].

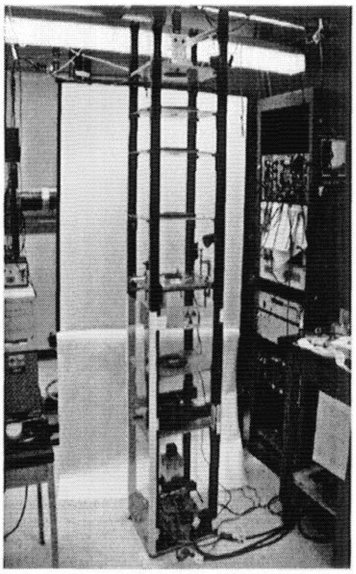

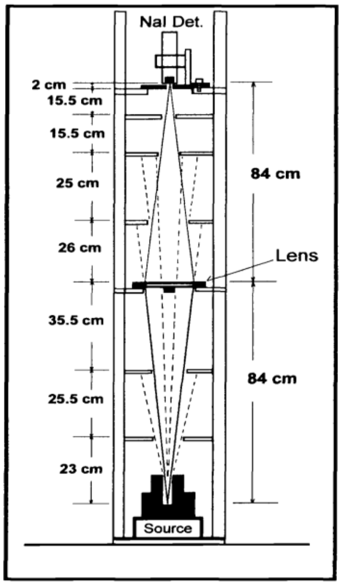

(a) **(b)**

Figure 2.25 (a) The Laue crystal lens test facility, (b) Drawing illustrating the elements of the lens test facility. The source is at the bottom, the lens in the middle and the detector at the top [238].

Gaps still exist in exploring possible uses of the Laue lens as a component of the gamma camera hardware for small medical imaging. The use of Laue lens diffraction in nuclear medicine prompted numerous researchers to suggest multiple concepts for radiotherapy systems based on the same principle.

2.4.5 Laue lens Applications: Radiotherapy

Approximately 60% of cancer patients undergo radiation therapy, primarily in the form of high-energy photons ($2 - 20MeV$), as part of their disease management [239]. Due to their penetrating power and ionization nature, they inflict damage on healthy and malignant tissue alike, so these high-energy photons pose numerous challenges [240]. Twenty years ago, the accuracy with which radiation therapy for cancer treatment could be used to precisely tailor the radiation dose around a patient's tumour was an order of magnitude lower than it is today [241].

For effective therapy, the overall dose delivered to the tumour must be greater than the dose to the surrounding tissue (the "therapeutic ratio"), so it would kill the tumour cells without harming healthy tissue [242]. Currently, a proper ratio is obtained by directing the beam in several directions at the tumour, either by scanning the beam or directing several beams at the tumour. Using this technique, the locations where the beams cross receive a larger radiation dose than the healthy tissue they must pass over on their path. Compton Scattering by electrons causes a rapid decrease in beam intensity as the beam passes through healthy tissue. For instance, by the time an X-ray beam reaches the centre of the brain, its intensity would have decreased to around 20% of what it was at the skin's surface. To restore the flux at the brain's centre to the still non-lethal level at the skin, irradiation from five different directions would be required. The approach is challenging because a proper ratio of tumour to skin exposure requires irradiation from many different directions [243].

The use of X-rays beams is a well-known technique for targeting deeper tissues [244]. The depth dose deposited by X-rays beams reach a maximum at the site of the targeted tissue, followed by a prolonged exponentially diminishing curve caused by tissue absorption. Recently, several methods for obtaining a convergent X-rays beam for radiotherapy applications have been developed. One of these methods relies on magnetic and electric field-applying equipment to precisely adjust the trajectory of an electron beam from a linear accelerator (LINAC) [245]. Using an X-rays tube with a polycapillary lens as a focusing device is another way to obtain a convergent X-rays beam for radiation applications [246]. A polycapillary lens utilises multiple complete reflections of X-rays within numerous hollow glass tubes to focus the high-energy photons beam on a target.

However, due to the fact that the critical angle for the entire reflection is inversely related to photon energy, this method is only effective for photons with energies up to 80 keV [247]. In addition, the depth of irradiation is normally restricted to 5 cm due to the limited radius of the channels. The focal spot is between $100 - 200\ mm$ wide. Such a narrow focal region suggests that even a $1\ cm^3$ tumour would necessitate an extremely time-consuming beam scan for uniform irradiation. A Laue lens is an optical component that could circumvent these restrictions. It is a focusing element capable of concentrating a photon beam on a target volume that would pave the way for a novel radiotherapy technique [248]. Paterno et al. proposed a radiotherapy system using an X-rays tube instead of a LINAC as the X-rays source [245]. The tumour is located at the focus at a depth of Z_f within the patient's body. The designed Laue lens was capable of diffracting a beam with standard energy ranging from tens to hundreds of $keVs$. Such lenses can be designed for specific treatments. The proposed system is shown in Figure 2.26. The lens focuses a portion of the X-rays released by the X-ray tube on a target volume that contains the tumour within the patient's body. The collimator positioned just in front of the patient and the beam stopper positioned in the centre of the lens prevent the direct beam and Compton-scattered photons from reaching the patient. Consequently, only the diffracted beam should ideally reach the patient. In the study, $80\ keV$ was considered as the minimum energy, which is greater than the maximum energy a polycapillary lens can accommodate.

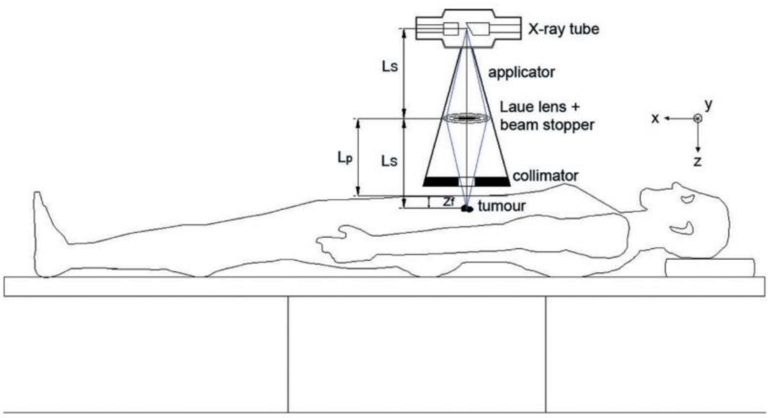

Figure 2.26 Schematic of a radiotherapy system employing a Laue lens [245].

Camattari et al. [249] initiated a feasibility study that was conducted on the placement tolerances of crystalline optical elements. It was demonstrated that a Laue lens can be utilized efficiently in the context of radiotherapy to treat tumours if the mounting errors were less than specific values, which are attainable with contemporary micromechanics.

Another study presented a potential method for generating a converging beam that preserves the skin by spreading the radiation exposure across a vast area. This is similar to the notion described in [250]. However, instead of a mechanical system with various sources and collimation, it employs an X-ray lens system. This is also distinct from polycapillary optics, which operate at a lower energy level and are hence inapplicable to deep-seated malignancies [251]. In the proposed Convergent Radiotherapy and RadioSurgery (CRnR) system, the converging beam geometry, as illustrated in Figure 2.27, exhibits an increase in dose up to the focal spot and then a decrease in dose as the beam becomes diverging. This is in contrast to the typical dose decrease with depth after the initial build-up region (orthovoltage build-up is negligible).

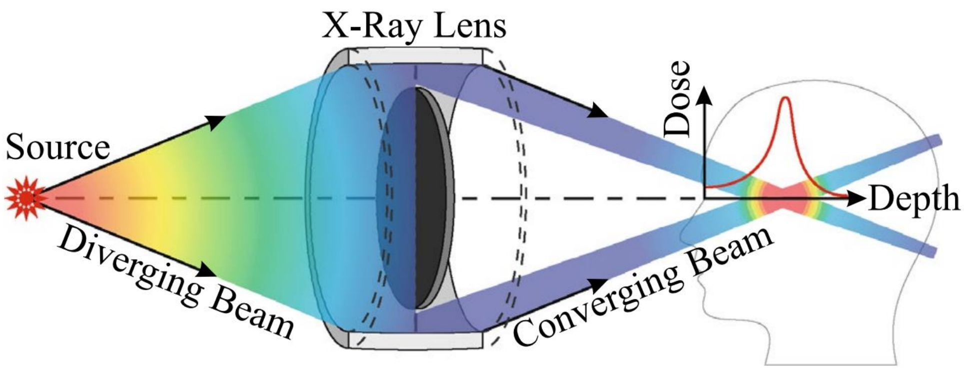

Figure 2.27 Conceptual illustration of the CRnR system where an X-ray lens converts a diverging beam into a converging beam, producing a localized dose peak within a target [251].

2.5 Recent Trends in SPECT Imaging: Lightfield Imaging

Lightfield cameras provide imaging systems with an increased level of efficiency. The primary driving force and incentive for lightfield imaging are post-image processing and focusing of the acquired image [252]. These are determined by analysing the directional and spatial distribution of light rays in every direction in space. Applying lightfield imaging to medical imaging systems based on X-rays and gamma rays, such as PET, SPECT, and CT have remained a difficult task for years, due to the difficulty of locating microlenses that can focus X-rays and gamma photons. Tahtali [253] proposed the application of the lightfield imaging concept to CT imaging. The proposed setup employed a multi-pinhole array instead of a lenslet array used in optical lightfield imaging to obtain simultaneous projections from numerous X-ray sources. Figure 2.28 depicts a pinhole acting as a lenslet, where *L* is the field of view, h is the distance between the detector an the collimator, α is the opening angle, and t is the pinhole depth [253].

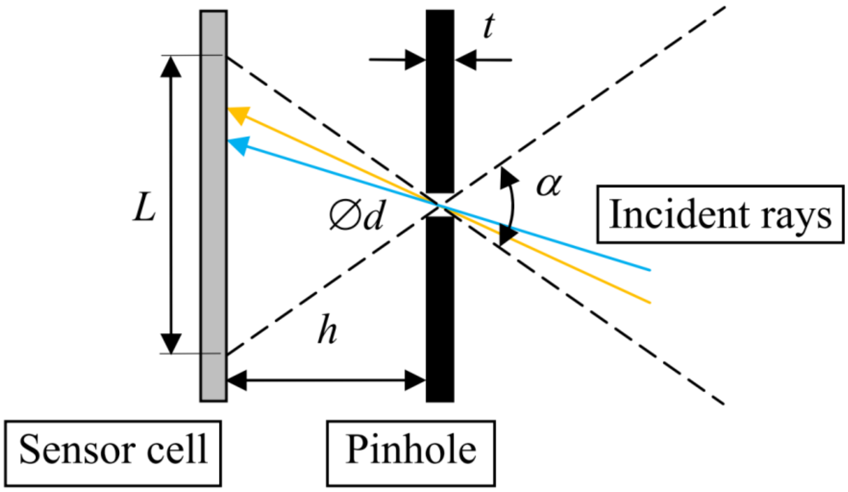

Figure 2.28 Pinhole acting as a lenslet [253].

Following this innovative pinhole concept, Saha et al. investigated the feasibility of a lightfield CT system along with suitable reconstruction algorithms for the type of sparse data produced by such a system [254]. The width of the X-ray beams in the proposed system is assumed to be equal to the size of the pinhole aperture. The system's maximum capacity to store directional ray data is predicted to be 20×20 projections beneath each pinhole using existing pixelated X-ray cameras. However, as it is the case with optical lightfield imaging, the number of useful projections would be reduced due to vignetting at the boundaries of each pinhole. Different from conventional multi-pinhole systems, the pinhole array is positioned at a minimum distance from the sensor plane to avoid multiplexing. Different configurations were simulated to establish the ideal angular projections in terms of enhanced image reconstruction quality while keeping an acceptable distance between the source and the detector and the least radiation dose required. Despite the ability of the described acquisition system to record active X-rays from many sources concurrently, the pinhole collimator is responsible for a significant amount of X-rays flux attenuation, which would have a considerable impact on system sensitivity. In addition, the dispersion effect was not taken into account in the study. Therefore, several of the reconstructed images contained artefacts. Based on the light-field imaging technique, Rahman et al. [255] investigated an array of 100 multi-pinhole collimators to increase the sensitivity and FOV while maintaining the spatial resolution. The GEANT4 Applications for Tomographic Emission (GATE) simulation software was used to model and test the initial system performance. Figure 2.29a,

Figure 2.29b, and Figure 2.29c show the modelled L-SPECT (Lightfield SPECT) system in the GATE environment, the 100 x 100 array of PSPMTs (Position Sensitive PMTs) and the pixels array behind each pinhole, respectively. The system's fundamental properties were examined in accordance with NEMA (National Electrical Manufacturers Association) standards. The proposed design can provide high resolution, system sensitivity, and count rate for SPECT imaging. This detector module could be utilized in a variety of scientific and clinical investigations. However, a specified design constraint was imposed in the presented study to evaluate only non-multiplexed projections. This is mostly due to the requirement of an expensive, high-resolution detector to avoid overlapping the large number of pinhole projections described in this work. Avoiding multiplexing would substantially impact the resolution and SNR of SPECT systems. The primary objective of considering multiplexing is to improve SNR while maintaining system sensitivity. Noting that developing a high-resolution imaging approach remains essential for the accurate and efficient early detection of malignant tumours. However, existing SPECT imaging systems suffer from a physics-imposed trade-off between resolution and sensitivity. With the multiplexing (overlapping) of the pinhole projections, a multi-pinhole system can increase sensitivity at the expense of increasing complexity. Consequently, this also increases the complexity of image reconstruction methods [256].

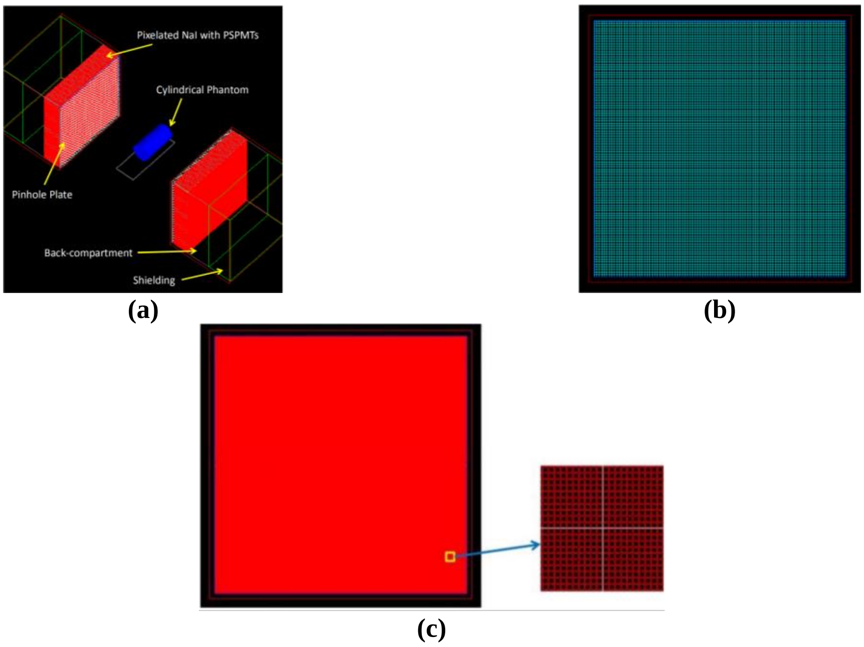

Figure 2.29 (a) Dual-head L-SPECT system, modelled in GATE, (b) 100 by 100 array of 0.48 mm x 0.48 mm PSPMTs, and (c) behind each pinhole, an array of 10 by 10 pixels with each array corresponding to a PSPMT [255].

2.5.1 The Next Paradigm in SPECT Imaging: Lens-Based SPECT Imaging

Introducing the notion of the Laue Lens into nuclear imaging systems would boost resolution substantially. In addition, it can potentially focus a large number of intense gamma rays released by energy sources within the patient’s body into a small focal area on the detector plane. This would result in radionuclide imaging with a significantly enhanced resolution, including small animals and humans, with high SNR [209]. To address the challenge of low sensitivity in smaller SPECT detectors, which is crucial for early cancer detection, larger detectors are employed. However, as the background's square root increases, the signal-to-noise ratio (SNR) decreases. Consequently, enlarging the detector size would lead to a reduction in SNR [209, 257]. By utilising focusing qualities, this issue could be resolved.

2.6 3D Image Reconstruction

CT image reconstruction is a mathematical procedure that builds tomographic images using X-rays projection data gathered from many angles surrounding the subject. It fundamentally affects both image quality and radiation dose [258]. Two primary classifications of reconstruction methods are: analytical reconstruction and iterative reconstruction (IR). The most prevalent analytical reconstruction method in commercial CT scanners is the filtered back projection (FBP), which applies a 1D filter to the projection data before back projecting (2D or 3D) [259]. The computational efficiency and numerical stability of FBP-type methods are the primary reasons for their widespread adoption. Various FBP-type of analytical reconstruction methods were developed for different generations of CT data-acquisition geometries, including 2D parallel- and fan-beam CT in the 1970s and 1980s, helical and multi-slice CT with narrow detector coverage in the late 1990s and early 2000s, and multi-slice CT with a wide detector coverage (up to 320 detector rows and 16 cm width). Scanners with more than 16 detector rows often employ 3D-weighted FBP algorithms [260]. Clinical applications dictate the selection of the reconstruction kernel. For instance, smooth kernels are typically used in brain examinations or liver tumour evaluations to reduce image noise and improve low contrast detectability. However, sharper kernels are typically used in medical imaging examinations or scans, such as X-ray, CT (computed tomography), or MRI (magnetic resonance imaging) to evaluate bone structures due to the clinical requirement for higher spatial resolution [261].

In SPECT imaging, the image captured at one viewing angle is the projection of the three-dimensional (3D) distribution of the radionuclide onto the two-dimensional (2D) detector plane. Due to the projection operation, no information is provided regarding the depth at which disintegrations occur. Furthermore, activities originating from distinct structures may overlap on the detector plane, and the contrast may be low [262]. With only one image of the projection, it is difficult to detect the activity distribution because an endless number of distributions can produce the same projection. However, the overlap visible in the projections depends on the detector's relative positions and the body's structures [262]. As shown in Figure 2.30, the radioactivity distribution data are projected onto the detector from each angle. Note that the location of any scintillation on a crystal reveals the direction of the incident photon (the dashed line) but not the distance between the detector and the photon's emission site.

The detector rotates around the object of interest and acquires projections of the emission pattern in its field of vision from many angles. The number of scintillations detected at any point $\mathbf{s}$ along the detector when the detector head is positioned at an angle is defined as $\mathbf{g}(\mathbf{s}, \boldsymbol{\theta})$, as shown in Figure 2.30. The quantity $\mathbf{f}(\mathbf{x}, \mathbf{y})$ is alternatively defined as the estimated number of photons emitted at any position $(\mathbf{x}, \mathbf{y})$ in the transverse slice in the field of view [262]. The function $\mathbf{g}$ is the projection of $\mathbf{f}$ onto the crystal as permitted by the collimator. This indicates that $\mathbf{g}(\mathbf{s}, \boldsymbol{\theta})$ represents the whole of the radioactive counts collected at a specific point during a given time span when the detector is at an angle $\boldsymbol{\theta}$. The collimator defines the kind of projection (e.g., an orthogonal projection for parallel collimators) and determines the direction of the incident photon for any scintillation in the crystal.

SPECT technique reconstructs 3D tomographic images from a sequence of 2D planar scintillation camera readings, where each image corresponds to a part of the body. Image reconstruction is necessary to acquire tomographic images from a series of SPECT projections [262, 263]. The filtered back-projection (FBP) method has been the most used approach to date. This process is quick and straightforward. However, some image processing is required due to the generally noisy data from scintillation cameras, and this is frequently accomplished by using a low-pass filter. The Butterworth filter is an often-used filter whose cut-off frequency and order can be used to define the filtering amplitude [264].

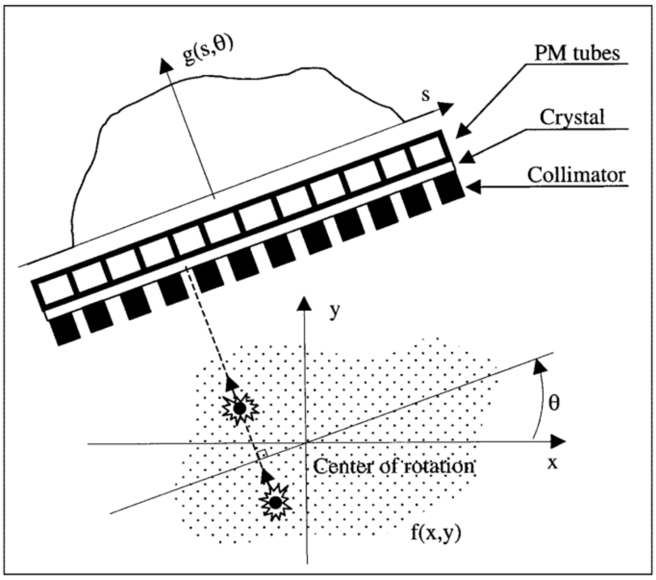

Figure 2.30 The principles of tomographic acquisition and geometric considerations [262].

The iterative approaches, particularly the MLEM/OSEM (The Maximum Likelihood Expectation Maximization/ Ordered Subsets Expectation Maximization) methods, are a group of reconstruction techniques that have attracted increasing attention. These approaches are based on an initial estimate of a reconstructed image and a step in which an estimated projection derived using knowledge of how a SPECT system works is compared to a measured projection [265]. A bin-by-bin error projection is generated, and the results are back-projected to produce an error image. After comparing data from all angles of projection, the original estimate is updated by multiplying the first estimate by the error image. This revised image can then be applied to calculating new error images. These iterations continue until the estimated-to-measured discrepancy is within an acceptable range. MLEM is the most widely used method for SPECT and PET since it was derived from Poisson statistics [262]. The slow convergence of MLEM has hindered the method's clinical implementation. However, Hudson and Larkin released the OSEM approach in 1994 [266]. OSEM is similar to MLEM in many ways, but only a small number of selected angles are utilized to produce the error image prior to the update. MLEM uses data from all 64 projections to build the error image, but OSEM only uses a selection (usually four) before updating the image. This means that the initial image will be updated 16 times per iteration, whereas the MLEM will only receive a single update. Therefore, the results will converge much more quickly, and the process has been improved [266].

Due to the inherent difference in data handling between FBP and iterative reconstruction (IR), IR images may have a different appearance in terms of noise structure. Moreover, the spatial resolution in a local region of IR-reconstructed images highly depends on the surrounding structures' contrast and noise, resulting from the non-linear regularisation term and other optimization-related factors [267]. Contrast- and noise-dependent spatial resolution has been measured using various commercial IR techniques [268, 269]. Due to this dependence, the amount of potential radiation dose reduction permitted by IR is dependent on the diagnostic task, as the subject's contrast and the exam's noise vary considerably in clinical examinations [270]. Several phantoms and human observer studies on multiple commercial IR methods demonstrated that only marginal or a small amount of radiation dose reduction is permissible for low-contrast detection tasks [271-273]. Before IR can be used routinely, careful clinical evaluation and reconstruction parameter optimization are required [274, 275]. Active research has been conducted on task-based image quality evaluation using model observers to quantify image quality and dose reduction objectively and efficiently [276, 277].

While post-reconstruction filters are utilized to eliminate noise, they also diminish spatial resolution and contrast and tend to blur the image's edges. This noise can also be decreased by employing the Bayesian approach or median root prior (MRP), a new Bayesian reconstruction algorithm utilized primarily in PET and later enhanced for pinhole SPECT. In image reconstruction, the ordered subset expectation maximization (OSEM) technique with a functionality dependent on the number of subsets and iterations is utilised. Even though its processing time is just 2.5 times longer than the FBP approach for one iteration and eight subsets, it provides much greater image quality while suppressing streak artefacts and non-amplifying noise [278]. According to reference [262], OSEM IR has become the preferred method for IR processing, in which data are grouped into subsets that enable more rapid and accurate data convergence than previous systems. OSEM images provide higher image clarity and more image contrast than FBP images [262]. Due to insufficient projection data collected from a single circular pinhole, blurring occurs. In contrast, a pinhole SPECT utilising two circular orbits and a three-dimensional OSEM can offer complete projection data and eliminate blurring edges in the reconstructed image. It can eliminate axial blurring and increase image resolution consistency. It has the potential to become the standard instrument for quantifying physiological activities in vivo in small animal imaging [279].

2.6.1 Central or Projection Slice Theorem

The central slice theorem is the fundamental basis of tomography. It has also known as the projection slice theorem and the Fourier slice theorem [280]. The central slice theorem in two dimensions (2D) states that the 1D Fourier transform $\mathbf{p}(\boldsymbol{\omega})$ of the projection $\mathbf{p}(\mathbf{s})$ of a 2D function $\mathbf{f}(\mathbf{x}, \mathbf{y})$ is equal to a slice (i.e., a 1D profile) through the origin of that function's 2D Fourier transform $\mathbf{f}(\boldsymbol{\omega}_{\mathbf{x}}, \boldsymbol{\omega}_{\mathbf{y}})$ which is parallel to the detector, as depicted in Figure 2.31

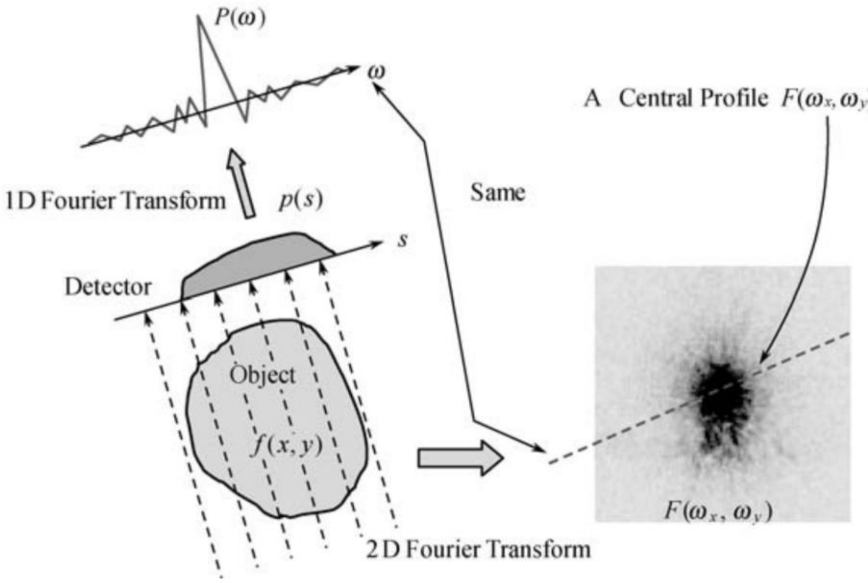

Figure 2.31 Illustration of the 2D central slice theorem [280].

2.6.2 Reconstruction Methods

If the detector is rotated around the object for at least 180 degrees, the corresponding "central slice" in the 2D Fourier transform $\mathbf{f}(\boldsymbol{\omega}_{\mathbf{x}}, \boldsymbol{\omega}_{\mathbf{y}})$ will rotate synchronously and cover the entire 2D Fourier space, that is, the x-y plane, as shown in Figure 2.32. In other words, by rotating the detector 180 degrees, the entire 2D Fourier transform $\mathbf{f}(\mathbf{x}, \mathbf{y})$ is "measured." Once $\mathbf{f}(\mathbf{x}, \mathbf{y})$ is available, the original 2D function $\mathbf{f}(\mathbf{x}, \mathbf{y})$ can be easily obtained by the 2D inverse Fourier transform is a mathematical procedure [280, 281].

Back projecting projection data at one view is the same as adding a "central slice" of $\mathbf{f}(\boldsymbol{\omega}_{\mathbf{x}}, \boldsymbol{\omega}_{\mathbf{y}})$ in the x-y plane (i.e., the Fourier space). Back projection of more than 180 degrees fully reconstructs the 2D Fourier transform $\mathbf{f}(\boldsymbol{\omega}_{\mathbf{x}}, \boldsymbol{\omega}_{\mathbf{y}})$. Because of the Fourier pair property, the original function $\mathbf{f}(\mathbf{x}, \mathbf{y})$ can be identified [280].

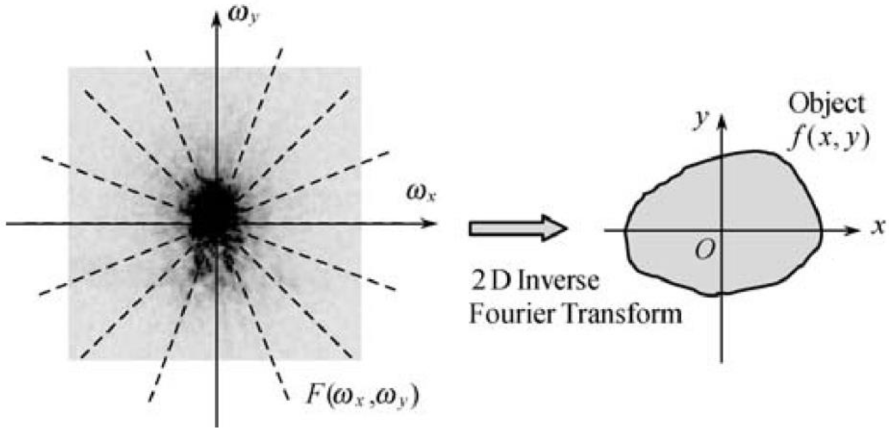

Figure 2.32 Central slice theorem: Each view adds a line in the Fourier space. The 2D inverse Fourier transform reconstructs the original image [280].

Filtered back projection (FBP) is one of the most prevalent reconstruction algorithms derived from the central slice theorem. This theory relates the 2D image to its 1D Fourier domain projections. The FBP consists of ramp-filtering and back projection steps. The filtering algorithm can be implemented as a multiplication in the Fourier domain or convolution in the spatial domain [282].

In 2D acquisition, each row of projections reflects the sum of all counts along a straight line through the depth of the object being scanned. The back projection technique redistributes the number of counts at each specific position back along the line from which they were originally detected. This procedure is performed for all pixels and angles. As a result of the limited number of projection sets, a star artefact and image blur were created, the algorithm is explained in Figure 2.33a, Figure 2.33b, and Figure 2.33c. To avoid this issue, the projections are filtered before being back projected into the image matrix. It should be noted that the back projection process takes place in the spatial domain, whereas data filtration takes place in the frequency domain [283].

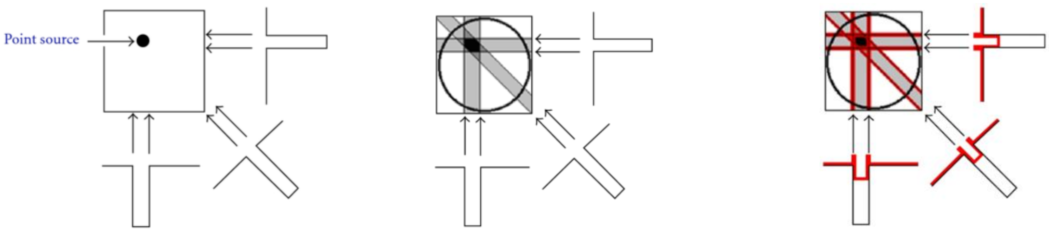

(a) **(b)** **(c)**

Figure 2.33 A simple representation of filtered back projection. (a) Acquisition of three projections, (b) Back projected projections, (c) Filtered back projected projections [147].

The filters used in FBP are essentially mathematical formulae that alter with frequency. The filters employed in SPECT imaging might vary to meet goals such as star artefact reduction, noise suppression, or signal augmentation and restoration. The selection of a filter for a given image reconstruction task is typically a balance between the level of noise reduction and fine detail suppression as well as the spatial frequency structure of the image data of interest [262, 283, 284].

2.6.3 Iterative Reconstruction Methods

Iterative algorithms are gaining popularity in medical image reconstruction due to the increasing availability of more powerful processors. The imaging problem is described as a system of linear equations, and an image is reconstructed by minimizing an objective function [283, 285]. Numerous algorithms are available for solving linear equations or minimizing an objective function. The likelihood function can be used to define the goal function, including prior knowledge about the image. In the projection measurements, the likelihood function models the noise distribution. The MLEM algorithm, also known as the OS-EM algorithm, is the most widely used iterative image reconstruction algorithm in emission tomography, and it has received major attention. Many noise-control solutions are presented. This chapter also discusses a recent research hotspot: image reconstruction with significantly under sampled data, often known as compressed sensing, which is simply another application of Bayesian image reconstruction [283, 286].

Iterative reconstruction begins with an approximation of the image [44]. Most of the time, the initial estimate is relatively basic, such as a uniform activity distribution. The initial estimate is then used to estimate a set of projection data via a mathematical method known as the forward projection. The generated projections are compared to the recorded projections, and the disparities between the two are used to update the estimated image. The iterative process is performed until the disparities between the computed and measured values are less than a predetermined value. Iterative reconstruction approaches include algebraic methods such as the algebraic reconstruction technique (ART) and statistical algorithms [82, 262].

2.7 Chapter Summary

This chapter thoroughly examined the different proposed designs of SPECT collimator and detector design optimization approaches from the perspective of the most recent advancements. Studies that would provide insights and expert comments on the direction and future of SPECT design research were presented. A comprehensive literature on the impact of pinhole size, shape, material, and geometry on the performance and resolution of SPECT imaging in identifying the optimal collimator design and the effect on the final 3D reconstructed images was discussed. Moreover, the proposed techniques to mitigate the multiplexing impact, system tailoring, and task-based imaging technologies that gave rise to adaptive SPECT were examined. The recently demonstrated technologies and geometries for SPECT detectors and the approaches available for enhancing light extraction are explored. In the light of the most recent technological advancements and the emerging trends in SPECT imaging based on lightfield is explored. The history of Laue lens uses in astronomy, and the extended applications to nuclear medicine are thoroughly reviewed.

2.8 Acknowledgement

This chapter articulates and expands on work for which the concepts and basic findings were partially published in:

1. A. Barhoum, M. Tahtali and R. Camattari, " Review Article: Recent Advances in SPECT Design and the History of Laue Lens in Gamma Focusing: Recent Trends in SPECT Based on Light Field" Medical physics (2022).

3. Methodology

This methodology chapter serves as a critical component of my research study, as it outlines the systematic approach employed to gather, analyse, and interpret data. It also provides a roadmap for the research process. In this chapter, I delve into the specific research methods and procedures employed in this study and the methodology followed in this thesis by describing the simulation tools and the designed environment set-up. Additionally, I briefly discuss the potential limitations and challenges associated with the chosen methods followed in this study and the steps taken to mitigate them.

This chapter is structured as follows: Section 3.1 discusses different aspects of the Monte Carlo methods as a simulation tool. Section 3.2 presents the developed environments for the thesis work and the 3D reconstruction tools. Section 3.3 discusses the limitations and challenges associated with the methodology, such as the computation time and code optimization. Section 3.4 concludes the chapter.

3.1 Monte Carlo Toolkits

The Monte Carlo approach is a technique for tackling issues involving random variables by designing a physical system of interest. Monte Carlo models processes and system interactions by randomly selecting the a priori probability density function for the occurrence of particular phenomena. H.O. Anger initially employed this technology to model the physical response of his innovative scintillation camera [287]. Since then, Monte Carlo-based simulations have gained popularity in the realm of nuclear medicine due to their ability to realistically simulate the random nature of radiation emission, detection, and transport.

In the late 1970s, Monte Carlo techniques began to gain popularity in medical physics, specifically for the modelling of imaging systems in nuclear medicine, the characterization of particle beam accelerators in radiotherapy, and the calculation of the absorbed dose in patients for treatment planning [288-291]. Since then, Monte Carlo simulations have become a prominent research and development (R&D) method for the design of nuclear imaging systems and dose calculation engines in treatment planning systems (TPS) [292, 293].

Technological developments in the field of Monte Carlo simulations have resulted in the emergence of generic computer codes, allowing the user to simulate a wide variety of particles, energies, geometrical elements, and physical interactions; for example, EGSnrc [294], MCNPX [295], Penelope [296], Fluka [297], GEANT4 [298, 299], Gate [300-302]. In addition to new experimental data, the accuracy of the underlying physical models and cross-section databases has been continuously enhanced. Inefficiency of Monte Carlo simulation approaches" refers to the fact that traditional Monte Carlo simulations can be computationally intensive and time-consuming. Monte Carlo simulations involve random sampling and can require a large number of iterations to achieve a desired level of precision or accuracy in the results. To combat the inefficiency of Monte Carlo simulation approaches, variance reduction techniques (VRT) have been developed [288, 303]. They are still being proposed to improve computation times at a given level of precision [292].

As the several software packages used for this research have their rootsin Monte Carlo simulations of particle behaviour, a brief discussion is presented in the next section of how Monte Carlo techniques are applied in this thesis and the different developed environments in three different toolkits used for this purpose.

3.1.1 MATLAB Toolkit

MATLAB is a licensed inter-programming language and quantitative computing environment created by MathWorks. Matrix manipulation, graphing of functions and data, algorithm implementation, construction of user interfaces, and connecting with programmes written in other languages are all possible with MATLAB. Although MATLAB is primarily meant for numeric computation, an optional toolbox employing the MuPAD symbolic engine enables symbolic computation [304]. Simulink is a supplementary programme that adds multi-domain graphical simulation and model-based design for dynamic and embedded systems.

MATLAB version R2020a was used for the thesis work to run the developed environment and the implemented reconstruction algorithms. The machine learning and image processing toolboxes were used alongside several other toolboxes.

3.1.2 GEANT4 Toolkit

GEANT4 (for GEometry ANd Tracking) is a platform that uses Monte Carlo methods to simulate "the movement of particles through matter." It is the successor to The GEANT4 collaboration's GEANT series of software toolkits and the first to employ object-oriented programming (in C++) [305]. The multinational GEANT4 Collaboration is responsible for its development, upkeep, and user assistance. High energy physics and nuclear experiments, medicinal, accelerator, and space physics research are examples of application areas. Many international research projects use this programme [306]. GEANT4 version 10.07.0 was used for this thesis work to run the developed environment.

3.1.3 GAMOS Toolkit

GAMOS stands for GEANT4 Based Architecture for Medicine-Oriented Simulations. It is a GEANT4-based framework that is both user-friendly and adaptable [307]. The extensive scripting language makes it simple to implement the most frequent requirements of a medical physics application without the need for C++ programming. The plug-in technology, together with a careful modular design, detailed documentation, and a set of examples and tutorials that explain in detail how to extend the framework in various directions, enables the full flexibility of GEANT4 to be exploited by creating new user code or by reusing any piece of GEANT4 code and integrating it seamlessly with the existing GAMOS components [308]. GAMOS version 6.2.0 was used for this thesis work to run the developed environment.

3.2 The Developed Environments for the Thesis Work

In this thesis work, I have developed three different environments for the proposed lens based-SPECT design in different Monte Carlo toolkits. The first implementation was in the MATLAB platform, the second was in GAMOS, and the third was in GEANT4.

The obtained projection image in each environment was calibrated against each other for the proof of concept. Moreover, the performance analysis parameters, including sensitivity and resolution, were compared in the three developed Monte Carlo implementations for the proposed lens-based SPECT.

3.2.1 MATLAB Implementations

Modified Monte Carlo environments tailored to the lens-based SPECT were developed to simulate the desired behaviour and response of the SPECT system augmented with a Laue lens. Several case studies were run using different types of phantoms. Several geometrical shapes were considered for the simulated source phantom.

Phantom dimensions and the system parameters are stored as input parameters to be changed for different case studies. The developed environment assumes ideal conditions for initial system evaluation and performance parameters analysis. The MATLAB developed Monte Carlo study did not consider scatter, attenuation, and absorption effects at the detector level. However, the designed environment incorporates realistic physical interactions, and nuclear event counts for possible absorption and attenuation phenomena within the Laue lens volume. I started by proposing the very initial geometry of the design by proposing a single lens-based SPECT geometry. Then, a single lens-based SPECT system fitted with partially curved detector modules and Laue lens arrays to boost sensitivity. I call it modular lens-based SPECT. The multi lens-based SPECT was the third geometry. For each of them, I developed a first Monte Carlo study devoted to each geometry requirement for the single and modular lens-based SPECT. The 3D images were reconstructed in both configurations. For the single lens, the validation study was based on assessing the detected depth and shift in the 3D images. However, for the modular one, the validation was based on mapping the sensitivity through the FOV. Performance parameters provide critical insights into how effectively a system operates and helps evaluate its efficiency, identify bottlenecks, prospect limitations and challenges and make informed decisions for design improvement. In this thesis work, resolution and sensitivity were the considered metrics for studying the envisioned system's performance. For both systems, I conducted a comparative study. In the single lens case, it was contrasted against the existing SIEMENS LEHR parallel SPECT. For the modular lens and since I reported progress on the single lens [133], I further compared it against the single lens-based and the SIEMENS LEHR parallel SPECT [309]. The multi lens-based SPECT was a more advanced geometry and more complicated in terms of developing forward projection and 3D reconstruction algorithms for a highly multiplexed system with an array of Laue lenses. A novel 3D reconstruction algorithm was developed as the first of its kind. The system's performance was contrasted against the SIEMENS LEHR parallel and Inveon multi-pinhole conventional SPECT systems. The flow of the work is described in Figure 3.1. This work is described in more detail in Chapters 4 and 5.

3.2.2 GAMOS Implementations

The lens-based SPECT analysis relies on simulating and modelling the gamma-focusing by diffraction process in a Monte Carlo environment. GAMOS is one of the most powerful and available Monte Carlo simulation toolkits for the movement of particles through matter. It is utilized in medical and space research as well as in high energy, nuclear, and accelerator physics [39]. As the process of diffraction is not yet implemented in the GAMOS toolkit yet, it does not support the modelling of wave-based properties; hence, the influence of wave nature cannot be simulated. Thus, I suggested an alternate method for simulating the effect of focusing gamma rays on the sensor plane and simulating detector response due to the focused projection in GAMOS. It's worth noting that the various detector effects were considered in the GAMOS implementations. Four case studies were considered, the single lens-based SPECT with single and three-point sources, and multi lens-based SPECT with single and three-point sources. The incident radiation field was modelled using the phase space file obtained from the MATLAB simulation described previously. The output of the MATLAB-based calculations was a phase space file with the energies, positions, and momenta of the diffracted photons, which were then used as input to the GAMOS environment. The proposed solution is based on simulating the detector response due to the diffracted gamma photons. Further details for the implemented environment for the phase space data will be discussed in Chapter 5. This work will be described in more detail in Chapter 6.

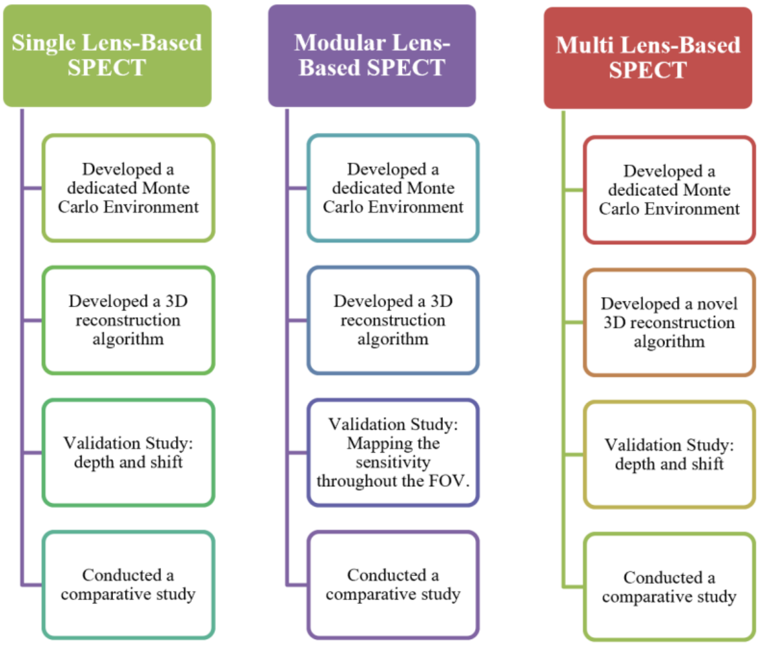

Figure 3.1 The MATLAB environments.

3.2.3 GEANT4 Implementations

Laue lens manufacturing is challenging due to the high precision in positioning and aligning diffractive crystals of diverse elements. Computer simulations of the Laue lenses in reliable, cutting-edge high-energy physics simulation environments are a readily accessible alternative to physical experiments. However, the Laue diffraction process has yet to be integrated with any of the available Monte Carlo simulation platforms, and the wave character of the phenomenon cannot be correctly modelled using any of the available platforms. This is one of the most significant challenges researchers have when attempting to model the Laue lens in a realistic particle tracking system.

I wanted to move further in this research, so I decided to develop the Laue diffraction process in one of the most stable and realistic Monte Carlo toolkits and compile it in GEANT4 and start with its very initial version.

Throughout this thesis work, I developed my own advanced example in GEANT4. I am presenting the first effort to model X-rays and gamma rays focusing based on Laue diffraction in the GEANT4 toolkit using an advanced example in its initial conception. It explains the essential components of the implemented Laue lens advanced example developed as part of the GEANT4 collaboration. Based on a Monte Carlo simulation, the developed example models the wave-based characteristics of gamma rays' and predicts diffracted, transmitted, and absorbed gamma rays locations on the detector plane. The model makes it easy to customize different input settings for various Laue lens designs.

The GEANT4 Laue diffraction project was envisioned to establish an open-source simulation software fully integrated within the GEANT4 Monte-Carlo simulation toolkit to simulate gamma rays diffraction based on the Laue lens focusing effect. Its functionality and features continue to grow while its performance improves. The necessary practical knowledge for developing and running the application that will be utilized in real experiments was acquired from the user's guide for Application Developers, Rev 6.0: GEANT4 Release 11.0, 10th. This implementation simulates the complete diffraction process starting with the source and ending with the detector response. Moreover, all detector effects and different phantom's volumes were considered to run in several case studies. The flow of the work is described in Figure 3.2. A thorough discussion of the developed advanced example is discussed in Chapter 7.

3.2.4 GEANT4 Implementations extended to GAMOS Users (Plugin)

After the successes in developing and validating the diffraction process (More details are discussed in Chapter 7) and running it as a GEANT4 advanced example, I decided to make it available for the GAMOS toolkit, which is a toolkit dedicated to a GEANT4-based architecture for medicine-oriented applications. The extension of the work and development of the Laue diffraction process makes it easy for GAMOS users to simulate the Laue lens diffraction by designing different geometries under various detector effects without any need for C++ coding. The flow of the work is described in Figure 3.3. A thorough discussion of the GAMOS case studies with the extended functionality is discussed in Chapter 8.

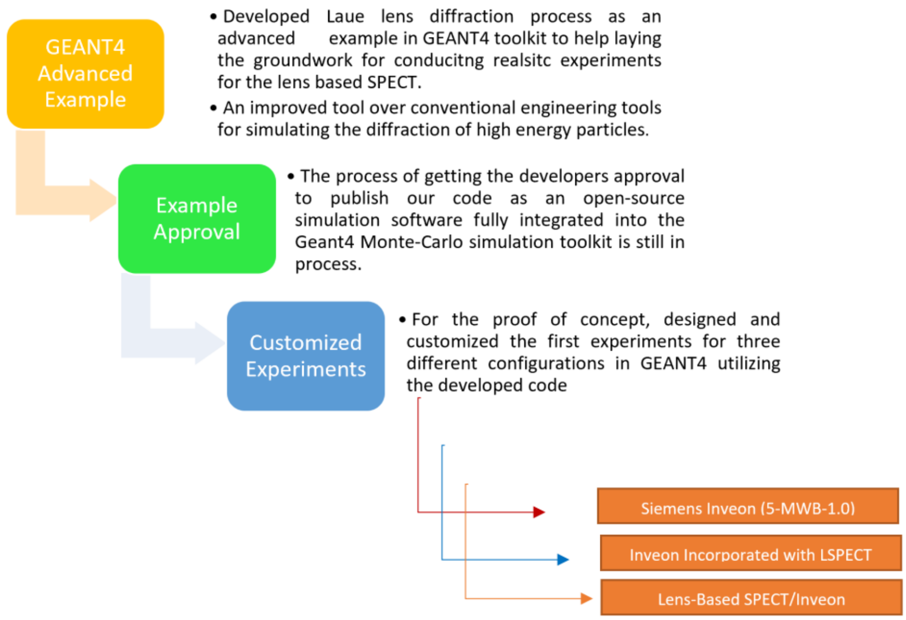

Figure 3.2 The GEANT4 advanced example and environments.

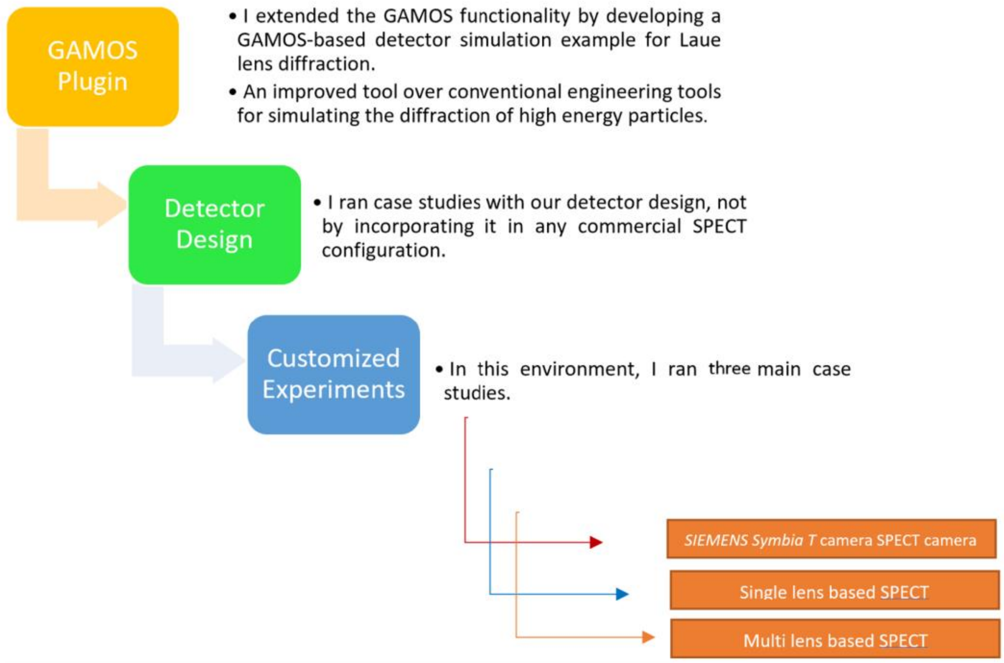

Figure 3.3 The extended work GEANT4 environment to GAMOS

3.2.5 Simulation Tools: 3D Image Reconstruction

In this work, I developed different 3D reconstruction algorithms specifically tailored to the three proposed geometries of the novel lens-based SPECT. These reconstruction algorithms demonstrate the first effort to reconstruct a meaningful 3D image from Laue lens projections. Thus, it was crucial to validate the developed algorithms. To this end, I ran several Monte Carlo simulations with various case studies for validation purposes. MATLAB version R2020a was utilized for this purpose. The machine learning and image processing toolboxes were used alongside several other toolboxes. This 3D reconstruction algorithms are discussed in further detail in Chapters 4 and 5.

3.3 Limitations and Challenges Associated with the Methodology

3.3.1 Computation Time and Code Optimization

This section briefly discusses the limitations encountered during this thesis work in developing the environments for the envisioned lens-based SPECT in the three different Monte Carlo toolkits. Moreover, I discuss the optimization methods used to mitigate these challenges and limitations.

3.3.2 MATLAB Environment

MATLAB, as opposed to compiled languages, executes code line by line, interpreting and executing each statement at runtime. Compared to compiled languages that directly transform code into machine instructions, this interpretative method may result in slower execution speeds [310].

To address the issue, I first identified the computationally extensive loops and executed them in parallel using **parfor loop** [311]. Moreover, with an isotropic source (radiating in all directions) defined as the particle generator in the MATLAB environment, only the gamma rays hitting the Laue lens lane were considered. This is achieved by directing the rays based on the angles that define the maximum and minimum deviation angles from the lenses plane. This is discussed in further detail in Chapter 4, Section 4.6.1.

3.3.3 GAMOS Environment

The computation time in GAMOS simulations is mainly impacted by the physics models and interactions that relies in GEANT4; these models are computationally extensive [299].

To minimize the length of the computational process, I modified the code to work with parallel job processing. This method allows the execution of simulations using multiple processors and computing resources. This would reduce the overall execution process as the jobs will be distributed among multiple processing units. This code optimization is discussed in further detail in Chapter 6, Section 6.2.3.

3.3.4 GEANT4 Environment

The high computation time in GEANT4 simulations was significant and presented one of the main challenges in this research [312]. The number of particles can be vast in high-energy physics experiments or complex detector geometries. Consequently, simulating the trajectories and interactions of all these particles can consume significant computational resources and time. Furthermore, the precision and practicality of the GEANT4 simulations, including many events and various real detector effects, also contribute to increased computation time [313].

To alleviate the problem, I optimized the code using the General Particle Source tool (GPS) in GEANT4 [306]. This is done by defining the energy, direction, and primary source properties, and most importantly, the distribution of the gamma rays. I set the source distribution angle based on the lens-based SPECT's defined geometry. Moreover, the distribution angle of the primary generator was tweaked to be directed only towards the Laue lens/pinhole plane in order to avoid generating unnecessary particles.

3.3.4.1 Running in a High-Performance Computer: NCI

Several simulations related to this thesis work were run utilizing Australia's preeminent computing facility the National Computational Infrastructure (NCI). However, several problems were encountered due to exceeding the limited execution time per run, which resulted in either terminating or killing the process of the running simulations.

To address this problem, it was essential to redesign the simulations with time constraints and consider the impact of process termination. Moreover, some of the codes were modified to save the data periodically during the execution process (checkpointing).

3.4 Chapter Summary

This chapter provided an overview of the research approach and the applied methods. The simulation tools and the different developed dedicated Monte Carlo environments in MATLAB, GAMOS, and GEANT4 toolkits were introduced.

Acknowledging the limitations and potential biases that may have influenced this research methodology is vital. To this end, I also discussed the limitations and challenges encountered associated with the method and the available tools as well as the measures implemented to address them, including the code and computation time optimization processes.

4. A Novel Ultra High-Resolution Lens-Based SPECT: Insight to Lightfield Imaging: MATLAB Monte Carlo Study

Developing nuclear imaging systems for diagnostic purposes is one of the most promising research fields. Optimizing the collimator's geometry for a given number of pinholes in a SPECT collimator has been challenging, prompting several researchers to suggest various SPECT collimator designs. Moreover, the pinhole geometry of the collimator has a significant consequence on the sensitivity and resolution of the imaging system [88]. One of the significant drawbacks of the conventional SPECT systems is the trade-off between resolution and sensitivity, or in other words, the sensitivity is not decoupled from system resolution. To tackle the constraints associated with the current SPECT imaging designs, this chapter presents a novel SPECT imaging method by introducing the notion of gamma focusing by diffraction [133]. The work described in this chapter represents the first realization of a novel Ultra-High-Resolution Lens-Based SPECT that does not require parallel collimators or pinholes. It also conducts a first-of-its-kind Monte Carlo analysis in this field. The proposed design would potentially lay the foundation for new SPECT imaging technology that can be extended to lightfield imaging.

This chapter discusses the initial and gradual development of the dedicated Monte Carlo simulation used for designing and optimizing the Laue lens tailored for the lens-based SPECT application. Moreover, it describes the initial design parameters and the tracking Monte Carlo models for the envisioned system. I started by proposing the initial idea of a single lens-based SPECT geometry. The designed environment incorporates a realistic physical interaction that accounts for possible absorption and attenuation phenomena.

Optimizing the lens for SPECT applications and detector geometries using simulations based on raytracing or Monte Carlo algorithms is time-consuming due to the need to vary many system parameters. As an efficient alternative, I developed a separate Monte Carlo environment to first optimize the lens design in Mathematica, and then tested its application in the SPECT gamma camera environment developed in MATLAB.

A 3D reconstruction algorithm that is customized to the focused Laue lens projections is also described in this chapter. The purpose of the reconstruction algorithm is to calculate an accurate 3D radioactivity distribution from the acquired projections. Thus, rigorously validating the reconstruction algorithm for a newly proposed SPECT design is crucial. To this end, I conducted validation studies that addressed two essential parameters, the mapping of the depth and shift information in the 3D reconstructed images of the lens-based SPECT and the sensitivity mapping over the field of view (FOV). For detailed comparison and rigorous evaluation, the lens-based SPECT parameters were downscaled to have comparable characteristics with current LEHR SPECT systems. The 3D reconstructed images of the proposed design were assessed against the existing parallel LEHR and multi-pinhole Inveon SPECT.

This chapter is structured as follows: Section 4.1 presents an introduction, then Section 4.2 gives a brief idea on lightfield imaging and discusses a prospective insight into advanced SPECT imaging using the focusing lenses instead of the conventional pinholes. Section 4.3 describes the methodology and the study of system characteristics. Section 4.4 discusses the Laue lens' design parameters and the developed environment for optimizing its function. Section 4.5 introduces the geometry and parameters of the proposed single lens-based SPECT design. Section 4.6 presents the experimental setup for the proposed system. Section 4.7 discusses the developed 3D reconstructing algorithm for the single lens-based SPECT. The findings and experimental results are presented in Section 4.8. The chapter concludes with a summary in Section 4.9.

4.1 Introduction

The spatial resolution and sensitivity influence the performance of SPECT systems. These two factors are determined by the collimator properties when the size and functionality of the detectors are identical across systems [314, 315]. Many collimators confine the incidence direction of gamma rays, where they strike the scintillation crystal to identify the radiation source. In SPECT imaging, many collimators are utilized depending on the application [98]. The parallel-hole collimator is often used for clinical imaging because of its excellent sensitivity and adequate spatial resolution for general clinical cases [88]. In small animal imaging, where spatial resolution is the most critical factor, the pinhole collimator is often employed to boost the system resolution [99, 316]. Despite the significant advancements in SPECT imaging technology over the past three decades, the fundamental design of imaging equipment has remained the same. In the past decades, the demand for high-resolution and high-sensitivity SPECT scanners triggered several efforts to design and optimize the collimator and detector parameters.

As we approach a new era of digital lightfield imaging and as the technology heads towards new fields, it is crucial to reflect on the developments and trends in what has become a thriving interdisciplinary field combining optical imaging, image processing, computer vision, and computer graphics. In light of existing SPECT systems' technical pitfalls and recent improvements that were recounted in Chapters 1 and 2, I propose an off-centre collimation system by exploiting the use of the Laue lens. Using this novel collimator would potentially open SPECT imaging to new imaging techniques, such as lightfield imaging. This reinterpretation in SPECT design would potentially provide a new perspective in changing traditional nuclear imaging.

Presently, nuclear medicine tools are often implemented using Monte Carlo (MC) methods. Monte Carlo simulations are an essential tool in SPECT and PET modelling, and they are ideal techniques because of the stochastic nature of radiation emission. The optimization of SPECT and PET cameras and the study of the significance of various physical processes involved in image generation can benefit significantly from MC simulations [317]. It contributes to system design and streamlining imaging and processing procedures. A variety of Monte Carlo simulation toolkits are currently accessible for simulating SPECT and PET configurations [318]. The available toolkits can be utilized to model the transport of photons and electrons in any material and account for many physical processes. The Monte Carlo approach allows researchers to comprehend the physics underlying the formation of images and aids them in developing enhanced processes. The impacts of phenomena such as Rayleigh and Compton scattering, fluorescence photons, and electron transport can be investigated independently of one another [317, 318]. Moreover, mathematical modelling is required to evaluate various parameters in nuclear medical imaging systems, since there is no analytical solution to the transport equation representing the interaction of photons with nonuniformly attenuating body structures and complex detector geometries [317].

This chapter presents a Monte Carlo simulation study for designing a Laue lens tailored to nuclear imaging applications and for assessing the feasibility of the novel SPECT nuclear imaging system proposed for imaging small animals and brain, based on incorporating the Laue lens as part of a multi-pinhole collimation system.

4.2 Lightfield Imaging

The lightfield concept is an established idea that has emerged in recent years due to the development of digital and optical technologies and a better knowledge of how the human visual system perceives and interprets the world [132, 319]. In contrast to a photograph, which represents visual information as a projection of light onto a 2D image plane, a lightfield portrays the world around us as a collection of light rays that fill the 3D space it represents [319]. Lightfield imaging's significant contribution is that a reframing of the conventional photographic imaging approach that separates the process of imaging a scene capture, from the actual realization of image synthesis, makes it possible for post-processing capabilities. The underlying concept is that the lightfield capture method enables intermediate processing that goes well beyond standard image processing. Modern cameras are sophisticated computers that execute complex algorithms to produce high-quality 2D images. However, lightfield imaging is growing beyond this generation by challenging existing optical systems to facilitate recording high-dimensional data sets, including rich scene information. The 2D visuals provided to the human observer are processed reproductions of the higher-dimensional data gathered by the sensor, which only the computer can see in its unprocessed form. This partial substitution of computers for physics facilitates the post-capture customization of images on an unprecedented scale [132, 320].

Lightfield cameras offer significant postprocessing capabilities, such as refocusing the image after it has been collected and shifting the point of view. Figure 4.1 illustrates the lightfield concept using a Micro Lens Array (MLA) camera. A plenoptic camera is not substantially different from a conventional one, except that a microlens array is placed right in front of the imaging sensor, allowing the directions and intensities of light rays to be concurrently recorded.

4.2.1 Lens-Based SPECT: A Paradigm Shift for Lightfield Imaging

At the start of this research, I was inspired by my supervisor's patent [253], where he proposed a 3D X-rays CT method based on lightfield imaging, and I then had the vision to propose a SPECT imaging system akin to the lightfield camera. However, finding a microlens array that operates for gamma rays to replicate the lightfield imaging concept remains challenging [321], as the they cannot be used for focusing photons with high energies that are emitted by SPECT radiotracers [127].

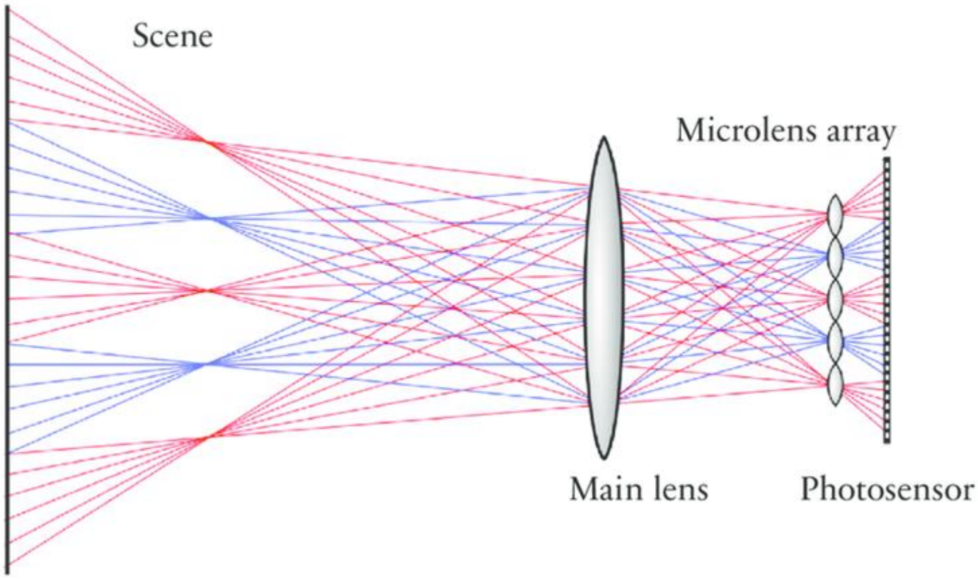

Figure 4.1 Lightfield imaging based on MLA [322].

To apply the lightfield concept to existing diagnostic imaging systems, optics capable of focusing gamma rays are required.

The underlying aim for exploring the effect of X-rays focusing and reflective optics was the requirement for focusing optics for intense gamma photons. Several attempts used grazing incidence optics to focus gamma rays. As discussed in Section 2.4, due to the inverse relationship between the angle of reflection and photon energy, gamma focusing using reflective ray optics is impractical for imaging radionuclides that generate gamma rays with energies between $100 - 200\ keV$. A complete focusing system will require more laboratory space than an absorptive collimation system since separating the small animal and the detector is equivalent to a few metres. Considering all the previous means of gamma focusing optics, their use will not be practical for SPECT applications. Consequently, bringing the concept of diffractive focusing to nuclear imaging via the Laue lens is a promising strategy for focusing energetic gamma photons and enhancing resolution.

As a glimpse into the future of improved SPECT imaging, I present a Laue lens SPECT that is based on gamma focusing by photon diffraction [133]. The proposed system has been designed and optimized for the $140.5\ keV$ photon emitted by Tc^{99}. The Laue lens would collect high-energy photons from a vast area and then focus them onto its focal point on the detector plane; the placement of the focal point is determined by the source's shifts relative to the lens' axis. For any source shift from the lens axis, the same shift will be duplicated in the opposite direction on the detector plane, just like an optical lens. The projections of the Laue lens dependent on source shifts from its axis are depicted in Figure 4.2. Using a Laue lens in a SPECT system would potentially permit radiation sampling by decoding the angular resolution with a higher spatial resolution. With this method, SPECT images would potentially be refocused while maintaining their resolution.

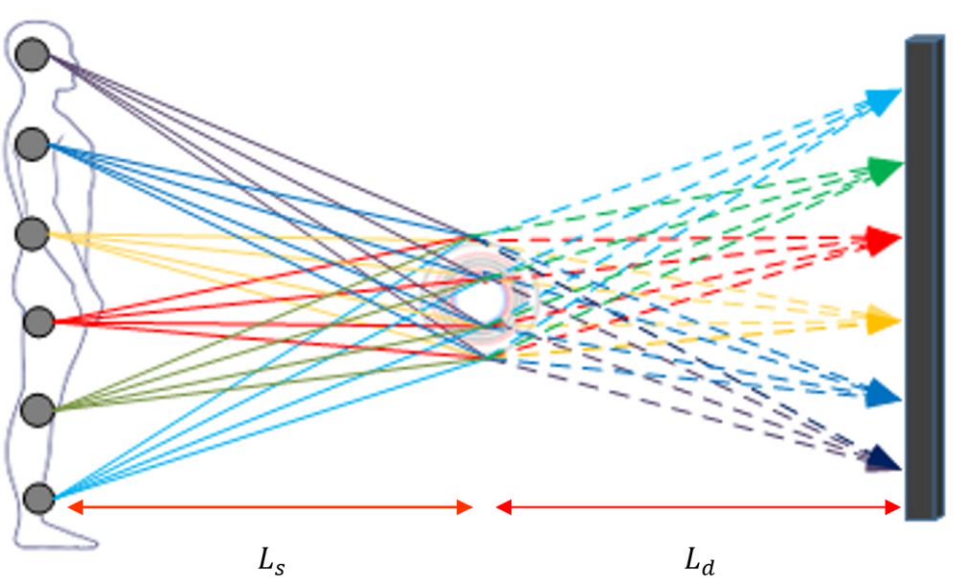

Figure 4.2 Novel Laue lens-based SPECT [133].

The Laue crystal lens acts similarly to a simple convex lens for visible light. The basic relationship is:

$$F \cong Constant \times E \qquad \textbf{Eq. 4.1}$$

where F is the focal length and E is the energy of the gamma rays. This relation holds as long as the sine of the Bragg angle is equal to its tangent. The Bragg angles are only a few degrees for the high-energy photons in the $100 - 150\ keV$ energy range that this lens is designed to focus. Thus, this approximation is accurate. The above equation can also be expressed as:

$$\frac{1}{L_s} + \frac{1}{L_d} = \frac{1}{Focal\ Length} \qquad \textbf{Eq. 4.2}$$

where L_s is the distance from the source to the lens, L_d is the distance from the lens to the detector.

4.3 Methodology

This section describes the methods used to model and characterise the design of the proposed single lens-based SPECT system. To model and study the envisioned system behaviour, I developed two different studies in Mathematica and MATLAB. The Mathematica-based study was developed for designing and optimizing the Laue lens tailored for a SPECT medical imaging application using a genetic algorithm [323]. The second one was developed to model the behaviour of the SPECT system augmented with a Laue lens in a gamma camera dedicated environment using MATLAB [133].

Whereas the forward projection and 3D reconstruction algorithms developed for the single lens-based SPECT would definitely differ from those currently utilized for the conventional parallel LEHR or the multi-pinhole SPECT and other tomographic modalities, it is possible to adapt existing techniques to analyse images acquired with the Laue lens. To this end, I developed a tailored forward projection and 3D reconstruction approaches/algorithms to analyse the acquired images from a lens-based SPECT system. The Monte Carlo simulations were based on the forward projection and ray tracing concept. Furthermore, I developed a customized 3D image reconstruction algorithm in MATLAB to reconstruct the projection images resulting from the focused photons. The purpose of the reconstruction algorithm is to calculate an accurate 3D radioactivity distribution from the acquired projections.

Validating the reconstruction algorithm for the new proposed SPECT design is crucial. To this end, I conducted validation studies that addressed two essential parameters, the mapping of the depth and shift information in the 3D reconstructed images and the sensitivity mapping over the field of view (FOV). The performance parameters of the proposed design were assessed against the existing parallel LEHR SPECT based on two figures of merits, sensitivity, and resolution, which were inferred based on standard methods.

I used simple phantoms for the initial characterisation of the system, the first was a single-sphere phantom, and the second was a three-spheres phantom.

4.3.1 Study of System Characteristics

The single lens-based SPECT scans were performed for 360° rotation at 10° steps. I used a one-point and a three-point phantom. The activity of the different point sources or volumes was selected to imitate cases of a suspicious mass or tumour in its initial stage compared to the background. The different activity simulates the cancerous tumour with higher radio tracer absorption of the gamma rays. The one-point phantom consists of the same spherical sources of $0.03\ mm$ radius. The three-sphere phantom consists of spherical sources spaced by $0.1\ mm$ from centre to centre. Each sphere has an activity of $0.1\ mCi$. Sub-millimetre sized spheres were chosen because the proposed crystal lens system has lower background noise and maintains the same overall sensitivity for small sources; thus, it should provide higher sensitivity than existing full-body scanners for small sub-millimetre sources [209, 257].

The resolution of the Laue lens for a particular radiation wavelength depends on the crystals' mosaicity. To this end, the spatial resolution study was performed using two different approaches; the first was based on the FWHM of the point spread function generated from the Gaussian distribution of the 3D reconstructed image of a single sphere point source. The second method used a three-point sphere. I ran several case studies to examine the minimum distance between three spheres the Laue lens can resolve. More details for the resolution analysis method are described in Section 4.8.3.

A point source of $0.03\ mm$ radius radiating $100{,}000\,\frac{photon}{projection}$ was used to evaluate the sensitivity. The work was performed with Monte Carlo simulations implemented in MATLAB. The sensitivity was studied by placing the three-sphere phantom at various axial shifts and distances from the Laue lenses' axis with respect to its centre within the lenses' FOV to represent different experimental scenarios. The actual sensitivity is calculated considering that the radioactive source is isotropic. More details for the sensitivity analysis method are described in Section 4.8.4.

In order to evaluate the proposed design and conduct a comparative analysis with conventional SPECT imaging systems, the parameters of the proposed system have been downscaled to those of the existing LEHR parallel and Inveon SPECT systems. In addition, MATLAB was used to model a LEHR parallel hole SPECT with two different geometries.

4.4 Laue Lens Design

4.4.1 The Gamma Diffractive Lens

In crystalline materials, parallel atomic planes generate a coherent effect known as X-rays diffraction. Each crystal can be viewed as a miniature mirror that redirects gamma rays from the incident beam to a focal point via Bragg reflection. Each crystal diffuses an energy spectrum proportional to the size of its mosaic (also called mosaicity) [324]. Placing the crystals on concentric rings around an optical axis and selecting the inclination angle on each ring allows the construction of a broad-band gamma rays lens with continuous energy coverage over a given band [325]. In a crystal, incident photons are scattered by the electrons. Reflected waves interfere constructively, resulting in a diffracted beam, provided their paths through the crystal result in a wavelength-multiple phase shift [326]. This condition is met when Bragg's law is fulfilled as in:

$$2d_{hkl} \ \sin\theta_B = \lambda \qquad \textbf{Eq. 4.3}$$

where d_{hkl} is the distance between atomic planes, θ_B is the angle between the incoming photon trajectory and the diffracting lattice planes, and λ is the radiation's wavelength. The Bragg's angle, θ_B, is dependent on the orientation of the lattice planes. The distance between surfaces for a crystal with a conventional cubic cell may be represented as:

$$d_{hkl} = \frac{a}{\sqrt{h^2+k^2+l^2}} \qquad \textbf{Eq. 4.4}$$

where a is the crystal's lattice constant and h, k, and l are the planes' Miller indices. Two possible diffraction geometries are available. The first one is referred to as Bragg's geometry, as shown in Figure 4.3a. In this instance, the diffracted beam emerges from the same crystal surface as the incident beam. In contrast, in the Laue geometry, as shown in Figure 4.3b, the diffracted beam emerges from the surface opposite to the incident beam. The Bragg angle is exceptionally narrow for high-energy photons, such as those emitted by a radiotracer, and a large crystal is required to diffract even a small beam. For this rationale, the Laue geometry seems to be the most practical option for the envisioned lens-based SPECT design.

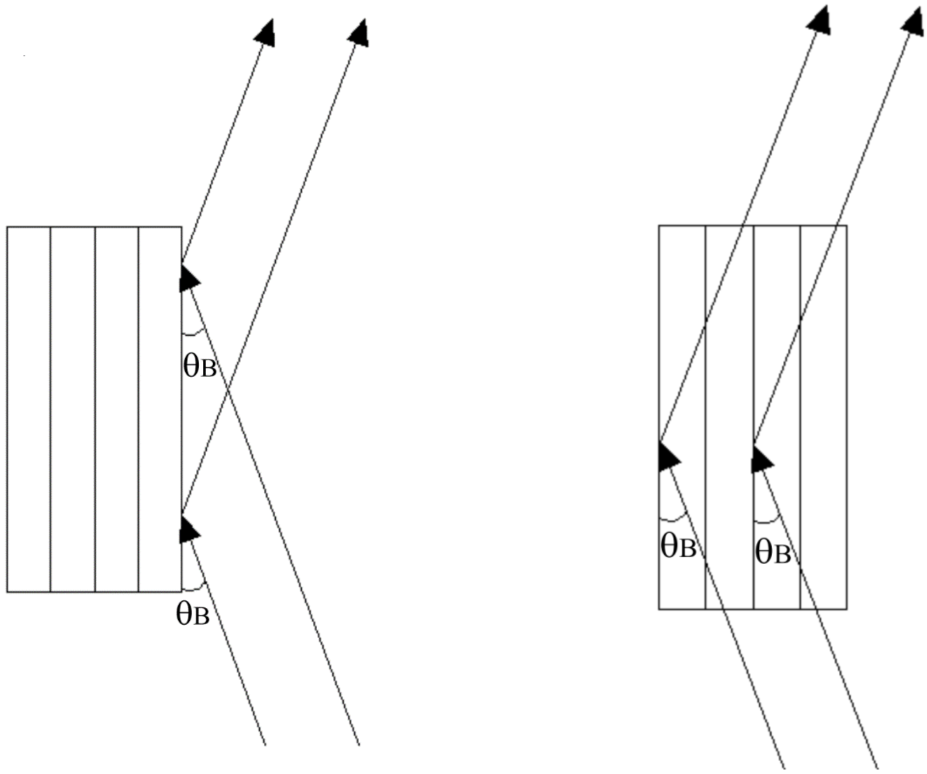

(a) (b)

Figure 4.3 Diffraction geometrical structures. (a) The Bragg's geometry: the diffracted beam emerges from the identical crystal surface as the incident beam, (b) The Laue geometry: the diffracted beam emerges from the opposite surface that the incident beam strikes [248].

The intensity of the diffracted beam relies on the crystal characteristics. The reflectivity of a crystal is defined as the ratio of the intensity of the diffracted beam to the intensity of the incident beam. Instead, the diffraction efficiency is defined as the ratio of the intensity of the diffracted beam to the intensity of the transmitted beam in the absence of diffraction. An extensive study of Laue lens features at the crystal level is presented in highly specialized review articles [257, 327, 328]. In this thesis, just the concepts pertinent to studying a Laue lens are examined.

4.4.2 The Dedicated Lens Design for SPECT Imaging

The primary goal of this research is to identify the characteristics of the Laue lens adapted for the lens-based SPECT. The design and operating mechanism of the crystal diffraction lens in this work were derived from the crystal lens telescope system intended to focus intense gamma rays between $300 - 700\ keV$ using crystal diffraction [329].

Even though the Laue lens' design parameters are comparable to those utilized in astrophysics applications, the design phase for each application is substantially different. Polychromatic parallel hard X-rays are emitted from distant galaxies and astronomical sources. This is contrary to what occurs in nuclear imaging when the patient is emitting gamma rays in all directions. Thus, it is vital to deal with monochromatic and divergent- not parallel - gamma rays.

The design of the lens is tailored to focus a restricted range of energies, in this case, the $140.5\ keV$ gamma rays emitted by Tc^{99}. The incoming photons will be diffracted by a unique set of crystalline planes for each ring. The radius of each ring is adjusted such that all rings concentrate the same photon energy at the same focal point. Each ring's radius is given by:

$$CR = L_d \times \theta_B$$

Eq. 4.5 [330]

where CR is the crystal ring radius. Crystal diffraction is the coherent reflection of a photon by successive layers of atoms in a crystal. If the diffraction angle, also known as the Bragg angle, is precisely optimal, the wavefronts from each reflection will be coherent, and their amplitudes will accumulate. The intensity of diffracted radiation is proportional to the square of its amplitude. For gamma rays with energies more than $100\ keV$, the diffraction process involves many thousands of atomic layers; accordingly, the intensity of the diffracted beam is many thousands of times greater than the sum of the individual reflections from the crystal layers. The following equations define the requisite diffraction conditions:

$$\mathrm{n}\,\lambda = 2 \times d \times \sin\theta$$

Eq. 4.6 [330]

$$\theta 1_{Incident} = \theta 2_{Diffracted}$$

Eq. 4.7

where n is the diffraction order, λ is the monochromatic light wavelength, d is the distance between consecutive atomic layers, and θ is the Bragg angle. $\theta 1_{Incident}$ is the angle between the direction of incoming radiation and the surface of the crystalline planes that induce diffraction, whereas $\theta 2_{Incident}$ is the angle between the diffracted beam and the crystalline planes that cause diffraction. The diffraction response of crystals in a Laue lens relies on the crystal's material, crystallographic orientation, and position. For X-rays diffraction, it may be beneficial to integrate various materials and crystallographic orientations to maximize integration while flattening the energy dependence of the collected photons. Figure 4.4 shows a schematic diagram of the diffraction process implemented by the Laue lens, r is the radius of the Laue lens, L is the focal length, and θ is the divergence angle.

This study implemented a tracking Monte Carlo genetic algorithm [40] to optimize the Laue lens for the intended application. Using a custom-built Monte Carlo technique in Mathematica, diffraction is characterized. Depending on the application, the precise characteristics of a Laue lens may vary significantly. To ensure the program's generalizability and adaptability, the user can give a variety of initial configurations. These features consist of the focal length for the energy band, the size of the crystals, the minimum and most effective radius of the Laue lens, the crystal material, and the diffracting planes [323].

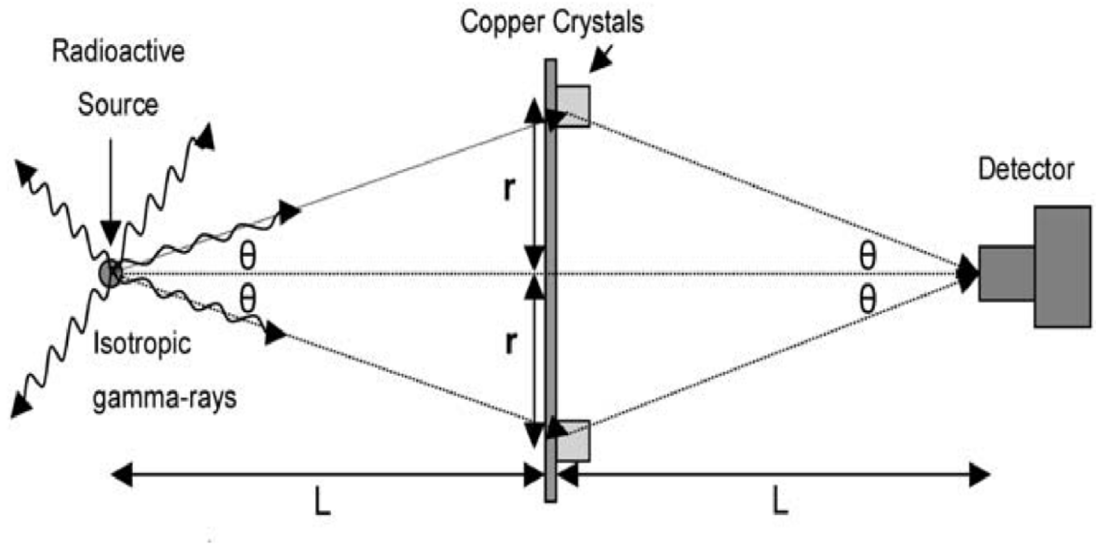

Figure 4.4 Schematic diagram for the diffraction process implemented using Laue lens, r is the radius, L is the focal length [331].

Once the initial parameters have been defined, the number of crystals in each ring, the thickness of diffracting planes, the material type, and the crystal configurations are computed. As a result of the code, the optimal Laue lens turned out to be comprised of seven rings of mosaic crystals, as seen in Figure 4.5. The lens' features are outlined in Table 4.1. As a function of focal length, the formula for obtaining the lowest lens radius is as follows:

$$R = \tan\theta_B \times F \qquad \textbf{Eq. 4.8}$$

where R is the radius, F and is the focal length. The Laue lens was generated by taking into account initial input parameters, such as the focal length and the photon energy. It was restricted to having a small focal length to fit in the SPECT application. Moreover, gaining the highest possible efficiency was one of the primary considerations. The lens comprises Al and Cu, and each of its seven rings has a unique number, arrangement, and crystalline composition. The reason behind selecting Al and Cu is that they are found to be the best in obtaining a small focal length combined with the best-achieved efficiency. It is assumed that the crystals in each ring are identical in material. However, as indicated in Table 4.1, each ring is created with various crystals. There are 606 crystals in total. The crystals' plane focuses photons on a detector 50 cm from the source. In this research work, a symmetric Laue geometry and the alignment of a perfect crystal were considered. Thus, the source-to-lens distance is equal to the lens-to-detector distance. Miller indices are a notation system used in crystallography to describe the orientation and planes of crystal lattice structures. There are four Miller indices: [111], [200], [220], and [311]; they were explicitly chosen using Monte Carlo simulation because they allow us to obtain the desired focal spot with the highest efficiency. The crystal size is 1 $mm \times 1$ mm, and the optimal crystal thickness for SPECT applications is 1 mm. While Figure 4.5 depicts the optimised Laue lens with default parameters, Table 4.1 details the lens' designed characteristics including the Miller indices in column one. Each ring of the proposed lens would have a distinctive Bragg's angle, as shown in Table 4.2.

Depending on the application, the properties of Laue lenses vary considerably. As a necessary consequence and to ensure the adaptability of the design to different nuclear applications, a scaling factor was added to the developed MATLAB Monte Carlo simulation in an attempt to scale the lens parameters for flexibility in design and as an additional feature for adapting the lens design to various nuclear applications. It is worth noting that the angles will still be the same for different scale factors. Hence, Bragg's law is still valid for all crystals. The scale factor is discussed in more detail in Chapter 7, Section 7.6.1.

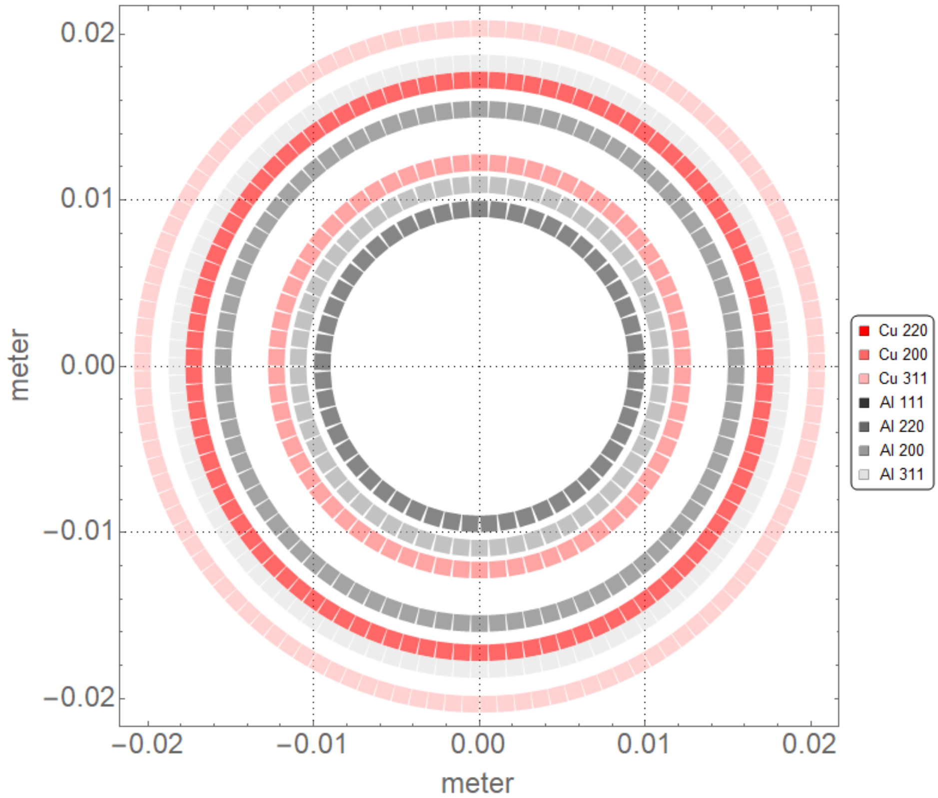

Figure 4.5 Front view of the designed and optimized Laue lens for lens-based PECT. The plot was generated with Mathematica.

Table 4.1 Features of the generated SPECT Laue lens using the genetic Monte Carlo algorithm.

Material	Reflectivity	Thickness (mm)	Ring Radius (mm)	Number of Crystals/Ring
Al (111)	37.42%	5.50	9.47	53
Al (200)	35.50%	6.36	10.94	62
Cu (200)	26.96%	1.81	12.25	70
Al (220)	29.64%	9.08	15.47	90
Cu (220)	24.30%	2.04	17.23	102
Al (311)	26.14%	10.77	18.35	108
Cu (311)	22.44%	2.20	20.33	121

Table 4.2 Distinctive Bragg's angles

Ring Number	Bragg's angle
Ring_1	$\theta_B \; for \; Al \; at \; 140 \; keV = 0.01894 \; rad$
Ring_2	$\theta_B \; for \; Al \; at \; 140 \; keV = 0.02187 \; rad$
Ring_3	$\theta_B \; for \; Cu \; at \; 140 \; keV = 0.02450 \; rad$
Ring_4	$\theta_B \; for \; Al \; at \; 140 \; keV = 0.03093 \; rad$
Ring_5	$\theta_B \; for \; Cu \; at \; 140 \; keV = 0.03456 \; rad$
Ring_6	$\theta_B \; for \; Al \; at \; 140 \; keV = 0.03093 \; rad$
Ring_7	$\theta_B \; for \; Cu \; at \; 140 \; keV = 0.04046 \; rad$

4.5 Single Lens-Based SPECT

This section discusses the initial design parameters and considerations for the proposed single lens-based SPECT system. The intended system comprises one Laue lens positioned at the pinhole centre in a geometry similar to that of a pinhole collimator, excluding the clinical collimator, the lens is positioned at equal distances from the detector and source planes, which was selected to be 50 cm.

Figure 4.6a shows the schematic diagram for the single lens-based SPECT Laue collimator with a lens at the pinhole's centre. Figure 4.6b shows the focused rays of one Laue lens for 3-point sources phantom. The Laue has radius of $20.3 \; mm$ placed in a planer plane with $42 \; mm \; x \; 42 \; mm$ dimensions. Figure 4.7 shows the measurements of a lens inside a pinhole.

As this is the first initiative to propose the architecture of the lens-based SPECT system, and as it has been developed from the foundation, the baseline parameters are kept simple. In addition, the concept considers the computational resources currently available to work with the computationally intensive Monte Carlo simulation.

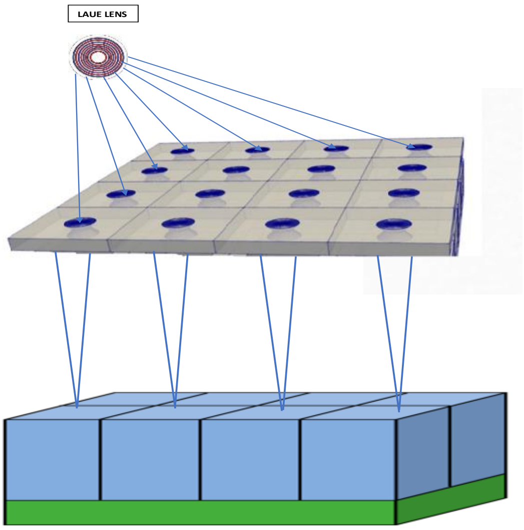

(a)

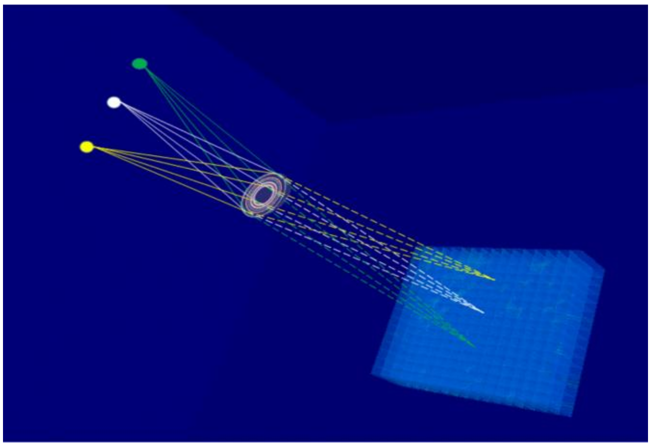

(b)

Figure 4.6 (a) Illustration of the single lens-based SPECT geometry, (b) The lens and detector geometry showing the focused rays of one Laue lenses for 3-point sources.

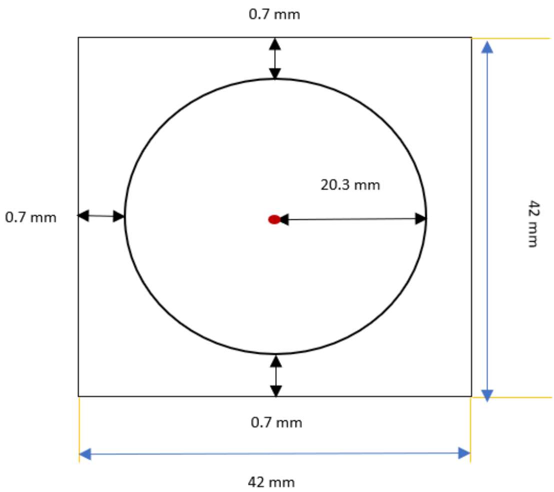

Figure 4.7 Illustration of Laue collimator with one lens inside a pinhole.

4.5.1 Detector Coupling with the Laue Lens

A gamma ray detector is a technology that can detect the presence of gamma radiation. Additionally, it may count the number of gamma rays hitting the detector. In the case of an imaging detector, it measures the direction of the incoming gamma radiation. The detector must be sensitive to the photon-to-matter energy transfer throughout all interaction processes. Numerous figures of merit characterise the detector: sensitivity and efficiency, energy resolution, response function spatial resolution, and response time.

Since the original purpose of a Laue lens in diagnostic nuclear medicine is to provide high-resolution functional images, the detector must have a greater spatial resolution than the lens not to compromise the imaging performance of the latter. The size of the detector constrains the field of view. The active area of the detector module is matched to the envisaged Laue-collimator, which has a $42 \times 42\ mm^2$ active area. The collimator of the lens-based SPECT design is intended to be simple yet practical.

4.5.1.1 Detector Shielding

By means of diffraction, the individual Laue lens will focus the rays that diverge and emerge in diverse directions from the object being observed. The rays can be transmitted, absorbed, or diffracted at the Laue lens plane. While absorbed photons will be stopped at the Laue lens plane, diffracted and transmitted photons will arrive at the detector plane at different locations. Therefore, appropriate shielding of the Laue lens is essential to prevent the sensor from detecting the stray photons. To this end, I set the forward projection and detection algorithms in such a way that all transmitted photons won't be detected by the detector and stopped from reaching the sensor plane. However, in a realistic experiment, physical detector shielding is necessary.

4.6 Simulation Design and Experiment Setup

As discussed in Chapter 3, the lens-based SPECT design was modelled in three different Monte Caro toolkits. In this chapter, I am presenting the MATLAB Monte Carlo environments that I developed for the single lens-based SPECT.

4.6.1 Forward Projection

The forward projection algorithm is a mathematical model to simulate the path of gamma rays and calculate their probability of detection by the gamma camera [332]. This generates expected data that can be compared to actual measurements to reconstruct the phantom's internal activity distribution [333]. A Laue lens is situated between the phantom and the detector. Tracing of rays is conditional on identifying the radiations to be traced based on Bragg's angle requirement. The algorithm generates random points within the spherical phantom. Then the algorithm uses a custom function to generate random azimuthal and polar angles for every arbitrary point. These angles are essential for identifying the cosine directions of the radiations. The angle between the randomly generated rays and the outer and inner rings determines the maximum and minimum divergence from the lens axis.

It is essential to propagate the rays according to the designated deviation limits to generate rays that only strike the Laue lens. In this simulation configuration, only the emitted radiation towards the lens is evaluated to reduce simulation time. Using algebraic equations, the ray vector for random radiations from those sites towards the Laue lens is determined; the deviation of the line from the lens axis must be less than the maximum deviation and more than the minimum deviation. At this point, the algorithm calculates the probability that a gamma photon will be transmitted, absorbed, or diffracted based on the angle of incidence on the Laue rings or the intersection angle. There are distinct probabilities for diffraction, absorption, and transmission.

The incident angle on the Laue rings - also known as the Bragg's angle- is calculated based on straight-line mathematical equations. As shown in Figure 4.8, if a ray struck any of the Laue rings with an incidence angle equal to Bragg's angle for that ring, it would be diffracted towards the detector with an angle equal to the diffraction angle. If not, it will be absorbed or transmitted. Figure 4.9a shows the generated rays in green and the focused rays in blue. Figure 4.9b shows absorbed rays in red at the Laue lens plane. Figure 4.9c shows the generated rays towards the Laue lens in green and the transmitted in yellow. Figure 4.9d shows an explanation for the forward projection algorithm starting from the source and ending on the detector plane.

Determining the pixel counts of the final focused rays on the detector identifies the intersection points of the beams with the sensor. The constructed Laue lens is shielded, therefore blocking transmitted rays. By mapping these intersections to pixel positions, the projection images are formed. Every time a diffracted ray strikes a pixel in the sensor plane, the image pixels of the projection images are incremented by one.

The lens/detector assembly is rotated around the phantom to obtain various view angles dependent on the angle shift/increment, also known as step angle. This process is performed for all radiations to develop a complete projection for a specific viewing angle. The procedure is continued by increasing the viewing angle until the entire object has been scanned in 360 degrees to generate sufficient 1 D projection images. The image output is in MAT format. The pseudo-code for the forward projection algorithm is given in Figure 4.10.

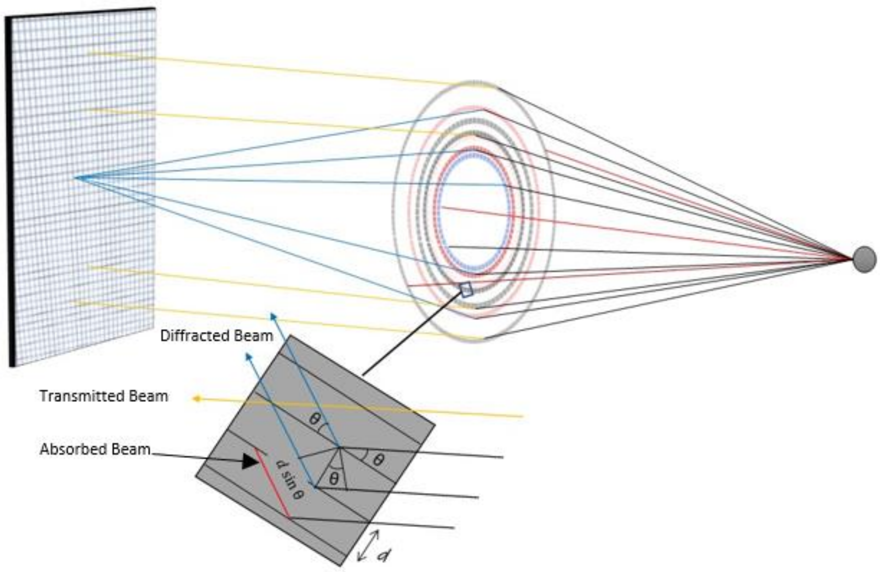

Figure 4.8 Three different scenarios for the radiations are either absorbed (Red), transmitted (Yellow), and diffracted (Blue) at the Laue lens crystals.

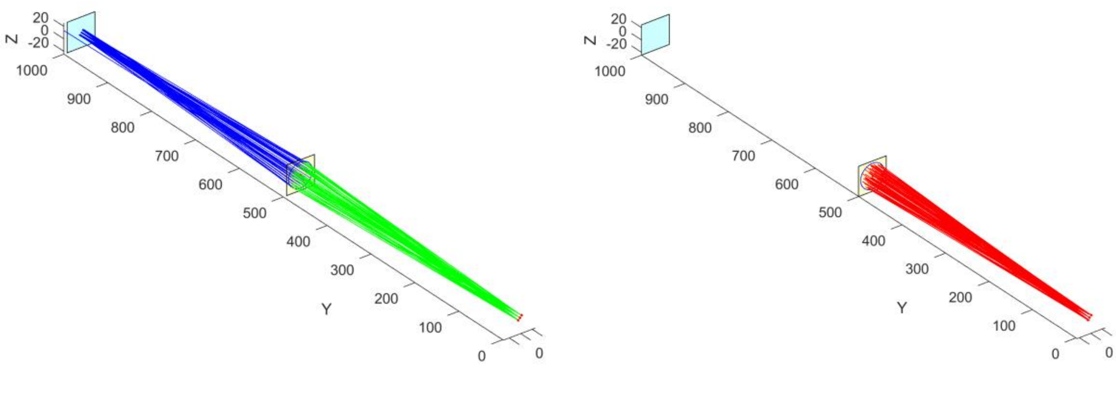

(a) (b)

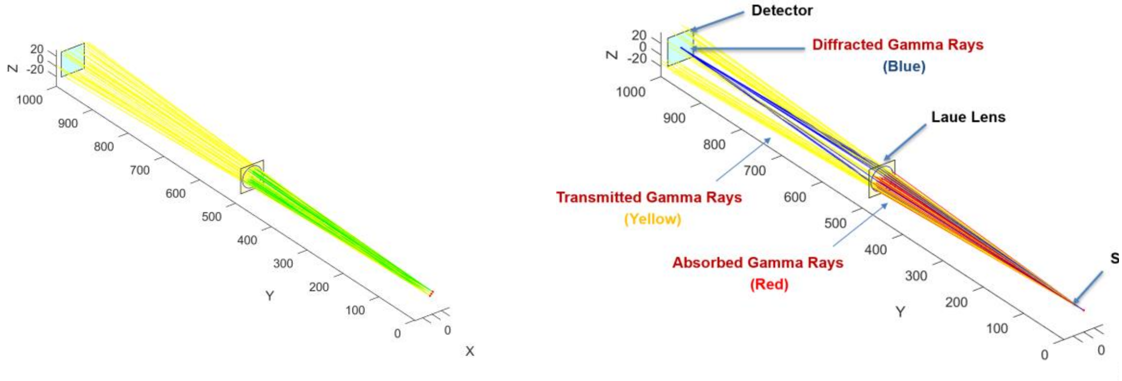

(c) (d)

Figure 4.9 In the forward projection algorithm. (a) The generated rays (green) and the focused rays by diffraction (blue), (b) The absorbed rays (red) at the Laue lens plane, (c) The generated rays towards the Laue lens (green) and the transmitted rays (yellow), (d) The forward projection explanation.

Algorithm: 3D Image Reconstruction

Initialization

```
Start
Do      Define isotropic source.
For     N=number of events.
Do      Generate random points inside the phantom.
For     N=number of generated random points.
Do      Generate random Azimuthal and Polar angles.
Do      Generate the cosine directions based on the defined Azimuthal and Polar angles.
Do      Generate the rays based on the cosine directions.
For     N=number of events.
If      <Ray intersect with the Laue lens> Then
Do      Generate the intersection angles of the rays with the Laue lens.
Else    Increment number of events by one.
If      <The intersection (incident) angle = Bragg's angle > Then
Do      Diffract the ray to the focal point on the detector pixels.
Do      Increment the pixels with diffracted rays count by one.
Else    Transmit or absorb the ray based on the intersection locations.
Else    Go to the next event.
End if
For     All pixels on the detector plane.
While   The pixel count on the detector lane ≠ zero.
Do      Assign XY points to the non-zero count pixel.
Do      Convert the points into pixel locations.
Do      Generate the projection image.
End
```

Figure 4.10 Pseudo-code for the Lens-based SPECT forward projection.

4.7 3D Reconstruction Algorithm

The first effort to reconstruct images from a Laue lens is presented in this section. I developed the 3D reconstruction algorithm (for more details see Chapter 2 Section 2.6.2) for the single lens-based SPECT's initial geometry. The 3D reconstructed images were generated using a dedicated algorithm for the focused Laue projections. The scanned phantom is reconstructed by projecting the diffracted points onto the detector plane using the ray tracing approach. The pixels behind each Laue lens determine the location of focused photons. When there are shifts from the lens axis, the spot will also shift.. From each non-zero projection pixel along the scanning axis, a perpendicular ray is generated towards the cube of interest. Then, Siddon's ray tracing algorithm is used to trace the rays that intersect the cube of interest [334]. This trace will include the number of intersecting voxels as well as the length of the intersection. The length of the intersected voxels is traced using a rapid voxel traversal algorithm and Siddon's tracing algorithm.

The values of intersecting voxels are updated using the product of the origin projection pixel value multiplied by the normalised intersection length. This procedure will be performed for all projection pixels as well as the acquired projection images with varying step angles. The flowchart for 3D reconstruction is shown in Figure 4.11.

4.8 Simulation Results

This section presents the initial single lens-based SPECT system performance results. To demonstrate and attest the validity of the proposed method, various case studies were conducted to ascertain the system's ability to preserve the depth and shifts in the 3D reconstructed images.

4.8.1 The Projection and 3D Reconstructed Images

Figure 4.12 shows a sampling of the 36 projection images of a single lens-based SPECT obtained by rotating the lens around three-point sources with a 10° step angle around a three-point source phantom. The x-axis and y-axis represent the column and raw indices of the pixelated projection image, respectively.

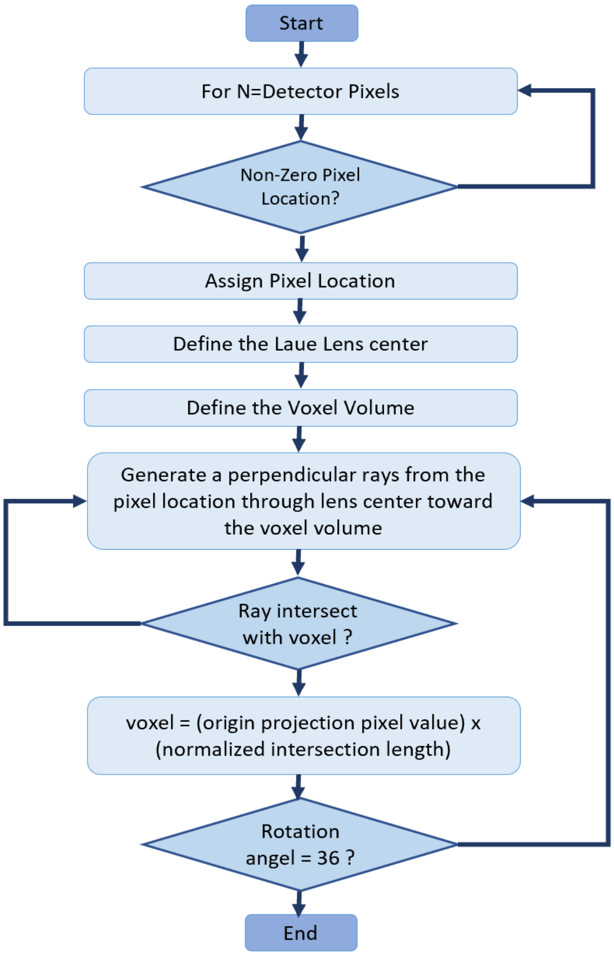

Figure 4.11 Flow chart of the 3D reconstruction algorithm dedicated for the single lens-based SPECT

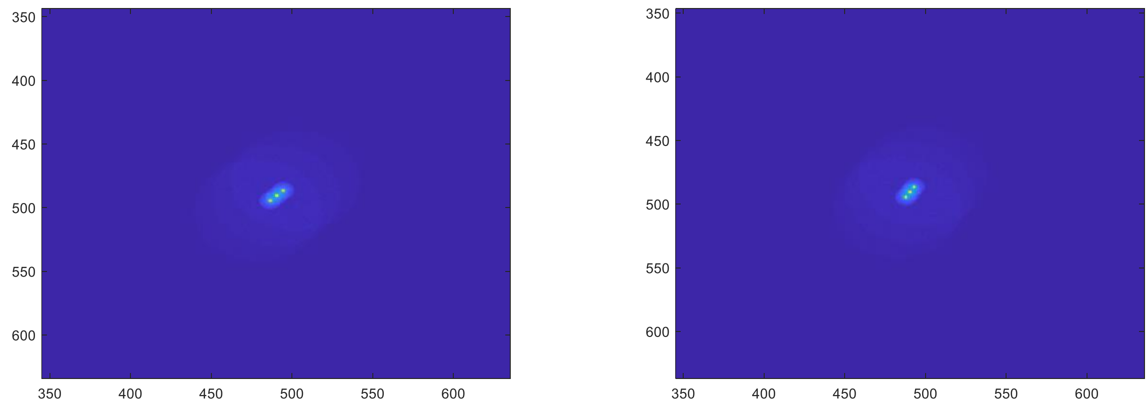

0° **20°**

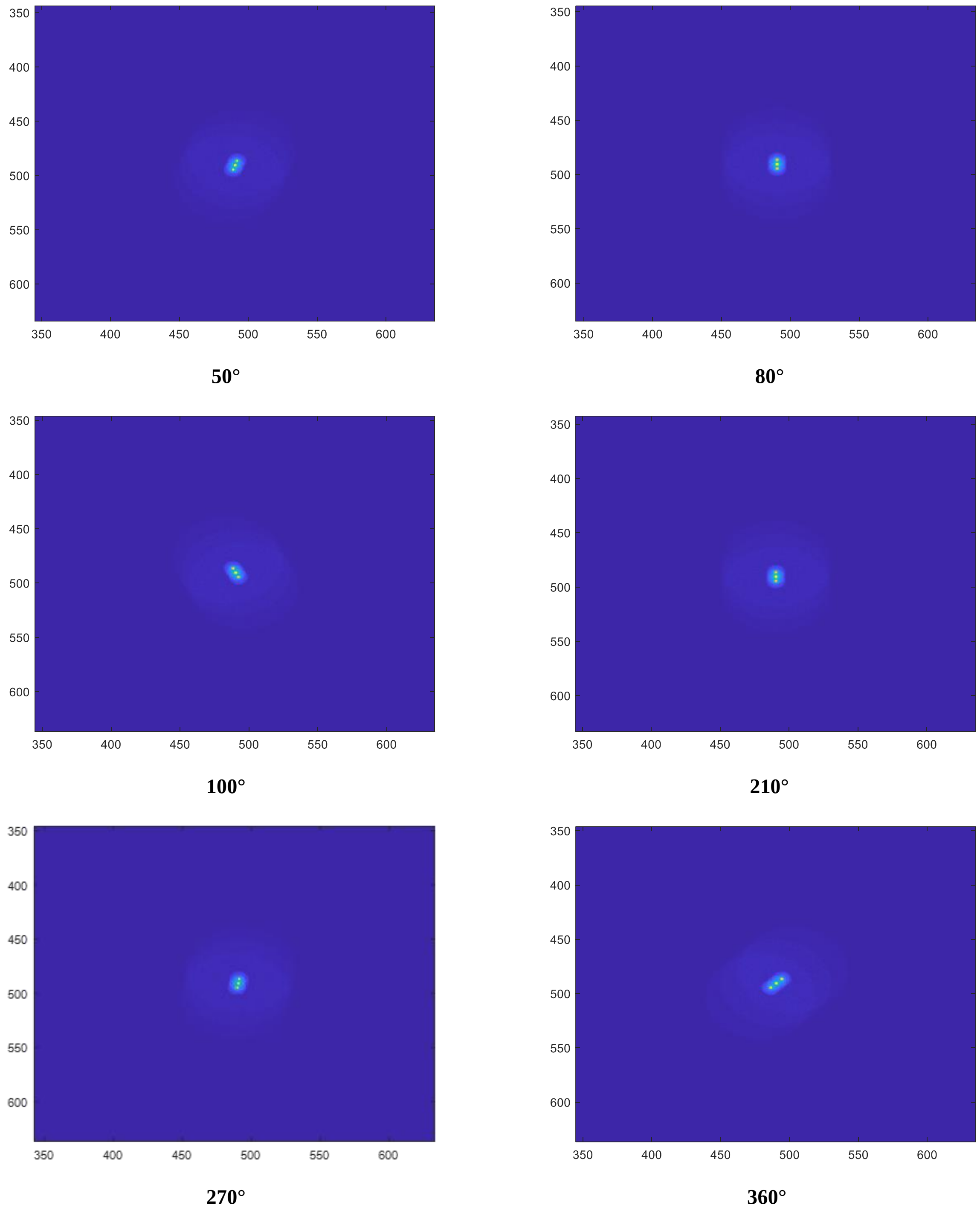

Figure 4.12 Single lens-based SPECT projections using phantom of 3 spheres, rotated at 10° step angle. The x-axis and y-axis represent the column and raw indices of the pixelated projection image, respectively.

Figure 4.13a and Figure 4.13b show the 2D XZ and the 2D YZ slice of the 3D reconstructed image, respectively. Figure 4.13c and Figure 4.13d show the 3D reconstructed image generated using MATLAB and the 3D reconstructed image generated using Volume Viewer, respectively.

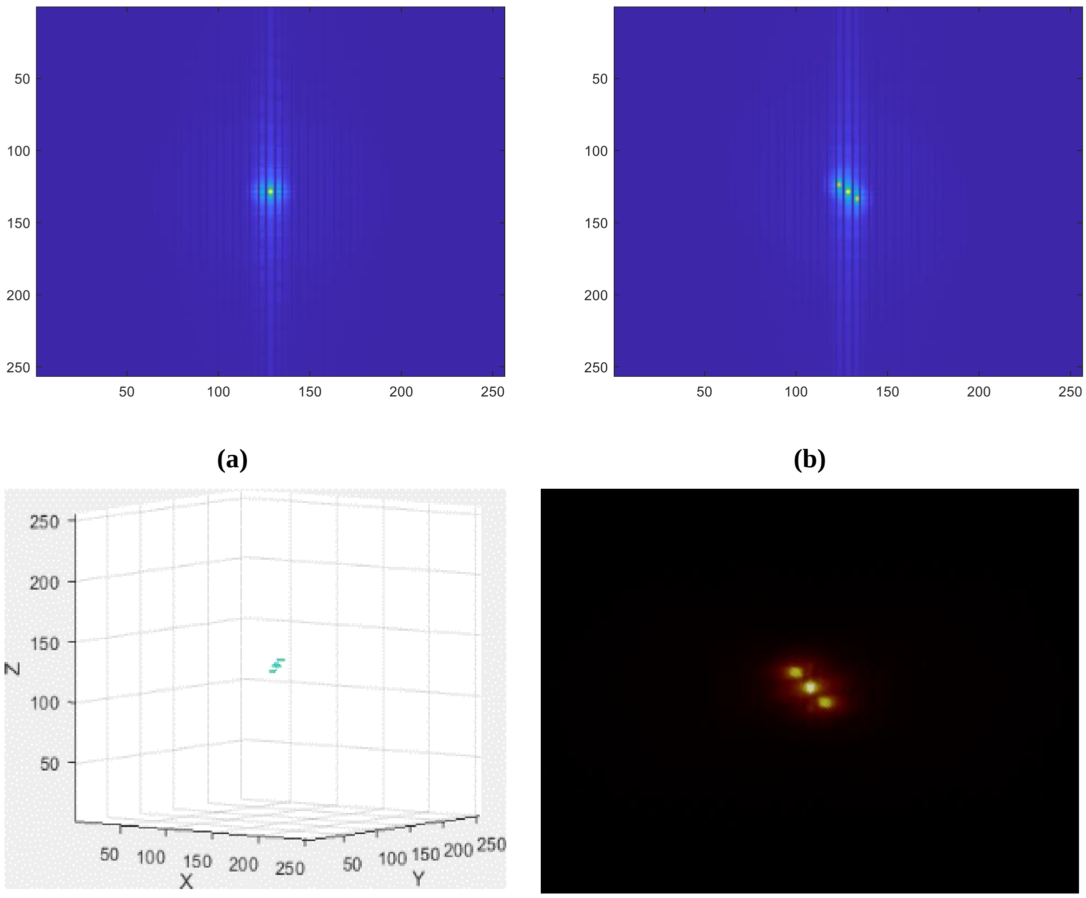

(a) (b)

(c) (d)

Figure 4.13 Reconstructed images (a) The 2D XZ slice of the 3D reconstructed image, (b) The 2D YZ slice of the 3D reconstructed image, (c) The 3D reconstructed image generated using MATLAB, (d) Top view of the 3D reconstructed image generated using Volume Viewer. Units are in mm (measurements are based in pixel locations).

4.8.2 System Validation: Phantom Depth and Shift in the 3D Reconstructed Images

This is the first attempt to reconstruct images from the Laue lens projections. Thus, it is crucial to ascertain the validity of the 3D reconstruction algorithm. In order to obtain in-depth knowledge about the lens' imaging properties when it is augmenting the conventional gamma camera design, several case studies were simulated by varying the lateral shift from the lens axis and depth of the simulated spherical sources. The depth is considered as the displacement of the source along the Z-axis, and the shift is the lateral displacement with respect to the lens' axis. The Laue projections for the different configurations were reconstructed based on the back projection of the focused radiations.

The phantom depth and shift information were determined using the pixel coordinates and voxel size in the 3D reconstructed image. The voxel volume was $256 \times 256 \times 256$, with a range of bounds from $-5\ to\ 5\ mm$ in both directions. The equation to calculate the shifts and the depths in the 3D reconstructed image is:

$$S_{x,y}/D_z = B_{Min} + \ PixelLoc_{Rec(x,y,z)} \ - \frac{B_{min} - B_{max}}{V} \qquad \textbf{Eq. 4.9}$$

where S is the shift in (x,y), D is the depth in (z), B_{min} and B_{max} are the minimum and maximum bounds, respectively. $PixelLoc_{Rec}$ is the pixel location of the phantom in the reconstructed images.

For the proposed system, the reconstructed depth information in the 3D reconstructed images was up to $\pm 30\ mm$ for one Laue lens inside a pinhole. Figure 4.14a and Figure 4.14b show the X and Y slices and pixel locations of the reconstructed images for a sphere placed at +1 mm depth, respectively. Figure 4.15a and Figure 4.15b show the X and Y slices and pixel locations of the reconstructed images for a sphere placed at +5 mm depth, respectively.

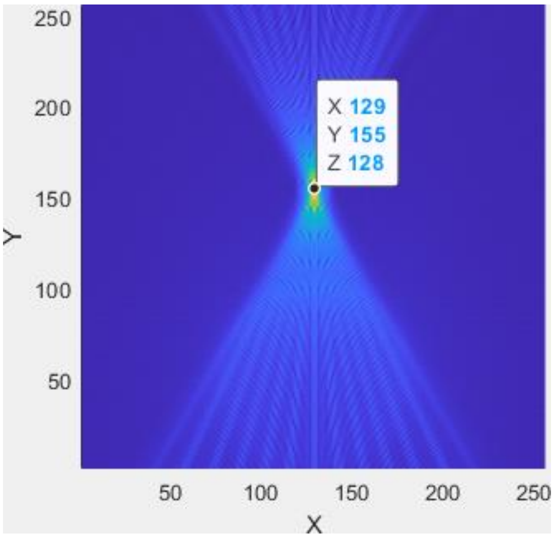

(a)

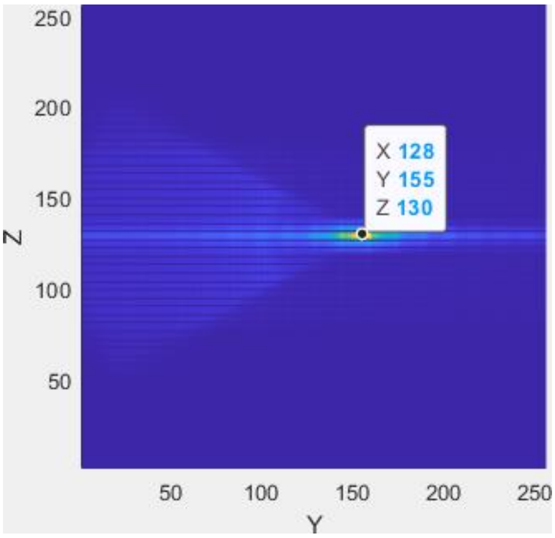

(b)

Figure 4.14 Depth and shift validation. (a) The projection of 3 sphere phantom of radius 0.03mm placed at shifts in X & Y of 0.1 mm and -0.1 mm from the Laue lens axis, (b) The X-Z slice of the reconstructed image for 3 spheres of radius 0.03mm placed at shifts in X & Y of 0.1 mm and -0.1 mm from the Laue lens axis. Units are in mm

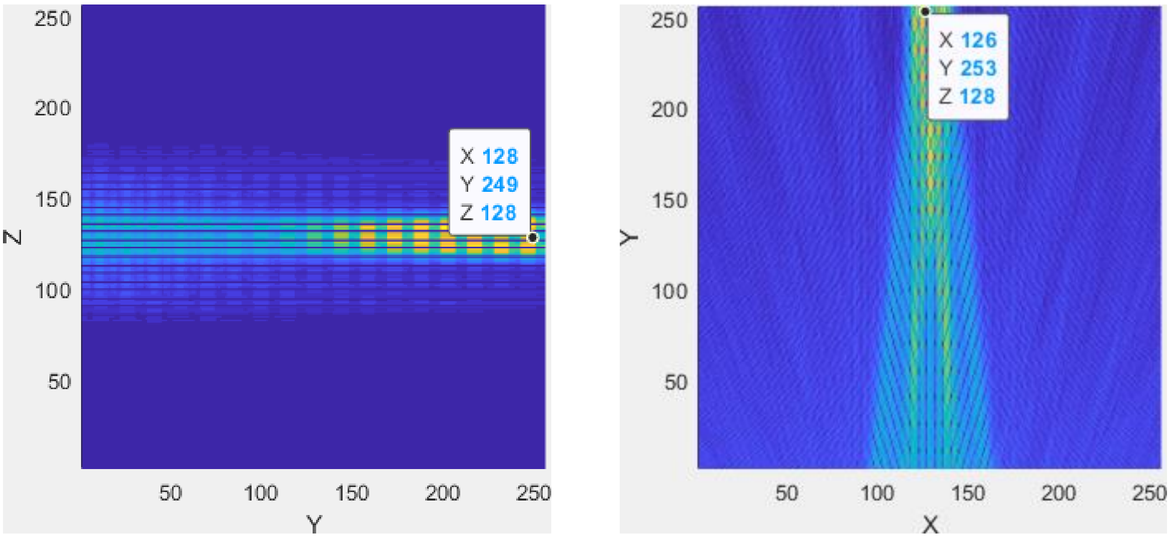

(a) **(b)**

Figure 4.15 Depth validation. (a) The projection image of a sphere for a point source of radius 0.03 mm placed at depth +5 mm as seen by one Laue lens, (b) The X-Z slice of the reconstructed sphere for a point source of radius 0.03 mm placed at depth +5 mm. Units are in mm

Figure 4.16a and Figure 4.16b show, for one case study, the projection image of three spheres of radius 0.03 mm placed at a shift in X & Y 0.1 mm and -0.1 mm from the Laue lens axis and the corresponding X-Z slice of the reconstructed image. Table 4.3 compares the estimated depth of the reconstructed images to the true depth of the phantom.

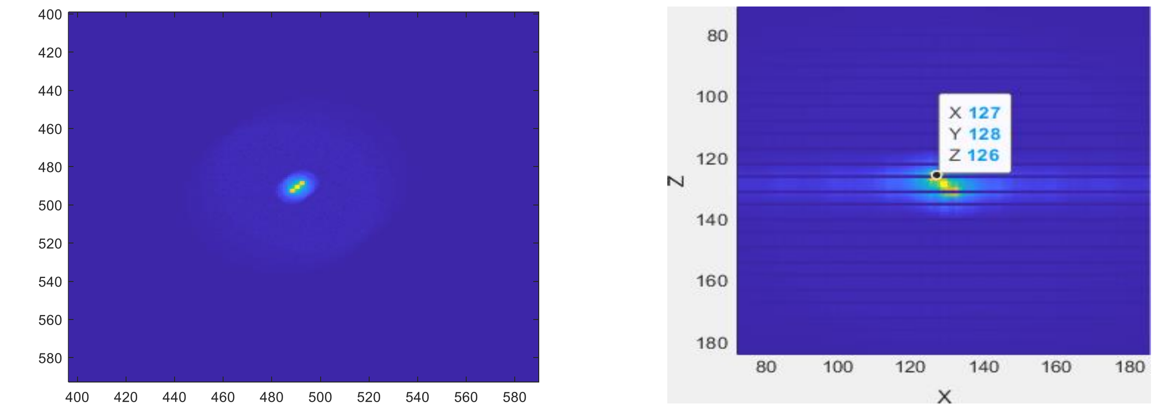

(a) **(b)**

Figure 4.16 Depth and shift validation. (a) The projection of 3 sphere phantom of radius 0.03mm placed at shifts in X & Y of 0.1 mm and -0.1 mm from the Laue lens axis, (b) The X-Z slice of the reconstructed image for 3 spheres of radius 0.03mm placed at shifts in X & Y of 0.1 mm and -0.1 mm from the Laue lens axis. Units are in mm.

The detected depth in the reconstructed phantoms for the off-axis sources was verified against the source-applied depth with high accuracy. For a sphere with a 0.1 mm X-shift from the lens axis and 1 mm Z-depth, the pixel locations in the reconstructed image were recovered as 131 and 155 pixels, respectively. Using the conversion formula in Eq.

4.9, the reconstructed shift and depth are $0.103\, mm$ and $1.005\, mm$, respectively. The observed depth and shift in the reconstructed images of the lens-based SPECT projections were consistent with the experimental phantom depth and shifts.

For the proof of concept, the 3D reconstructed phantom's depth (displacement of the phantom along the Z-axis) information from the photon distribution in the focal plane/detector was contrasted against the applied experimental depths of the source phantom, as shown in Table 4.3.

Similar work was repeated for the 3D reconstructed lateral shifts (with respect to the Laue lens axis); information from the photon distribution in the focal plane/detector was contrasted against the applied experimental lateral shifts of the source phantom. Figure 4.17 shows the photon distribution in the focal plane as a function of a lateral shift of the source for 0, 0.25, 0.5, and 0.75 mm shifts in the x-axis. Figure 4.18 shows photon distribution in the focal plane as a function of a shift of the source along the Z-axis. The photon distribution in the focal plane for a lens placed at the pinhole centre for various indicated shifts are shown in Figure 4.19.

Table 4.3 Simulated and reconstructed phantom pixel locations at various depths from the Laue lens focal.

Source	Depth of The Simulated Phantom	Pixel Location	Voxel size	Upper & Min Bounds	Depth of the reconstructed phantom	Accuracy
1 sphere	Z=1mm	155	10/256	-5 -5	1.005 mm	99.995%
1 sphere	Z=5mm	254	10/256	-5 -5	5.000 mm	100%
1 sphere	Z=10mm	252	20/256	-10 10	9.9700 mm	99.97%
1 sphere	Z=15mm	252	30/256	-15 15	14.9670 mm	99.967%
1 sphere	Z=30mm	252	30/256	-15 15	29.9660 mm	99.97%

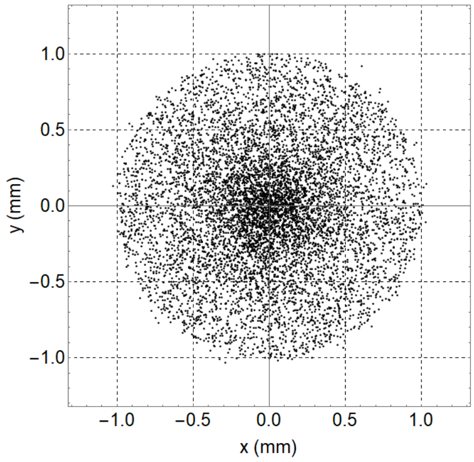

0.0 mm shift

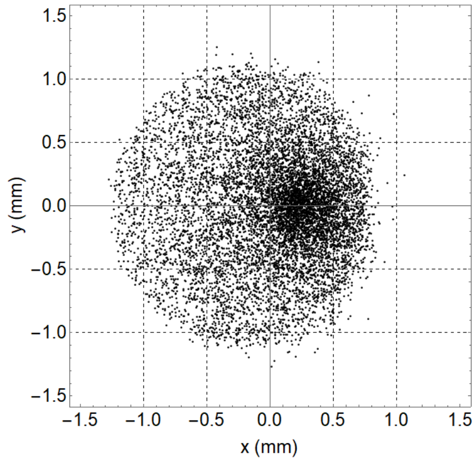

0.2 mm shift

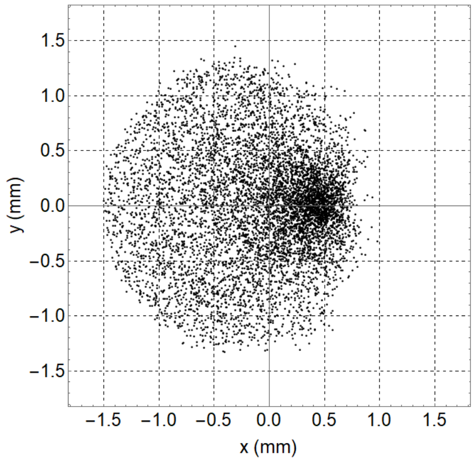

0.5 mm shift

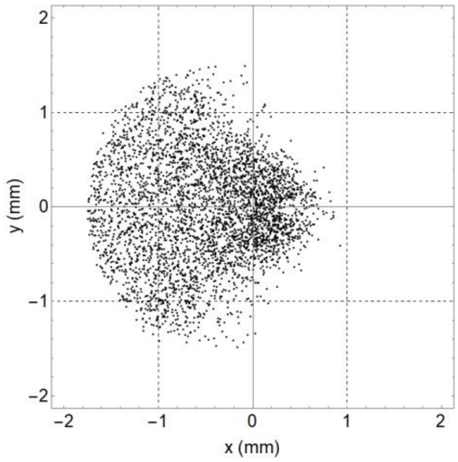

0.75 mm shift

Figure 4.17 Photon distribution in the focal plane (detector) as a function of a lateral shift of the source.

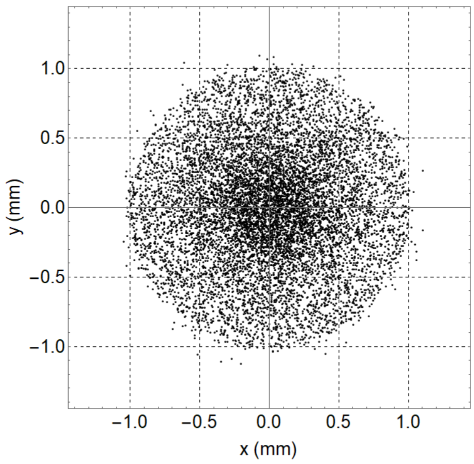

5 mm shift

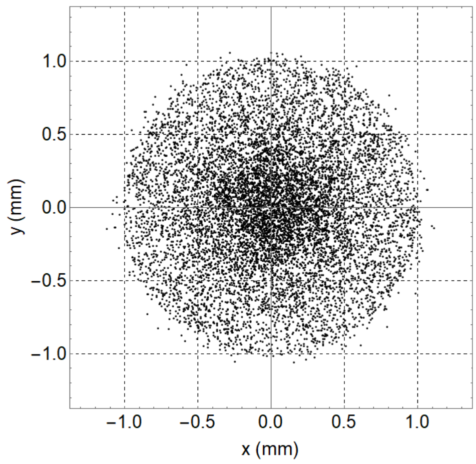

-5 mm shift

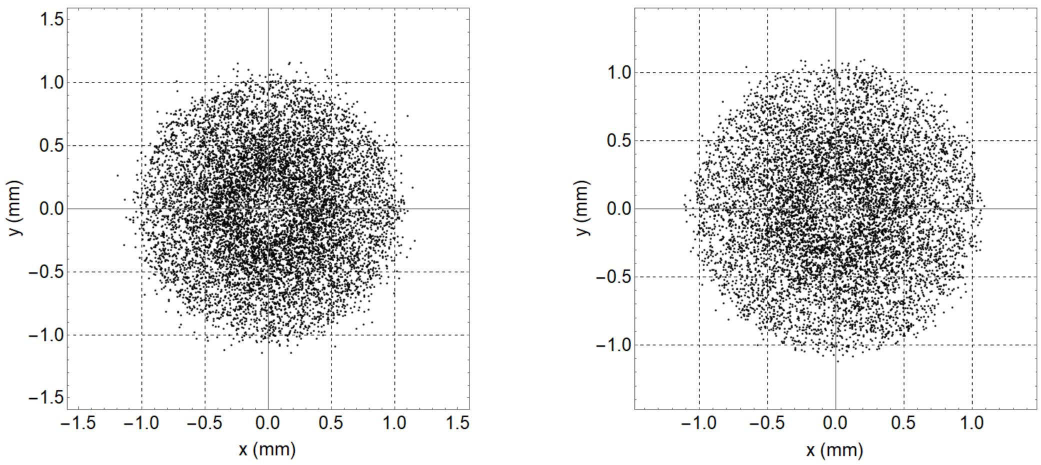

10 mm shift **-10 mm shift**

Figure 4.18 Photon distribution in the focal plane (detector) as a function of a lateral shift of the source.

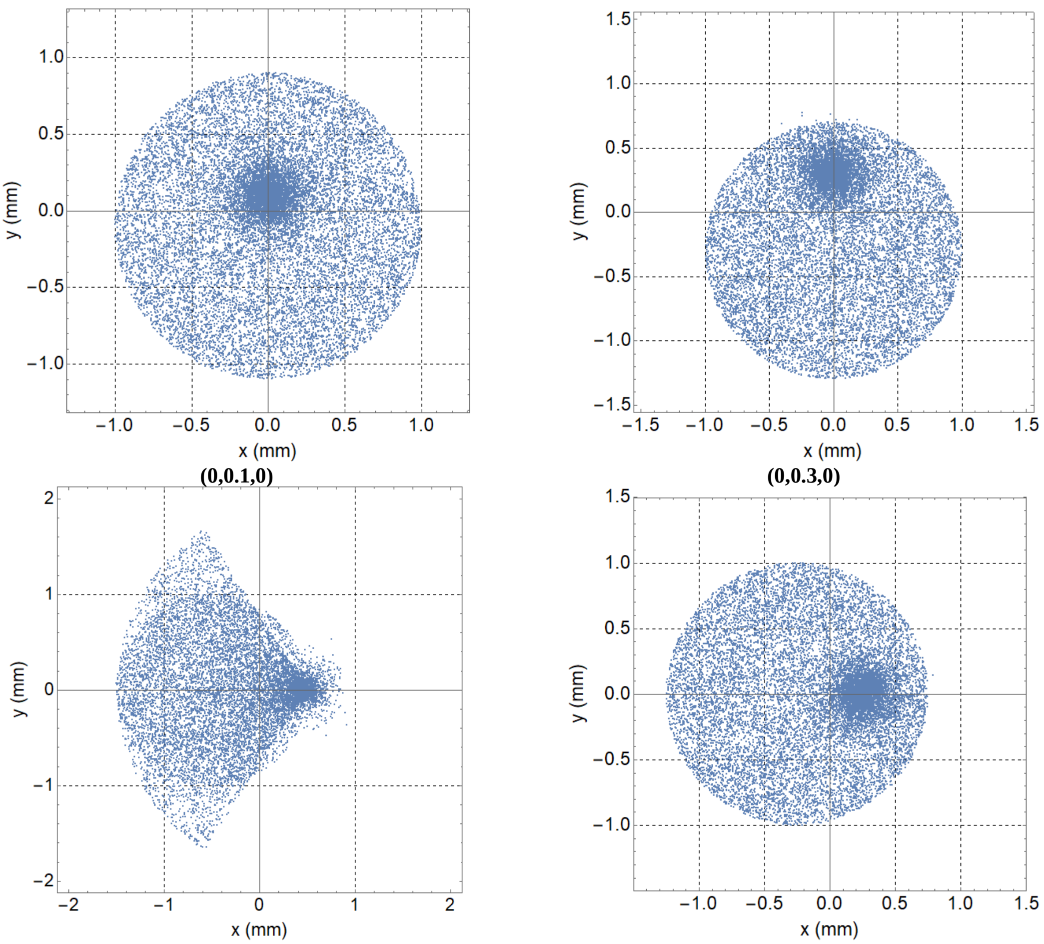

(0.5,0,0) **(0.25,0,0)**

Figure 4.19 Photon distribution in the focal plane for a lens placed at the pinhole centre for (0,0.1,0), (0,0.3,0), (0.5,0,0) and (0.25,0,0).

4.8.3 Resolution Analysis

According to the Raleigh criterion, the minimum resolvable power of an optical lens system is given by [335]:

$$x = 1.22\frac{\lambda d}{D} \quad \textbf{Eq. 4.10}$$

where x is the minimum resolvable distance between two points, d is the distance from the object to the lens, D is the lens diameter, and λ is the wavelength of the rays. However, this law is valid for optical lenses and is not applicable in the case of the Laue lens. The Laue lens resolution for a given radiation wavelength is constant and dependent on the mosaicity[i] of the crystals. To find the minimum resolvable distance between multiple source points that the Laue lens system can separate, several case studies were simulated. The resolution study was conducted in two distinct ways: the first one by using the point spread function's FWHM (Full Width at Half Maximum) analysis using the 3D reconstructed images, while the second was through using a resolution phantom.

4.8.3.1 FWHM

The point spread function (PSF) is the impulse response of an imaging system, or how a bright point source is distributed through the imaging system [127]. Therefore, it is a measure of its resolving ability, and the narrower the PSF, the higher the resolution. The following convolution equation describes a perfect imaging system devoid of noise:

$$g(x,y) = f(x,y) * h(x,y) \quad \textbf{Eq. 4.11}$$

In the Fourier domain, the convolution becomes a multiplication:

$$G(u,v) = F(u,v) \times H(u,v) \quad \textbf{Eq. 4.12}$$

where g is the recorded image, G is its Fourier transform, f is the input truth object, F is its Fourier Transform, and h is the PSF of the imaging instrument, and H is its Fourier transform.

The uncertainty information relating to the origin of detected photons is modelled by thePSF, which, in the literature, is typically assumed to be a Gaussian function whose FWHM is proportional to the standard deviation. In the first approach, to determine the spatial resolution of all slices of the reconstructed images in each direction (x, y, z), each

[i] Mosaicity The term "mosaicity" refers to the precision or regularity with which crystal lattices align within a crystallographic sample. It describes the distribution of crystal orientations around a given average orientation.

count profile was fitted with a Gaussian function, and its FWHM value was used to calculate the resolution along the specified direction. The mean of the reconstructed image is initially determined using samples from the reconstructed image. The centre row of the central slice is then extracted from the mean reconstructed image, plotted against the row location, and the FWHM calculated.

Figure 4.20a shows the projection image of a point source of 0.03 mm radius placed at the Laue lens focus. Figure 4.20b and Figure 4.20c show the XY slice and the XZ slice of the reconstructed image of a point source of 0.03 mm in radius, respectively. Figure 4.21a and Figure 4.21b show the 3D reconstructed image generated using MATLAB and the 3D reconstructed image generated using volume viewer, respectively.

Figure 4.22a and Figure 4.22b show the fitted Gaussian of the projection image and reconstructed image, respectively. Based on the obtained fitted Gaussian, the FWHM is found to be approximately $0.07\,mm$ for the projection image and $0.11\,mm$ for the 3D reconstructed image. The FWHM of the system is determined based on the 3D reconstructed image.

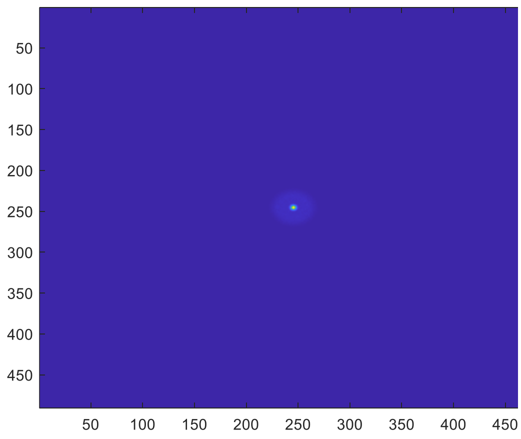

(a)

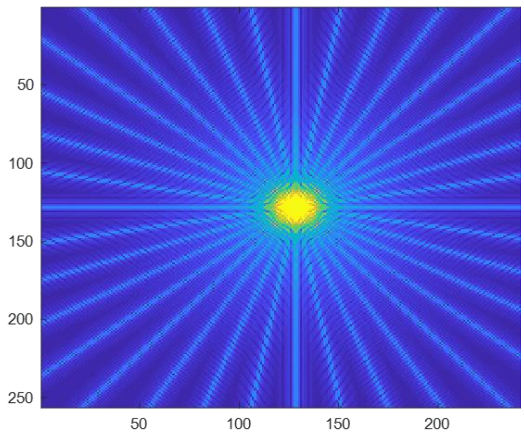

(b)

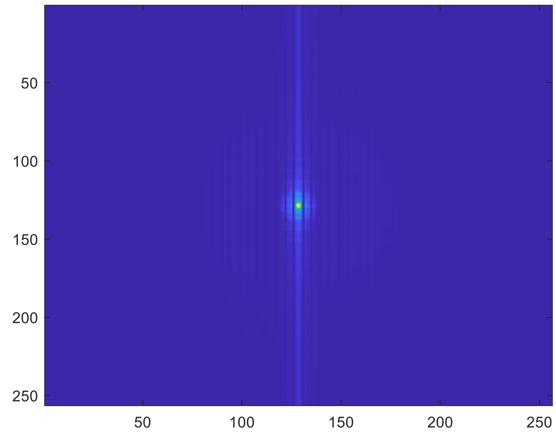

(c)

Figure 4.20 (a) Projection image of a point source of 0.03 mm radius placed at the Laue lens focus, (b) The XY slice of the reconstructed image of a point source of 0.03 mm radius, (c) The XZ slice of the reconstructed image of a point source of 0.03 mm radius. The x-axis represents the column index, and the y-axis represents the raw index of the pixelated projection image.

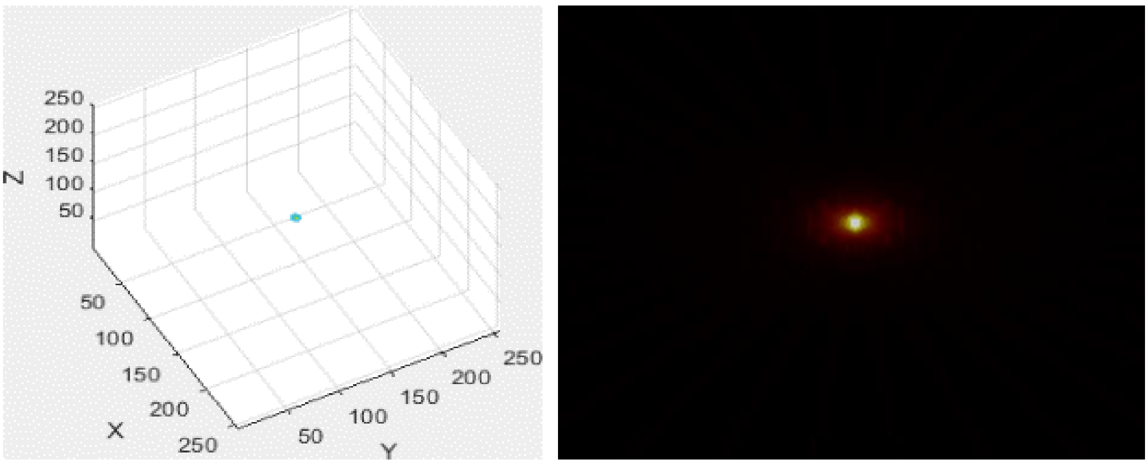

(a) **(b)**

Figure 4.21 (a) The 3D reconstructed image of a point source of 0.03 mm radius placed at the Laue lens focus, (b) The 3D reconstructed image of a point source of 0.03 mm radius placed at the Laue lens focus generated using Volume Viewer.

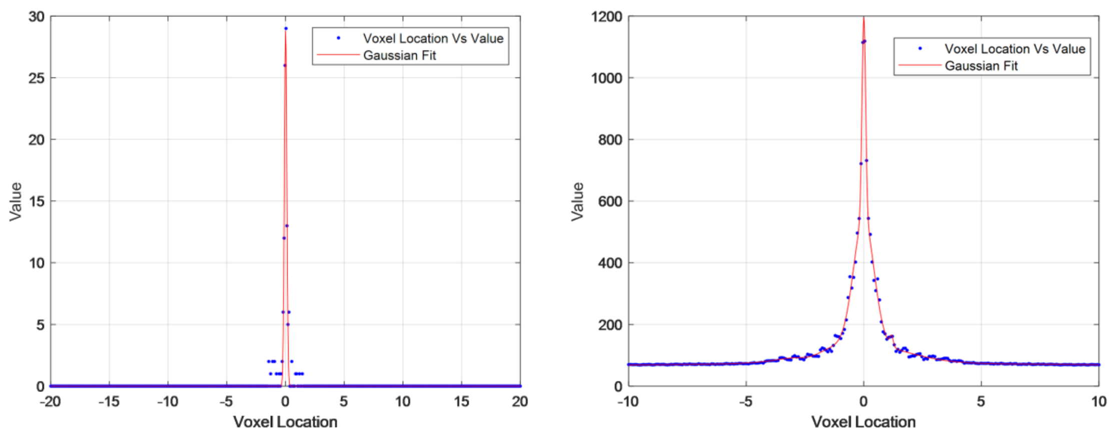

(a) **(b)**

Figure 4.22 FWHM resolution. (a) Fitted Gaussian of the projection image, (b) Fitted Gaussian of the reconstructed image.

4.8.3.2 Resolution Phantom

I employed two distinct case study phantoms to validate and ascertain the consistency of the system's resolution results.. A three- sphere phantom of 0.03 mm in radius, the first set is spaced by 0.1 mm and the second one spaced by 0.05 mm. Figure 4.23a and Figure 4.23b show the point spread function and the photon intensity on the focal spot for these two sets of phantoms, respectively. Figure 4.24a and Figure 4.24b show the XZ slice of the reconstructed image for three spheres of 0.03 mm in radius and 0.1 mm and 0.05 mm distance between the sphere's center, respectively. The 3D images of the reconstructed three sphere phantom with 0.03 mm sphere radius spaced by 0.1 mm and 0.05 mm are shown in Figure 4.25a and Figure 4.25b, respectively.

Figure 4.26 shows the focused Laue projections for three spheres placed at shifts of (0,0,0), (0.1,0,0) and (-0.1,0,0) mm from the lens axis. The resolution of the single lens-based SPECT was obtained based on the simulation of several case studies. The results indicated that the system could completely resolve two-point and three-point sources with a radius of 0.03 mm spaced by 0.1 mm from center to center.

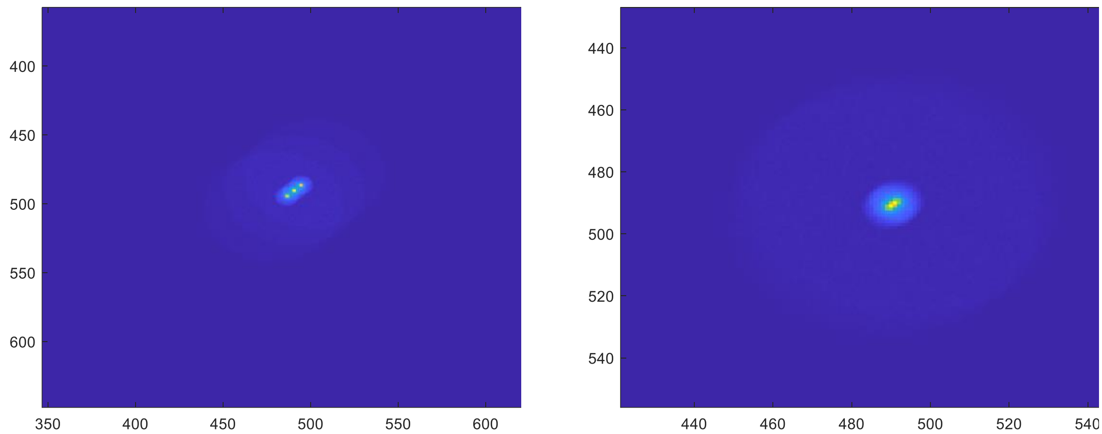

(a) (b)

Figure 4.23 Phantom resolution analysis. (a) The projection image for three spheres of radius 0.03 mm distance from center to center is 0.1 mm, (b) The projection image for three spheres of radius 0.03 mm distance from center to center is 0.05 mm. The x-axis represents the column index, and the y-axis represents the raw index of the pixelated projection image.

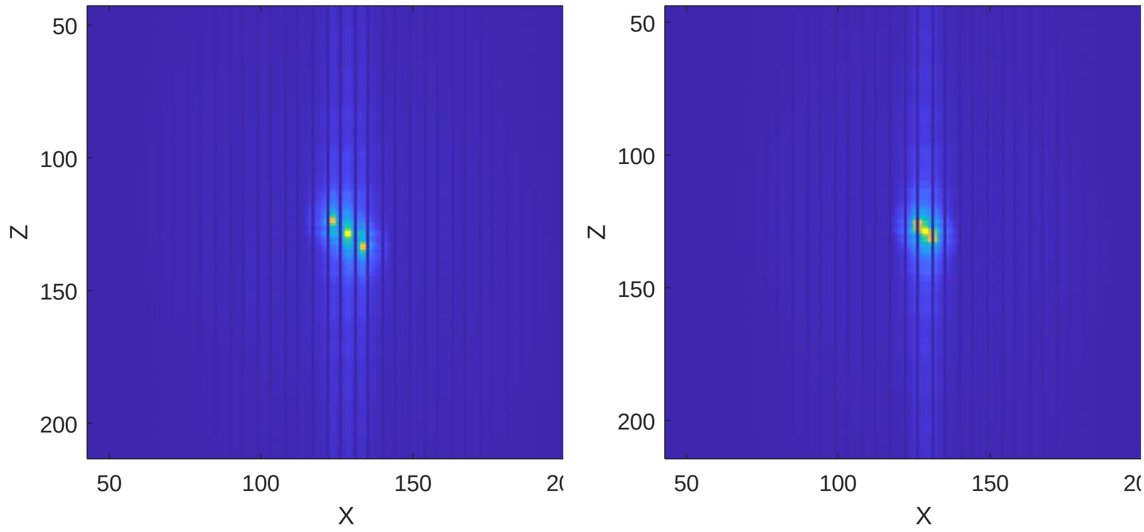

(a) (b)

Figure 4.24 Phantom resolution analysis. (a) The X & Z slice of the reconstructed 3 spheres for a phantom with 0.03 mm radius distance from center to center is 0.1 mm, (b) The X & Z slice of the reconstructed 3 spheres for a phantom with 0.03mm radius distance from center to center is 0.05 mm. The x-axis represents the column index, and the y-axis represents the raw index of the pixelated projection image.

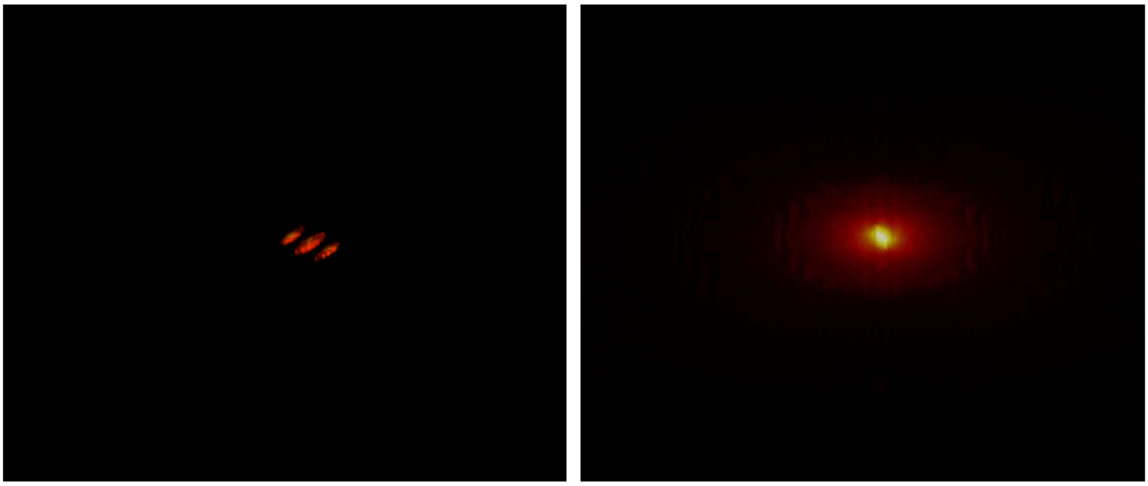

(a) (b)

Figure 4.25 (a) 3D images of the reconstructed three-point spheres for a phantom with 0.03 mm sphere radius spaced by 0.1 mm, (b) The 3D images of the reconstructed three-point spheres for a phantom with 0.03 mm sphere radius spaced by 0.05 mm.

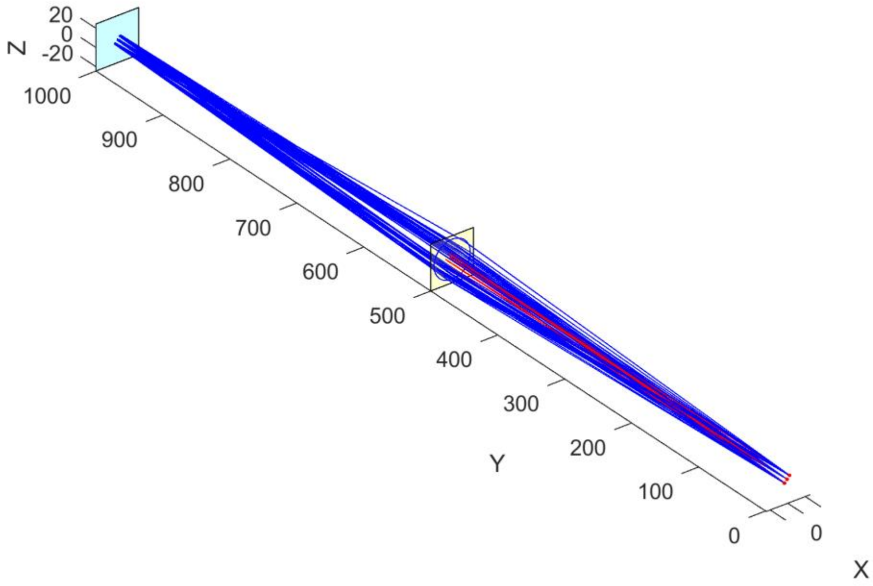

Figure 4.26 Focused Laue projections for three spheres placed at shifts of 0,0,0), (0.1,0,0) and (-0.1,0,0) mm from the lens axis. Units of measurements are in mm.

4.8.4 Sensitivity Analysis

A point source of $0.03\ mm$ radius radiating $100{,}000$ photon/projection equivalent to $0.1\ mCi$ ($0.113\ nL$ volume) was used to evaluate the sensitivity. The system is validated using different lens configurations by running the Monte Carlo simulation for the lens-based SPECT. For one Laue lens system combined in a SPECT gamma camera configuration, the total focused gamma rays' ratio to the total number of incident rays on the Laue lens' crystal surface was found to be 2.4%. This obtained sensitivity of one Laue lens is comparable to the expected theoretical sensitivity of 3% stated in the realized prototypes in the literature [209]. The sensitivity is given by :

$$S_{Laue} = d/i \qquad \textbf{Eq. 4.13}$$

where S_{Laue} is the sensitivity of the Laue lens and d is the diffracted photons, and i is the incident photons. The diffracted photons on the detector plane are the focused rays by the lens, i.e., the hit counts. In contrast, the incident photons are the ones that fall on the lens, from the total emitted by an isotropic source in all directions. Thus, the sensitivity of the Laue lens at a distance L_s from the point source is calculated by multiplying the efficiency of the lens by the fraction of the captured gamma rays from the total emitted in all directions.

As isotropic radiation spreads as a spherical front, the law of inverse squares dictates that the fraction of gamma rays captured by the lens is the ratio of the solid angle subtended by the lens ($\frac{A_{Lens}}{L_S^2}$) to the total solid angle of a sphere (4π), the ratio is:

$$\Omega_S = \frac{A_{Lens}}{4\pi L_S^2} \qquad \textbf{Eq. 4.14}$$

where A_{Lens} is the active area of the lens excluding the white spaces between the rings, and L_S is the distance from the lens to the source. We can recognize that the denominator of this ratio is the surface area of the spherical front with radius L_S, which is $4\pi L_S^2$. The sensitivity of the Laue lens at a distance L_S from an isotropic source is then equal to $S_{Isotropic}(L_S)$:

$$S_{Isotropic}(L_S) = S_{Laue} \times \frac{A_{Lens}}{4\pi L_S^2} \qquad \textbf{Eq. 4.15}$$

The sensitivity of the Laue lens can also be expressed in becquerels, as counts per second. Based on the Monte Carlo simulation of an isotropic point source of $0.1\ mCi$, the lens-based SPECT sensitivity is estimated using the below expression:

$$S = 3 \times 10^{-5}\ H/E \ \cong 27\ cps/MBq \qquad \textbf{Eq. 4.16}$$

where H are the diffracted and E are the isotopically emitted radiations from an isotropic point source.

4.8.5 Comparative Analysis: Single Lens-Based SPECT VS LEHR Parallel SPECT

In order to assess the proposed design and perform a comparative analysis with conventional SPECT imaging systems, the parameters have been downscaled to be match those of the existing LEHR parallel SPECT. MATLAB was used to model a LEHR parallel hole SPECT with 39×39 pinholes, pinhole diameter of $1.2\ mm$, pinhole pitch of $0.2\ mm$, and a collimator thickness of $35\ mm$. In both systems, the collimator and detector sizes were kept comparable. In the lens-based system, the distances between the collimator/lens-to-detector and the source-to-collimator/lens were fixed. In contrast, the parallel SPECT simulation is conducted by varying both distances. To get the maximum attainable resolution, the collimator-to-detector distance was varied between $20 - 10\ mm$, while the source-to-collimator distance was simulated at $25\ mm$. A second geometry for parallel hole SPECT was simulated with 121×121 pinholes of $0.4\ mm$ diameter, $0.2\ mm$ pitch, and $35\ mm$ collimator thickness. As discussed in Chapter 1, the design and geometry of the collimator parameters directly impact the resolution and sensitivity of the SPECT system. The following equation determines the resolution of a parallel hole collimator [336]:

$$Res_{Parallel} = d \times \frac{(a+h)}{a} \quad \textbf{Eq. 4.17}$$

where d is the diameter of the hole, h is the perpendicular distance between the point source and the detector, and a is the collimator thickness or pinhole depth. The following equation determines the sensitivity of a parallel hole collimator [88]:

$$Sens_{Parallel} = \frac{\sqrt{3}}{8\pi} \frac{d^2}{a^2} \frac{d^2}{(d+t)^2} \quad \textbf{Eq. 4.18}$$

where t is the septal thickness. The sensitivity and resolution findings for parallel LEHR and single lens-based SPECT are listed in Table 4.4. The sensitivity and resolution of the LEHR collimator are illustrated for several collimator setups by altering the pinhole depth and diameter. The resolution sensitivity trade-off restricts the capabilities of the parallel hole collimator, as an increase in system resolution would result in a decrease in system sensitivity. Reducing the diameter of the pinhole and expanding its length would increase the resolution, but the sensitivity would be drastically diminished. In contrast, increasing the diameter of the pinhole increases the acquired sensitivity at the expense of resolution. However, the Laue lens-based system's sensitivity is independent of lens geometry [337]. This constitutes an additional benefit.

Table 4.4 Sensitivity and Resolution Comparison Between single lens-based SPECT and Parallel LEHR Collimator

System	Configuration	Resolution (mm)	Sensitivity $(hits/emitted)$
***Parallel SPECT (LEHR)** **39 × 39 Pinholes**	Pinhole diameter 1.2 mm, septal thickness 0.2 mm, pinhole depth 35 mm, source-to-collimator distance 25 mm.	1.9	3×10^{-5}
***Parallel SPECT (LEHR)** **39 × 39 Pinholes**	Pinhole diameter 1.2 mm, septal thickness 0.2 mm, pinhole depth 30 mm, source-to-collimator distance 20 mm.	2.5	3.2×10^{-5}
***Parallel SPECT (LEHR)** **121 × 121 Pinholes**	Pinhole diameter 0.4 mm, septal thickness 0.2 mm, pinhole depth 30 mm, source-to-collimator distance 20 mm.	0.8	1.2×10^{-5}
Single lens-based SPECT **One lens**	Laue lens diameter 41.66 mm, thickness 1 mm, source-to-lens distance 500 mm.	0.1	2.9×10^{-5}
***Collimator set is simulated in present study.**			

4.9 Chapter Summary

A novel lens-based SPECT design for high resolution molecular imaging was simulated. The lens-based SPECT combines a collimator with a Laue lens and a moving detector setup. The focusing feature significantly improves the proposed system over conventional collimation methods. The characterization of the initial performance of the system based on sensitivity and resolution was evaluated for different phantom experiments. The attained resolution is unmatched by any of the previous conventional SPECT systems. The focused imaging enables studying a specific region of interest with improved sensitivity. The simulation experiments and ideas given in these results presented in this chapter may provide insight for further advancements beyond the existing state-of-the-art in small animal SPECT imaging.

For the sake of enhancing the sensitivity, in the following chapter, I present and elaborate on the attempts to develop a high-resolution SPECT system with a Laue lens by investigating the performance parameters of a lens-based SPECT system with partially curved detector modules and Laue lens arrays. I then moved on further and proposed a more complicated geometry consisting of an array of diffraction lenses placed at the pinhole centres of a SPECT multipin hole collimator, which is the multi lens-based SPECT.

4.10 Acknowledgement

This chapter articulates and expands on work for which the concepts and basic findings were partially published in:

1. Barhoum, A., Francis, M., Camattari, R., & Tahtali, M. (2021, October). Design and Evaluation of a Novel Ultra High-Resolution Lens-Based SPECT: Insight to Light Field Imaging. In 2021 IEEE International Conference on Systems, Man, and Cybernetics (SMC) (pp. 1436-1442). IEEE.
2. A. Barhoum, M. Tahtali, R. Camattari, and Susanna Guatelli " Ultra-High-Resolution Lens Based SPECT Based on Laue Gamma Diffraction: A First GAMOS/GEANT4-MATLAB Monte Carlo Study" Physica Medica (2023). This article is under: (Under Review).

5. Modular and Multi Lens-Based SPECT Geometries with Dedicated 3D Reconstruction Algorithm: Monte Carlo Study

As demonstrated in Chapter 4, the single lens-based SPECT guarantees high spatial resolution imaging with comparable sensitivity with existing SPECT. However, the detection efficiency of the single lens-based SPECT system is inevitably reduced due to having only one diffraction lens, which limits the number of focused gamma rays needed for sufficient 3D image information.

In this chapter, I report and provide an in-depth analysis to establish a high-resolution system based on augmenting an existing SPECT technique by introducing diffraction focusing using a Laue lens [133]. For the purpose of boosting sensitivity, I proposed a second geometry, a single lens-based SPECT system fitted with partially curved detector modules and Laue lens arrays. I call it modular lens-based SPECT. The Laue lenses are positioned in inclined planes in a modular fashion and with detector geometry so that their fields of view converge. Having an array of lenses in a plane was the next level I aimed to examine. The multi lens-based SPECT is a more complicated geometry consisting of an array of diffraction lenses placed at the pinhole centres of a multi-pinhole SPECT collimator. In this chapter, I am thoroughly examining the imaging capabilities of these two novel geometries. For the two envisioned geometries, customized 3D reconstruction algorithms tailored to the focused Laue lens projections is presented and utilized to generate the 3D images as a first attempt.

This chapter is organized as follows: Section 5.1 describes the methodology and the study of system characteristics. Section 5.2 represents a feasibility study of the modular lens-based SPECT. This section encompasses various subtopics that contribute to the overall assessment of the system. The simulation design, experimental setup and phantom case studies are discussed in Sections 5.2.1 and 5.2.2, respectively. The 3D reconstruction algorithm dedicated to modular lens geometry and the experimental results are discussed in Sections 5.2.3 and 5.2.4, respectively. The system validation and the sensitivity analysis are discussed in Sections 5.2.5 and 5.2.6, respectively. The modular lens geometry is evaluated against the existing designs and based on two figures of merit: system resolution and sensitivity in Section 5.2.7.

In a similar manner, Section 5.3 provides a comprehensive analysis of the multi lens-based SPECT system. This section is divided into several subsections that discuss different aspects of the study. The simulation design, experimental setup along with phantom case studies are discussed in Sections 5.3.1 and 5.3.2, respectively. The 3D reconstruction algorithm dedicated to multi lens geometry, and the experimental results are discussed in Sections 5.3.3 and 5.3.4, respectively. The system validation and the sensitivity analysis are discussed in Section 5.3.5 and 5.3.6, respectively. In order to validate the system's ability to detect tumours, Section 5.3.7 is dedicated to a case study called "Lesion Detection." This case study focuses on assessing the system's performance in identifying and localizing tumour lesions using the modular lens-based SPECT system. The multi lens geometry is evaluated against the existing designs and based on two figures of merit: system resolution and sensitivity in Section 5.3.8.

5.1 Methodology

This section describes the methods used to model and characterize the design of the proposed modular and multi-lens-based SPECT systems. To model and study the envisioned systems behaviour, I developed dedicated Monte Carlo simulations for the envisioned SPECT in MATLAB for Laue lenses positioned in inclined planes in a modular fashion, representing the modular lens-based SPECT.

A module typically refers to a discrete, self-contained unit within the overall detector system. Each module contains a set of individual detector elements or sensors that work together to capture data, while tilt in detector geometry refers to the angle at which a detector module or the entire detector system is positioned relative to the object being imaged.

I used the same Laue lens design I proposed to be augmented with the single lens-based-SPECT (discussed in Chapter 3). The Monte Carlo simulations for the ray propagation were based on the ray tracing concept. However, in this work, the forward projection algorithms developed for both of the envisioned modular and multi lens-based geometries were tweaked differently. The forward projection algorithm in the case of the modular lens-based geometry has the same concept I followed for the single lens-based SPECT; however, it was modified to account for the modules placed in a circumferential ring. This is in contrast to the dedicated forward algorithm for the multi lens-based SPECT, which was revised to accommodate the behaviour of an array of Laue lenses in a planer plane. Furthermore, I developed a customized 3D image reconstruction algorithm in MATLAB to reconstruct the projection images resulting from the focused photons. For the modular lens-based SPECT, the 3D reconstruction algorithm was similar to the one developed for single-lens-based SPECT. However, I had to design a novel 3D reconstruction algorithm for the multi-lens-based SPECT, considering that having a highly multiplexed system (overlapping of projections) where each lens can diffract projections behind other Laue lenses.

Validating the reconstruction algorithm for the new proposed SPECT design was the next step. To this end, I conducted validation studies that addressed two essential parameters: the mapping of the depth and shift information in the 3D reconstructed images in the case of the multi lens geometry. For the modular geometry, the validation is based on mapping the sensitivity through the FOV.

The performance parameters of the proposed design were assessed against the existing parallel LEHR and multi pinhole Inveon SPECT based on two figures of merits, sensitivity, and resolution, which were inferred based on standard methods.

5.1.1 Study of System Characteristics

The modular and multi-lens-based SPECT scans were simulated for 360° rotation with 10° step angle. A one-point and three-point source, a resolution phantom consisting of cylindrical capillaries inside a cylindrical volume, and a customized cylinder-sphere phantom were used. The geometry of the phantoms will be described in the coming sections. The activity of the different point sources or volumes was selected to imitate cases of a suspicious mass or tumour in its initial stage compared to the background. As mentioned earlier, the resolution of the Laue lens for a particular radiation wavelength depends on the crystals' mosaicity. To this end, the spatial resolution study was performed using two different approaches; the first was based on the FWHM of the point spread function generated from the Gaussian distribution of the 3D reconstructed image of a single sphere point source. The second method used the customized resolution phantoms.

5.2 Sensitivity Boosting: Modular Lens-Based SPECT

After the success in reconstructing 3D images from a single lens, and before I proceeded further, I had to step back and think of proposing a more efficient lens-based SPECT with improved performance parameters. By exploring the pioneering work introduced in several designs and the concept of hemispherical system design, where modular cameras were setup in a hemispherical geometry surrounding the patient's head and attached with a multiple-pinhole collimator [338], similarly, I decided to study the behaviour of a SPECT system equipped with modular partially curved detectors and Laue lens arrays. The Laue lenses and their detectors are placed in tilted planes in a modular fashion such that their fields of view converge.

By proposing the modular lens design, I demonstrate that combining the effects of more than one lens would offer an interesting approach for the future ultrahigh-resolution lens-based SPECT imaging design without sacrificing system sensitivity and FOV. I utilized the same Laue lens as for the single lens-based SPECT design. As described previously, the Laue lens is adjusted to diffract $140.5\ keV$ gamma rays. The Laue lens comprises seven concentric rings, each containing a unique set of diffraction planes. The lens is composed of aluminium and copper, and each of its seven rings has a distinct number, arrangement, and crystalline composition. The crystals in each ring are identical in terms of design and dimensions. However, each ring is distinctive in terms of the number of crystals. The ring's radius is modified so the diffracted beam is focused on a focal point. Gamma rays emitted inside the solid angle of a lens are focused on the sensitive area of the detector. Modules of the lenses were mounted 500 mm from the source. The initial conception of the modular lens-based SPECT consists of one ring and three modules, with one Laue lens per module mounted on a partial ring. The minimum width of the tile is modified to match the diameter of the Laue lens. The modules are placed in a circumferential ring. Figure 5.1 depicts the proposed geometry.

The total view angle covered by the modular partial ring detector is proportional to the perpendicular distance between the module where the lens is located, the object's center, and the module's width. The width of the module is $42\ mm$, and $500\ mm$ separates the module's center from the central axis, where the object is positioned. If the system is intended for stationary applications, 24 stationary full-ring modular cameras are planned. In the suggested modular SPECT approach, the individual camera tiles are grouped in a ring geometry to cover the whole transverse field of view. Utilizing extra rings to cover the entire phantom can expand the axial field of view. The total view angle of the modular partial detector is determined as follows:

$$View\ Angle = 2N\, tan^{-1}\frac{W}{F} \qquad \textbf{Eq. 5.1}$$

where N represents the number of detector modules, W represents the width of each module, and F represents the distance between the source's center and the Laue lens module, which equals the lens's focal length. The number of scans or camera rotations required for a complete object scan is:

$$Number\ of\ Scan = 360°/View\ Angle \qquad \textbf{Eq. 5.2}$$

For the detector shielding and detector coupling with the Laue lens, I followed the same criteria mentioned in Chapter 4, Section 4.5.

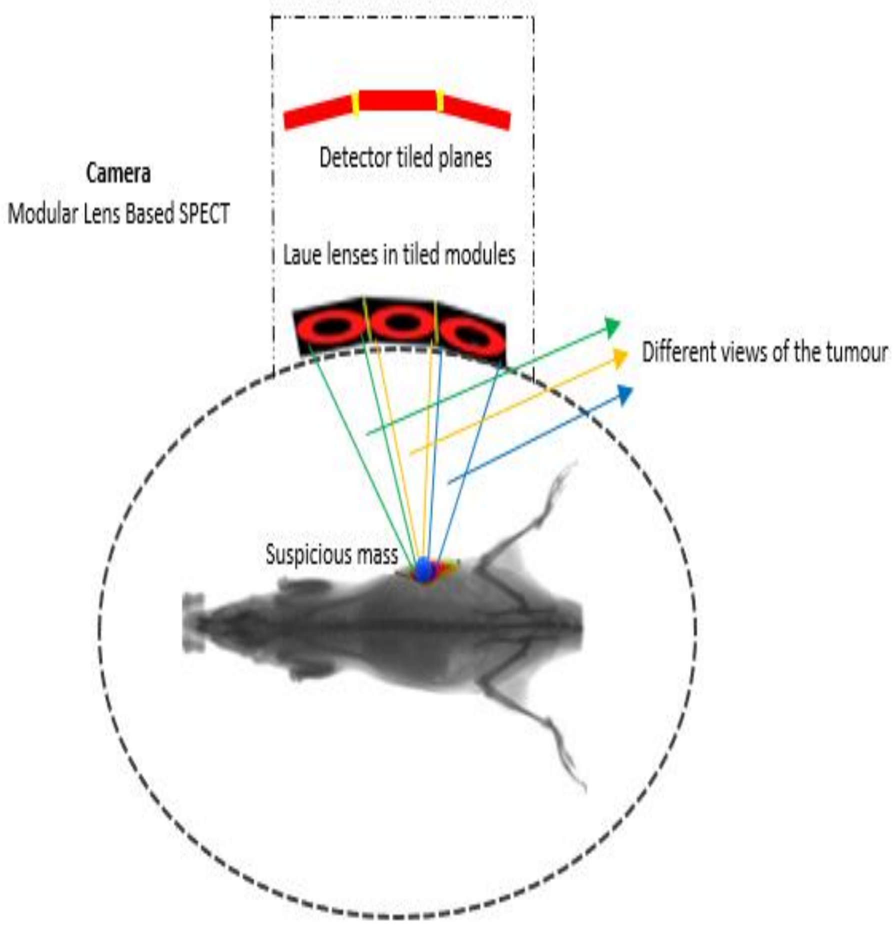

Figure 5.1 Proposed geometry for the modular lens-based SPECT.

5.2.1 Simulation Design and Experiment Setup

In this section, I am discussing the experimental setup for the modular lens-based SPECT geometry.

5.2.1.1 Forward Projection

Although the forward projection algorithms developed for single lens-based SPECT would undoubtedly differ from the approach for modular lens-based SPECT, I tweaked the method to analyse the acquired images from the Laue lenses in a partial ring. The concept is similar to what I discussed in Section 4.6.

The partial ring of the modular lens-based SPECT environment was modelled using a tracking Monte Carlo method. The algorithm aims to estimate the pattern of high-energy photons diffraction using the Laue lens paradigm of diffraction. In numerous ways, rays can be transmitted, absorbed, or diffracted at the Laue lens plane. All projections of the modular partial ring detector modules are simulated by rotating one module by the set step angle, as given by:

$$Step\ Angle_{Module} = 2\,tan^{-1}\frac{W}{2F} \qquad \textbf{Eq. 5.3}$$

where W is the width of the module (the Laue lens diameter), and F is the distance between the object centre to the detector module.

Based on the above given equations, the step and view angles for the modular lens-based SPECT are calculated as shown in Table 5.1.

Table 5.1 The step and view angles of the modular lens-based SPECT

$Step\ Angle_{Module}$	$2\,tan^{-1}\frac{41.6}{2\cdot 500} = 4^{o}$
$View\ Angle$	$2 \times 3\,tan^{-1}\frac{41.6}{500}{}^{o}$

5.2.2 Phantom Studies

Several case studies with various phantoms have been conducted. As I mentioned earlier in Section 4.8.3, the criterion for determining the system resolution for optical lenses does not apply to Laue lenses; for the Laue lens, the resolution at a given wavelength depends only on the diffracting crystals' mosaicity. The three-sphere phantom shown in Figure 5.2 was used to evaluate the system's resolution and collect reliable performance data. The three-sphere phantom of 0.03 mm radius each, spaced by 0.1 mm from centre to centre.

5.2.3 3D Reconstruction Algorithm: Modular Lens-Based SPECT

To demonstrate the potential of this simulated SPECT system, I developed a reconstruction technique as the next step of this study, with a similar concept to what I did for the single lens-based SPECT. A phantom consisting of three spheres 0.03 mm in radius arranged along the z-axis of the detector. The scanned phantom is reconstructed using the ray-tracing concept by projecting the diffracted points back to the volume of interest in parallel. A perpendicular ray towards the cube of interest is formed from each nonzero projection pixel on the detector plane. All generated beams are contained within the scanning axis. The intersecting rays within the cube of interest are traced using Siddon's technique for ray tracing. This tracing will output the index and length of the voxels that are intersected, as shown in Figure 5.3a. The values of the crossed voxels are modified by multiplying the original projection pixel value by the normalised intersection length. This technique is carried out for all projection pixels and acquired projection images with varying degrees of step. Figure 5.3b depicts the process of back projecting rays from the sensor plane to the voxel volume. The procedure is repeated for each module rotation to generate the entire number of projection angles. Individually, the images were reconstructed from each module. Therefore, the projection images generated by the three modules were combined to create a single projection image. Practically, the projections of the multiple modules will be combined on the detector plane.

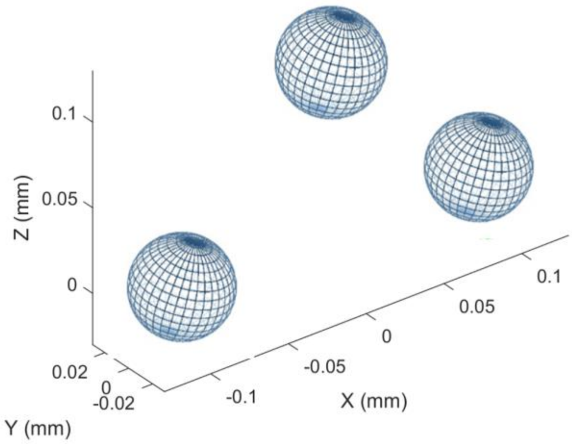

Figure 5.2 Three-sphere phantom.

.

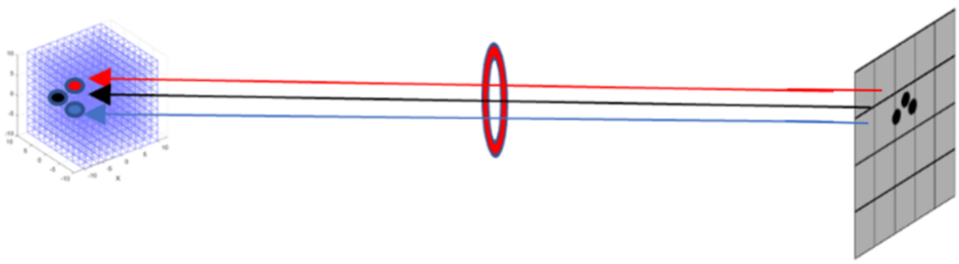

Rays are projected back from the detector to the voxel volume perpendicular to the Laue lens axis

(a)

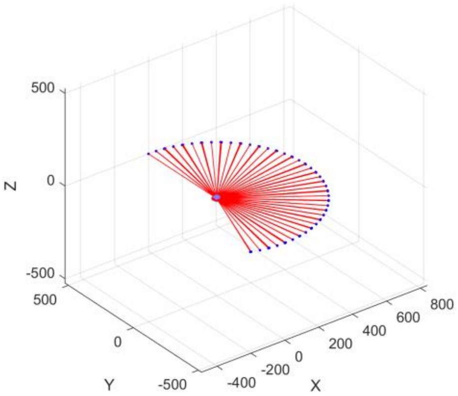

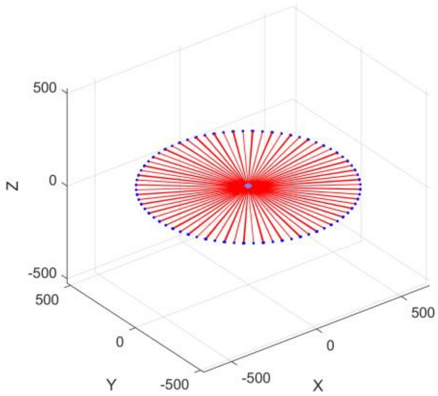

(b)

Figure 5.3 3D reconstruction. (a) The rays are projected back through the Laue lens center towards the voxel volume, (b) Reconstruction for different number of rotations at different step angles on parallel basis.

5.2.4 Experimental Results

This section presents the preliminary testing data for the modular lens-based SPECT system.

5.2.4.1 Projection and 3D Reconstructed Images

The projection images of the modular lens-based SPECT are generated by rotating the Laue lens modules around the three-point sources with a 10° step angle. Figure 5.4a shows the projection image behind a single module, which represents the projection of a single Laue lens. Figure 5.4b and Figure 5.4c show the projection images for all three modules of the partial ring for three-point spheres at step angles of 10° and 90°, respectively.

Figure 5.5a and Figure 5.5b show the XZ and the YZ slice of the reconstructed image for three spheres of 0.03 mm radius and 0.1 mm distance between the spheres' centers, respectively. The 3D reconstructed image and the top view of the 3D reconstructed image generated using the volume viewer are shown in Figure 5.5c and Figure 5.5d, respectively.

5.2.5 System Validation: Sensitivity Mapping Over the FOV

As I did for the single lens-based geometry, I have conducted a validation study for the Modular SPECT as well. But, in this case, I mapped the sensitivity over the FOV for different axial shifts of the source for each module separately, and after that, I evaluated the combined sensitivity for the three modules for the modular lens-based SPECT geometry. Table 5.2 shows the sensitivity mapping over the FOV for different axial shifts of the source for each module separately and the combined sensitivity for the three modules of the modular lens-based SPECT.

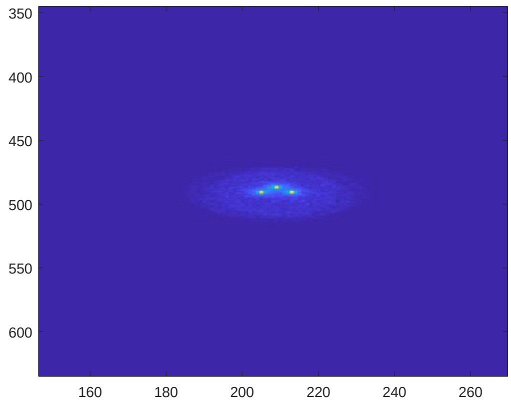

(a)

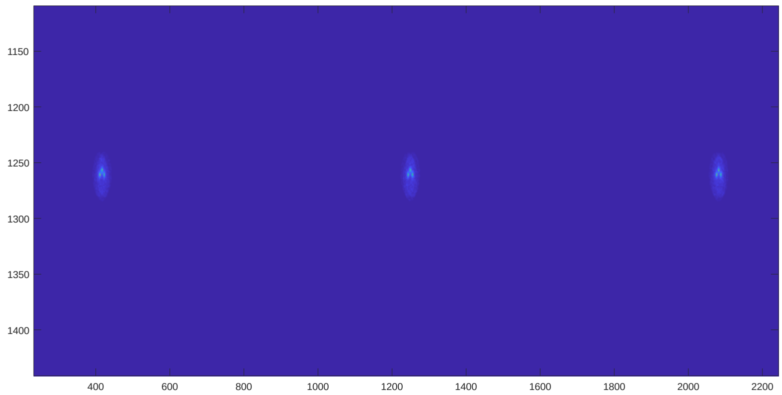

(b)

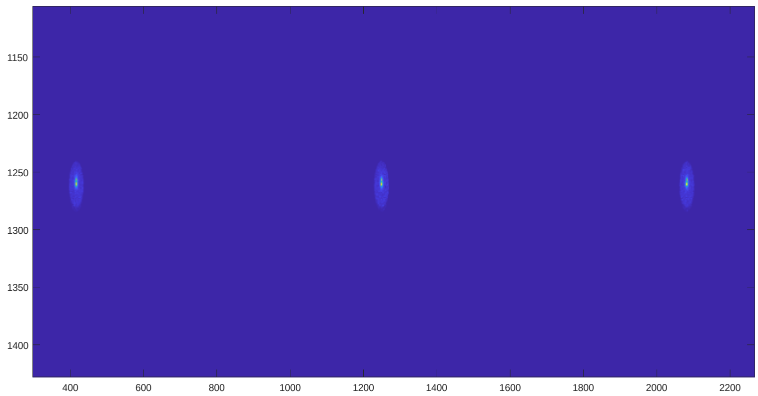

(c)

Figure 5.4 Forward projection. (a) The projection image of one module, (b) The projection image of the three modules at 10° rotation, (c) The projection image of the three modules at 90° rotation. The x-axis represents the column index, and the y-axis represents the raw index of the pixelated projection image.

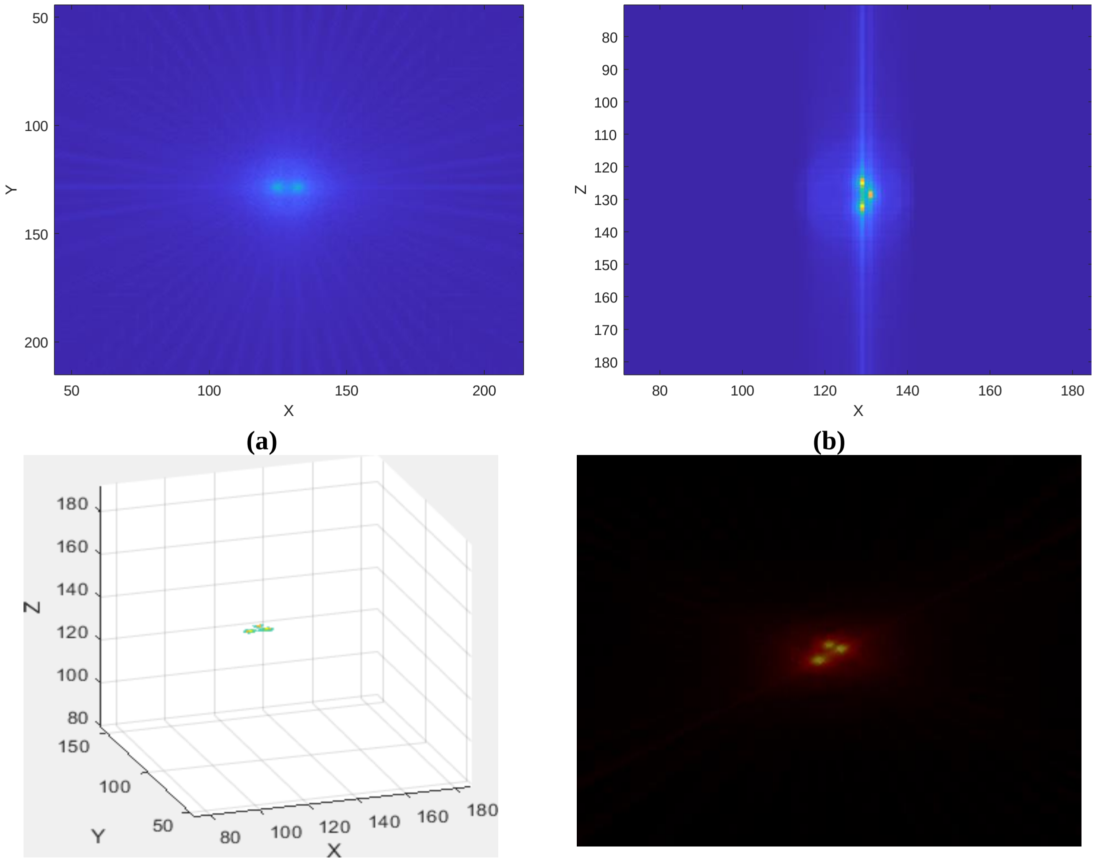

(a) (b) (c) (d)

Figure 5.5 3D reconstruction. (a) The XY slice of the reconstructed image for three spheres of 0.03 mm radius and 0.1 mm distance between the spheres' centres, (b) The XZ slice of the reconstructed image for three spheres of 0.03 radius mm and 0.1 mm distance between the spheres' centres, (c) The 3D reconstructed image for three spheres of 0.03 mm radius and 0.1 mm distance between the spheres' centres, (d) Top view of the 3D reconstructed image generated using volume viewer. The X, Y and Z measurements are in mm

Table 5.2 Sensitivity mapping over the FOV for different axial shifts of the source

Axial shift of the source	Efficiency of Module 1	Efficiency of Module 2	Efficiency of Module 3	Efficiency of the three Modules	Sensitivity hits/emitted
X=+0.1, Y=0.	2.20%	2.00%	1.98%	6.20%	7.8×10^{-5}
X=+0.3, Y=0	1.96%	1.91%	1.85%	5.72%	7.2×10^{-5}
X=+0.5, Y=0	1.86%	1.81%	1.80%	5.47%	6.9×10^{-5}
X=+0.7, Y=0	1.78%	1.76%	1.67%	5.21%	6.6×10^{-5}
X=+0.9, Y=0	1.67%	1.66%	1.63%	4.95%	6.2×10^{-5}
X=0, Y=+1.5	1.56%	1.50%	1.40%	4.46%	5.7×10^{-5}
X=0, Y=+2	1.39%	1.36%	1.32%	4.07%	5.2×10^{-5}

X=+2.5, Y=0	1.23%	1.20%	1.09%	3.52%	4.6×10^{-5}
X=+3, Y=0	0.98%	0.92%	0.90%	2.80%	3.8×10^{-5}
***The efficiency is calculated based on the percentage of the diffracted photon to the emitted ones by the source. *The sensitivity is approximated based on the Monte Carlo simulation of an isotropic point source.**					

5.2.6 Sensitivity and Resolution Analysis

A fully optimized lens is expected to have a diffraction efficiency of 3% [209]. Using the sensitivity obtained in earlier work conducted at the beginning of this endeavour[133, 309], the sensitivity of a single lens system for small sources is 2.4%. The total sensitivity for the three modules cannot be approximated by simply multiplying the sensitivity of each module, as it is highly dependent on the source shift from the lens's axis. Thus, it was deduced based on Monte Carlo simulations. Table 5.3 Shows the sensitivity for a single lens, the cumulative sensitivity for the three proposed modules.

Table 5.3 Sensitivity of the modules in modular lens-based SPECT

$Single\ Lens_{\ Planer}$	$3 \cdot 10^{-5}\ hits/emitted$
$Multi\ Module\ Lens_{Modular}$	$9 \cdot 10^{-5}\ hits/emitted$

Small sources with low activity would be detected at a higher count rate compared to the parallel LEHR collimator with such activity. $3.7 \cdot 10^{4}$ gamma rays per second are emitted by *a single micro-Curie source.* With the proposed geometry, the lens system's count rate is 4 $counts\ /\ second.$

Since the resolution of the Laue lens cannot be estimated using the Rayleigh criterion, which is only applicable to optical lenses, the resolution of the system was deduced based on the smallest distance between adjacent spheres that could be resolved, which is 0.1 mm.

5.2.7 Comparative Analysis: Modular Lens-Based SPECT VS Parallel LEHR SPECT

In a similar manner to what I presented in Chapter 4, Section 4.8.5, I conducted a comparative study with the existing LEHR parallel SPECT, and the previously proposed geometry for the Signal Lens-Based SPECT. The comparative study is based on two figures of merits, resolution, and sensitivity. The comparative analysis is shown in Table 5.4.

5.3 Further Step for Geometry and Performance Optimization: Multi Lens-Based SPECT

The modular lens-based SPECT geometry enhanced the sensitivity compared to the single lens and preserved the submillimeter resolution. Moreover, by placing the lenses in a modular plane, each lens in the array will be positioned 50 cm away from the patient and mounted such that all three lenses will be gazing at the same area, but from various angles. The data from each lens can be examined independently or fed into a matrix to generate a three-dimensional image.

Table 5.4 Comparative study between modular lens-based-SPECT and the single lens-based SPECT and LEHR SPECT

System	Configuration	Resolution (mm)	Sensitivity $(hits/emitted)$
***Parallel SPECT (LEHR)** **39 × 39 Pinholes**	Pinhole diameter 1.2 mm, septal thickness 0.2 mm, pinhole depth 35 mm, source-to-collimator distance 25 mm.	1.9	3×10^{-5}
***Parallel SPECT (LEHR)** **39 × 39 Pinholes**	Pinhole diameter 1.2 mm, septal thickness 0.2 mm, pinhole depth 30 mm, source-to-collimator distance 20 mm.	2.5	$3.2 .\times 10^{-5}$
***Parallel SPECT (LEHR)** **121 × 121 Pinholes**	Pinhole diameter 0.4 mm, septal thickness 0.2 mm, pinhole depth 30 mm, source-to-collimator distance 20 mm.	0.8	1.2×10^{-5}
Single Lens-Based SPECT **One lens**	Laue lens radius 20.83 mm, thickness 1 mm, source-to-lens distance 500 mm	0.1	2.9×10^{-5}
Modular Lens-Based SPECT **Three modules, each module with one Laue lens**	Three modules, each module consists of a Laue lens radius 20.83 mm, thickness 1 mm, source-to-lens distance 500 mm.	0.1	9×10^{-5}
***Collimator set is simulated in present study.**			

However, the FOV in the case of the modular lens-based SPECT is small. Thus, I had to take a step forward and propose an alternative for a prospective ultrahigh-resolution lens-based SPECT imaging without sacrificing the system FOV.

Functional imaging based on multi-pinhole (MPH) geometry has witnessed a tremendous change over the last decade. Several research initiatives were triggered to propose optimized designs for MPH SPECT [160, 339, 340]. Enhancing the performance parameters further was the driving force to study the behaviour of multi-Laue lens in a SPECT environment. The preliminary conceptualization of the multi lens-based SPECT geometry is shown in Figure 5.6.

The envisaged system consists of nine Laue lenses, placed at the pinhole centres in a geometry similar to a multi-pinhole collimator with the clinical collimator removed. The lenses are placed in 3×3 array for the initial geometry. The Laue-collimator is positioned at equal distances from the source and the detector plane. The pitch or the distance between the centres of one Laue lens and the adjacent one equals the lens's diameter to minimize blind areas. It is worth mentioning that the multi lens-based SPECT is a highly multiplexed system. The Laue lens would collect high-energy photons from a wide area and focus them onto its focal points on the detector plane; the location of the focal points is determined by the source's shifts from the lens axis. Any shift in the source's position relative to the lens axis is replicated on the detector plane but in the opposite direction. For larger shifts from the lens axis, one Laue lens would project on the adjacent lens' focal spot, resulting in a multiplexed projection. The active area of the detector module is matched to the envisaged Laue-collimator, which has a $150x150\ mm^2$ active area. The Laue collimator is linked to $150x150x10\ mm^3$ crystals in the detector module and $0.48\ x0.48\ x10\ mm^3$ pixelated scintillator. However, to keep track of the shifted projection from the off-axis sources, it is kept slightly bigger.

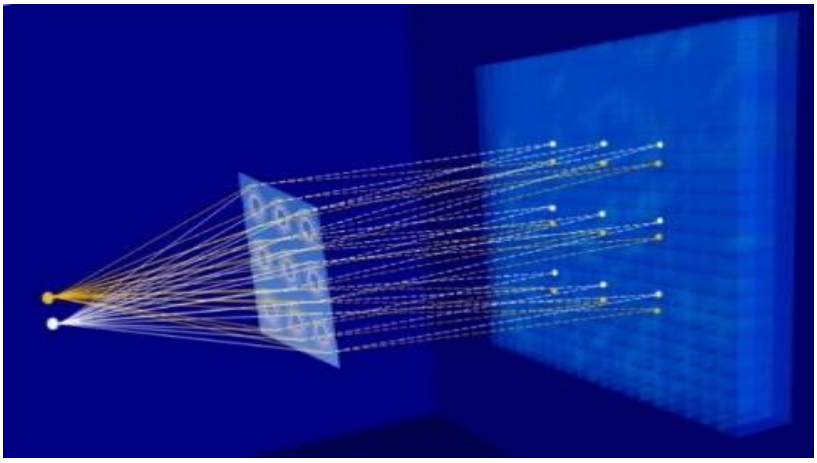

Figure 5.6 Illustration of the multi lens-based SPECT showing the focused rays from nine Laue lenses at the pinhole centres and the detector.

5.3.1 Simulation Design and Experiment Setup

In this section, a description of the simulation set-up for the multi Laue lens-based SPECT is presented.

5.3.1.1 Forward Projection

The forward projection algorithm presented in Chapter 4; Section 4.6.1 was revised to meet/accommodate the behaviour of an array of Laue lenses in a planar plane. The source distribution method was adjusted to ensure that it covers the nine lenses plane while simultaneously optimizing the simulation time. The procedure presented in Section 4.6.1 is repeated for all radiations and Laue lenses in order to generate an entire projection for a given view angle. The lens/detector assembly is rotated around the phantom in accordance with the angle increment, referred to as the step angle. This rotation is repeated until the entire object is scanned 360 degrees. The output image is in MAT format.

5.3.2 Phantom Studies

I used one-point and three-point sources, a resolution phantom consisting of cylindrical capillaries inside a cylindrical volume, and a customized cylinder-sphere phantom for the multi lens-based SPECT experiments. The sphere phantom was used to determine the quality of the projection and reconstructed images by assessing the FWHM of the point spread function, which is the main parameter in spatial resolution. The three spheres phantom and a resolution phantom with three small cylinders were used to validate the system resolution and provide consistent performance information. The desired goal of this work is the ability to detect tumours at the submillimeter range. A case study for studying the system performance in lesion detection using the customized cylinder-sphere phantom is presented. The sphere simulates the typical lesion characteristics by emitting six times the radiation compared to the background area inside the cylinder [337]. The cylindrical phantom is shown in Figure 5.7.

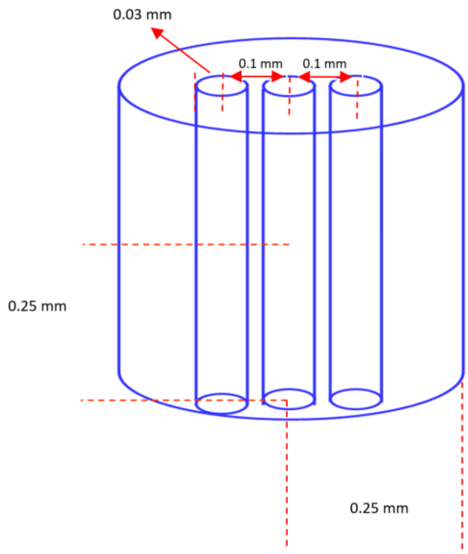

Figure 5.7 Cylindrical resolution phantom (sagittal view).

5.3.3 3D Reconstruction Algorithm: Multi Laue Lens-Based SPECT

It is crucial to develop the appropriate 3D image reconstruction algorithm and evaluate the performance of each new imaging system. This study developed a dedicated 3D Laue reconstruction algorithm as a first attempt to reconstruct 3D images of projections of an array of Laue lenses in a planer plane. Various forms of phantom data were generated with the application of Monte Carlo simulations. Based on the reconstructed images' quality, the systems' performances are evaluated. Given the geometry and data acquisition protocol for the multi lens-based SPECT, it is impossible to project the rays back to the voxel volume in a straightforward manner. However, a precise and reliable reconstruction technique is required to account for the effect of diffraction in the acquisition protocol and the diffraction angles of the focused rays. The Laue lenses would collect high-energy photons from a wide area and focus them onto their focal points on the detector plane; the locations of the focal points are determined by the sources' shifts from their respective lens' axis. Any shift in the source's position relative to the lens axis is replicated on the detector plane but in the opposite direction. For more significant shifts from the lens axis, one Laue lens would project on the adjacent lens' focal spot, resulting in a highly multiplexed projection.

The projections overlapping poses challenges and places additional constraints on developing a practical 3D reconstruction algorithm for an array of Laue lenses geometry. This was the primary challenge of this study and the first attempt to successfully reconstruct the array projection of Laue lenses in three dimensions. The point of focus will be changed for varied lens axis shifts. The technique determines the nonzero sensor plane pixels and converts their row and column coordinates to XYZ coordinates. Next, random points are generated within each lens. This is followed by generating radiations back projected towards the random points within the Laue lens plane by assigning each XYZ point on the sensor plane with a randomly generated azimuthal and polar angle using a custom-made random function comparable to the one used for the forward projection. These angles are essential for establishing the cosine directions of the emitted radiations. It is necessary to propagate the rays in accordance with the set deviation limits so that they converge to the Laue lens collimator plane. At the Laue lens plane, the algorithm identifies two primary important radiation conditions. First, determines which lens the radiation is emanating from. The second step is determining the likelihood that the back-projected beams reaching the lens will be absorbed, diffracted, or transmitted based on their direction. The direction probability entails looking for the likelihood angle for generated lines pointing towards the cube of interest, with a unique fit based on the Laue lens ray propagation behaviour. Those rays satisfying the requirement of hitting the Laue crystals at an angle equal to the Bragg's angle would have a high probability of being diffracted by this particular lens. Once a potential diffracted beam has been detected, the algorithm doesn't project back the rays in a complex manner. Instead, it projects back to the cube of interest based on the Bragg's angle condition. If the rays do not satisfy the Bragg's angles, they are immediately disregarded and assumed to be diffracted by another lens. A fast voxel traversal approach and Siddon's tracing algorithm are utilized to trace the intersected voxel ray intersection lengths. The tracing will return the index of intersecting voxels and the intersection's length. Figure 5.8a shows the multi lens-based SPECT defined detector, the nine lenses inside a multi-pinhole collimator, and the voxel volume. Figure 5.8b shows the back-projected rays through the Laue lens centre. Figure 5.8c shows the voxel volume and the back-projected rays based on the Laue law of diffraction algorithm. The back-projected rays converge at the voxel volume. The 3D reconstruction flowchart is shown in Figure 5.9.

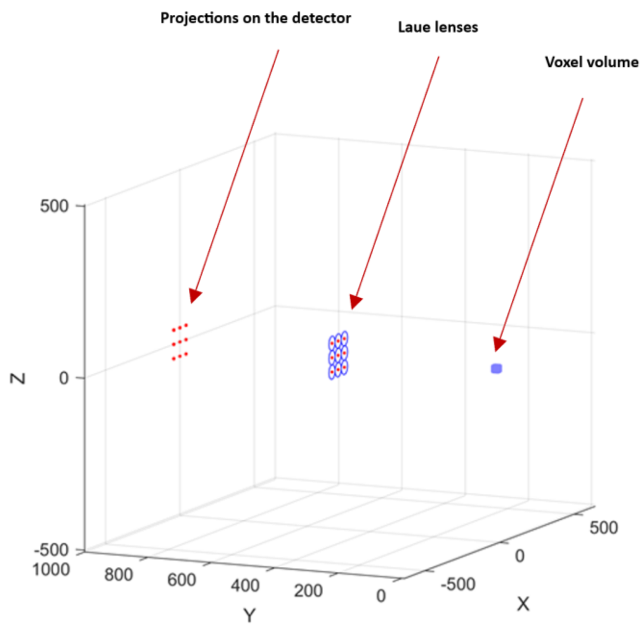
Projections on the detector
Laue lenses
Voxel volume
500
0
-500
Z
1000
800
600
400
200
0
Y
-500
0
500
X

(a)

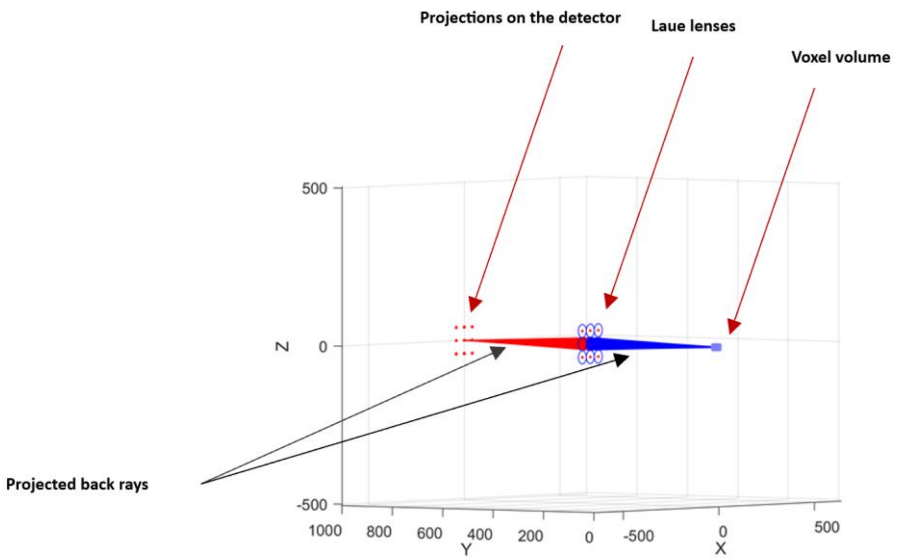
Projections on the detector
Laue lenses
Voxel volume
Projected back rays
500
0
-500
Z
1000
800
600
400
200
0
Y
-500
0
500
X

(b)

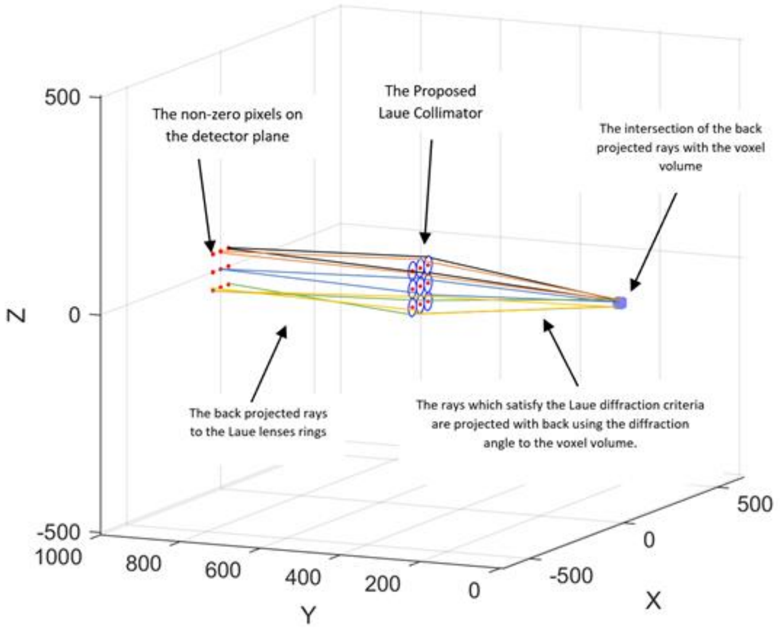

(c)

Figure 5.8 Multi Laue lens forward projection (a) The Lens-Based SPECT defined detector, LAUE collimator and the voxel volume, (b) The back projected rays based on through the Laue lens volume, (c) The back-projected rays based on the Law of Laue lens diffraction; the rays converge at the voxel volume.

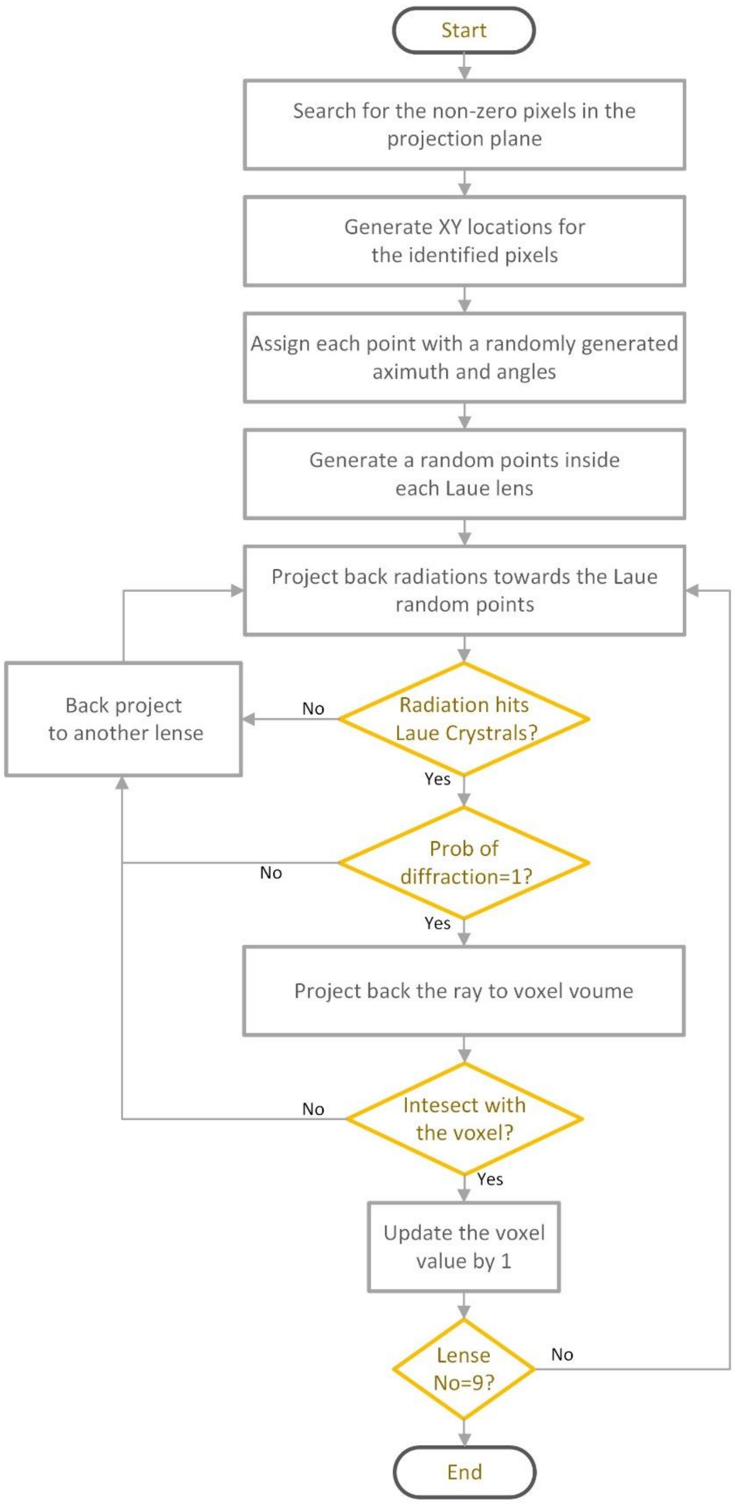

Figure 5.9 3D reconstruction algorithm.

5.3.4 Experimental Results

This section presents the initial system performance results. Moreover, for a rigorous comparison, the achieved performance parameters were contrasted against the existing parallel LEHR and multi-pinhole Inveon SPECT imaging modalities.

The conducted phantom experiments to prove the initial system performance are discussed in this section. The phantoms were placed at various shifts and depths within the lenses' FOV. The distribution of the reconstructed single point source phantoms was used to determine system resolution. The sensitivity was determined for the array of Laue lenses. A series of point-source acquisitions were performed using the scanning pattern to compare the proposed SPECT sensitivity and resolution with a conventional scanner. The radius of the point source is $0.03\ mm$, which is equivalent to a $0.113\ nL$ volume, and the radiation points were equivalent to an activity of $0.1\ mCi$.

5.3.4.1 Projection and 3D Reconstructed Images

Figure 5.10 shows part of the 36 projection images of the multi lens-based SPECT generated by rotating the Laue collimator around the three-point sources with a $10°$ step angle. Figure 5.11a, Figure 5.11b, and Figure 5.11c show the 2D XZ, 2D XY, and the 2D YZ slice of the 3D reconstructed image, respectively. Figure 5.12a and Figure 5.12b show the 3D reconstructed image for three spheres of 0.03 mm radius and 0.1 mm distance between the sphere's centres and the surface plane of the 3D volume of the reconstructed image generated using Volume Viewer, respectively. By referring to the phantom in Figure 5.2 and the clearly 3D reconstructed images in Figure 5.12b, the multi lens-based SPECT allows resolving adjacent volumes as small as $0.113\ nL$, which has a significantly smaller size compared to any conventional SPECT system. Figure 5.12a shows a top view while Figures 5.12c and 5.12d shows the spheres from different axis.

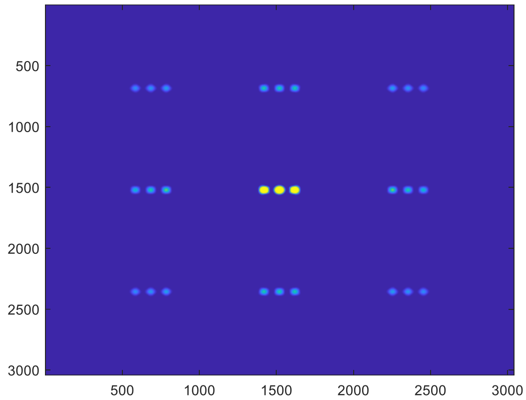

0°

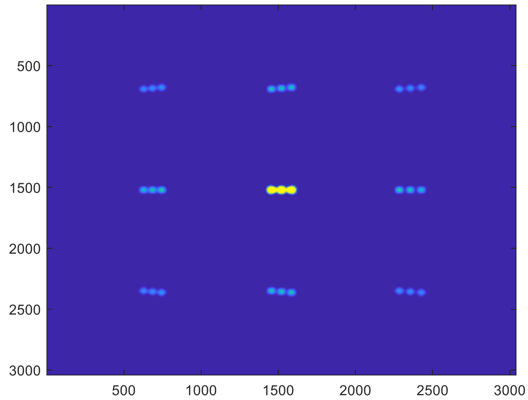

40°

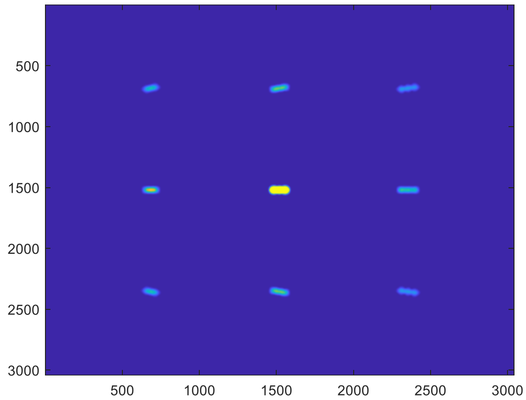

60°

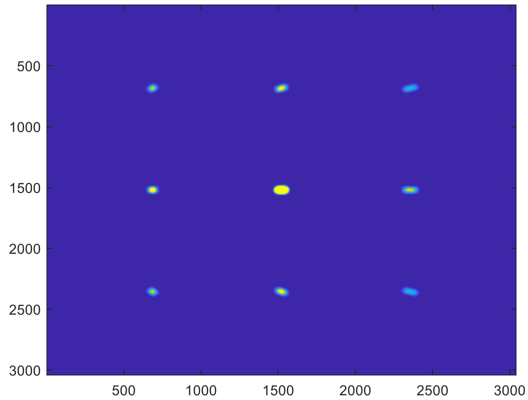

80°

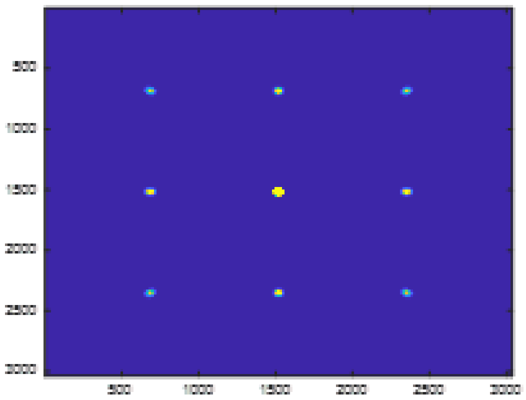

100°

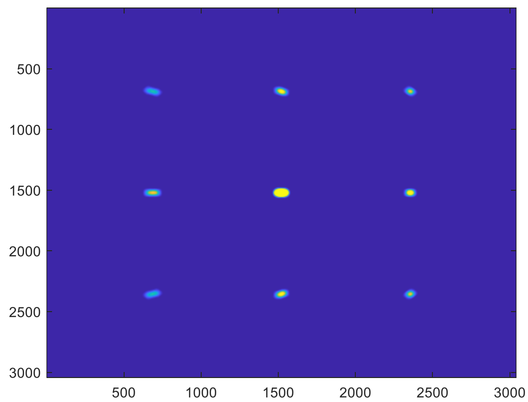

140°

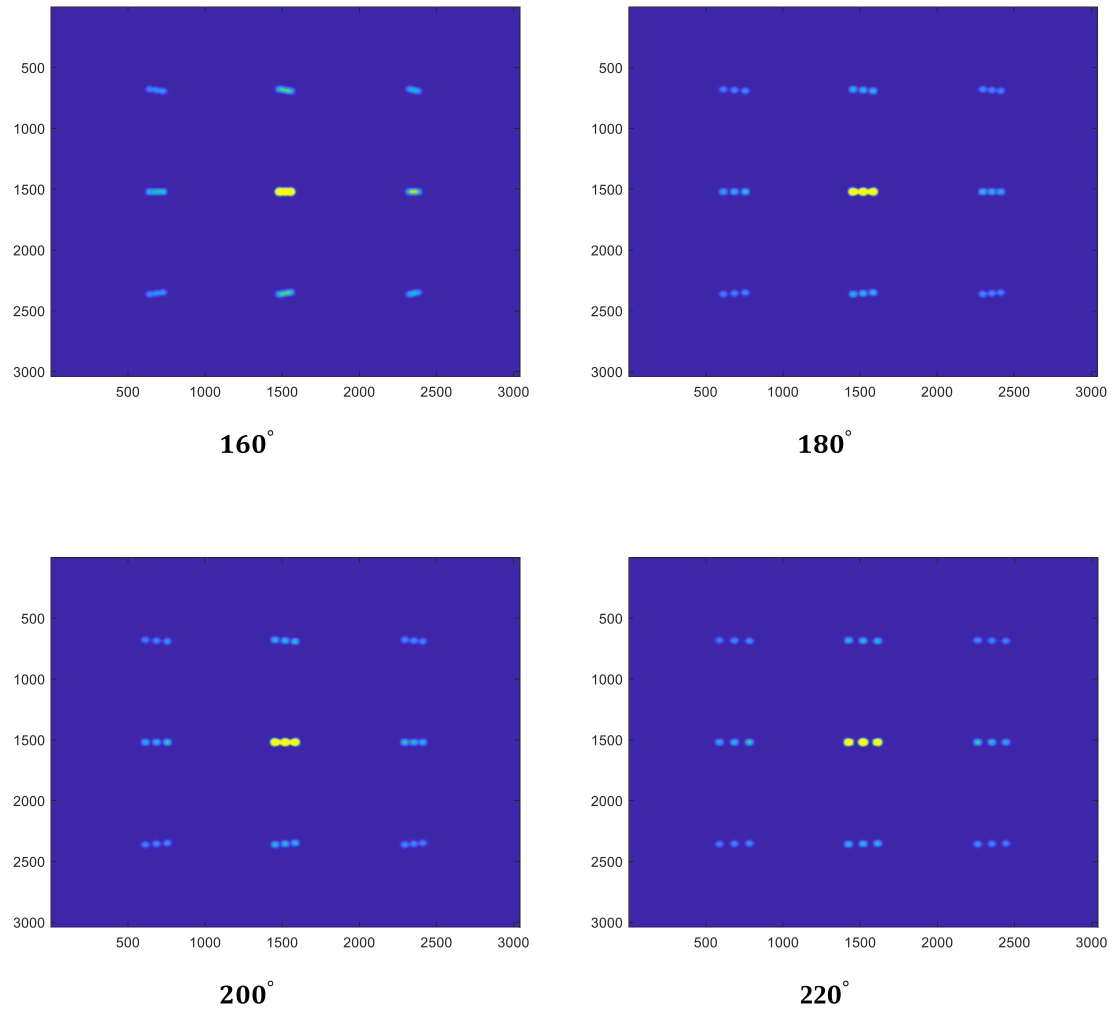

Figure 5.10 Multi Laue lens projections of three spheres placed at 0.1 mm from center to center rotated at 10-degree step angles. The x-axis represents the column index, and the y-axis represents the raw index of the pixelated projection image. The step angles are indicated below each figure.

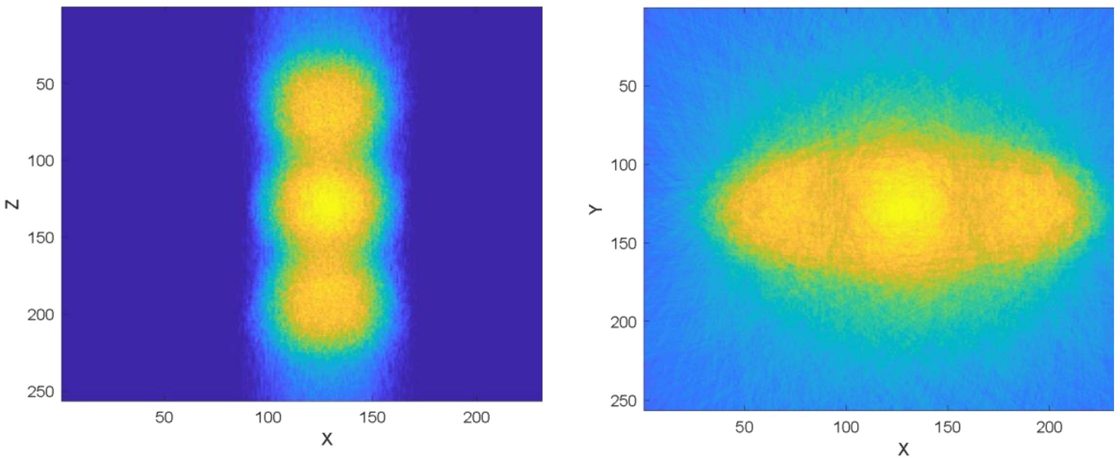

(a) **(b)**

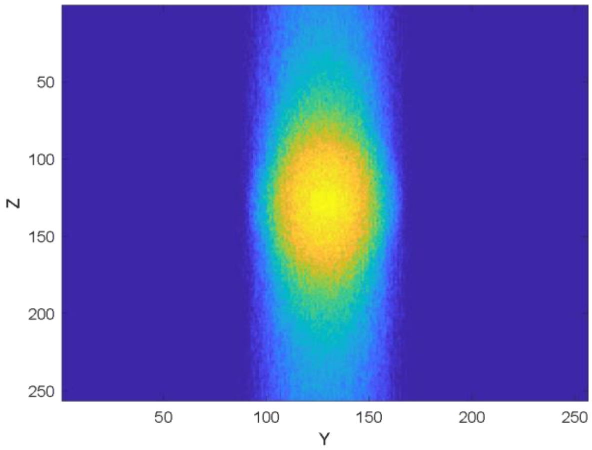

(c)

Figure 5.11 3D reconstruction images. (a) The 2D XZ slice of the 3D reconstructed image for three spheres of 0.03 mm radius and 0.1 mm distance between the spheres' centers, (b) The 2D XY slice of the 3D reconstructed image for three spheres of 0.03 mm radius and 0.1 mm distance between the spheres' centers, (c) The 2D YZ slice of the 3D reconstructed image for three spheres of 0.03 mm radius and 0.1 mm distance between the spheres' centers. Units of measurements are in mm

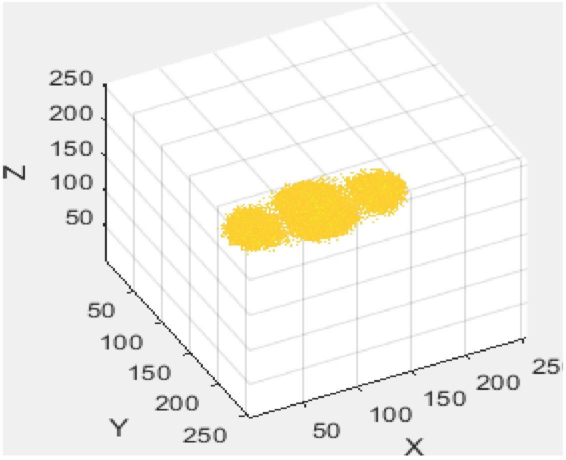

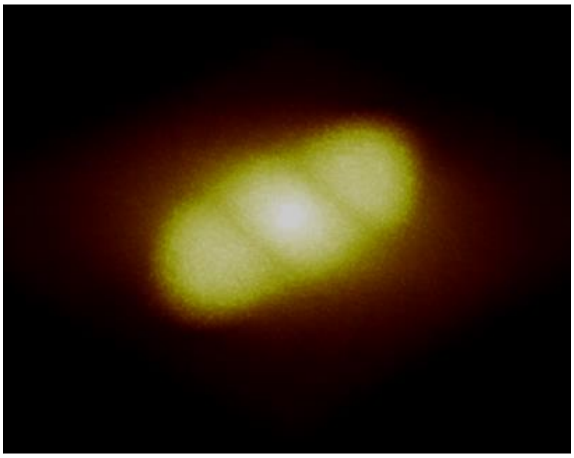

(a) **(b)**

Figure 5.12 Multi Laue lens 3D reconstructed images. (a) The 3D reconstructed image for three spheres of 0.03 mm radius and 0.1 mm distance between the sphere's centers, (b) The surface plane of the 3D volume of the reconstructed image generated using Volume Viewer. Units of measurements are in mm

5.3.5 System Validation: Depth and Shift Validation

The validation methods conducted in Chapter 4; Section 4.8.2 were used to estimate the 3D reconstructed depth and shifts in the case of modular geometry. Table 5.5 shows the applied/experimental phantom shifts and depth versus the detected ones in the 3D reconstructed images XY and XZ slices.

Table 5.5 Comparison between the applied XY phantom shifts in the case studies and the detected shift in the 3D reconstructed images.

	Phantom Shift (x) (mm)	Shift in the reconstructed image (x) (mm)	Phantom Shift (y) (mm)	Shift in the reconstructed image (y) (mm)	Phantom Depth (z) (mm)	Depth in the reconstructed image (z) (mm)
Study 1	0.08	0.080	0.08	0.080	1	1.000
Study 2	-0.10	-0.098	0.10	0.098	3	3.000
Study 3	0.30	0.300	0.30	0.300	5	4.97
Study 4	0.50	0.496	0.50	0.496	10	9.967
Study 5	0.70	0.687	0.70	0.687	15	14.967
Study 6	-1.0	-0.980	1.0	0.998	30	29.987

5.3.6 Sensitivity and Resolution Analysis

For determining the system's resolution, the two approaches conducted in in Chapter 4, Section 4.8.4 were used. The first one was the FWHM method which is based on point source analysis. Figure 5.13a and Figure 5.13b show the projection image of a point source for nine Laue lenses and the XY slice of the 3D reconstructed image, respectively. Figure 5.13c and Figure 5.13d show the 3D reconstructed image for three spheres of 0.03 mm radius and 0.1 mm distance between the sphere's centres and the top view of the 3D reconstructed image generated using volume viewer, respectively.

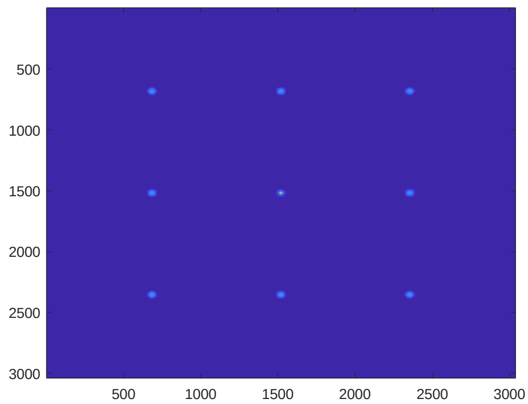

(a)

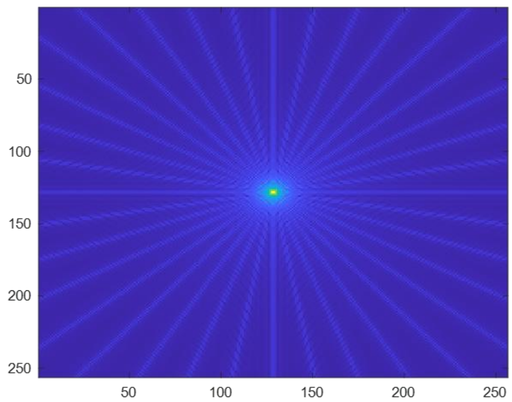

(b)

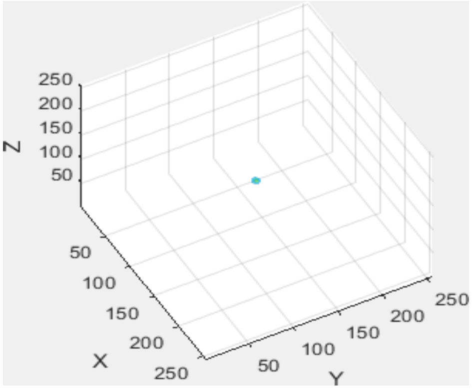

(c) **(d)**

Figure 5.13 Point source analysis. (a) The projection image of a point source using the multi lens-based SPECT, (b) The XY slice of the 3D reconstructed point source, (c) The 3D reconstructed image for three spheres of 0.03 mm radius and 0.1 mm distance between the sphere's centres, (d) Top view of the 3D reconstructed image generated using volume viewer. The x-axis represents the column index, and the y-axis represents the raw index of the pixelated projection image.

Figure 5.14a and Figure 5.14b show the fitted Gaussian of the projection and the reconstructed images, respectively. Based on the FWHM analysis, the resolution is deduced to be 0.1 mm. The plateau signal around the spinous process of the Gaussian fitted curve is a distribution of the background region in the phantom. Using a Laue lens thus reduces blurring caused by radiation penetration and scattering in the aperture edge material that is common in conventional collimators. This is evident from the sharp-fitted Gaussian of the projection and the 3D reconstructed images.

A resolution phantom of three small cylindrical capillaries as small as 0.03 mm in radius and separated by 0.1 mm was distinguished clearly in the reconstruction. Figure 5.15 shows the top view of the 3D reconstruction of the 3 cylinders. In terms of phantom volumes, the lens-based SPECT allows resolving adjacent volumes as small as 0.113 nL approximately, which is substantially smaller than any conventional SPECT system can resolve.

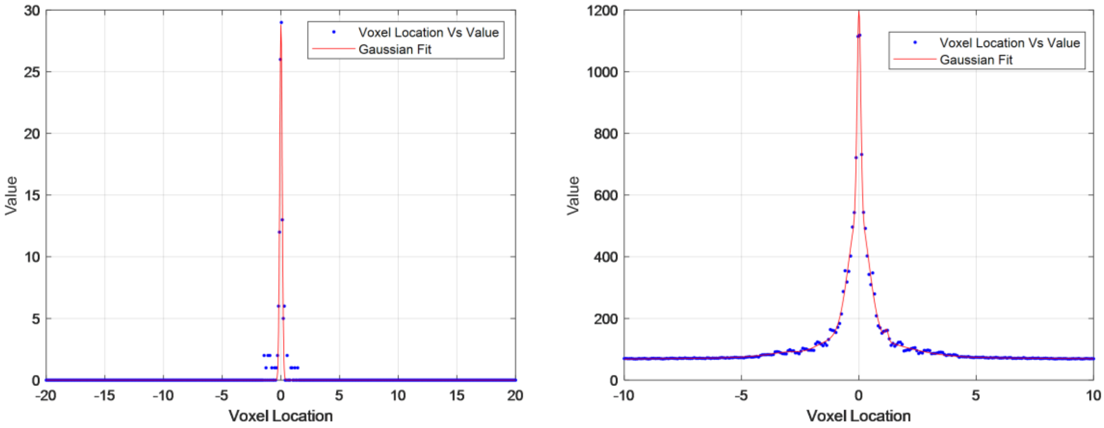

(a) (b)

Figure 5.14 FWHM analysis. (a) The Gaussian fitted point source of 0.03 mm radius of the projection image, (b) The Gaussian fitted point source of 0.03 mm radius of the projection image.

Figure 5.15 Top view of the 3D reconstruction of the 3 cylinders.

As mentioned in Chapter 4, Section 4.8.4, the real sensitivity of a Laue lens system is calculated by dividing the number of diffracted photons by the emitted gamma rays. However, to conclude/ascertain the sensitivity for an array of nine Laue lenses combined in a SPECT gamma camera configuration, a ray counter at the entrance and at the exit of the Laue lens plane was setup to determine the total number of incident rays over the diffracted beams from the crystals. The final sensitivity of the Laue collimator is deduced by taking into account the contribution of the array of Laue lenses for both on-axis and off-axis sources. Knowing the contribution of each Laue lens to the image acquisition is crucial in optimizing the geometry customized for the desired imaging application in future work. The lens counter determines the below ratio:

$$Counter\ Ratio = \frac{Diffracted\ Gamma\ Ray}{Emitted\ Gamma\ Rays_{Isotropic}}$$ **Eq. 5.4**

The order of the Laue lenses is shown as in Figure 5.16:

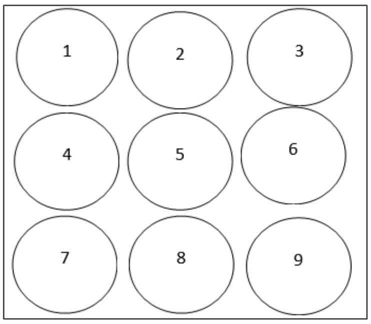

Figure 5.16 Lenses order in the multi-Laue lens geometry.

The counter records for the diffracted photons per each lens are listed in Table 5.6:

Table 5.6 The sensitivity counter for the nine Laue lenses.

Rotation	Lens 1	Lens 2	Lens 3	Lens 4	Lens 5	Lens 6	Lens 7	Lens 8	Lens 9
0°	16421	27837	16736	26523	198398	26810	16528	27842	16709
10°	16734	27313	16470	26998	199243	26736	16590	27504	16773
20°	16709	27718	16845	26828	201613	26776	16539	27298	16702
30°	16624	27434	16640	26948	205783	26895	16551	27448	16708
40°	16602	27566	16477	27480	211376	27077	16733	27296	16790
50°	16755	27349	16864	27026	219444	27085	16700	27199	17024
60°	16718	27135	16543	27094	229940	27140	16500	27396	16534
70°	16523	26960	16698	27080	243868	27169	16582	27258	16760
80°	16617	27242	16728	27275	260324	27299	16496	27013	16593
90°	16514	27182	16561	27043	270405	27158	16699	26889	16504
100°	16665	27170	16597	27007	260328	27114	16563	27018	16599
110°	16775	27268	16213	26947	243789	26899	16655	27351	16626
120°	16605	27356	16638	26967	230065	27076	16372	27067	16713
130°	16701	27637	16623	27323	219228	26850	16603	27117	16572
140°	16606	27378	16439	26932	211230	27080	16633	27475	16465
150°	16745	27319	16591	27189	205735	26990	16824	27972	16669
160°	16655	27149	16445	26808	201535	26793	16452	27342	16498
170°	16765	27800	16593	26689	198977	26985	16691	27467	16568
180°	16766	27150	16506	26867	198438	26830	16527	27534	16532
190°	16406	27280	16823	27142	199148	27017	16549	27582	16675
200°	16262	27599	16755	27154	201585	26930	16855	27824	16533
210°	16459	27614	16747	26878	205503	26889	16635	27792	16748

220°	16777	27218	16681	27052	211443	27000	16673	27060	16725
230°	16718	27231	16869	26897	219610	27159	16700	27427	16614
240°	16798	26867	16807	27153	229855	27346	16635	27201	16602
250°	16607	27071	16728	27154	243996	27383	16483	27051	16611
260°	16793	27171	16599	26941	260794	27117	16538	26994	16609
270°	16622	27166	16384	27350	270130	27483	16592	26794	16576
280°	16672	26930	16541	27128	260737	27265	16780	26965	16765
290°	16571	27340	16616	27133	243723	26935	16478	27407	16604
300°	16378	27123	16616	27247	230345	27088	16860	27096	16530
310°	16824	26783	16718	26933	219675	26828	16592	27370	16693
320°	16387	27261	16738	26987	211347	27244	16688	27215	16878
330°	16582	27564	16620	27178	205763	26818	16572	27346	16898
340°	16783	27667	16633	26823	201501	26847	16415	27300	16729
350°	16845	27420	16773	26900	198945	27006	16324	27327	16487

Based on the Monte Carlo simulations, the sensitivity of the multi lens-based SPECT using an array of nine Laue lenses in a planer plane and an isotropic source radiating gamma rays in all directions was found be $6.2\ e^{-5}$ $(hits/emitted)$, which is equivalent to $57\ cps/MBq$.

5.3.7 Multi Lens-Based SPECT: Capturing Views from Different Angles.

As stated in Chapter 4, Section 4.2, the proposed system is envisioned to be akin to a lightfield camera, with each lens looking at a different view from the organ. The data from each lens can be viewed independently or can be entered into a matrix that can, subsequently, produce a 3D image containing precise information on the size of the tumour and its location.

Figure 5.17a and Figure 5.17b show the projection images for multi lens-based SPECT for a point source, and the zoomed projection image behind the white highlighted projection, respectively. Figure 5.17c and Figure 5.17d show the zoomed image projection image for the red and green highlighted projections, respectively. The projection image behind each lens represents a different view of the scanned object. Based on these resultswith each lens looking at the same target but from different angles [133]. It is worth mentioning that the multi-lens-based SPECT is a highly multiplexed system, one Laue lens would project on the adjacent lens's focal spot for larger shifts from the lens axis, resulting in a multiplexed projection. The Laue lenses would collect gamma rays from a wide area and focus them onto their respective focal points on the detector plane; the locations of the focal points are determined by the source’s shifts from the lenses’ axes. Any shift in the source’s position relative to a lens axis is replicated on the detector plane but in the opposite direction.

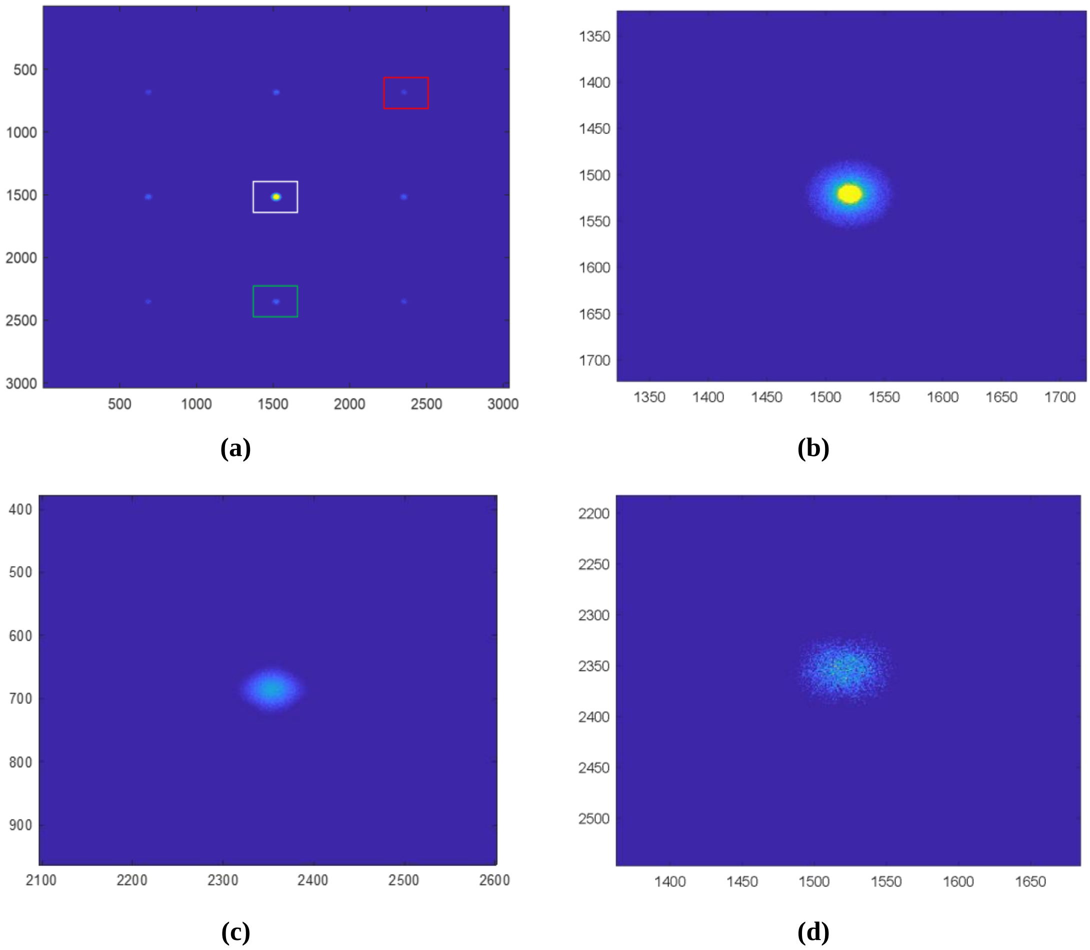

Figure 5.17 Lenses’ different views (a) Multi lens-based projection image of point source, (b) Zoomed view of the white highlighted projection, (c) Zoomed view of the red highlighted projection, (d) Zoomed view of the green highlighted projection. The x-axis represents the column index, and the y-axis represents the raw index of the pixelated projection image.

By encoding the angular resolution with a higher spatial resolution, Laue lenses in SPECT systems enable sampling of the radiation in 4D. This method allows for the refocusing of SPECT images while preserving the spatial resolution, in an approach akin to lightfield imaging (see Chapter 4, Section 4.2.1, Figure 4.2).

5.3.8 Comparative Analysis: Multi Lens-Based SPECT VS SIEMENS LEHR Parallel Hole and Inveon Multi-pinhole SPECT.

To provide a quantitative performance assessment and to evaluate the proposed system’s performance, a comparative study with conventional SPECT was conducted. Table 5.7 shows the comparison between the different geometries of LEHR, Inveon, and the lens-based SPECT in terms of system's resolution and sensitivity. The lens-based SPECT, whether it is with single, modular or multi geometry, outperformed the existing systems in terms of resolution while having a comparable sensitivity in the case of single lens-based SPECT. However, the sensitivity is improved in the case of multi, and modular Laue lenses geometry compared to the conventional SPECT. CPS/MBq is used to express the detector's counting rate per unit of radioactivity, where CPS represents the rate at which a radiation detector and MBq is a unit of radioactivity.

Table 5.7 The comparison between the different geometries of LEHR, Inveon, and the lens-based SPECT in terms of system's resolution and sensitivity.

System	Configuration	Resolution FWHM (mm)	Sensitivity cps/MBq
Parallel SPECT (LEHR) *	*Pinhole diameter 1.2 mm, septal thickness 0.2 mm, pinhole thickness 34 mm, source-to-collimator distance 2.5 cm [341].	1.9	33.5
	*Pinhole diameter 1.2 mm, septal thickness 0.2 mm, pinhole thickness 30 mm, source-to-collimator distance 2 cm [341].	2-2.5	33.5
Inveon SPECT**	**Mouse Collimator**		
	Single pinhole		
	Inveon **1-MHR-0.5, s**ingle pinholes Mouse collimator, source-to-collimator distance 2.5 cm [342].	0.7	70
	Rat Collimators		
	Single pinhole		
	Inveon **1-RGP-1.5** single-pinholes rat collimator, **SPECT** Pinhole diameter 1.5 mm, source-to-collimator distance 50 cm [342].	1.6	90
	Multi-pinhole		
	Inveon **3-RWP-1.2** single-pinholes rat, **SPECT** Pinhole diameter 1.2 mm, source-to-collimator distance 50 cm collimator [342].	1.2	95
Multi lens-based SPECT	Nine Laue lenses, Laue lens radius 20.83 mm, thickness 1 mm, lens to detector distance 50 cm.	0.1	57

Modular lens-based SPECT	Three modules, each module consists of a Laue lens of radius 20.83 mm, thickness 1 mm, lens to detector distance 50 cm.	0.1	81
Single lens-based SPECT	One Laue lens, Laue lens radius 20.83 mm, thickness 1 mm, lens to detector distance 50 cm.	0.1	27
*: Experiment was simulated in this study **: Measured form the literature			

5.4 Case Study: Lesion Detection

A customised cylinder-sphere phantom was used to study the system's performance in lesion detection. It consists of a sphere with $0.03\ mm$ radius (representing a defect) placed inside a cylinder (representing the background) with is $0.5\ mm$ height and $0.5\ mm$ diameter. The sphere activity is three times higher than in the rest of the cylinder. The different activity simulates the cancerous tumour with higher radio tracer absorption, thus with higher activity. The phantom experiments were conducted twice using different activities and sphere sizes. A tomographic acquisition with 36 projections at $50\ cm$ rotation radius was used. Figure 5.18a shows a projection image for the phantom on the detector plane. Figure 5.18b and Figure 5.18c show the XY slice of the 3D reconstrued image and the 3D reconstructed image, respectively. The different activity highlighting the cancerous tumour with higher radiotracer absorption, thus higher gamma counts, was detected clearly by the Laue lenses.

A 0.1 mCi source gives off 3.7×10^6 gammas per second. With such activity and multi lens SPECT efficiency of 6.2×10^{-5}, based on Monte Carlo simulations, the radiation count rate is found to be $299\ counts/second$.

Clinically, organs that contain a large amount of blood retain approximately 2.2 μCu per cc (cubic centimeter). A malignancy contains approximately six times this amount, or about thirteen μCu per cc [209].

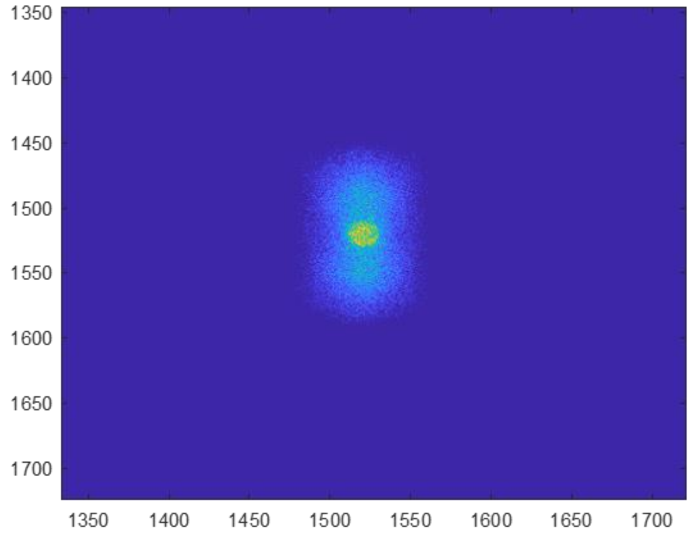

(a)

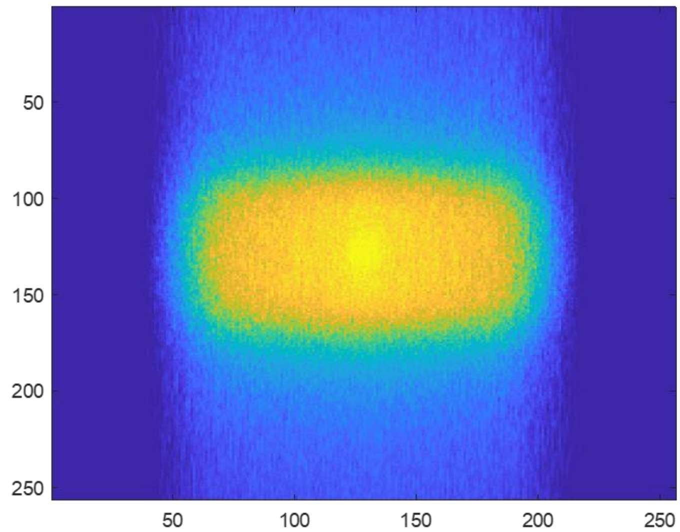

(b)

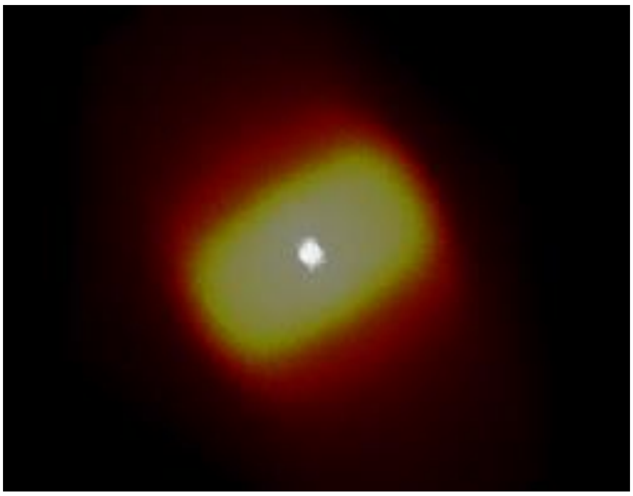

(c)

Figure 5.18 Projection image of a sphere phantom inside a cylinder, (a) Projection image behind the centred lens, (b) XY slice of the 3D reconstructed image, (c) 3D reconstructed image generated using Volume Viewer. The X and Y axis measurements are in mm.

5.5 Chapter Summary

In this chapter, I introduced and elaborated upon the proposed system together with an appropriate validation method and evaluated the high-resolution capabilities of the improved lens-based SPECT geometries. I started by introducing the modular lens-based SPECT system design and assessed its performance parameters. The Laue lenses are placed on tiled planes in a modular fashion and with the detector geometry in such a way that their fields of view are converging. The feasibility of the proposed system is demonstrated by the Monte Carlo simulation. Given the new geometry and data acquisition protocol for the modular multi lens-based SPECT, the FOV cannot be determined in a straightforward way. The overall FOV of the system is the portion of the potential FOV, which can be reconstructed by having sufficient or scans and enough disparity between the acquired projection data of the views. Hence, the FOV was determined based on the module width and the lens' focal length. The performance parameters were contrasted against the existing SPECT for system validation purposes. Moreover, the sensitivity mapping over the modules' FOV showed a gradual degradation; however, it still outperforms the parallel LEHR. The lens has two distinguishing features: first, its effectiveness does not diminish when the size of the source decreases, as it happens in many existing imaging systems. Second, it can locate and identify objects with millimetre resolution. The preliminary evaluation of the system using 3-point sources is presented. By scanning the source with multiple lenses that look at the same volume from different angles, one can generate a three-dimensional image. Monte Carlo simulations were used to accurately model and evaluate the proposed concept and design. Furthermore, a dedicated image reconstruction algorithm was developed and validated for the system.

Then, I moved further and described the development and analysis of a new multi lens-based SPECT in a planer plane geometry that would potentially provide improved performance compared to conventional SPECT. Physical principles governing the design of this system are presented, along with a series of measurements analysing various characteristics of the generated projection and 3D reconstructed images.

5.6 Acknowledgement

This chapter articulates and expands on work for which the concepts and basic findings were partially published in:

1. Barhoum, A., Tahtali, M., & Camattari, R. (2022, October). Feasibility Study of a Lens-Based SPECT With a Tiled Lens and Detector Geometry for Animal Research: Simulation Results. In 2022 IEEE International Conference on Systems, Man, and Cybernetics (SMC) (pp. 3143-3149). IEEE.

2. A. Barhoum, M. Tahtali, R. Camattari, and Susanna Guatelli " Feasibility Study of Multi-Lens-Based SPECT with a Dedicated Laue Reconstruction Algorithm: A First Monte Carlo Study" Scientific Reports (2023). This article is under: (Under Review).

6. Detector Analysis GEANT4/GAMOS: Single and Multi-Lens-Based SPECT

As demonstrated in Chapters 4 and 5, the single, modular and multi lens-based SPECT guarantee submillimeter resolution imaging with improved sensitivity in the cases of multi and modular versions. I designed and programmed MATLAB environments that incorporate realistic physical interactions and account for possible absorption and attenuation effects for the envisioned lens-based SPECT with three different geometries. However, the MATLAB model was running under ideal detector conditions. To ascertain the validity of the argument presented throughout this thesis, it was necessary to build up on the previous work and further study the response of a real detector design to the focused gamma rays in a stable Monte Carlo environment dedicated to medical physics applications. To this end, I started examining the possibility of incorporating a real detector design to a collimator augmented with a Laue lens, the work presented in this chapter focuses on introducing and discussing this novel approach.

This chapter is structured as follows. It begins with an introduction in Section 6.1, providing an overview and context for the subsequent sections. Section 6.2 focuses on the material and methods employed in the study. Within this section, subsections include the geometry setup and visualization (6.2.1), the source generator using a diffracted TXT file (6.2.2), and the GAMOS Monte Carlo simulation framework, including physics modelling and parallel job execution (6.2.3). Section 6.3 delves into the GAMOS simulations, specifically investigating the single lens geometry without considering any detector effects. This section is further subdivided into subsections covering aspects such as the geometry (6.3.1), source generator (6.3.2), 3D DOSE analysis (6.3.3), deposited energy (6.3.4), reconstructed hits (6.3.5), step and track data histograms (6.3.6), and reconstructed hits' 3D reconstruction (6.3.7). The subsequent sections, including Section 6.4 and Section 6.5, present case studies involving detector effects and a three-point source, respectively. In Section 6.4, the focus is on studying the system performance considering the presence of detectors. In Section 6.5, the three-point source scenario is analysed.

Section 6.6 entails a MATLAB calibration against GAMOS, specifically examining the system resolution. Finally, Section 6.7 encompasses GAMOS simulations using a multi-lens geometry without considering detector effects. By following this chapter structure, the reader gains insights into the introduction, materials and methods, GAMOS simulations in various scenarios, case studies with different configurations, system calibration, and multi-lens geometry simulations.

6.1 Introduction

The lens-based SPECT analysis depends upon imitating and modelling the gamma focusing by the diffraction process in a Monte Carlo simulation. One of the available and most powerful Monte Carlo simulation toolkits for the movement of particles through matter is GEANT4. It is used in high energy, nuclear, and accelerator physics, as well as medical and space scientific research [299]. However, it does not support the simulation of wave-based interactions, hence the process of diffraction is not implemented yet. This was one of the main limitations that I encountered in this work. Thus, I proposed an alternative method to simulate the effects of focusing the gamma rays at the sensor plane, and then simulate the detector response separately in GAMOS/GEANT4. I developed a custom-made Monte Carlo code in MATLAB that simulates the Laue lens behaviour placed at the centre of a conventional SPECT pinhole and generated the coordinates and the momentums of the diffracted photons. Those coordinates and momentums were used to set up the TXT files exported to GAMOS and then used as inputs for the source generator. GAMOS has different generators where the user can choose various particles and generator distributions or define customized source data that reads primary particles from a TXT file. In GAMOS, the detector hits were generated by running a random number of events for different step angles. The hits are utilized to set up the projection images. The projection images were exported back to MATLAB for image reconstruction and further analysis. The GAMOS geometry was used to characterize the detector. The ***GmGeneratorFromTextFile*** command defines the input text file for the focused beams at the detector surface [343]. This file was used as a particle generator in the input script. Figure 6.1 shows the proposed solution for studying the detector response in GAMOS/GEANT4.

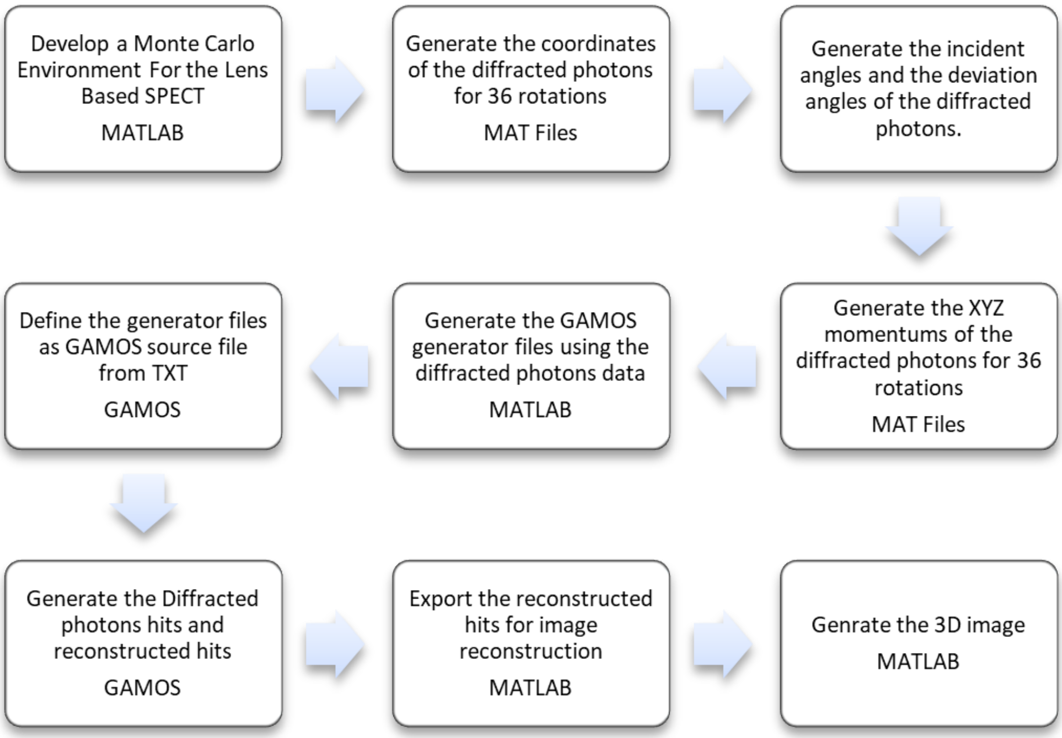

Figure 6.1 Proposed flowchart for studying the detector response due to the diffracted photons using MATLAB and the GAMOS/GEANT4 Monte Carlo toolkit.

6.2 Material and Methods

Monte Carlo simulations were used as a supplementary tool to characterize and optimize certain medical imaging systems. This was accomplished using GAMOS (GEANT4-based Architecture for Medicine-Oriented Simulations) [343].

The format of the TXT files that is used as a source generator is shown in Figure 6.2. It is programmed in GEANT4 and covers different medical applications, from radiation therapy to nuclear medicine, including specific application packages for PET and SPECT [307]. It has code, libraries, and particle transport techniques identical to those produced by GEANT4 and includes nuclear medicine-specific applications. The version of GAMOS used is V6.2.0 on a cluster that has two computers, each one with 4 cores, type i7 CPU at 2.8 GHz with 4GB RAM. The images were obtained after executing the files as WRL outputs and displayed using the Deep View viewer (version 6.3.1.7961) and ParaView.

Event ID	Particle Name	X Position	Y Position	Z Position	X Momentum	Y Momentum	Z Momentum	Time	Weight
1	gamma	-0.557356011	-0.0892199	-445.5	0.002220575	-0.002725377	0.139955855	0	1
2	gamma	-0.666280498	-0.14831681	-445.5	-0.001532481	-0.003489987	0.139948103	0	1
3	gamma	-0.048480582	0.04258058	-445.5	-0.005128646	0.001179731	0.139901055	0	1
4	gamma	0.529994695	0.60432343	-445.5	-0.002365268	0.001152271	0.139975276	0	1
5	gamma	-0.008724722	0.0082374	-445.5	-0.001739503	-0.001946122	0.139975665	0	1
6	gamma	-0.018147708	-0.22588057	-445.5	-0.003279872	-0.001198816	0.139956441	0	1
7	gamma	0.476248452	-0.45134025	-445.5	-0.003101655	-0.00146363	0.139957985	0	1
8	gamma	-0.026690444	-0.01778052	-445.5	-0.00249052	0.00477246	0.139896465	0	1
9	gamma	-0.070852205	-0.17383673	-445.5	-0.00264753	0.003123534	0.139940109	0	1
10	gamma	-0.359340253	0.82787709	-445.5	-0.003707065	0.00068549	0.139949233	0	1
11	gamma	-0.823555213	0.21365823	-445.5	-0.00472021	0.003118407	0.13988565	0	1
12	gamma	0.009658294	-0.21741297	-445.5	-0.004194068	0.002225828	0.139919461	0	1
13	gamma	0.454746137	0.74422586	-445.5	-0.002319049	0.00185873	0.13996845	0	1
14	gamma	0.009947716	0.0651319	-445.5	-0.003290782	0.003819098	0.139909204	0	1
15	gamma	0.024981174	-0.04509374	-445.5	-0.003469027	-0.000576759	0.139955826	0	1
16	gamma	-0.058729724	0.00164077	-445.5	0.000708357	-0.00553607	0.139888706	0	1
17	gamma	0.209909702	0.03171959	-445.5	0.005657645	0.001241038	0.13988013	0	1
18	gamma	0.756252964	0.17268259	-445.5	0.004704773	0.002046147	0.139905963	0	1
19	gamma	0.149932671	0.05688205	-445.5	-0.002995457	0.001979321	0.139953955	0	1
20	gamma	-0.033502072	0.10197844	-445.5	0.003253745	0.002159032	0.139945531	0	1

Figure 6.2 TXT file format used as source generator in GAMOS.

6.2.1 Geometry Setup and Visualization

The description of the geometries is based on tags [343]. The Laue-collimator plane is generated using a single placement, whereas the Laue SPECT detector crystals were placed using the square parametrization placement. The parent volume, XYZ position and the rotation matrix must be defined before placing any volume inside the SPECT box volume. The verbosity level was set to 99, and it serves to print the hierarchical tree of geometry volumes. VRML was used for 3D visualization, visVRML2FILE.in file will generate one file for the geometry and another one for the tracks. This is done by adding the following entry to the GAMOS script file:

/control/execut/visVRML2FILE.in

The label: VOLU defines a GEANT4 logical volume and, PLACE is used for the placement of a volume, PLACE_PARAM is used for a parameterized placement, which can be linear, square or circle [343]. The number of radial and tangential crystals are defined as parameters:

: *P NCrystaLax No*

: *P NCrystaLtran No*

To associate a GAMOS sensitive detector with a logical volume, the following command is used:

/gamos/SD/assocSD2LogVol GmSDSimple Scatterer DETECTOR_LOGICAL_ NAME

/gamos/SD/assocSD2LogVol GmSDSimple Absorber DETECTOR_LOGICAL_ NAME

GAMOS supports several data analysis formats. The ROOT format was selected. The histogram analysis is performed using the ROOT software.

6.2.2 Source Generator: Diffracted TXT File

GAMOS has different generators that are generic and allow the user to choose from various particles and generator distributions [343]. In this work, the primary source generator was defined in a text file. The format is based on assigning a different line to primary particle variables. The event ID, the initial XYZ coordinate of the gamma particles, and the photon XYZ momentum were specified for all particles. This is done by calling the GAMOS user action:

/gamos/generator GeneratorFromTextFile

The user action GmTrackDataTextFileUA may be used to generate a file of this type using the following list of data: EventID Particle InitialPosX InitialPosY InitialPosZ Initial- MomX InitialMomY InitialMomZ InitialTime InitialWeight. In the lens-based SPECT GAMOS simulation, the thirty-six data files were used as input files to define the GAMOS generator from a TXT file, each file contains the focused photon coordinates and momentums for each detector rotation angle. Around 100,000 primary photons were considered. In this simulation, I utilized the PENELOPE physics lists for photons, electrons, and positrons.

6.2.3 GAMOS Monte Carlo Simulation: Physics and Running Parallel Jobs

The physics list illustrates the most frequently seen processes using gamma rays, electrons, and positrons, along with optical photons [307]. The following command is used to access this physics list:

/gamos/physicsList ttmEMPhysics

GEANT4 user actions define how a user can interface with a task at the start/end of each run, event, track, or step [305]. They allow the user to create a class that inherits from one of the abstract GEANT4 user action classes, and GEANT4 will handle the user code call. In this work, several GAMOS user actions were used to produce the output files:

/gamos/userAction ttmCountTracksUA

/gamos/userAction ttmHitsWriteUA
/gamos/userAction ttmHitsHistosUA

In the proposed lens-based SPECT, the Laue collimator and the detector planes are rotated with a radius of rotation of $500\ mm$ rotated and a step angle of 10 degrees over the 360 degrees. The obtained thirty-six projections and the saved output files provide the coordinates of the focused photons and momentum. GEANT4's random number management or the GAMOS method was utilized in this work to execute several tasks with identical configurations but distinct random seeds. The initial random seeds were set in the input file. Initializing the random number seeds, GAMOS provides a single command to specify a distinct beginning random seed for each job, ensuring statistical independence of the results:

/gamos/random/setSeeds INITIAL SEED N RANDOM NUMBERS

Where two integers are specified to ensure the results are random. INITIAL SEED is the initial random seed, and N RANDOM NUMBERS is the number of times the initial random seed is sampled before initiating the simulation. This is activated by including the below command in the input file:

/gamos/random/setSeeds 1111 1111.

6.3 GAMOS Simulations: Single Lens Geometry with No-Detector Effects

6.3.1 Geometry

The analysis of a single lens system is crucial in validating, predicting, and determining the initial system parameters. This is the first attempt to propose a collimator SPECT augmented with a Laue lens, and it has been developed from scratch, thus the initial system geometry and parameters are kept simple. The scintillator is connected to a 100 × 100 array of 0.48 mm × 0.48 mm Position Sensitive Photomultiplier Tubes (PSPMTs). The maximum active imaging region is 48 mm × 48 mm, and the energy range detectable is 20 keV to 160 keV. The detector is shown in Figure 6.3.

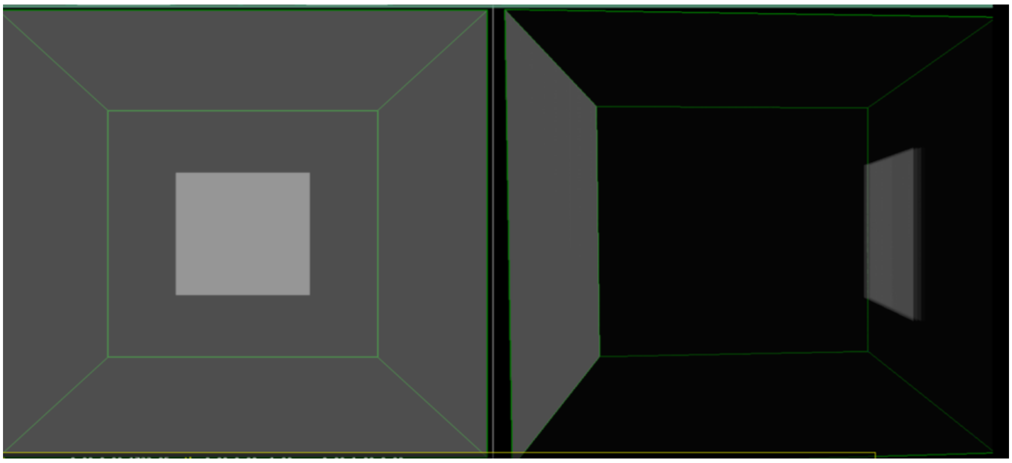

Figure 6.3 The world and detector volumes for the Lens-Based SPECT system, front, and side view.

6.3.2 Source Generator

The TXT files for the different rotation angles with the focused photons coordinates are exported and converted to TXT files readable by GAMOS. Those files are employed as the source generator. Figure 6.4 shows the particle tracking of the focused rays of the generator source. Figure 6.5a and Figure 6.5b show the spot of the focused photon on the detector plane, and the focused photons by diffraction on the scintillator plane, respectively.

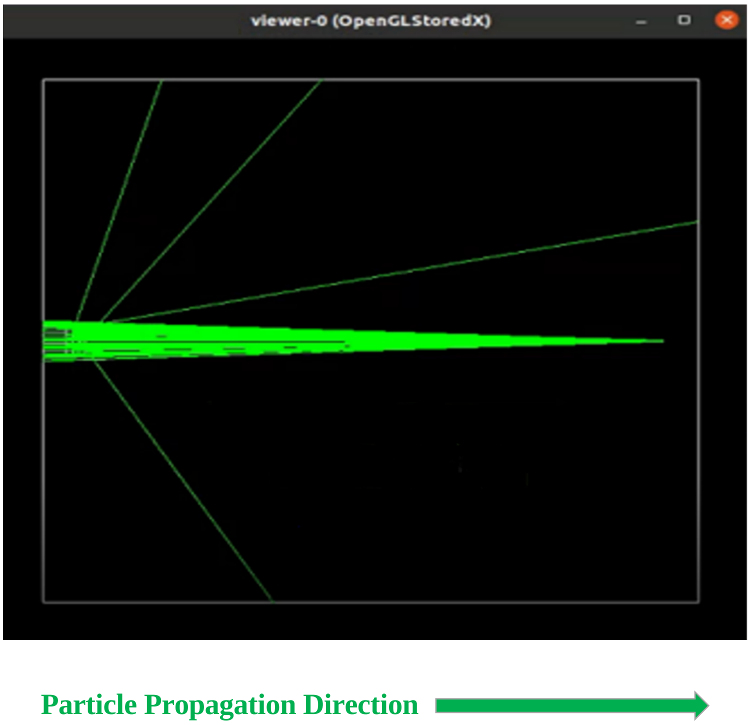

Figure 6.4 The particle tracking of the focused rays of the generator source.

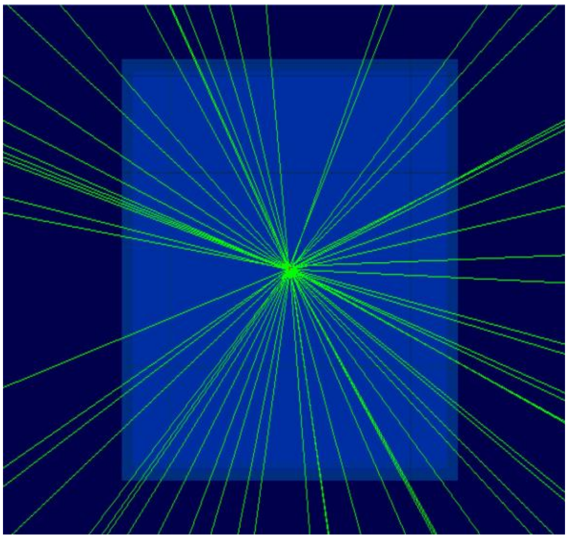

(a)

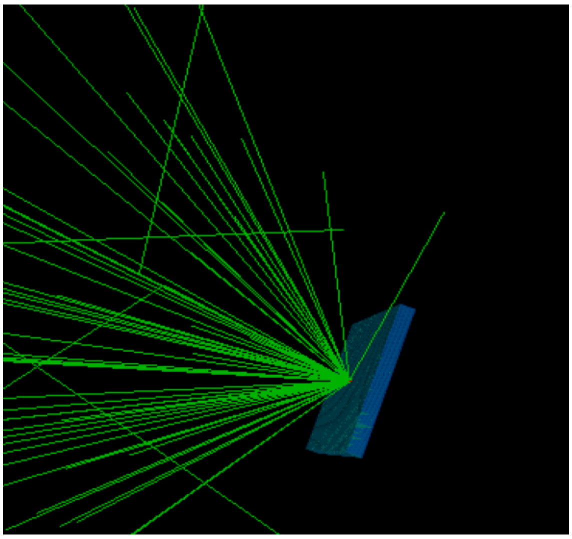

(b)

Figure 6.5 Generated source radiations using the imported data of the diffracted photons. (a) The spot of the focused photons on the detector, (b) The diffracted radiations on the scintillator plane.

6.3.3 3D DOSE Analysis

GAMOS batch jobs for the 36 angles were run, and hits files were generated in TXT format. The position-dependent point-source sensitivity within the Laue lens axis was measured using the same scanning point source as used for system calibration. Using GAMOS utilities and selecting the scorer GmG4PSDoseDeposit, the score dosage or the XY dose distribution in the detector voxels can be detected. The standard output from the dose analysis represents the dose by event deposited in each voxel. The generated output files for the diffracted gammas are text files with the dose, and the dose errors in each voxel are calculated. The number of voxels in the X, Y and Z directions, the array of voxel boundaries in the X, Y, and Z directions, the array of dose values and the array of dose relative error values are listed in the generated text files. The projection images for the point source are generated based on the dose distribution. Figure 6.6 shows the XY dose distribution on the detector voxels for a focused Laue lens projection.

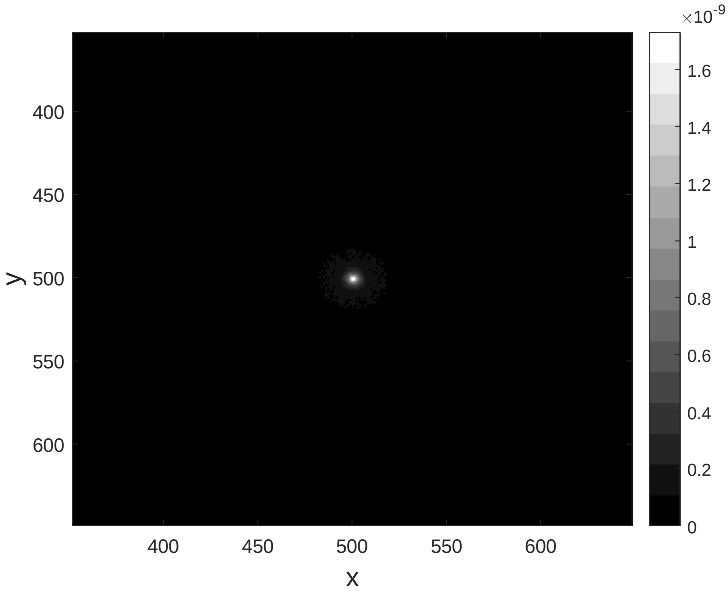

Figure 6.6 The XY dose distribution in the detector voxels for a focused Laue lens projection. All measurements are in mm.

6.3.4 Deposited Energy

Figure 6.7a and Figure 6.7b show the diffracted photons that are detected, and the spot for the focused rays on the detector plane and the back scattered rays for the one Laue lens, respectively.

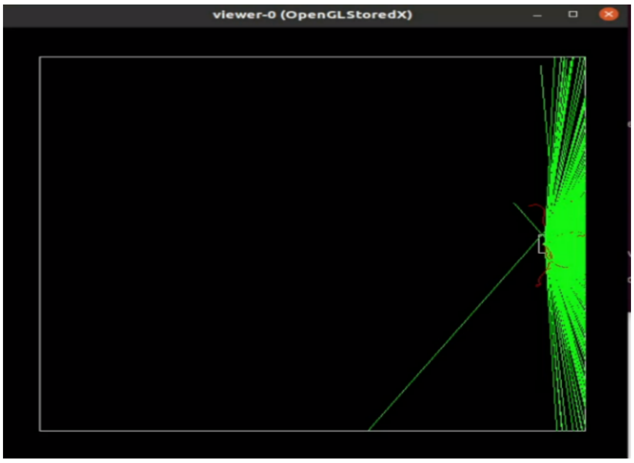

(a)

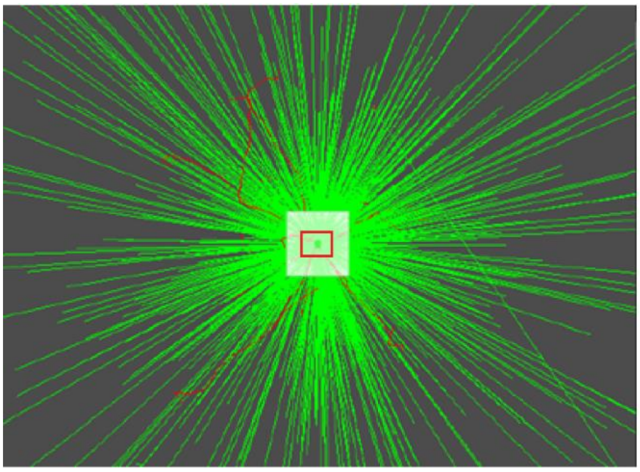

(b)

Figure 6.7 (a) Diffracted photons that represents the detector hits, (b) Spot for the focused rays on the detector plane (highlighted red) and the back scattered rays for the one Laue lens.

Histograms are graphical representations of the distribution of specific features or characteristics of produced particles, such as their energy, moments, or locations. Any discrepancies or inconsistencies in the histograms indicate issues with the simulated geometry, such as incorrect dimensions, placement, or materials. This is important to ensure a more accurate representation of the physical system under investigation. The source position is the most critical to confirm, followed by the detector position and the phantom position. As set up in the simulation of source position at the origin (0,0,0) mm, the predicted source hits X, Y and Z positions are shown in Figure 6.8a, Figure 6.8b, and Figure 6.8c, respectively. This is in agreement with the exact source generator location in GAMOS. Figure 6.9a and Figure 6.9b show the total number of deposited energies accumulated on the detector crystals and the distance between hits as selected to be zero (as defined in the configuration), respectively.

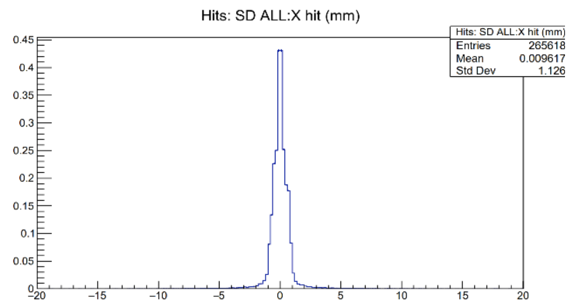

(a)

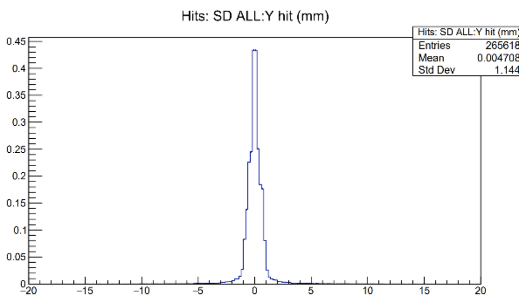

(b)

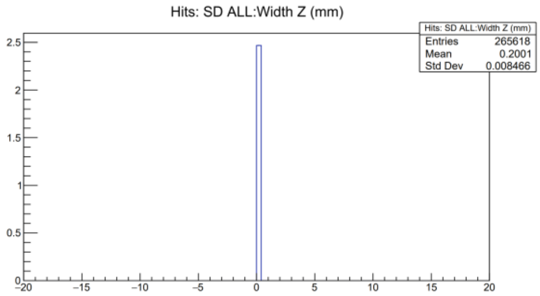

(c)

Figure 6.8 Hits energy deposition (a) X positions histograms, (b) Y positions histograms, (c) Z positions histograms.

Hits have positions in space, their Z and phi are their cylindrical coordinates. PHI and Width phishown in Figure 6.10a and Figure 6.10b, respectively. SD stands for the standard deviation of the quantity plotted. It is a measure of the dispersion of a set of particle interactions. "ALL PHI" refers to the histogram that includes data for all particle interactions. Phi represents the azimuthal angle, which describes the rotation angle around the z-axis in a cylindrical coordinate system. ***WIDTH PHI*** is the maximum distance between two of these energy depositions, energy depositions of the hits.

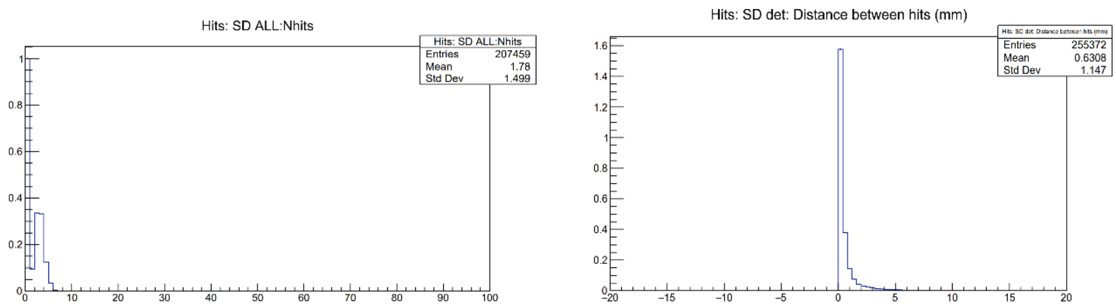

(a) **(b)**

Figure 6.9 (a) Number of hits on the detector, (b) The distance between hits selected to be zero.

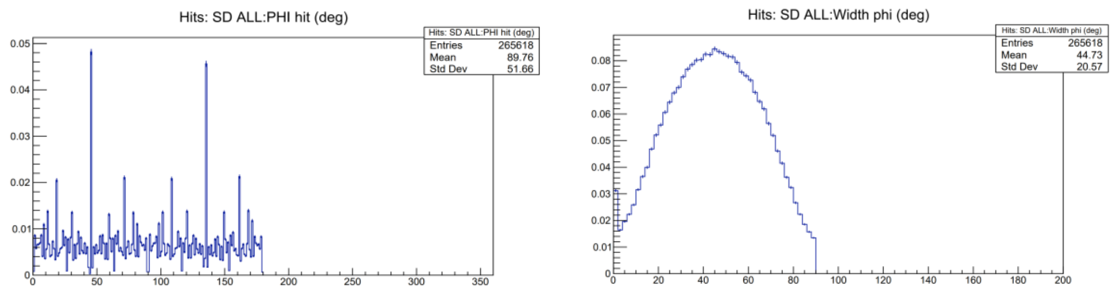

(a) **(b)**

Figure 6.10 (a) The phi angle of the hits' radiations. (deg), (b) The width of phi angle of the hits' radiations.

The primary objective of this Monte Carlo simulation is to generate a realistic environment that closely reflects real-world experimental conditions. This model simulates realistic physical interactions and takes into account all conceivable scattering and attenuation effects. Figure 6.11a shows the energy spectrum of the hits after encountering the scattering and attenuation effects, the dominant energy is at 40 keV. However, additional energy ranges from $40 - 130\ keV (0.04 - 0.13\ MkeV)$. Figure 6.11b shows the deposited energy for the simulated hits. The reconstructed impacts' energy spectrum after they have been subjected to scattering and attenuation effects; the primary energy is 40 keV. Additional energy, ranging from $40 - 130\ keV$, is available. These are reconstructed hits, so they merge the energy in a crystal of tracks for different events if they are in the measuring time window. So, we see 140 keV from one event and 40 keV from another. And the normalization is always per event (the default in GAMOS for all histograms). A "hit" is not the signal of one interaction. It is the energy collected in one crystal. So, there can be several interactions in one crystal, and all will be collected, and the energy summed up. Moreover, if we have a "measuring time" it means the detector cannot distinguish the events that arrive in that fraction of time as separated events so that all interactions of any of those events very close in time will be collected in a single hit. Apart from that, there is a second phase of "hits reconstruction," in which most detectors merge signals in a contiguous crystal to build a unique reconstructed hit (this is done because it is quite frequent that one particle leaves signals in contiguous crystals). So, a reconstructed hit can have energy much bigger than 140 keV: if several 140 keV gammas left signals in contiguous detectors in times that are separated less than the defined "measuring time".

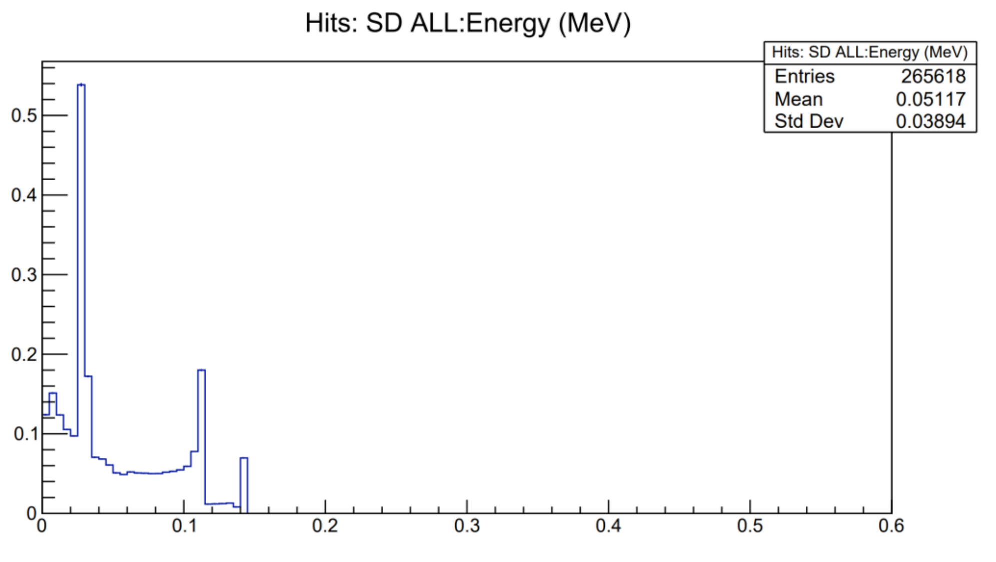

(a)

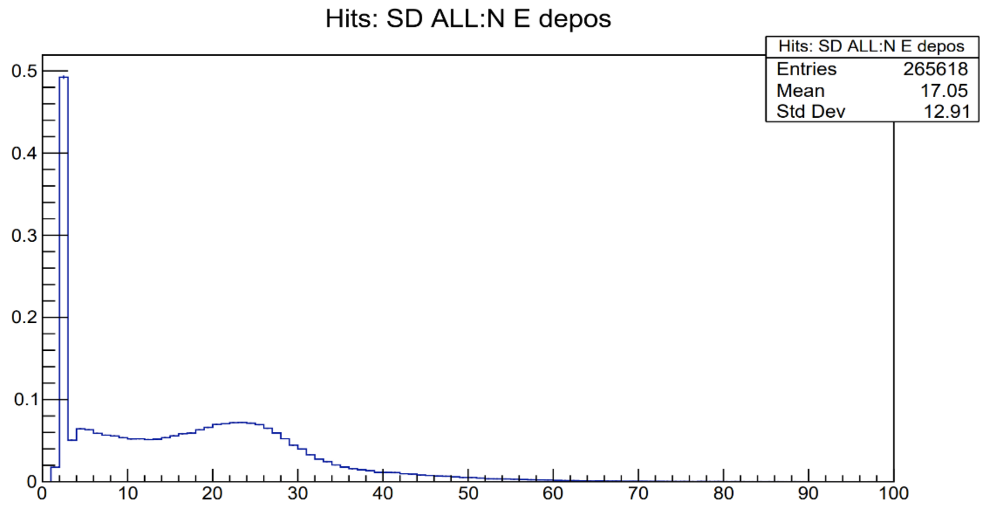

(b)

Figure 6.11 (a) The energy spectrum of the hits after Compton's, absorption, and scattering effects, (b) The deposited energy for the simulated hits, energies are stated in $MkeV$.

6.3.5 Reconstructed Hits

The predicted width R3 and width Z of the detector reconstructed hits are shown in Figure 6.12a and Figure 6.12b, respectively. The width R3 histogram represents the distribution of the radial distance or position in a three-dimensional Cartesian coordinate system, like the distance from the origin. The width Z histogram presents the distribution or variation of the Z-coordinate values of particles in a simulation. It represents the position and depth along the longitudinal axis of the detector geometry.

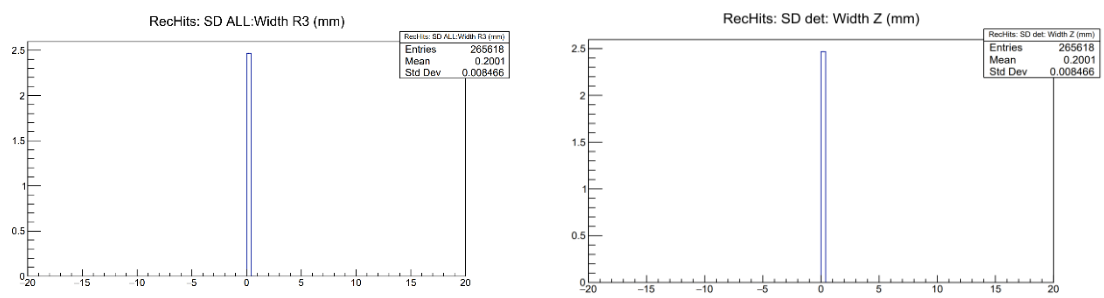

(a) **(b)**

Figure 6.12 Reconstructed hits energy deposition (a) Width R3 cylindrical positions histograms, (b) Width Z histograms.

Figure 6.13a shows the number of deposited energy and reconstructed hits. The energy deposition histogram of the ***Width phi***, is shown in Figure 6.13b. The ***Width phi*** histograms show the variation of the azimuthal angle, which is the angle of rotation around the z-axis in the cylindrical coordinate system. Figure 6.13c shows the energy spectrum of the reconstructed hits after encountering the scattering and attenuation effects. The dominant energy spectrum is $40\ keV$. However, additional energy ranges from $40-130\ keV$. The description of the energy response shown in Figure 6.13c is described in Section 6.3.4.

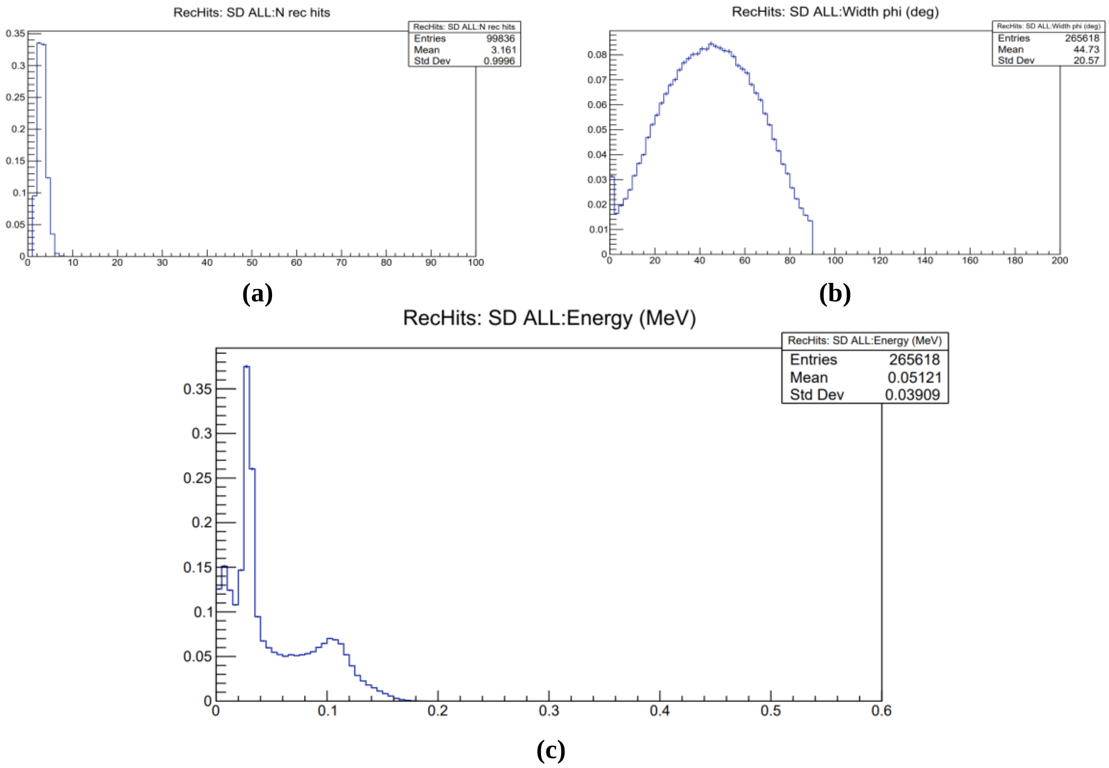

Figure 6.13 (a) Number of reconstructed hits, (b) The width of phi angle of the hits radiations in (deg), (c) The energy spectrum of the hits after Compton's, absorption, and scattering effects,

6.3.6 Step and Track Data Histograms

As set up in the simulation of source position at the origin, the histograms of event generator particles may confirm the generated radiation positions.

6.3.6.1 Step Data Histograms

Figure 6.14 shows the initial theta direction of the generated gamma rays. The diffracted gamma rays by the Laue lens are focused at a spot on the detector plane. The initial direction theta histogram shows the distribution of the polar angle theta. The polar angle theta is the angle between the particle's initial direction and the positive Z-axis in a Cartesian coordinate system. When the simulations show that the Z-direction (dirZ) is much more significant than the direction (dirX) and direction (dirY). Particles predominantly moving or being directed along the Z-axis suggests the initial directions of the particles are more aligned with the Z-axis compared to the X and Y directions, which indicates a focusing effect. This means that the particles tend to concentrate or converge towards the Z-axis as they move through the simulation. This confirms that the system configuration with the Laue lens truly focus the incident radiations.

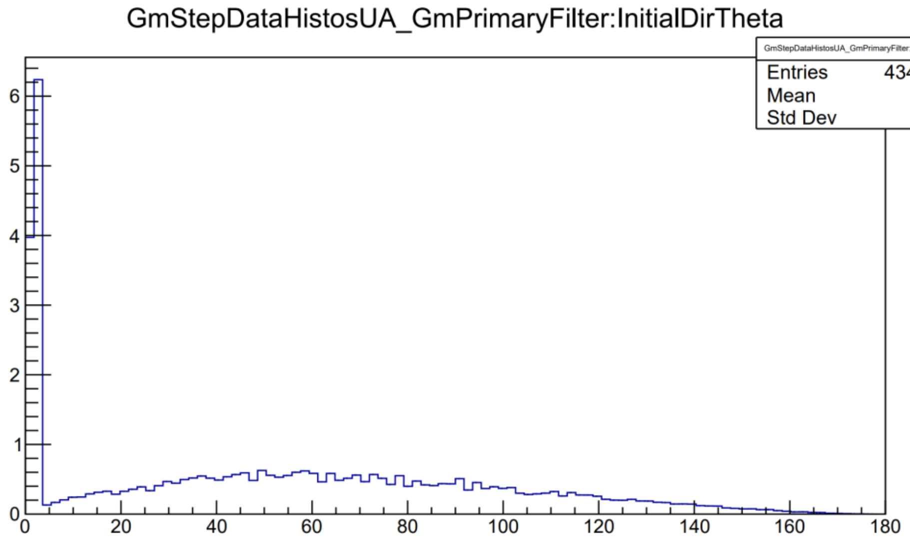

Figure 6.14 Step data for the initial gamma rays theta directions.

6.3.6.2 Track Data Histograms

Figure 6.15 shows the tracking histograms of the source data. The initial source X and Y positions are shown in Figure 6.15a and Figure 6.15b, respectively. The source energy of the simulated gamma rays, a peak at 140 keV, as seen in Figure 6.15c. The simulated source spot on the detector plane is shown in Figure 6.15d. The tracking histograms confirm the tracking of the source data starting at the origin as it was set in the experiment. Moreover, the focused photons all forming the spot on the detector plane.

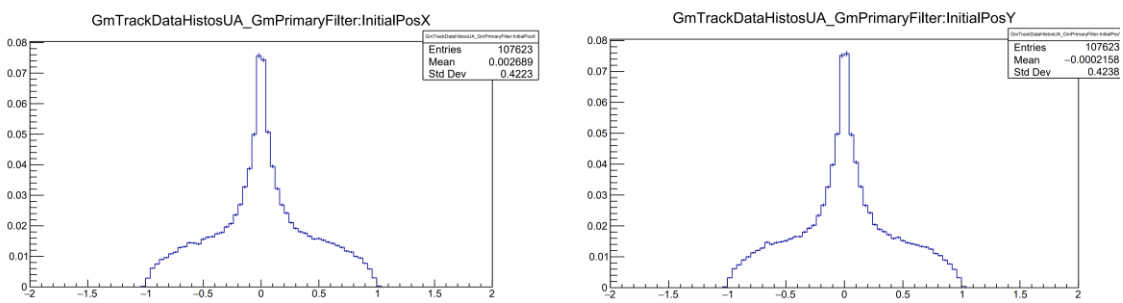

(a) **(b)**

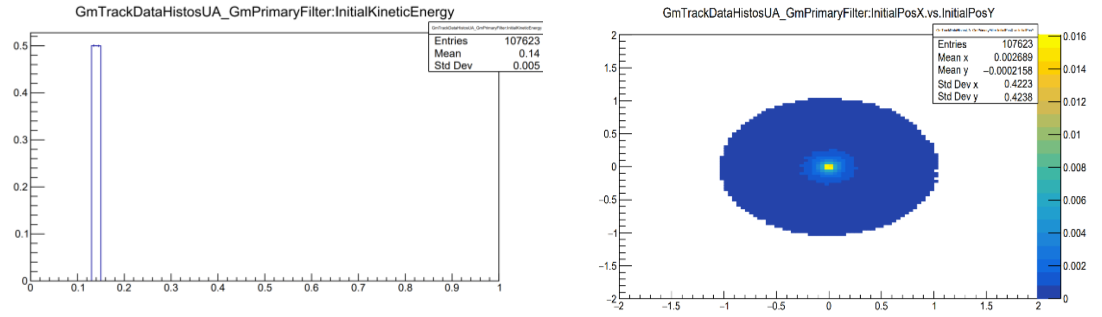

(c) (d)

Figure 6.15 Tracking histograms of the source data. (a) Initial source X positions of the simulated source, (b) initial source Y positions of the simulated source, (c) source energy of the simulated gamma rays, a peak at 140 keV, (d) simulated source spot on the detector plane.

6.3.7 Reconstructed Hits 3D Reconstruction

The generated GAMOS reconstructed hits were first exported as CSV files, then imported into MATLAB and saved in MATLAB's native MAT format. The GAMOS hits were reconstructed to generate the 3D images by utilizing the developed 3D reconstruction algorithm, which was discussed in Chapter 4. Figure 6.16a, Figure 6.16b, and Figure 6.16c show the 2D XZ, the 2D XY slice of the 3D reconstructed image, and the surface plane of the 3D volume of the reconstructed image, respectively.

6.4 Case Study with Detector Effects.

There are a number of detector effects that can be simulated. The detector effects are applied to the reconstructed hits. These hits are meant to simulate the digitization and reconstruction process that happen in the detector. These detector effects are:

- **Energy Resolution**

The NaI(TI) based SPECT system has a typical energy resolution of 10% FWHM 140 keV.

- **Dead Time**

A detector converts an energy deposit into an electronic signal in a finite amount of time. During that period, it is inactive and cannot account for any additional energy deposition. The activity should be low enough so that data loss because of camera dead time is negligible.

- **Energy Window**

A minimum hit energy threshold can be set to prevent hits from less energetic particles from being detected. The NaI(TI) based SPECT system has a typical energy resolution of 15% FWHM 140 keV and it allows good rejection of scatter photons. The advantage of NaI(Tl) detectors is that it has one of the best energy resolution values when compared with other available detector materials.

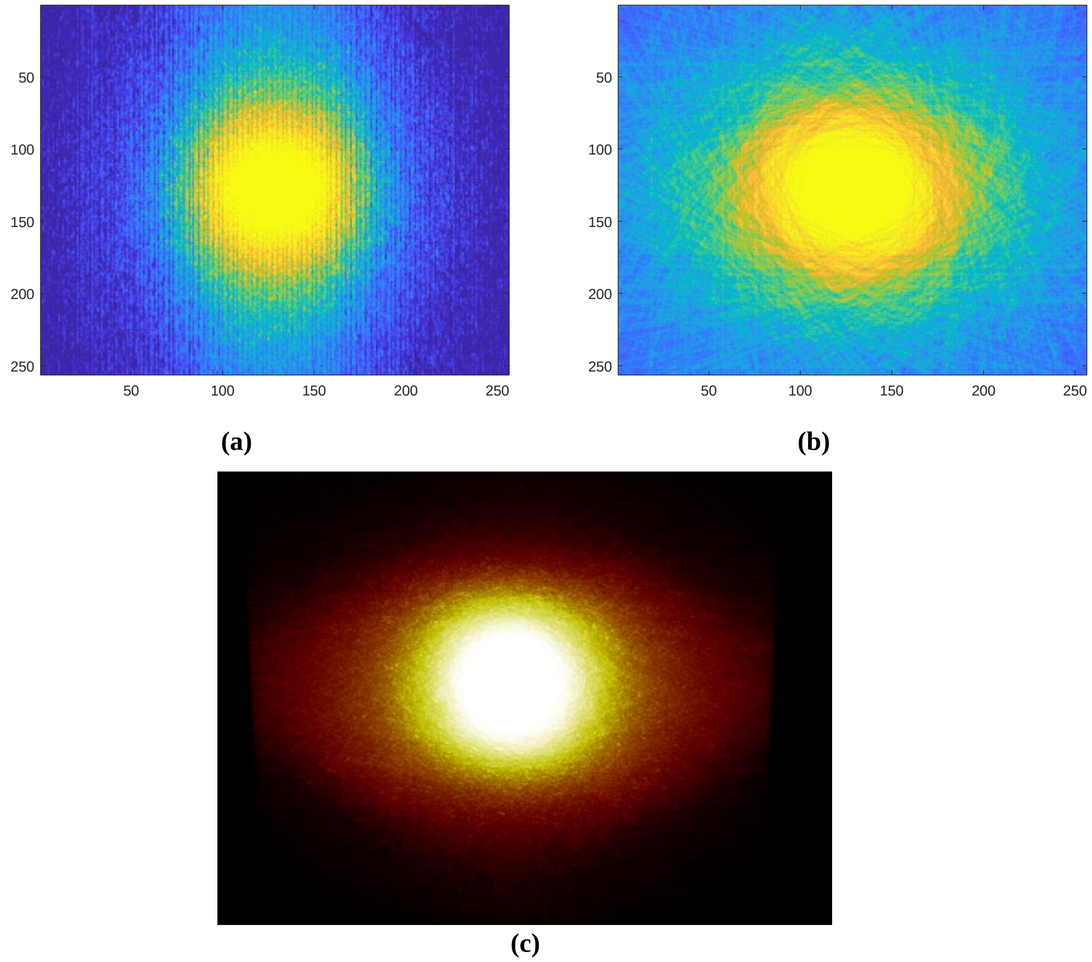

Figure 6.16 2D XZ slice of the 3D reconstructed image for one point sphere of 0.03 mm raduis, (b) 2D XY slice of the 3D reconstructed image for one point sphere of 0.03 mm raduis, (c) Surface plane of the 3D volume of the reconstructed image for one point sphere of 0.03 mm raduis.

6.4.1 Deposited Hits: Detector effects

The predicted hits X, Y and Z positions with applied detector effects are shown in Figure 6.17a, Figure 6.17b, and Figure 6.17c, respectively. Figure 6.18a and Figure 6.18b show the total number of simulated hits and the distance between hits as selected to be zero, respectively. The histograms of the hits PHI and ***Width phi*** are shown in Figure 6.19a and Figure 6.19b, respectively. Figure 6.20 shows the energy spectrum of the hits after encountering the scattering, attenuation effects, and the applied detector effects. The dominant energy is 40 keV. However, additional energy ranges from 40-130 keV. All the parameters mentioned here, and the corresponding histograms have been explained in detail in Section 6.3.4.

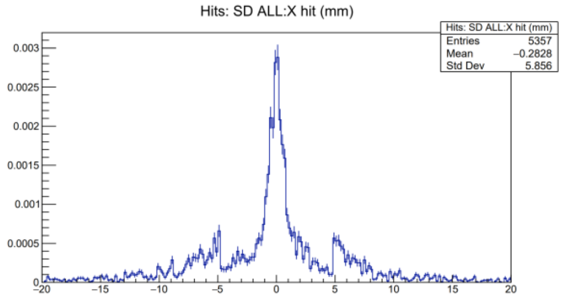

(a)

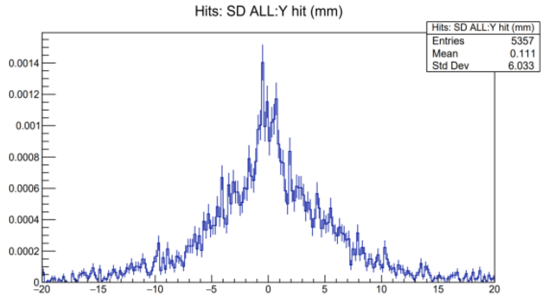

(b)

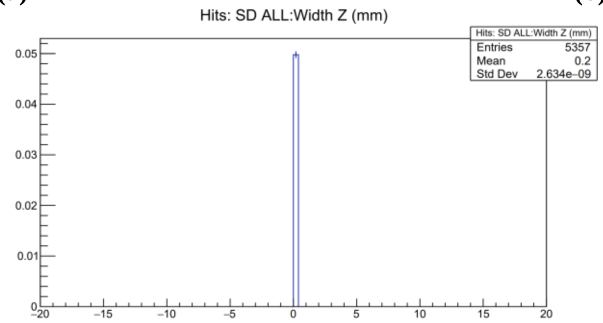

(c)

Figure 6.17 Hits energy deposition: Case study with detector effects (a) X positions histograms, (b) Y positions histograms, (c) Width Z histograms.

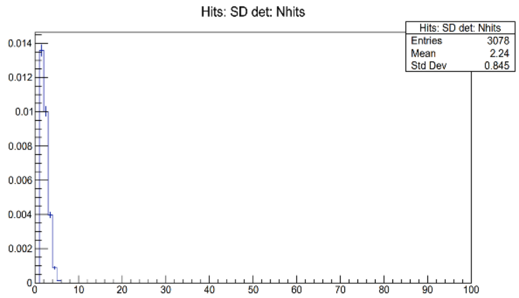

(a)

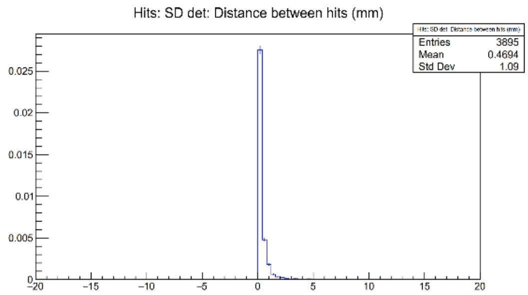

(b)

Figure 6.18 (a) Number of hits on the sensitive detector, (b) Distance between hits selected to be zero.

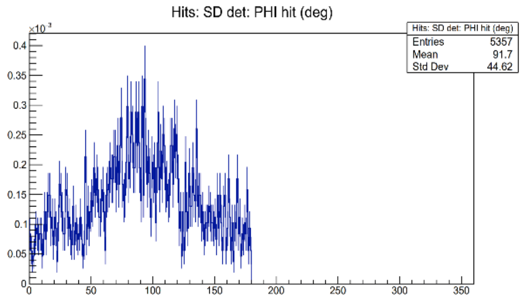

(a)

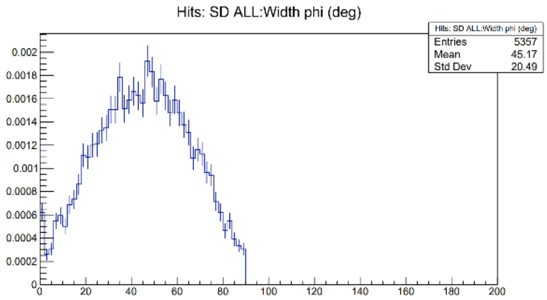

(b)

Figure 6.19 (a) Width of phi angle of the hits radiations in (deg), (b) Phi angle of the hits' radiations

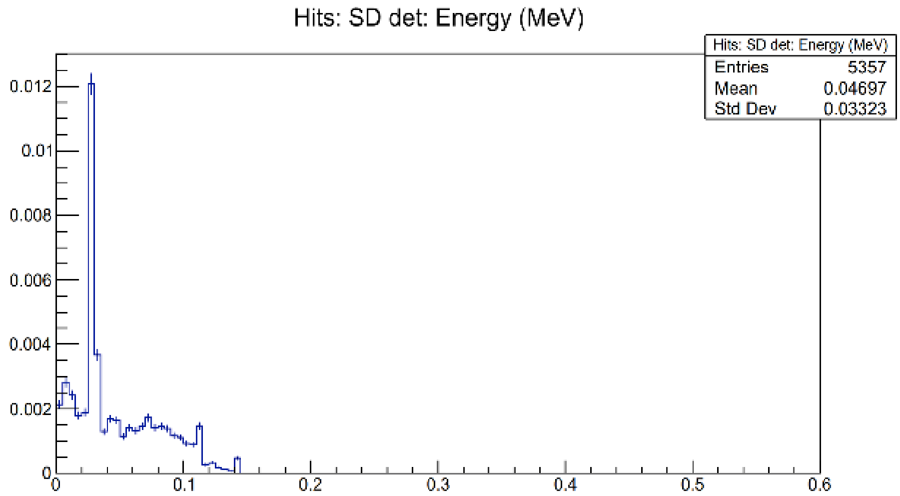

Figure 6.20 Energy spectrum of the hits after Compton's, absorption, and scattering effects.

6.4.2 Reconstructed Hit: Detector Effects

The predicted cylindrical and Z positions of the detector reconstructed hits with applied detector effects are shown in Figure 6.21a and Figure 6.21b, respectively. Figure 6.22a shows the number of simulated and reconstructed hits. The cylindrical representation of the hits is shown in histograms of the ***Width phi*** in Figure 6.22b. Figure 6.23a shows the energy spectrum of the reconstructed hits after encountering the scattering and attenuation effects. Figure 6.23b shows the projection image on the detector plane for the reconstructed hits. It is essential to assess the system impact of the detector effect on particle interaction for any design. Histograms with applying detector effects consider the defined detector effects, in our case, it includes, energy deposition, energy loss, detector response that occur when particle interacts with the detector. By looking at the histograms shown above with applied detector effect, it can be noticed that there are distortions and fluctuations resulting from the real interaction with the detector material. Also are shown deviations from the idealized ones (without applied detector effect). All the parameters mentioned here, and the corresponding histograms have been explained and discussed in detail in Section 6.3.4.

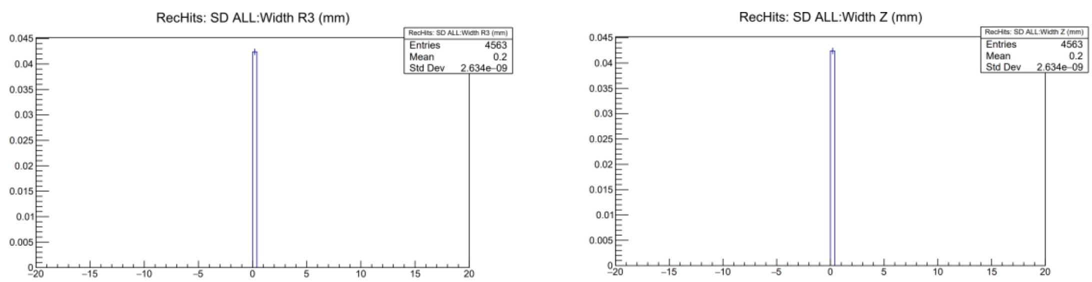

(a) **(b)**

Figure 6.21 (a) R3 cylindrical positions histograms, (b) Z positions histograms

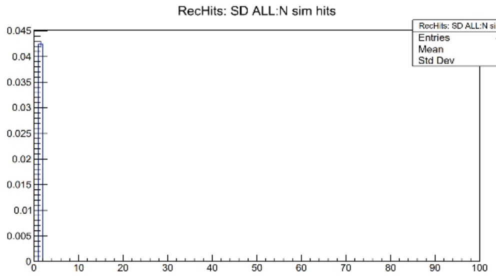

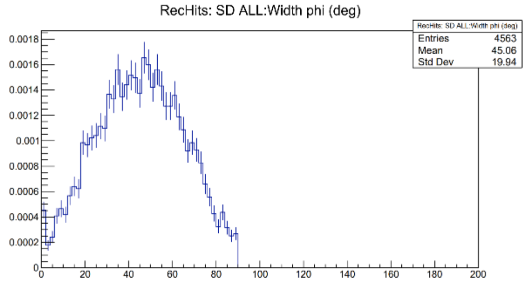

(a) **(b)**

Figure 6.22 (a) Number of reconstructed hits, (b) Width of phi angle of the hits radiations in (deg).

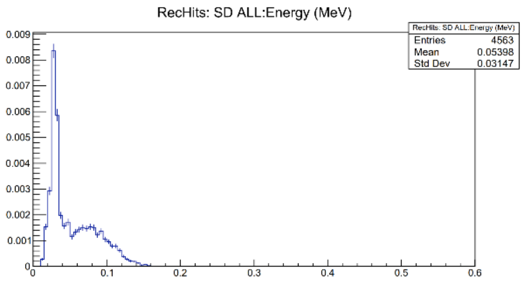

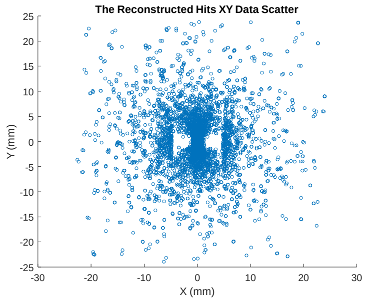

(a) **(b)**

Figure 6.23 (a) Energy spectrum of the hits after Compton's, absorption, and scattering effects, (b) Projection image of the reconstructed hits, shown in XY scatter.

6.4.3 Reconstructed Hits 3D Reconstruction: Detector Effects.

The generated GAMOS reconstructed hits with applied detector effects were converted into .MAT files and exported to MATLAB. The GAMOS hits were reconstructed to generate the 3D images by utilizing the developed LAUE reconstruction algorithm. Figure 6.24a, Figure 6.24b, and Figure 6.24c show the 2D XZ slice of the 3D reconstructed image, the 2D XY slice of the 3D reconstructed image, and the surface plane of the 3D volume of the reconstructed image, respectively. The 3D reconstructed images with the applied detector effect provide a more accurate representation of the system behaviour. However, it shows variations and distortions because of the defined detector properties compared to the figures presented in Section 6.3.4.

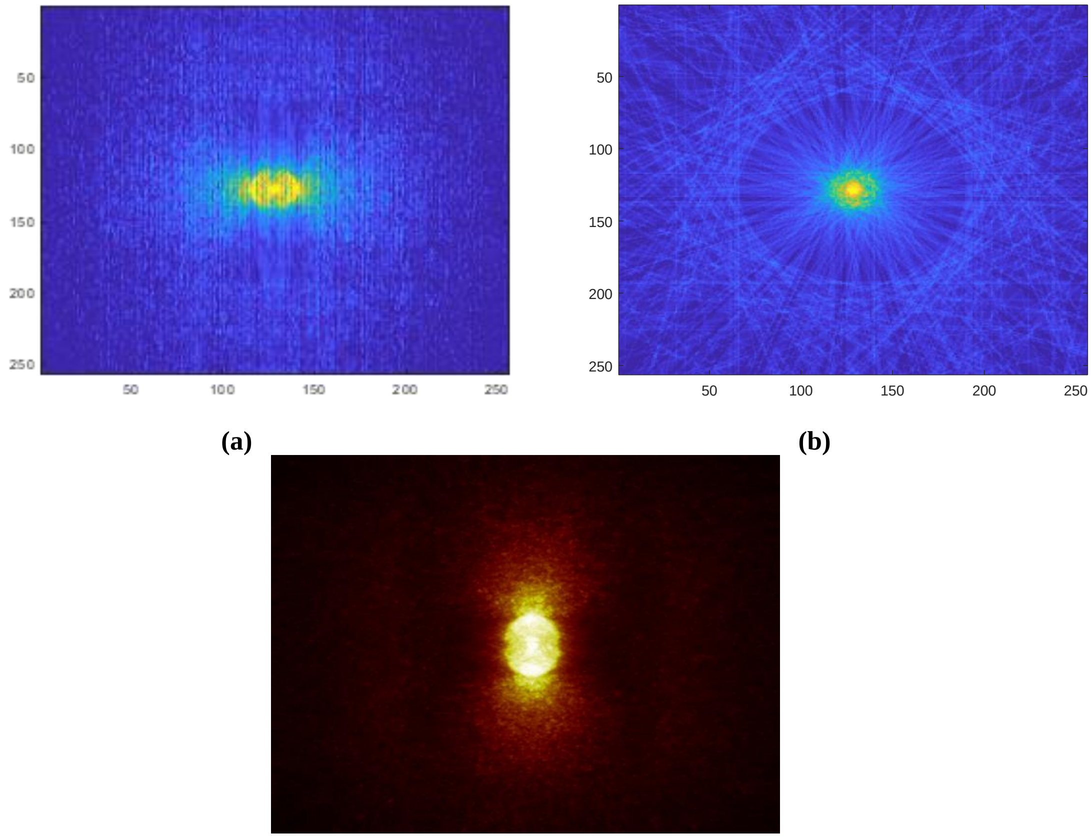

(a) **(b)**

(c)

Figure 6.24 2D XZ slice of the 3D reconstructed image, (b) The 2D XY slice of the 3D reconstructed image, (c) Surface plane of the 3D volume of the reconstructed image.

6.5 Case Study with Three-Point Source.

A three-point sphere phantom with 0.03 mm radius and 0.1 mm distances from centre to centre was used to run this case study in order to calibrate the obtained results in MATLAB and GAMOS. Figure 6.25 shows the particle tracking of the focused rays of the generator source and the spot of the deposited hits and the backscattered rays. The zoomed view of the deposited energy for the three-point sources and the spots of the deposited energy on the detector plane are shown in Figure 6.26a and Figure 6.26b, respectively. We can see that the three spheres are resolved in the projection image on the detector plane.

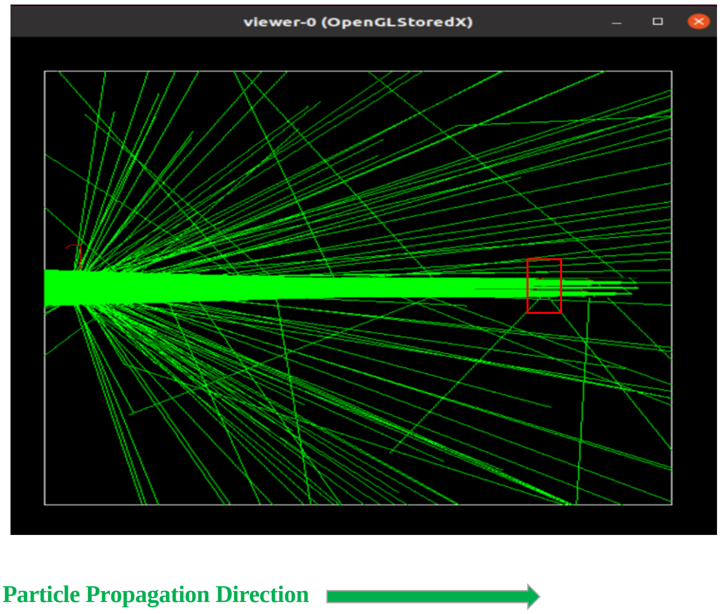

Figure 6.25 The particle tracking of the focused rays of the generator source, the gamma focus projects three distinct focused beams onto the small detector plan. The focused beams belong to the three spheres projections and converges to three small spots as noted red dots.

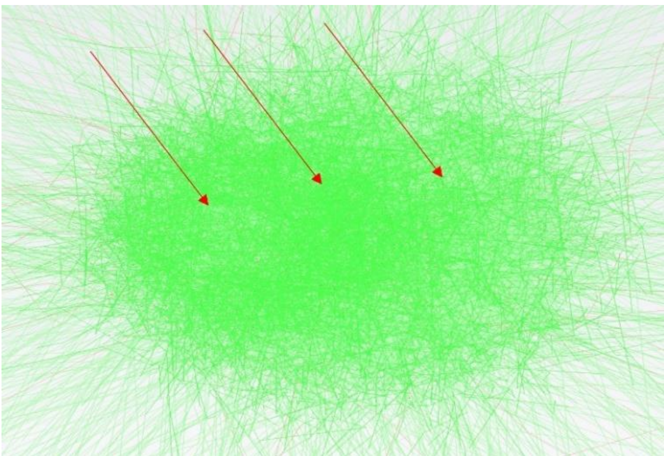

(a)

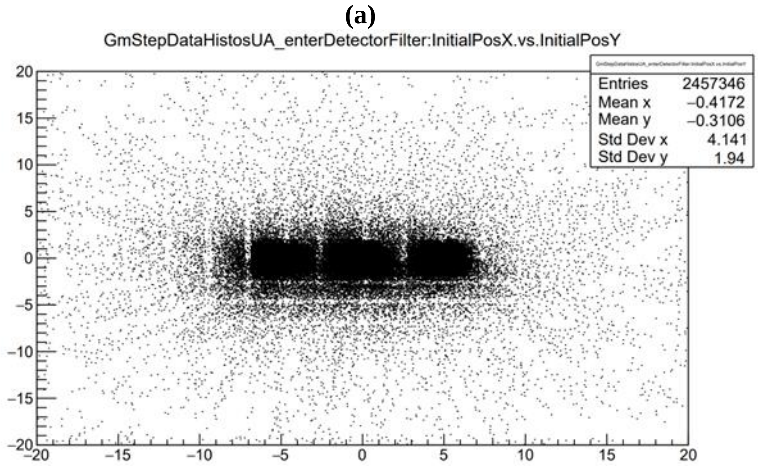

(b)

Figure 6.26 (a) Zoomed view for the deposited energy for three-point source using one Laue lens (the red arrows are pointing to the centre of each projection), and the backscattered rays due to detector back shielding, (b) deposited hits on the detector plane.

6.5.1 Deposited Hit and Track Data Results.

The histogram of the initial positions of X of the focused photons is shown in Figure 6.27a. The predicted source hits X positions are shown in Figure 6.27b. "InitiaPosX" refers to the initial position of the primary particles along the X-axis. It represents the X-coordinate of the primary particle's starting position in the simulation geometry (the initial photon locations defined in the TXT file that is used as the source generator).

The ability of the system to differentiate the associated peaks with each spot of the three spheres implies that generated histogram aligns with the expected or defined source generator data. In other words, the peaks observed in the system's histograms confirm that the emitted signals or radiation from each spot of the spheres correspond to the defined sources or properties for three-point source.

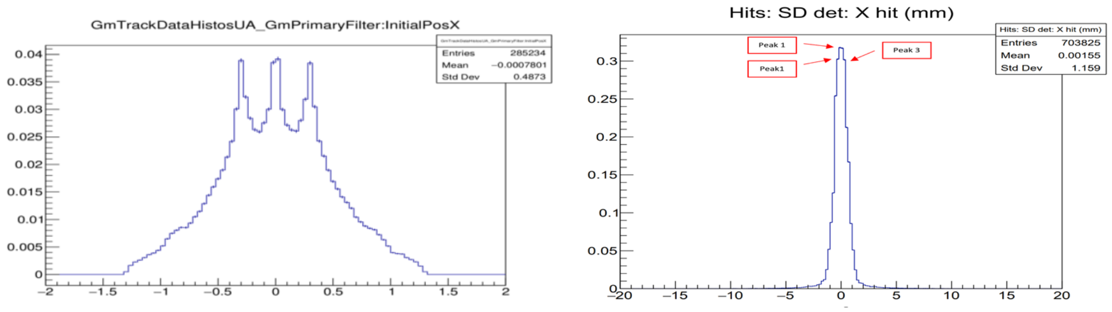

(a) **(b)**

Figure 6.27 (a) X positions histograms with three peaks presenting the distance between the sphere phantom of 0.1 mm. 3 peaks at the detector surface for the simulated hits, (b) Initial Y positions of X and Y.

6.5.2 Experimental Results

6.5.2.1 Reconstructed Hits 3D Reconstruction

Figure 6.28a and Figure 6.28b show the surface plane of the 3D volume of the 3D reconstructed image for one Laue lens and three-point sources without and with applied detector effects, respectively. As expected, the number of events detected in the ideal case is much higher than the ones that was detected using a detector with realistic detector effects applied. The energy window effect (specified range or window of energy levels is selected for data acquisition or analysis) by itself has a significant impact on the quality of the 3D reconstructed images; it basically filters out unwanted energies, so it selectively considers the interactions based on their energies. However, the image quality in Figure 6.28b is enhanced compared to the 3D reconstructed image without detector effects. This is due to filtering out of the background noise associated with the windowing effect.

(a) (b)

Figure 6.28 (a) Surface plane of the 3D volume of the reconstructed image for 1 Laue lens and three-point sources with no detector effects, (b) Surface plane of the 3D volume of the reconstructed image for one Laue lens and three-point sources with applied detector effects.

6.6 MATLAB Calibration Against GAMOS: System Resolution

To assess whether the resolution obtained in the idealized environment using MATLAB simulations (Chapters 4 and 5) can be replicated with the more realistic case studies, I sought to validate the results of the GAMOS study. Unlike the idealized setup in MATLAB, the GAMOS study incorporates the influence of real detector effects. In this section, the objective was to compare the attained resolution of the 3D reconstructed images between the two simulation approaches. Based on the respective 3D reconstructed images, the FWHM was 0.1 mm and 0.12 mm in MATLAB and GAMOS simulations, as shown in Figure 6.29a and Figure 6.29b, respectively. The close alignment of these figures further validates the reliability and effectiveness of the simulations performed using both MATLAB and the GAMOS toolkit.

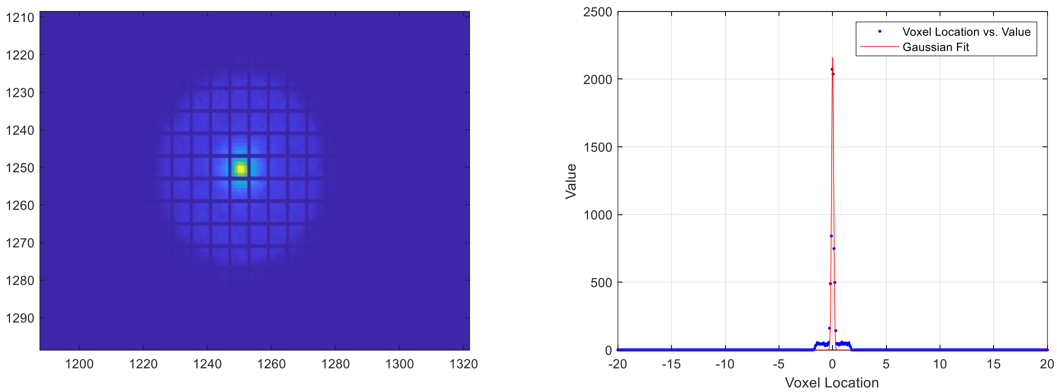

(a) (b)

Figure 6.29 (a) Projection image of the GAMOS hits, plotted using MATLAB, (b) Gaussian fitted point source of 0.03 mm radius of the GAMOS projection image.

6.7 GAMOS Simulations: Multi Lens Geometry with No-Detector Effects.

6.7.1 Geometry

The detector was modelled accurately in terms of sizes and materials. The scintillator is coupled to a light guide, which in turn is connected to a 100×100 array of $0.48\ mm \times 0.48\ mm$ Position Sensitive Photomultiplier Tubes (PSPMTs). The detectors are shielded by lead septa of $48\ mm \times 48\ mm \times 10\ mm$. The maximum active imaging region is 48 mm 48 mm, and the energy range detectable is 20 keV to 160 keV.

Figure 6.30a and Figure 6.30b show the front view and view of the modelled detector, respectively. Figure 6.31a, Figure 6.31b, Figure 6.31c, and Figure 6.31d show the particle tracking generated from the Laue lens, from and upper Laue lenses, from the three adjacent Laue lenses, and for large number of events generated from the nine Laue lenses, respectively. Figure 6.32a, Figure 6.32b, Figure 6.32c, and Figure 6.32d show the spot for focused rays on the detector plane and the back scattered rays for the centred Laue lens, for the second adjacent Laue lens, for three adjacent Laue lenses, and the side view for the focused gamma rays on the detector plane for the nine Laue lenses and the back scattered rays, respectively. These Figures provide a clear visual representation of the experimental results and provide valuable insights into the trajectory of photons through the lens arrangement, and it confirms having all the generated particles converting at the focal spot on the detect plane.

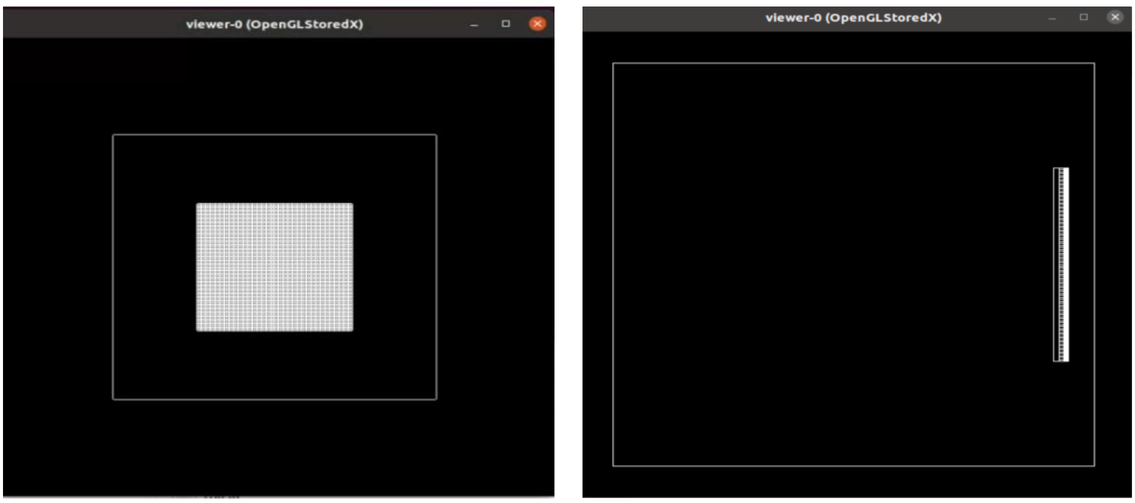

(a) **(b)**

Figure 6.30 (a) Front view of the modelled detector, (b) Side view of the modelled detector.

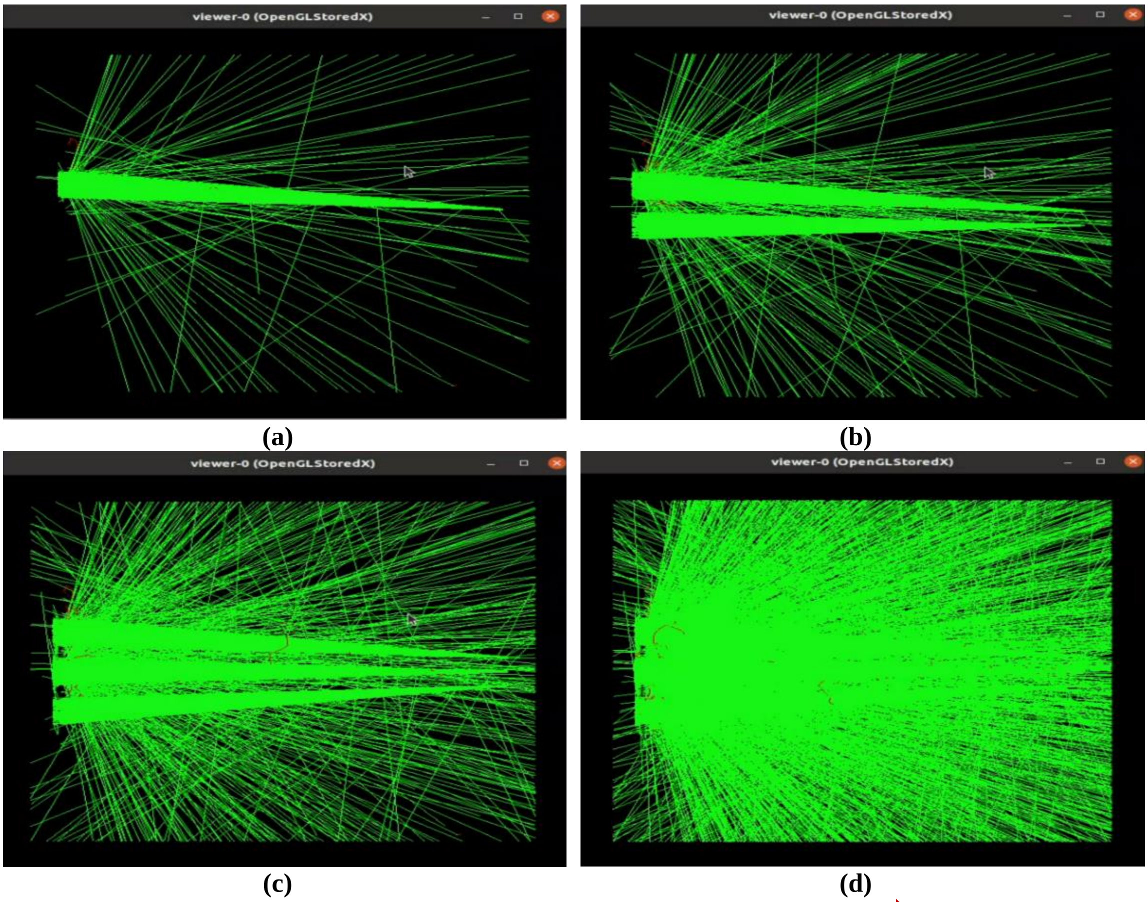

Particle Propagation Direction

Figure 6.31 Particle tracking of the focused rays (a) Particle tracking generated from the centred Laue lens, (b) Particle tracking generated from centred and the upper Laue lenses, (c) Particle tracking generated from the three adjacent Laue lenses, (d) Particle tracking of the focused photons for large number events generated from the nine Laue lenses.

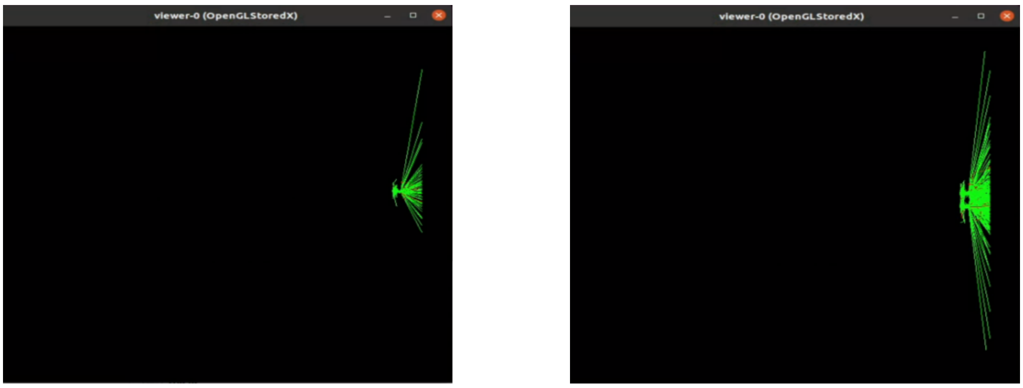

(a) (b)

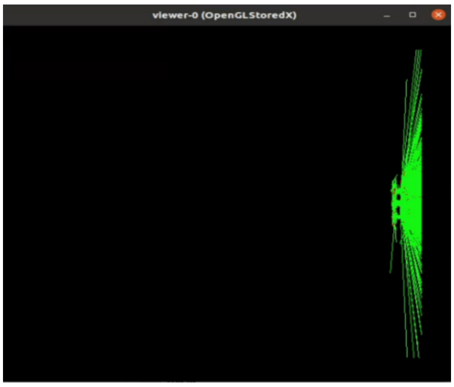

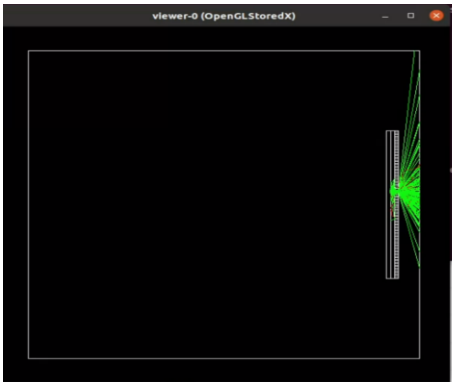

(c) (d)

Figure 6.32 (a) Spot for focused rays on the detector plane and the back scattered rays for the centred Laue lens, (b) Spot for the focused rays on the detector plane and the back scattered rays for the second adjacent Laue lens, (c) Spot for the focused rays on the detector plane and the back scattered rays for three adjacent Laue lens, (d) Side view for the focused gamma rays on the detector plane for the nine Laue lenses and the back scattered rays.

6.7.2 Deposited Hits and Reconstructed Hits

The tracks' energy deposited on the defined sensitive detector is saved as GMHits. The GmHit stores the number of variables as long int. Table 6.1 lists the stored variables of the deposited tracks on the sensitive detector. The detection of hits and their conversion to digital signals is highly dependent on the detector. Typically, digital signals are processed so that they become "reconstructed hits" that contain sensible factors such as energy, time, etc.

Table 6.1 Stored variable of the deposited tracks on the sensitive detector

Variable	Description
G4int the EventID	Identification of the touchable
G4int the EventID	Event number
G4double theEnergy	Total deposited energy on the sensitive detector

A reconstructed hit's energy equals the total of the hits' energies, while the position is equal to the weighted sum of the hits' positions. As a result, GAMOS offers a general class, GmVDigitizer. Since this conversion relies on the defined parameters of the detector, GAMOS provides only a generic class, GmVRecHitBuilderFromDigits. Another class, GmVRecHitBuilderFromHits, is practical if the user wants to directly change the hits into reconstructed hits. Each time a hit is added, the position of the previous hit is reassessed. The reconstructed hit position can be calculated in one of two ways: by default, it is specified as the barycenter, the average position of all hits weighted by their energy. If the parameter

/gamos/set is set to SD:RecHit:PosAtBarycentre:SDTYPE 0, GAMOS assumes that the reconstructed hit position corresponds to the hit with the maximum energy. In this work, GmRecHitBuilder1to1 was used; where two hits are never combined, resulting in constructing a reconstructed hit for each hit. Figure 6.33a and Figure 6.33b show zoomed views for the deposited hits on the detector plane and the backscattered rays for two Laue lenses and five Laue lenses, respectively.

(a) (b)

Figure 6.33 Zoomed view for the deposited hits on the detector plane and the backscattered rays. (a) One point source and two Laue lenses, (b) One point source and five Laue lenses.

6.7.3 Deposited Hits

Figure 6.34a, Figure 6.34b, and Figure 6.34c show the X, Y, and Z histograms, respectively. The X and Y hits histograms show three peaks with significantly higher counts behind the centred Laue lens. The distance between the Laue lenses is $42\ mm$, which is also equal to the lens diameter; this is reflected in the same distances measured between the different peaks in the histograms. The higher peaks associated with the centred lens compared to the adjacent ones reflect the decrease in the sensitivity of the process when the radiation is captured from off-axis directions. These results suggest that the arrangement of the lenses and the associated geometry have a direct impact on the distribution of hits in the X and Y directions. The higher counts associated with the centred lens, in comparison to the adjacent lenses, highlight the decrease in sensitivity when capturing radiation from off-axis directions.

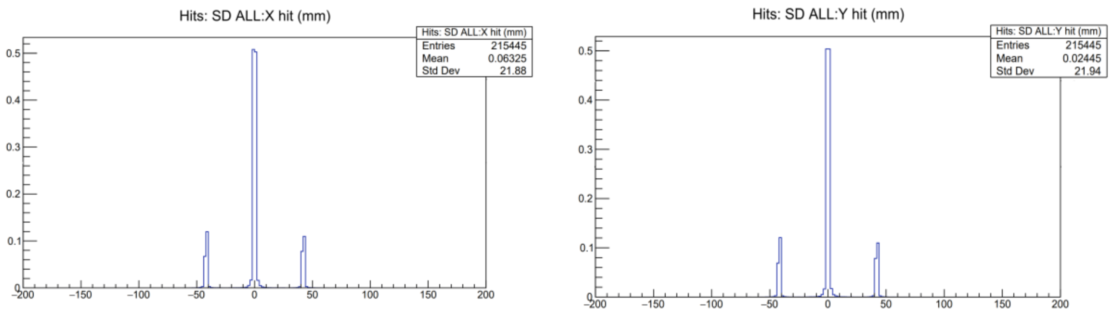

(a) (b)

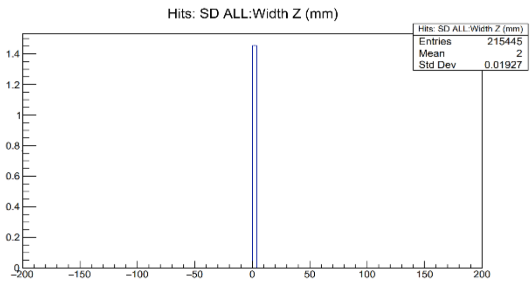

(c)

Figure 6.34 Hits energy deposition (a) X positions histograms, (b) Y positions histograms, (c) Z positions histograms,

6.7.4 Reconstructed Hits

Figure 6.35 shows the reconstructed hits' [ii] projection image on the detector plane. The projection image captured on the detector plane exhibits the presence of precisely nine discernible spots, with each spot representing the focal point of an individual Laue lens. These nine Laue lenses are spatially arranged in a planar configuration.

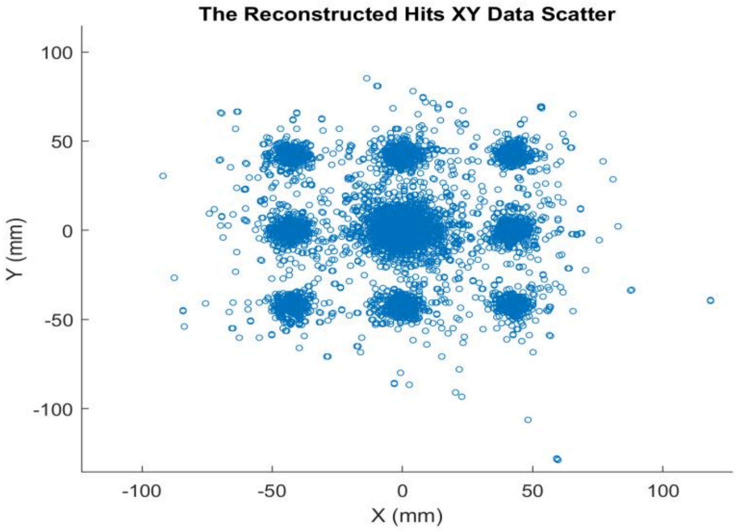

Figure 6.35 Projection image of the reconstructed hits, shown in XY scatter.

6.7.5 3D Reconstruction

Initially, the 3D reconstruction algorithm that I developed for the multi lens-based SPECT, discussed in Chapter 5, was used to reconstruct the multi Laue lens hits that were generated using GAMOS half process simulations, but did not return any meaningful results. Consequently, I had to revise the simulations and the 3D reconstruction algorithm, as follows. The work conducted in this chapter deals with a real pixelated detector in contrast to the

[ii] Reconstructed hits: Refers to the detection and localization of particles or radiation within a particle detector system.

simulations I conducted in Chapter 4 based on MATLAB using an idealized environment and an ideal detector. Thus, to make it work for the case studies presented in this chapter, I added the exact pixel sizes designed in the GAMOS detector simulations. Moreover, I updated the code to convert the detector hits into pixilated images and then reconstruct and perform the 3D reconstructions.

6.7.5.1 Deposited Hits Histograms

Figure 6.36 shows the X hit positions on the detector plane for the multi Laue lens case study with a three-point source phantom. The projection behind each Laue lens represents three focused projections. The distance between each spot is $5\ mm$, the distance between the point sources from centre to centre. The focused projection of each Laue lens is distanced $42\ mm$ from each other as the diameter of the Laue lens is equal to the pitch ($42\ mm$). The geometry of the multi lens is the same as in Figure 5.16.

6.7.6 Validation

6.7.6.1 GAMOS Hits 3D Reconstruction

Figure 6.37 shows the XY slice of the reconstructed image from an array of Laue lenses and three-point sphere using the initial LAUE 3D reconstruction algorithm. It is clear from the generated image that the three-point sphere phantom needed to be appropriately reconstructed. As I mentioned in Section 6.7.5, I had to modify the 3D reconstruction algorithm. I added the precise pixel sizes specified in the GAMOS detector simulations. Moreover, I made adjustments to convert the detector hits into pixilated images, enabling the subsequent reconstruction and analysis of 3D images.

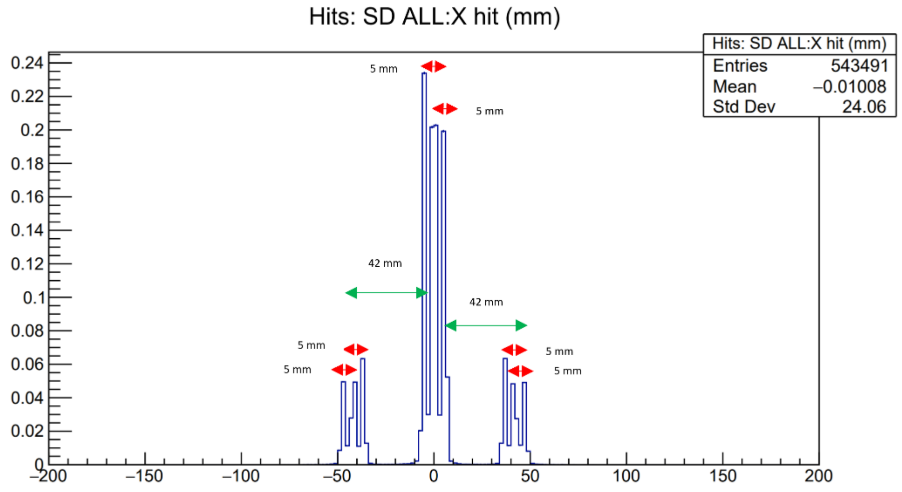

Figure 6.36 X hits positions for multi Laue lens with three-point source case study, the focused spots behind the three Laue lenses represents the projection of the three-point sources placed at 5 mm from centre to centre, pitch were set to zero.

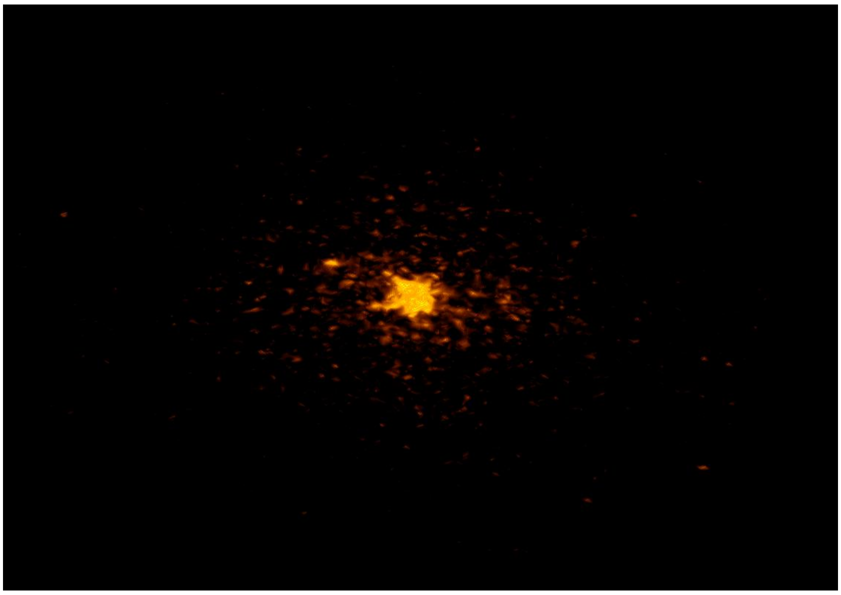

Figure 6.37 3D XY slice of the reconstructed image for an array of lenses and three-point sources. The spheres were not properly reconstructed, and no useful information was reconstructed.

Figure 6.38 shows the pixelated images generated from the GAMOS detector hits with 10° step angle between each frame. Figure 6.39a, Figure 6.39b, and Figure 6.39c show the 2D YZ, XY, and XZ slices of the 3D reconstructed images using the revised LAUE reconstruction algorithm, respectively.

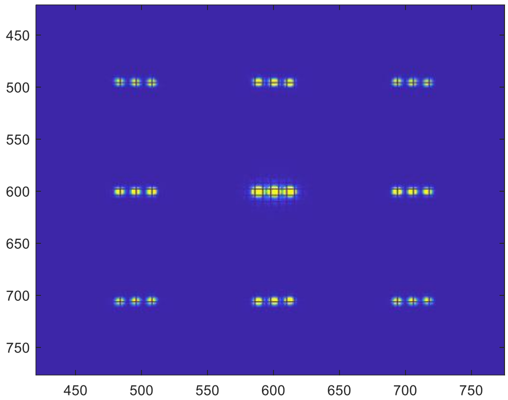

0 °

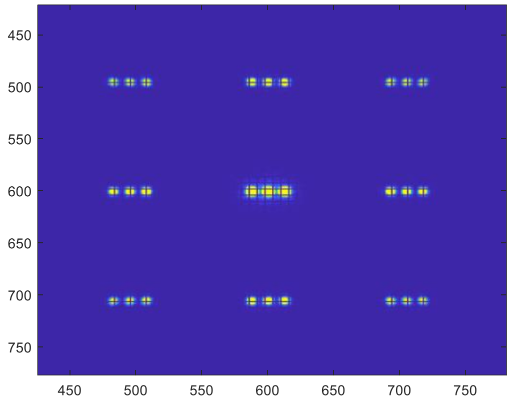

10 °

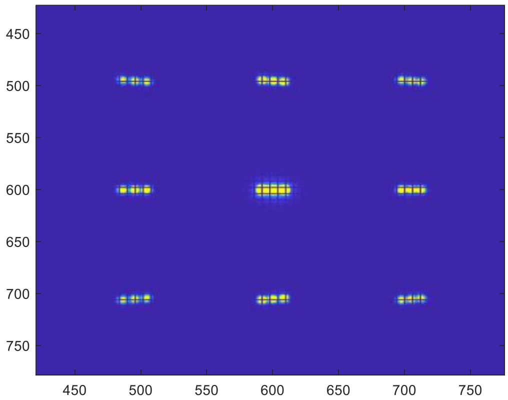

20 °

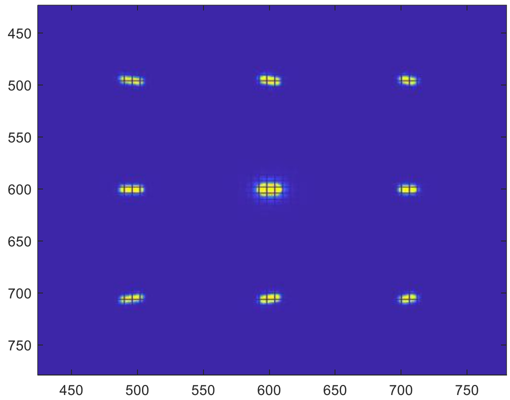

30 °

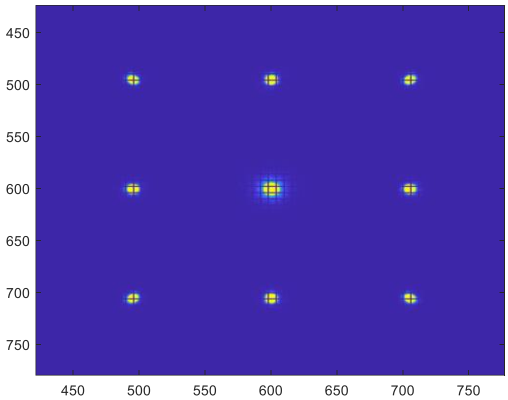

40 °

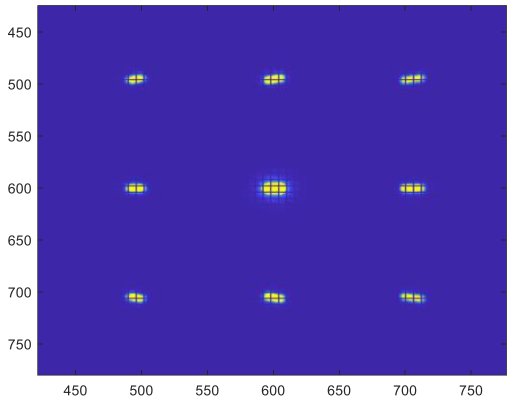

50 °

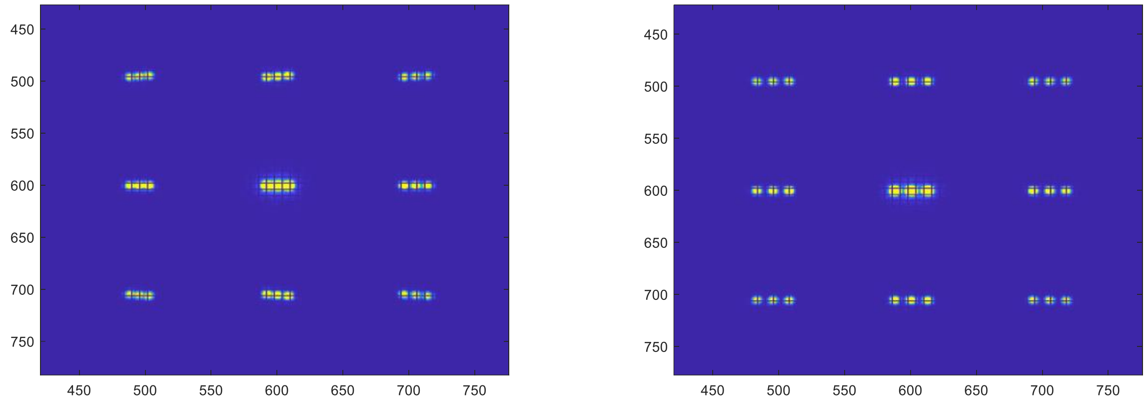

60 ° **70 °**

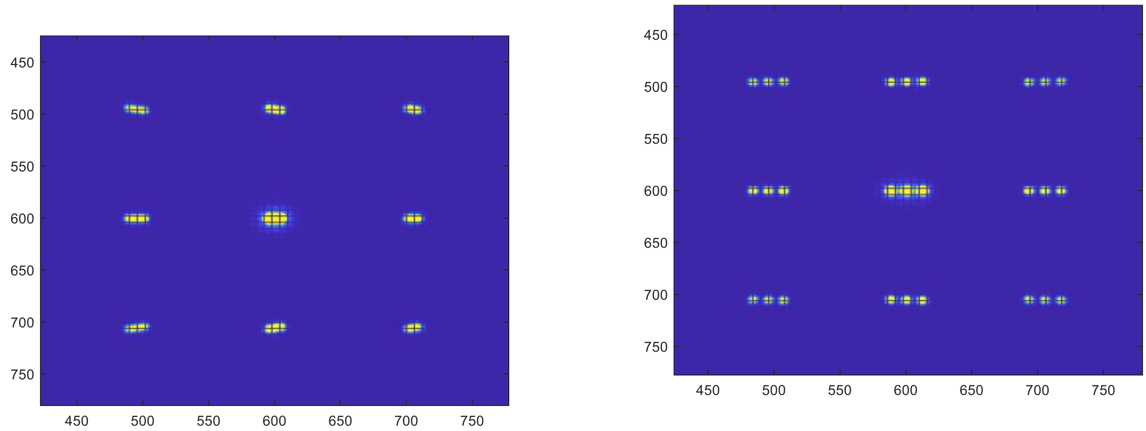

80 ° **90 °**

Figure 6.38 Pixelated projection images generated from the GAMOS detector hits. The x-axis represents the column index, and the y-axis represents the raw index of the pixelated projection image. The step angle is 10° between each frame.

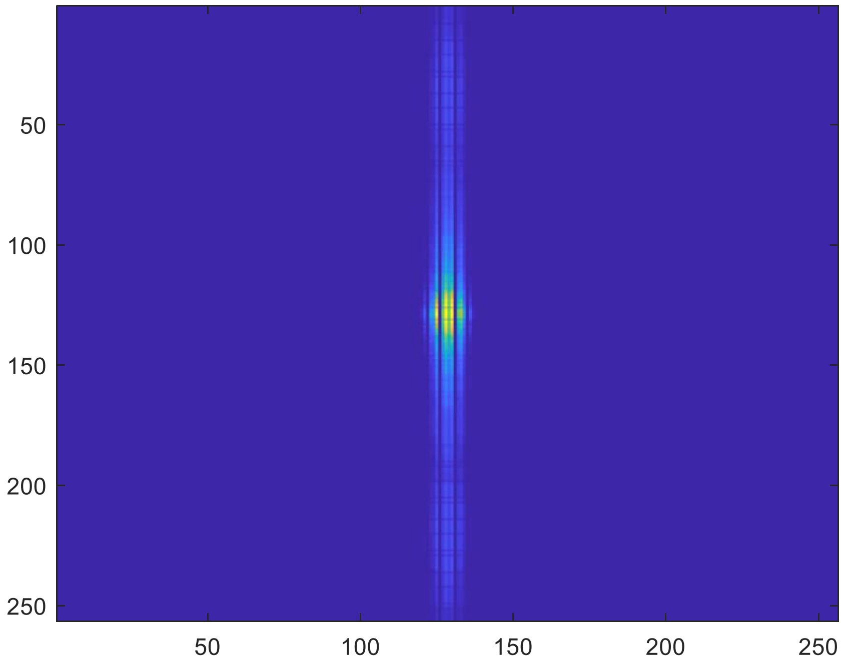

(a)

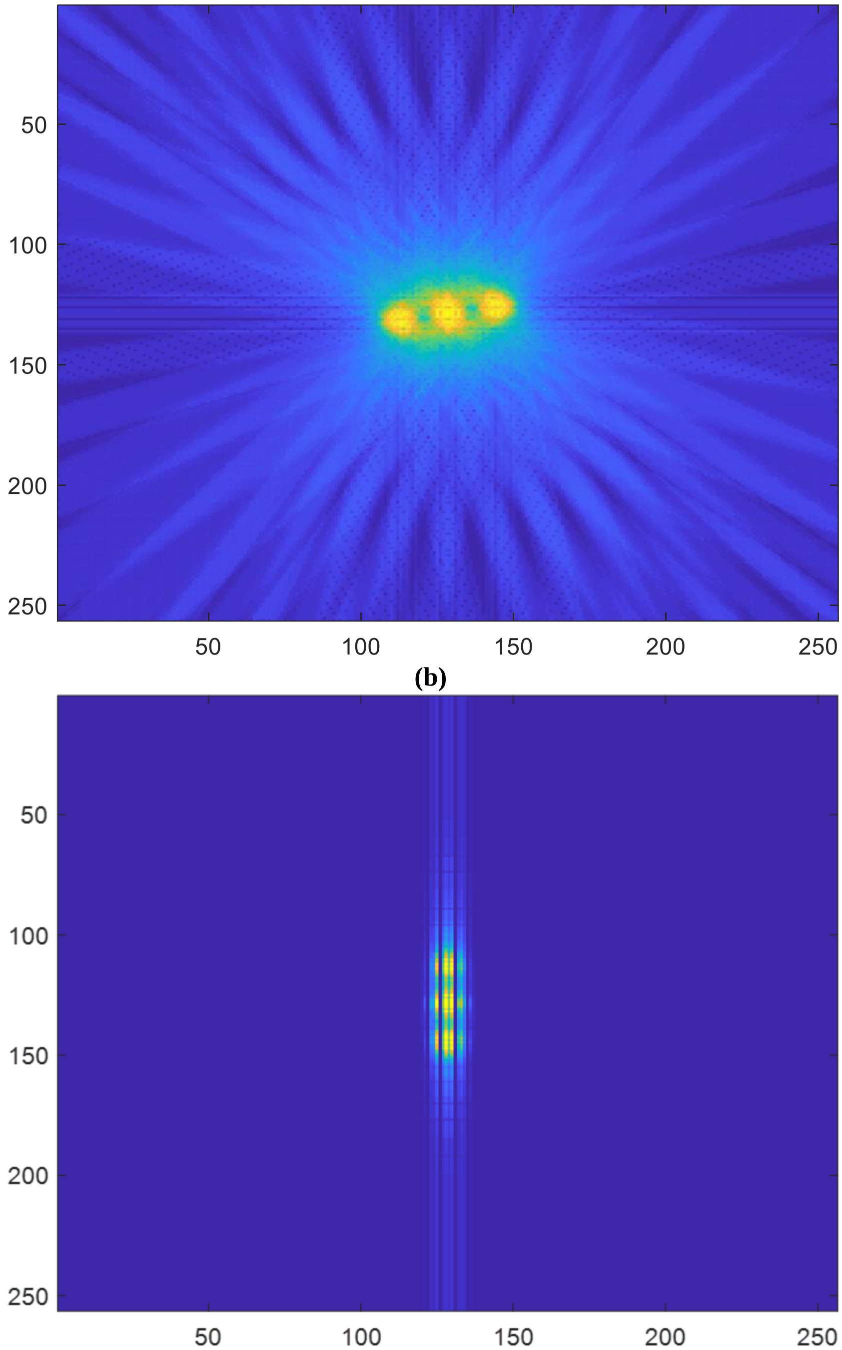

(c)

Figure 6.39 3D reconstruction of the generated GAMOS hits. (a) 2D YZ slice of the 3D reconstructed image, (b) 2D XY slice of the 3D reconstructed image, (c) 2D XZ slice of the 3D reconstructed image. The X and Y measurements are in mm.

6.8 Chapter Summary

6.9 In this chapter, I aimed to assess the validity of the claim stated throughout this thesis by expanding on the prior work and analysing the response of an actual detector design to the focused

Laue lens gamma rays in a stable Monte Carlo setting specialized for medical physics applications. However, none of the available Monte Carlo toolkits provides the simulation of wave-based properties since the diffraction process is not implemented in either. To this end, I proposed an alternative method to simulate the effect of focusing the gamma rays at the sensor plane and simulate detector response due to the focused projection in GAMOS/GEANT4, besides the MATLAB Monte Carlo simulations. I developed a customised Monte Carlo simulation in MATLAB that simulates the Laue lens behaviour placed at the SPECT pinhole and then generated the coordinates and the momentums of the diffracted photons. Those coordinates and momentums were used to set up the TXT files, which were imported to GAMOS and served as the source generator input. Moreover, the histograms of event generator particles may confirm the generated radiations positions were generated. Then, the hits were exported as CSV files and imported to MATLAB. The GAMOS hits were reconstructed to generate the 3D images by utilizing the developed LAUE reconstruction algorithm. To simulate a real detector behaviour, a number of detector effects were included to reflect the real detector design. Then the 3D image reconstruction algorithm was applied to the deposited and generated hits with imposed detector effects. The ability to replicate and confirm experimental outcomes, as seen in the consistent results in the previous chapters, adds a layer of confidence to the results,. At the same time, the validation

process ensures that our methods and data align with established standards and expectations. Acknowledgement

This chapter articulates and expands on work for which the concepts and basic findings were partially published in:

1. A. Barhoum, M. Tahtali, R. Camattari, and Susanna Guatelli " Ultra-High-Resolution Lens Based SPECT Based on Laue Gamma Diffraction: A First GAMOS/GEANT4-MATLAB Monte Carlo Study" Physica Medica (2023). This article is under: (Under Review).
2. A. Barhoum, M. Tahtali, R. Camattari, and Susanna Guatelli " Feasibility Study of Multi Lens-Based SPECT with a Dedicated Laue Reconstruction Algorithm: A First Monte Carlo Study" Scientific Reports (2023). This article is under: (Under Review).

7. Design Foundation and Implementation of the First Set of Models in GEANT4 for Laue Lens Diffraction: Laue lens Modelling

For many years, "theory" and "experiment" were the driving forces behind the scientific enquiry. However, in recent years a new technique has come into its own: simulation. Many fields of science and engineering have been innovated by computer simulations, and their increased use as a substitute for traditional, practical learning interactions with physical systems has been made possible by significant improvements in computer processing speeds and access to computing resources. Astrophysical environments, while offering unparalleled opportunity, are not without their challenges. Physics is an experimental science, and as such, the empirical basis for any physical theory is essential [344]. With advancements in computer and network technology and codes for energetic particle transport, thorough Monte Carlo (MC) simulation seems no longer a technique confined to research scientists but is increasingly being used as a critical engineering tool and would contribute to modelling new technologies in physics [345].

7.1 Introduction

Laue's discovery of X-rays diffraction paved the way for two new disciplines of physics, crystallography and X-rays spectroscopy [346, 347]. These findings have generated a wave of new gamma rays' facility proposals and programs. Presently, great interest and scientific expertise are available to push forward new technologies in gamma rays lenses [348]. Laue gamma diffraction has recently attracted considerable attention as a powerful method for developing a high-energy rays focuser. So, our team (me and the supervisors) was also intrigued with the challenges of manufacturing a functional Laue lens for medical applications.

This chapter is structured as follows: In Section 7.1, an introduction sets the context and outlines the scope of the chapter. Section 7.2 focuses on investigations related to the manufacture of the Laue Lens, exploring the various aspects and considerations involved in its production. In Section 7.3, the GEANT4 toolkit is introduced, highlighting its flexibility and discussing its lack of diffraction functionality. Section 7.4 delves into the specific version of GEANT4 used in the study, along with available resources related to it. The implementation of the Laue lens gamma diffraction process in GEANT4 is detailed in Section 7.5. This includes the diffraction code, requirements for developing the diffraction example in GEANT4, and the steps involved in the example development, such as geometry setup and physics list. Simplifications and assumptions made during the implementation are discussed in Section 7.5.3, followed by volume definition and input parameters in Section 7.5.4. Code flexibility is explored in Section 7.6, explicitly addressing the scale factor and detector position. Section 7.7 discusses the results obtained from the advanced example and guidelines on how to visualize these results effectively. Section 7.8 provides instructions on running the GEANT4 diffraction example, covering the steps for compilation and visualization. Section 7.9 focuses on the designed experiments conducted using GEANT4. Section 7.10 offers a discussion of the results and limitations, providing insights and observations derived from the study. Finally, Section 7.11 concludes the chapter with a summary, highlighting the key points and findings.

7.2 Investigations about Manufacturing of the Laue Lens

Conducting physical experiments to study the Laue lens behaviour seems to be a fundamental tool for understanding the physical issue and elucidating the main concept in gamma diffraction [320]. However, Laue lens manufacture is quite challenging as it requires high precision manufacturing techniques to position and align diffractive crystals of various elements [321].

I stand in need of manufacturing the Laue lens to test the proposed design using physical experiments. However, there are always two sides to every story. The main challenge lies in developing a fabrication method for a miniaturized version of the Laue lens where the crystal mosaics are deposited using advanced fabrication methods. That is why I sought collaboration partners to develop the fabrication method. I was looking to fabricate a cm-size Laue lens and, ultimately, an array of such lenses. After several meetings with experts in nanotechnology fabrication, I have been told that the maximum thickness they can achieve is $200\, nm$. Most of the structures they use (which are designed for the visible spectral range) are relatively small, and the thicknesses they used were up to $1\mu m$ (each layer), but the envisioned Laue lens thickness is in the order of $2 - 11\ mm$. That was the first obstacle.

The good news is that it is not necessary to use ablation to transform an amorphous phase into a crystalline one, thus I do not need to fabricate the crystals. There are experts in this field who manufacture the crystals. There are several companies like Mateck, Advatech, Epic-crystal, and Saint-Gobain who offer these crystals commercially.

Nonetheless, fixing all the crystals in a frame is a challenging task. Also, maintaining the crystals at the right angle and alignment of the X-rays requires high precision in the diffraction plane in the order of $10\ \mu rad$, which is very demanding.

7.2.1 What's Next?

The Laue lens couldn't be manufactured due to the reasons I stated in Section 7.1. A readily feasible alternative to physical experiments are computer simulations in a stable state-of-the-art high-energy physics simulation environment such as GEANT4. However, the Laue diffraction process has not been implemented in any of the available Monte Carlo simulation platforms so far. In other words, the wave nature of the Laue diffraction phenomenon cannot be simulated accurately in any of the available Monte Carlo Toolkits. This is one of the primary obstacles researchers encounter in their attempts to model the Laue lens in a realistic particle tracking environment.

The contribution presented in this chapter was basically inspired by the core aim of this research, and it is directly related to the argument being made throughout the thesis. To examine the authenticity/validity of the argument stated throughout the thesis, it was necessary to study the designed system's behaviours with the complete diffraction process in a Monte Carlo simulation toolkit. The lens-based SPECT analysis relies on simulating and modelling the gamma focusing by the diffraction process. However, as was mentioned in Chapter 6, the effect of wave nature cannot be simulated in any of the available Monte Carlo toolkits. Based on the outcomes of the conducted experiments on the proposed lens-based SPECT, I developed a particle transport code for modelling the gamma rays focusing by a particular type of lens, named the Laue lens, with a focus on its application, SPECT oncology.

The developed diffraction GEANT4 plugin and example tool lays the groundwork for this ongoing project. More importantly, it presents a significantly improved tool over conventional engineering tools for simulating the diffraction of high energy particles.

In this chapter, I present the first attempt to model the X-rays and gamma rays focusing based on Laue diffraction in the GEANT4 toolkit using an advanced example in its early conception. This chapter discusses the critical aspects of the implemented Laue lens advanced example created as part of the GEANT4 partnership. The developed example models the wave-based properties of gamma rays and predicts the diffracted, transmitted, and absorbed gamma rays' locations on the detector plane based on a Monte Carlo simulation. The model provides flexibility to control several input parameters for various Laue lens designs. GEANT4 functionality and capabilities carry on expanding at the same time as its performance is being improved. The manufacturing of the lens has been established as both reliable and feasible; however, our progress in the manufacturing process was impeded due to the unavailability of funding and the necessary facilities

7.3 GEANT4 Toolkit

7.3.1 What Is GEANT4

GEANT is an abbreviation for "GEometry ANd Tracking" and is typically pronounced like the French word ***"géant",*** which translates to "giant." Its beginnings can be traced back to the 1970s [305]. GEANT4 is a free software toolkit composed of tools that can accurately simulate the passage of particles through matter. Over the past several years, significant modifications have been made to the toolkit to satisfy the needs of these user communities and leverage the increase in processing power [349].

All aspects of the simulation process are included in the toolkit: the geometry of the system, the materials involved, the fundamental particles of interest, the generation of primary events, the tracking of particles through materials and electromagnetic fields, the physics processes governing particle interactions, the response of sensitive detector components, the generation of event data, the storage of events and tracks, the visualization of the detector and particle trajectories, and the capture and analysis of simulation data at different levels of detail and refinement [350]. It was developed and maintained by an international partnership between physicists and software engineers. It is implemented in the C++ programming language. It has been employed in particle physics, nuclear physics, accelerator design, astrophysics and space sciences, space engineering, and medical physics applications [305].

GEANT4 is based on the accumulated knowledge of several Monte Carlo simulations of physics detectors and physical processes. Even though geographically distributed software development and large-scale object-oriented systems are no longer novelties, the GEANT4 Collaboration, in terms of the size and scope of the code and the number of contributors, is one of the largest and most ambitious projects of this type. It has proved that rigorous software engineering approaches and object-oriented methods can be used profitably to construct a coherent and maintainable software product, even when faced with the rapidly changing and open-ended requirements of physics research [305].

Two studies conducted at CERN and KEK investigated how computing techniques could enhance the GEANT43 programme [351][3], which served as a benchmark and a source of valuable ideas and experience. These two initiatives were integrated, and a proposal was submitted to the CERN Detector Research and Development Committee (DRDC) to develop an object-oriented simulation tool [305]. Approximately one hundred scientists from Europe, Russia, Japan, Canada, and the United States collaborated globally. The international GEANT4 Collaboration has managed GEANT4's production service, user support, and development since 1999 [352].

7.3.2 Flexibility of GEANT4

GEANT4's flexibility could be emphasized in numerous ways. It has many processes for different particles, such as slow neutron, optical photon, Parton string models, shower parameterization, and event biassing approach. In physics processes, for instance, a mixture of theory-driven cross-section tables and empirical formulas provides a considerably broader coverage of physics [353]. The polymorphism mechanism allows cross-sections and models to be arbitrarily merged into a single process. Everything in GEANT4 is available to the user, allowing them to select physics processes and models, magnetic/electric field integrators, GUI, visualization technologies, energy deposition, histogramming and persistence mechanisms based on their surroundings or preference. Because events and tracks are regarded as class objects, overlapping events, suspension of sluggish looping tracks, postponement of these tracks until the next event, and priority control of tracks in the stacks are all possible without incurring any additional performance expense. In addition, because of abstraction and polymorphism, there are numerous sorts of geometrical descriptions.[354].

7.3.3 Diffraction in GEANT4 Functionality

Users other than the GEANT4 collaboration can contribute to the software in a manner similar to that of open development. Contributor rights and responsibilities are comparable to those of a full GEANT4 member, with the primary differences being the size and complexity of contributions (these are limited to relatively small additions and bug fixes that do not require new expertise) and the absence of responsibilities related to sharing the collaborative effort necessary to maintain GEANT4. In the case of more advanced or significant developments, the user will be requested to become a full collaborator with maintenance responsibilities. The benefit of becoming a contributor is of actively developing new features or bug fixes and controlling and monitoring these developments directly.

7.4 GEANT4 Version

The version of GEANT4 that I used is 10.7.0. It was first released on 4 December 2020 (patch-04, released on 9 September 2022), with dependencies on *gcc/6.1, cmake/3.11.0*. It was installed on a cluster of two computers, each one with 4 core type i7 CPU at 2.8 GHz with 4GB RAM.

7.4.1 Resources

The necessary practical knowledge for developing and running the application that will be utilized in real experiments was acquired from the user's guide for Application Developers, Rev 6.0: GEANT4 Release 11.0, 10th December 2021. The User's Guide for Toolkit Developers includes thorough information on the design of GEANT4 classes and the information necessary to extend the current functionality of the GEANT4 toolkit [355]. This manual is intended to provide a repository of information for those who want to understand or refer to the detailed design of the toolkit, and to provide details and procedures for extending the functionality of the toolkit so that experienced users can contribute code that is consistent with the overall design of GEANT4The contributor is presumed to be familiar with the functionality of the GEANT4 toolkit as described in the "User's Guide for Application Developers" and to have a working knowledge of C++ programming. Object-oriented analysis and design knowledge also aid comprehension of this guidebook [355].

7.5 Implementation of the Laue lens Gamma Diffraction Process in GEANT4

7.5.1 Diffraction Code

The original diffraction algorithm for the Laue lens was written in Mathematica by Camattari [323]. I converted the code to C ++, in which GEANT4 is written. The code takes the source points and finds the hit points on a defined volume (call it the Laue lens). The rays emanate from various directions from the object under study and will be focused by the Laue lens via diffraction. Depending on the hitting points in the lens volume, the algorithm determines the three different possibilities: transmission, absorption, or diffraction at the Laue lens plane. The absorbed rays will be halted, while diffracted and transmitted photons will arrive at the detector plane at different places. Thus, adequate Laue lens shielding is critical to prevent the sensor from detecting the transmitted photons. For the diffracted photons, the code provides the interaction point in the lens, the direction towards the detector, and the hit points on the detector plane as (XD, YD, ZD). The resulting position of a diffracted photon at the focal plane depends on the source position, the photon direction, the photon energy, and the interaction point inside the crystal (not the interaction point on the lens, but on the single crystal it enters). Since the algorithm is simplified, this last point is not simulated. The photon distribution—due to the entire Laue lens—on a plane at a given distance from the lens results to be the sum of the contributions of all the crystals that constitute the lens. Moving the source along the x- or y-axis has no difference since the system has cylindrical symmetry. For the ray propagation, random points (xS, yS, zS) within the source are generated. This can be done in various ways, depending on the source type. The direction of the emitted photon, namely the azimuthal angle (azS > uniformly distributed between $0 - 2\pi$) and the polar angle (we need a spherical coordinate system). In the generation of the polar angle ($polS$) attention must be paid as we cannot simply generate a number uniformly distributed between 0 and $\pi,$ the below formula is used instead:

$$polS = \cos^{-1}\{\cos(divSmin) - [\cos(divSmin) - \cos(divSmax)] \times rand()\} \qquad \textbf{Eq. 7.1}$$

where the $divSmin$ and $divSmax$ limits, as mentioned in Section 4.6, are used to propagate the photons only towards the lens to shorten the computation time, since photons that don't hit the lens are for sure not focused.

7.5.2 Requirements to develop the Diffraction GEANT4 Example

To get the Laue lens diffraction process running in GEANT4, the code should satisfy the following:

- The code must change primaries and/or generate secondaries.
- The code should return distance travelled by a particle before it undergoes a given interaction (Mean Free Path).

In this GEANT4 example, I followed the philosophy of the optical processes, thus, the code changes the primaries only. However, there were several limitations related to the mean free path, which will be discussed in below:

7.5.2.1 The Mean Free Path

The Laue lens diffraction code for the Laue lens diffraction doesn't generate the mean free path, which hindered developing the code in the GEANT4 toolkit since it is a requirement for any GEANT4 example. I endeavoured to devise a resolution to this issue. To this end, the team and I had several meetings with the GEANT4 developers (*Prof. Susanna Guatelli and Prof. Pedro Arce*) and discussed this obstacle.

The mean free path is the distance travelled by a particle before it undergoes a given interaction. In my case, the particle will interact at a known position (Laue lens volume). So, my initial clue was provided by the developers to set the mean free path to a very large number (DBL_MAX parameter in GEANT4) and put the logic as to whether a particle interacts in the PostStepDoIt (the final position parameter in GEANT4). In my code, I can just implement the process by defining the border where the photons are diffracted. In this case, the mean free path would be either a dummy number or a high value. In GEANT4, it is essential to tell the particle where to interact, as described in the logic in *G4OpBoundaryProcess in source/process/optical*.

My subsequent clue was provided by the developers was to check the *Step* of the emerging photon from the lens. Then change the position and momentum of the particle as follows:

```
G4Track *track = aStep->GetTrack();
track->SetPosition(vevtor_of_position);
```

```
track->SetMomentumDirection(vevtor_of_momentum)
```

After several trials, I could set the mean free path to a high value. The code executes if the material has the LaueLens properties defined. The lines below show the solution I have done:

```
G4double G4LaueLensProcess::GetMeanFreePath(const G4Track&, G4double,
G4ForceCondition* condition)
{
*condition = StronglyForced;
return DBL_MAX;
…
…
}
```

where DBL_MAX in C++ is the maximum finite representable floating-point number.

7.5.2.2 Steps for Example Development

To develop the first Laue lens diffraction code in GEANT4, generally, there are several crucial steps that must be followed.

7.5.2.2.1 Geometry

Create a simple geometry with default physics and then shoot optical photons. Throughout code developing, I followed the philosophy of optical physics. Thus, a good starting point was the GEANT4/extended/optical/OpNovice2 example. The geometry is simply a box. However, the geometry needs to be changed to a more appropriate one matching the Laue lens volume.

However, in the developed example, the geometry is not needed. The process will run if the user sets the Laue lens properties to the material. I followed the optical processes' philosophy of using a G4MaterialPropertiesTable, but I attached the process to a logical volume instead of checking if it has one. This is implemented in the code below:

```
G4MaterialPropertiesTable* MPT = mate->GetMaterialPropertiesTable();
if( MPT ) {
G4cout << "@@@FOUND MPT: " << G4endl;
MPT->DumpTable();
G4cout << "............" << G4endl;
if( MPT->GetProperty("AverageAbsorption",false) ) {
//      Average absorption of a crystal for the given energy and crystal size
bLaueVolFound = true;
break;
```

```
}
}
```

7.5.2.2.2 Physics List

The next step involves modifying the physics. I implemented a separate physics list for the Laue lens diffraction with *G4LaueLensProcess.* After that, I needed to implement the method in my *OpBVoundaryProces* and define the new particle direction. However, in my code, the Laue lens works by taking the properties of the volume, not the boundary properties. I used the Laue lens physics list and set the class variable to work with any momentum and generate *New_Momentum* for the diffracted photons.

7.5.3 Simplifications and Assumptions

Camattari [323] has developed a tracking Monte Carlo algorithm to predict the photon distribution of diffracted high energetic photons using the Laue lens diffraction concept. The LaueGen algorithm was used to design dedicated Laue lenses for different applications [323]. The material selection for the lens elements was based on a Monte Carlo analysis of different single crystal materials with preferable lattice plane orientations. In the current example, the study's first goal is to determine the parameters of the Laue lens tailored to medical applications. However, the user can run different Lens configurations by modifying the user input parameters.

Crystals are the core of the Laue lens. A Laue lens for radiotherapy is constituted of hundreds of mm-sized optical elements that require a positioning precision typical of micromechanics. The spaces between the Laue lens rings, namely the white spaces, are where there are no crystals, as shown in Figure 7.1. Still, the photons here are transmitted or absorbed at these spaces. Thus, shielding for the lens frame is needed. However, to keep the complexity of this example to a reasonable level, this is not considered in the development process. The algorithm in its current version doesn't take into account the rings and the behaviour of the whole Laue lens consisting of seven rings was simplified by dealing with a tube with inner and outer diameters with average properties, as shown in Figure 7.2. There are also no empty spaces between the minimum and maximum Laue lens radii.

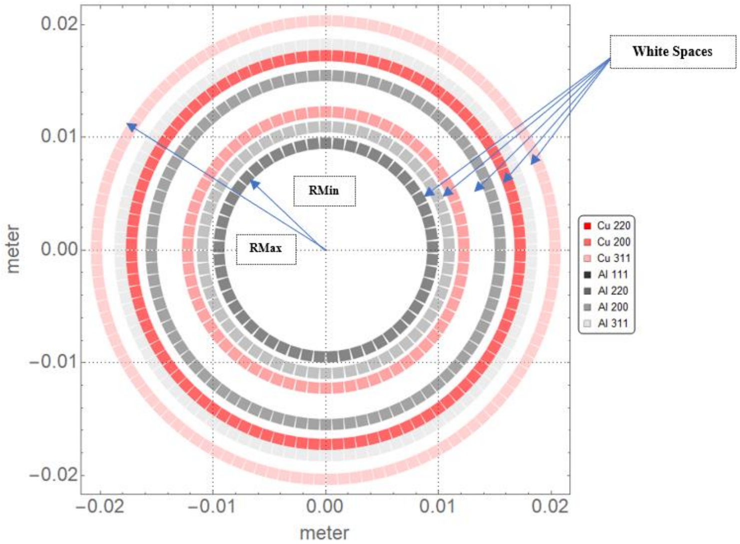

Figure 7.1 Actual Laue lens design with seven rings. The white spaces, inner Radius RMin and outer Radius RMax are noted

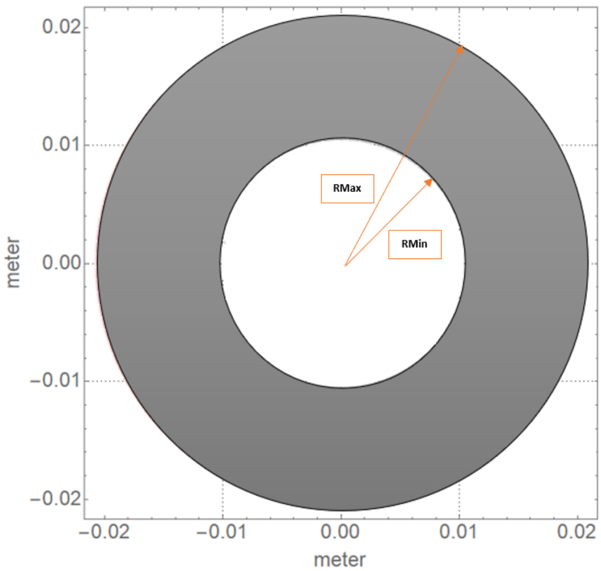

Figure 7.2 Simplified Laue lens represented as a tube with inner and outer diameters (noted). There are no empty spaces between the minimum and maximum lens radii.

The Laue lens algorithm is a simplification of the behaviour of the gamma rays hitting the Laue lens crystals. Its behaviour is controlled by the formulae given in the class G4LaueLensProcess, derived from G4VRestDiscreteProcess. This is included in the physics list *ExLLPhysicsList*, which is based on the "*emstandard_opt0*". The physical interactions of the gamma rays in the Laue lens are not taken into account, as they are included in the Laue lens algorithm. For this reason, it is recommended to use a very thin Laue lens, as the exiting lens position is moved to be in the middle of the preStep and the postStep point.

The resulting position of a diffracted photon at the focal plane depends on the source position, the photon direction, the photon energy, and the interaction point inside the crystal (not the interaction point on the lens, but on the single crystal). Since the algorithm is simplified, this last point is not visible.

7.5.4 Volume Definition and Input Parameters.

7.5.4.1 Laue Lens Volume

The Laue lens volume is represented as a tube of dimensions (mm): $RMin = 8.9710^{-3} \times ScaleFactor$, $RMax = 20.83 \times 10^{-3} \times ScaleFactor$, and $Z_{halfDim} = 110^{-3}\ mm$. These are the default dimensions; the set of default parameters are shown in Table 7.1. However, the user can control the Laue lens parameters by modifying the scale factor in the input file. Section 7.6 explains the procedure for designing a devoted Laue lens that suits the user's application. When a gamma ray enters the lens, it is absorbed, diffracted or transmitted by the algorithm. Interactions in the Laue lens are included in the algorithm; therefore, the lens Z dimensions should be very small so that there is only one step in the lens, which ends at the track exiting the lens.

Table 7.1 The initial set Laue lens parameters in the Algorithm

Parameter	Default Set Values (m)
Inner Radius	8.9710^{-3}
Outer Radius	20.8310^{-3}
Focal Length	0.5
Scale Factor	1
Detector position	(0,0,1)

7.5.4.2 Input Parameter

There are several parameters related to the Laue lens properties:

- The tangential length of the crystal L_{tan}
- The radial length of the crystal L_{rad}
- The average absorption of a crystal for the given energy and crystal size $AbsMean$
- The outer radius R_{Max}, and the inner radius R_{Min}

Also, the focal length is a characteristic of the lens. The parameters related to the lens' characteristics are not considered input parameter, instead, they are already defined in the code. However, the scale factor is a variable that I created to control several parameters, which are R_{Max}, R_{Min}, and the focal length L_d. The control of this parameter is discussed in detail in the section 7.6.

The lens properties are defined using a *G4MaterialPropertiesTable*, which is attached to the lens material. The following properties are defined:

- */exLaueLens/LaueProperty/AverageAbsorption*: the probability of the gamma to be absorbed. Values are provided for three energies:
    - 150-0.01keV: 0.3174
    - 150keV: 0.3174
    - 150+0.01keV: 0.3174

As it is a G4MaterialPropertiesTable property, the AverageAbsorption will be the lowest energy value if the gamma kinetic energy is smaller than the lowest energy, and the highest value if it is highest.

The following properties are defined by the command*/exLaueLens/LaueConstProperty* (with their default values):

- LensLRad: length of the crystals along the radial direction with respect to the lens, on the lens plane.
- LensLTan: length of the crystals along the tangential direction with respect to the lens, perpendicular to LensRad, on the lens plane. Figure 7.3 explains the LensLRad and LensLTan parameters.
- VertexOnAxisLimit: 2D radius to define if photon vertex is on/off lens axis or not: 0.5 mm.
- LensCenter: probability radius to define if the diffracted angle is calculated as "center" or "halo", when the photon vertex is on of lens axis: 0.3
- Diffraction efficiency is defined with the formula:

```
G4double effalg=(fDiffNorm1*exp(-pow(posR2*1.E0,2)/(2*pow(fDiffSigma1,2)))
+fDiffNorm2*exp(-pow(posR2*1.E0,2)/(2*pow(fDiffSigma2,2)))) *exp(-
pow(posZ*1.E0,2)/(2*pow(fDiffSigma3,2))).
```

where posR2 and posZ are the transversal and Z positions of the gamma vertex, respectively. In the GEANT4 example, the xInter and yInter and the coordinate of the interaction point with the lens. xS, yS, zS are the coordinate of the source (S is source). xD, yD and zD are the coordinates of the interaction point with the detector.

The efficiency of a lens or a single crystal highly depends on how it is considered, and it is a matter of definition. For example, I obtained an efficiency of 95% with a single crystal. But I used a perfectly collimated, very small beam, super monochromatic, highly aligned, the best possible conditions. If, for the efficiency, we consider only the photons that hit the lens, the efficiency increases. The efficiency decreases if we also consider the photons that don't hit the lens. In this thesis, I considered the efficiency as the number of diffracted photons divided by the number of generated photons.

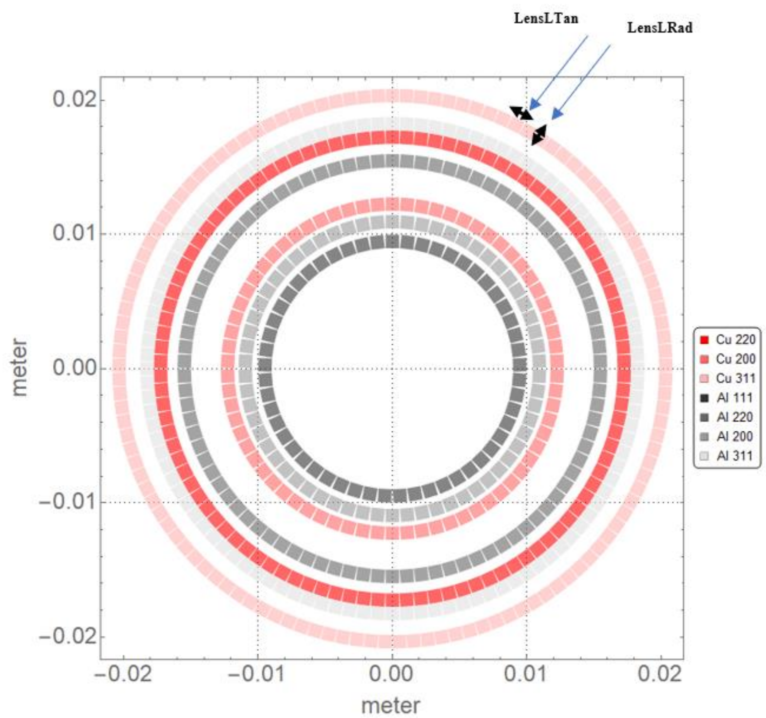

Figure 7.3 Length of the crystals along the radial direction with respect to the lens (LensLRad) and length of the crystals along the tangential direction with respect to the lens (LensLTan).

7.6 Code Flexibility

7.6.1 The Scale Factor

As I mentioned earlier, I aimed to have a more versatile and flexible code that can be used to design a Laue lens for different applications by either upsizing or downsizing the

Laue lens dimensions. To this end, I added to the code an input parameter, called the scaling factor. $ScaleFactor$, is set as an input parameter so that the user can change the Laue lens design and apply the diffraction for different system designs and configurations. The default value for this parameter is set to 1. Changing the scaling factor would consequently modify the inner and outer radii of the lens, which are shown in Table 7.1. Moreover, it directly sets the focal length (where the detector should be placed) Ld, as well as the optimal distance from the source to the Laue volume Ls will be automatically modified depending on the modified scale factor parameter, as shown in the equations below:

$$RMin \ = Default\ set\ Value \times ScaleFactor \qquad \textbf{Eq. 7.2}$$

$$RMax \ = \ Default\ set\ Value \times ScaleFactor. \qquad \textbf{Eq. 7.3}$$

$$RFocal\ Length = \ Default\ set\ Value \times ScaleFactor \qquad \textbf{Eq. 7.4}$$

$$Detector\ Location = Ld = Focal\ Length \qquad \textbf{Eq. 7.5}$$

It is worth mentioning that the source location (Ls) and the detector location (Ld) can be placed at any distance from the Laue lens centre. However, the optimal case is achieved by placing the source at a distance equal to the lens's focal length, that is Ls=Ld.

7.6.2 Detector Position

The detector position is set at $2 \times Ld$. The code takes a gamma ray produced at (0,0,0), sends it towards the Laue lens and calculates the position on the detector plane. In the code, I have eliminated the detector, because the Laue lens only diffracts the gamma ray without knowing if there is a detector after it. I have substituted the detector with the lens focus since the focal length is the detecting area in the Laue lens case. This adds more flexibility as the user can choose to place the detector at any position other than the lens's focus. The code in its current version has a detector placed at the focus position to count the number of photons diffracted. It is a box of 6 mm half-length in X and Y and 0.510^{-3} in Z made of G4_Si (Silicone material implemented in GEANT4. It is filled by a grid of 240×240 voxels. The user can change the detector position along the lens axis, and as a result, the efficiency would be smaller. If the source is displaced, the image on the detector, instead of a disk shape, will have a doughnut shape, which will be symmetrical for both -Z and +Z shifts. The detector is placed at a distance equal to the focal length from the source as in the following GEANT4 code:

```
G4double LaueLens_posZ = fFocalLength;
 G4RotationMatrix* rotLL = new G4RotationMatrix();
fLaueLens = new G4PVPlacement(rotLL, G4ThreeVector(0,0,LaueLens_posZ), fLaueLens_LV,
"LaueLens", fWorld_LV, false, 0);
```

The location at the lens is split into a halo and a centre. Given the source and the lens, the distribution is reproduced by using the halo and the centre locations. The blue is the halo, and the red is the centre, as shown in Figure 7.4. This is a practical trick to reconstruct the shape of the diffracted photons. 30% of the photons are of type "centre" and 70% of the photons are type "halo". The "centre" photons are centred in offset. The other photons are centred in -offsetR. This is produced with the following GEANT4 code:

```
if(trkPosPerp > 0.5e-3) { // (*source in axis / not in axis*)
if(CLHEP::RandFlat::shoot() <= 0.3){ //     If[rType==="center",(*if it is a point of the center, it is
centered in trkPosPerp, otherwise in -trkPosPerp*)
If trkPosPerp > 0.5*10^-3, the source is not on axis, otherwise the source is on axis
```

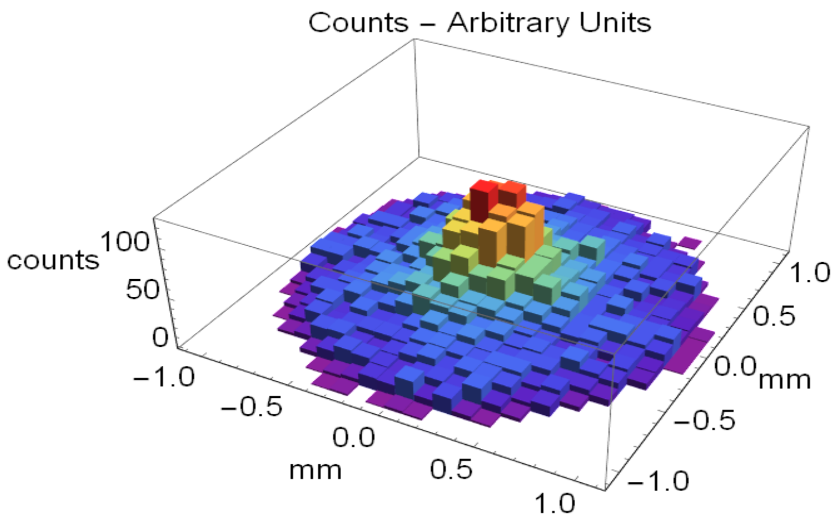

Figure 7.4 Photon distribution at the lens' focus. The blue is the halo, and the red is the centre.

When the gamma rays are propagated, it is possible that they will interact with the air in the middle or even with other materials if there are materials between the lens and the focus. This new gamma direction can be calculated as $(position\_on\_focus - position\_on\_lens)$. In the code, there are interaction points with the lens, which are $xInter$, $yInter$, and $zInter$. The $xInter$ and $yInter$ have values while $zInter$ is always zero, because the lens is approximated as a plane.

7.6.3 Photon Interactions

If the gamma ray enters the lens before it has deviated, it can suffer an interaction (Compton, photoelectric). In the developed code, the *absorbed* represents all the Compton and photoelectric effects, all the effects that are not diffraction. However, the transmitted photons experience no interactions. In the code, ***Efalg function*** takes into account all the interactions that the gamma rays undergo.

A table of the run summary is printed at the end of the run with the proportion of the gamma rays diffracted, transmitted, and absorbed.

7.7 Results

7.7.1 Histograms

There are several predefined 1D and 2D histograms:

1. 1D histograms
   - 0 : X coordinate of diffracted gammas at lens focus
   - 1 : Y coordinate of diffracted gammas at lens focus
   - 2 : Theta angle of diffracted gammas at lens focus
   - 3 : Perpendicular coordinate of diffracted gammas at lens focus
   - 4 : Theta angle of gamma vertices
   - 5 : Phi angle of gamma vertices
   - 6 : Energy of primary particles entering Laue lens
   - 7 : Energy of secondary particles entering Laue lens
2. 2D histograms: exLaueLens has several predefined:
   - 0 : X vs Y coordinates of diffracted gammas at lens focus, for gammas out of lens axis

- 1 : X vs Y coordinates of diffracted gammas at lens focus, for gammas on lens axis in beam center
- 2 : X vs Y coordinates of diffracted gammas at lens focus, for gammas on lens axis in beam halo
- 3 : Perpendicular i coordinate vs theta angle of diffracted gammas at lens focus, for gammas out of lens axis
- 4 : Perpendicular coordinate vs theta angle of diffracted gammas at lens focus, for gammas on lens axis in the beam center
- 5 : Perpendicular coordinate vs theta angle of diffracted gammas at lens focus, for gammas hitting the lens's axis in beam halo
- 6 : X vs Y coordinates of gammas at detector entrance
- 7 : X vs Y pixel numbers of gammas at detector entrance

The histograms are managed by *G4Analysis classes*. The name of the histograms file can be selected with the command:

```
/analysis/setFileName  name
```

All selected histograms will be written in a file name.root (default xrays.root). The user can choose the format of the histogram file: root (default),

```
hbook, xml, csv, by using namespace in HistoManager.hh
```

Two macros are included:

- xrays.mac: Shoots a gamma with the parameters defined.
- vis.mac: same as xrays.mac but visualize with OGL.

7.8 Run the GEANT4 Diffraction Example

7.8.1 To Call the Diffraction Process

In order to call the Laue lens diffraction process (the example that I developed) to any defined volume in GEANT4, the user has to use the physics list of the Laue lens that is defined in the example and attach it to the volume so that it can behave as a lens. This process is only applicable for gamma rays, and for those volumes which have a G4MaterialPropertiesTable which contains the property "AverageAbsorption".

7.8.2 The Primary Generator

The particle, energy, position, and direction are set in the PrimaryGeneratorAction class. The primary kinematics consists by default of a single 150 keV gamma ray placed at position (0,0,0). Its direction is directed to interact with the lens (LensRmin and LensRmax define the gamma theta limits). Several macro commands can be used to change the default behaviour:

- **/exLaueLens/generator/position POS_X POS_Y POS_Z UNIT** (default = 0 0 2*focal_length mm)
- **/exLaueLens/generator/Nprimaries VAL**. Defines the number of primary particles generated in each event. (default = 1)
- **/exLaueLens/generator/primaryXSepar VALUE UNIT**. If 2 primary particles are selected, it sets the X distance between the two particles initial position. The set of X positions will be centred at 0. (default = 0.)
- An extra generator command can be used to generate different initial random seeds (default = 1111) **/exLaueLens/generator/setRandomSeed INITIAL_SEED**
- **/exLaueLens/generator/primarySphereR**: Defines the radius of the sphere inside which primary particles are randomly sampled (default = 0.0).

It is worth noting that if the source is other than a point source, the Laue diffraction code will run for the extended source. The parameter "rSphereMax", which is the radius of the spherical source. Then, (xS, yS, zS) random points are generated inside the spherical source (they aren't always (0,0,0), as in the not extended case). If the user aims to run the code for a point source, the parameter rSphereMax has to be set to zero.

7.8.3 Compilation

Execute exLaueLens in 'batch' mode from macro files:

```
% exLaueLens xrays.mac
```

Execute exLaueLens in 'interactive mode' with visualization (it will execute the macro vis.mac):

```
% exLaueLens
Idle> type your commands
Idle> exit
```

It will show the compiling process as in Figure 7.5:

Figure 7.5 Example compiling process

7.8.4 Steps to Visualization

To open the GUI:

- Build the example using *build*.
- Make using ccmake.
- Then type: *./ExLaueLens.*

Once the above steps are followed, it will display the GUI for the Laue lens developed example as in Figure 7.6. To run it:

- Type: */vis.open/ OGL*.

This will show a rotating geometry for the Laue lens and the detector placed at the focal length. Figure 7.7a shows the Laue lens geometry generated from the developed example. After that:

- Type: *control execute/ xrays/.mac*. This command will execute the macro file and will start shooting photons.

Figure 7.7b shows the GUI for the Laue lens simulating only the diffracted photons gamma radiations from a Tc^{99} point source directed towards the Laue lens. Figure 7.8a shows the GUI for the Laue lens simulating the diffracted, transmitted, and absorbed photons gamma radiations from a Tc^{99} point source directed towards the Laue lens. The yellow line is the side view of the Laue lens volume. The distribution angle of the source was optimized to reduce the computation time. Figure 7.8b shows the transmitted and diffracted photons, and the Laue lens volume in a different view. Figure 7.8c shows the spot of the focused photons on the detector lane. The detector and the focused photons are marked with a red arrow. Figure 7.8d shows the zoomed view of the focal spot on the detector plane for the diffracted gamma rays and the transmitted rays.

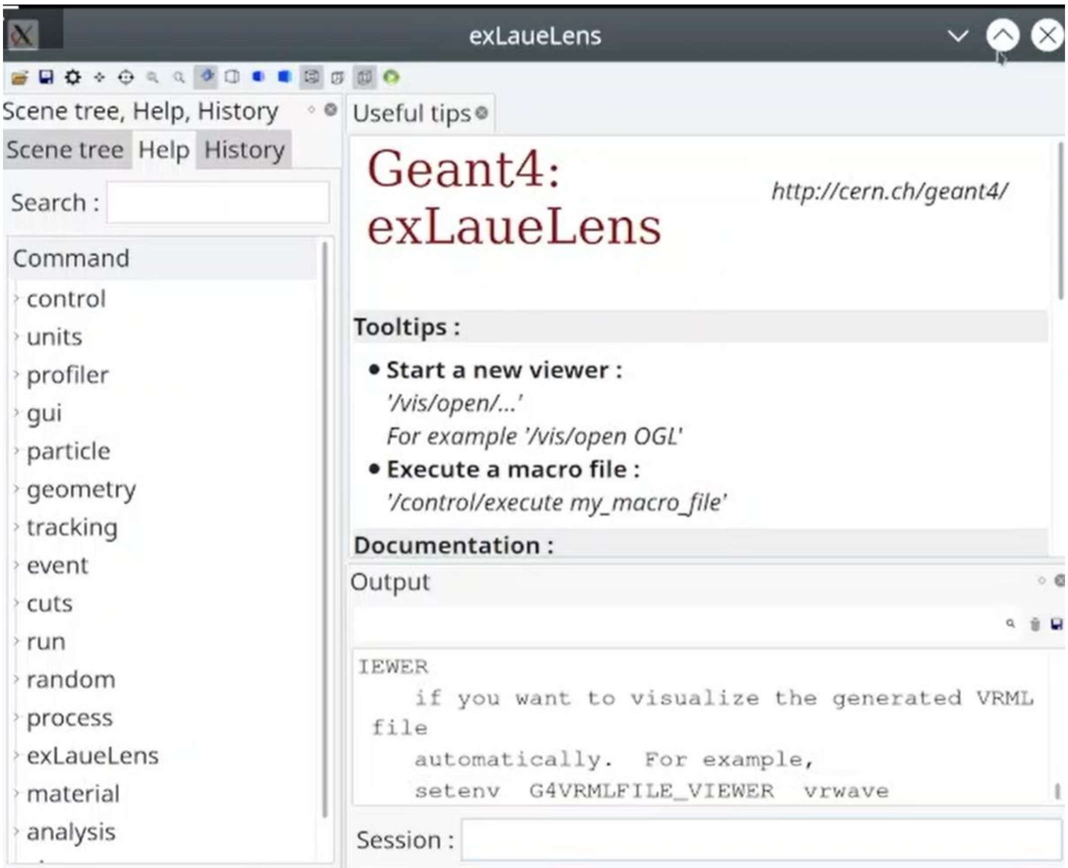

Figure 7.6 The GUI of the GEANT4 Laue lens example.

(a)

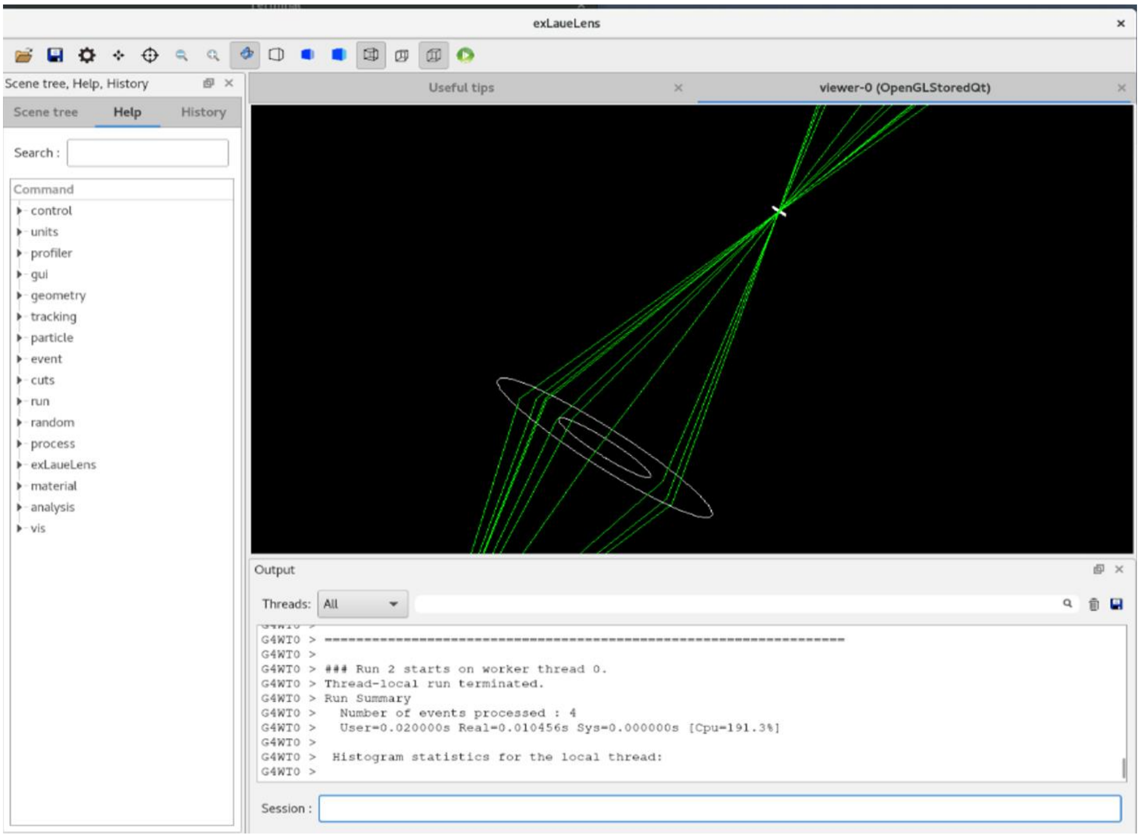

(b)

Figure 7.7 (a) The geometry of GEANT4 Laue lens example showing the lens and the detector, (b) The GUI for the Laue lens simulating only the diffracted photons.

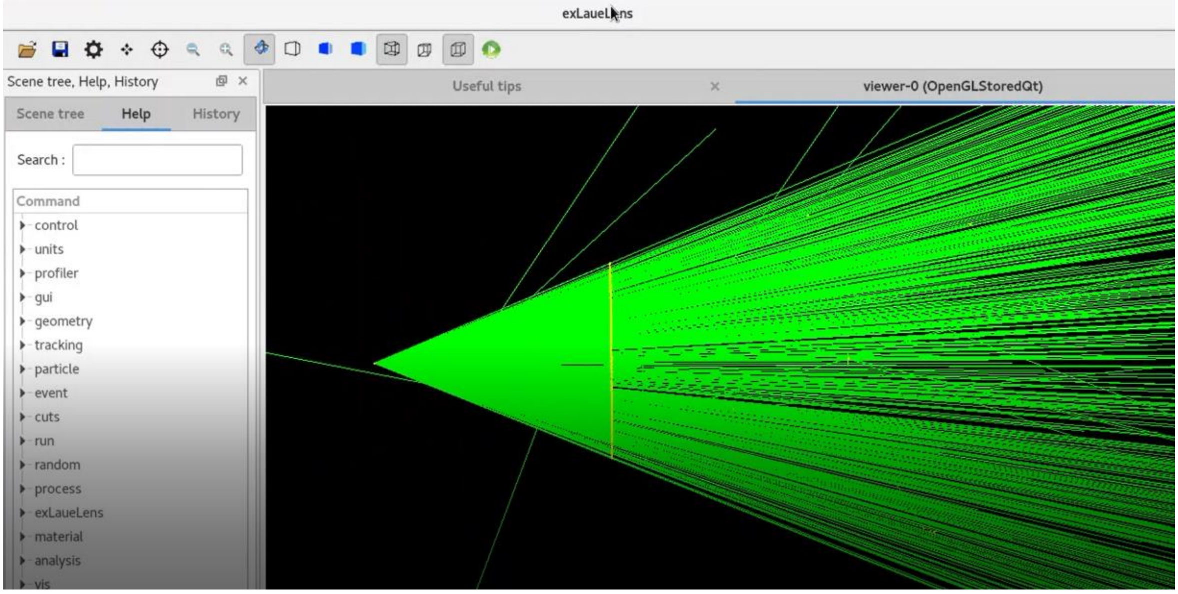
exLaueLens
Scene tree, Help, History
Useful tips
viewer-0 (OpenGLStoredQt)
Scene tree
Help
History
Search :
Command
control
units
profiler
gui
geometry
tracking
particle
event
cuts
run
random
process
exLaueLens
material
analysis
vis

(a)

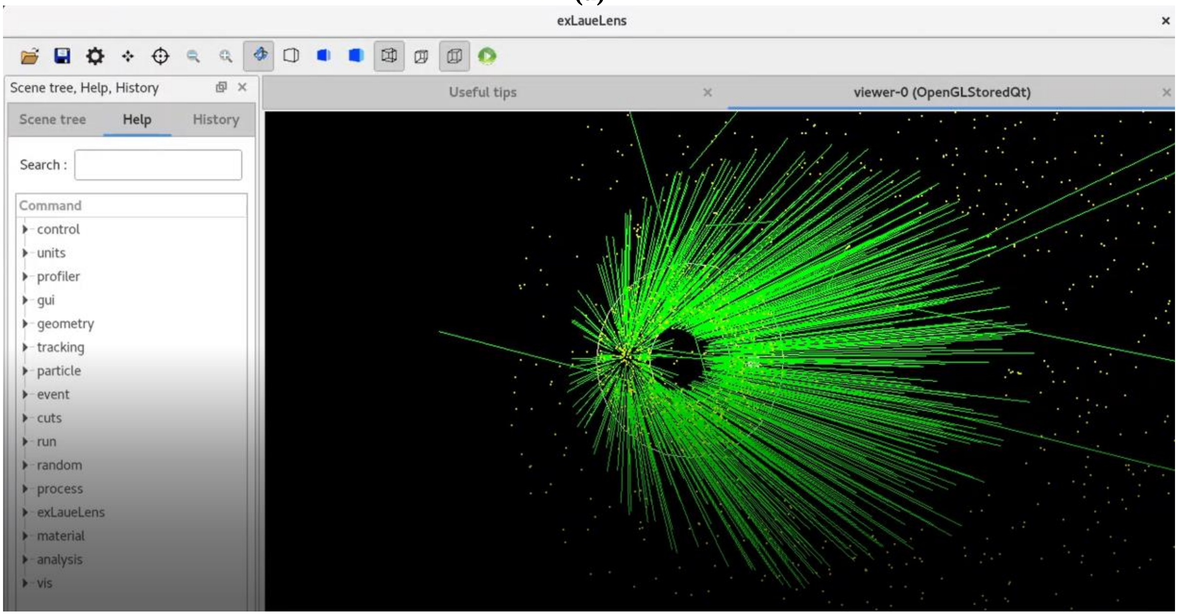
exLaueLens
Scene tree, Help, History
Useful tips
viewer-0 (OpenGLStoredQt)
Scene tree
Help
History
Search :
Command
control
units
profiler
gui
geometry
tracking
particle
event
cuts
run
random
process
exLaueLens
material
analysis
vis

(b)

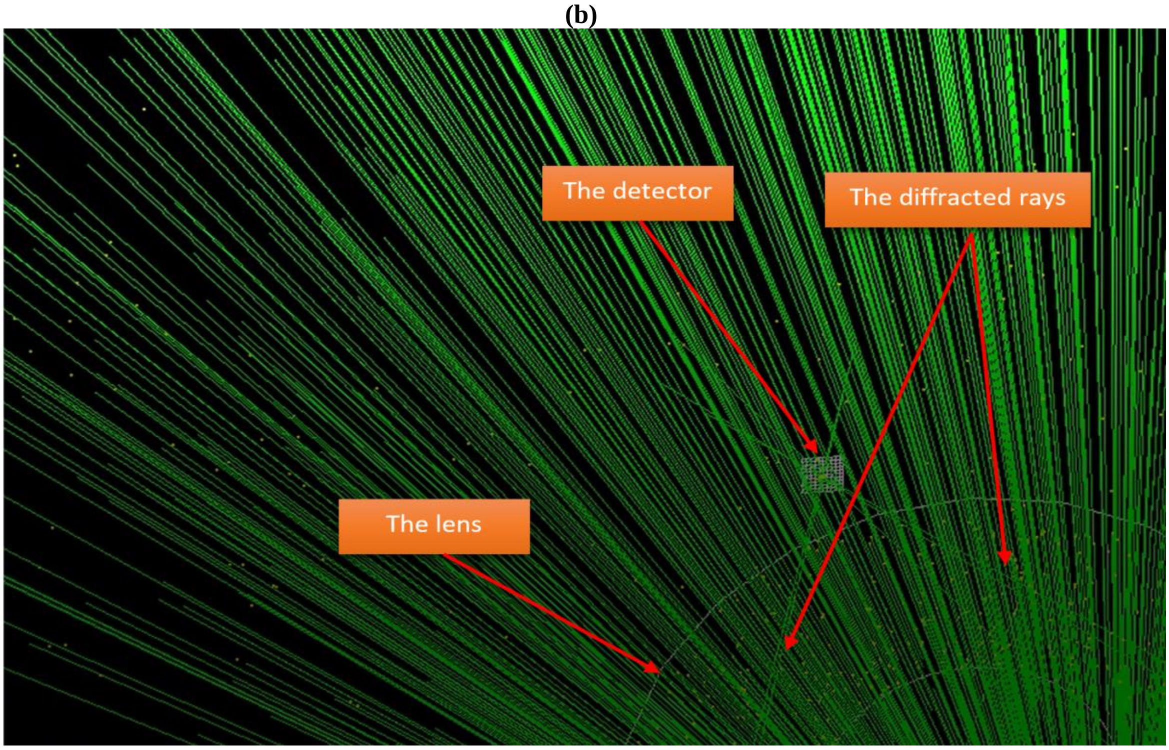
The detector
The diffracted rays
The lens

(c)

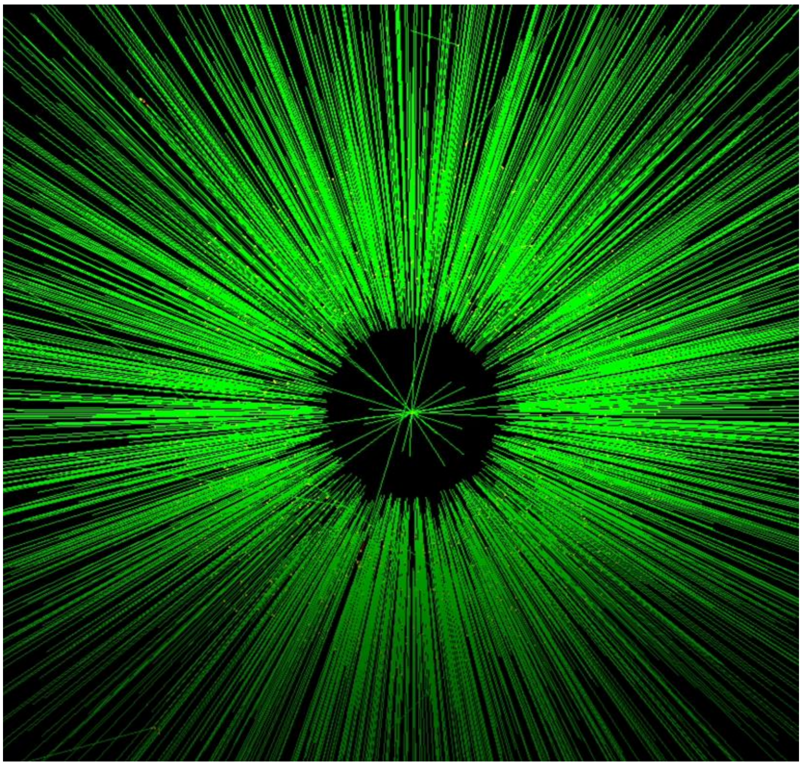

(d)

Figure 7.8 (a) Gamma radiations from a Tc^{99} point source directed towards the Laue lens rings. The yellow volume is the side view of the Laue lens volume, (b) Different views for the transmitted photon, diffracted and Laue lens volume, (c) The spot of the focused photos on the detector lane. The detector and the focused photons are marked with a red arrow, (d) shows the zoomed view of the focal spot on the detector plane for the diffracted gamma rays and the transmitted rays.

7.8.5 To Set Up Customized Case Studies

This example was developed to utilize the Laue lens diffraction process in different applications. Before the user starts to design customized case studies using the Laue lens diffraction code, several things should be taken into account, which will be explained in this section 7.6.

The Generator:

In the generator file in the Laue Lens Example, the user needs to define the desired source characteristics with paying attention to the source distribution angle. The rays must be directed towards the lens to reduce the computation time. In my case, I defined a Tc^{99} point source, the radiotracer used in SPECT imaging.

The Detector:

The detector, up to now, is a thin disk; no interaction is produced. The user can change the detector material and dimensions in *ExLLDetectorConstruction.cc* file.

Output Files:

The code does not give any output file. To generate the desired output data, The user can follow the below steps:

- *Edit manysendjobs and put IOPT=1*
- *bash manysendjobs*
- *Edit manysendjobs and put IOPT=2*
- *bash manysendjobs*

7.9 The Designed Experiments in GEANT4

As I mentioned in Chapter 4, at the start of this research, I was inspired by my supervisor's publication [253], which proposed a 3D X-rays CT method based on lightfield imaging. The idea was extended to SPECT imaging in [356]. They first introduced the lightfield SPECT (L-SPECT) by considering an array of pinholes as focusing elements instead the conventional collimator. Following GEANT4 simulations, preliminary phantom imaging experiments were conducted with an Inveon SPECT system modified to incorporate a tungsten pinhole array The results were inconclusive because certain physical parameters of the Inveon system were not accessible for proper calibrationsHaving thought of using the Laue lens as the focusing element, I aimed to pick up where they left off in the lightfield SPECT experiments and utilize the experiences I gained in GEANT4 to duplicate the real experiments they had done, but with the lens-based SPECT I proposed. The L-SPECT and lens-based SPECT both were the product of several attempts to reframe conventional nuclear imaging based on introducing new methods and technologies, such as lightfield imaging.

However, I understand that the conventional planar performance metrics may not be applied to these theoretical systems. The challenging part has been to demonstrate how this concept applies to experimental practice. The National Electrical Manufacturers Association (NEMA) has standardized the procedures for specifying instrument performance. Thus, to demonstrate the performance, I intended to conduct a series of case studies for the previously proposed L-SPECT, and the lens-based SPECT incorporated in a well-known SPECT configuration which is the SIEMENS Inveon Multi-Modality System “5-MWB-1.0” and having the NEMA NU-4 as the phantom. Figure 7.9 shows the NEMA NU-4 I developed in GEANT4.

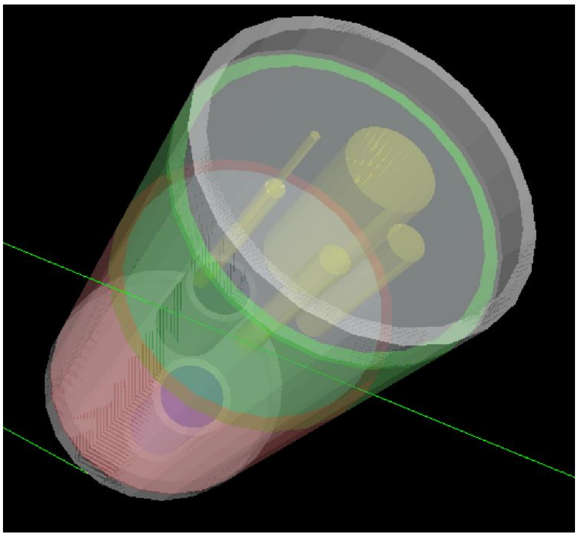

Figure 7.9 NEMA NU-4 phantom.

7.9.1 Simulations Protocol

- The geometries are developed using the GEANT4 ASCII file format.
- Primary generator is based on GEANT4 GeneralParticleSource.
- I used the GEANT4 Standard electromagnetic physics list.

The signal processing:

- Hits are created in the logical selected volume (defined as a G4VSensitiveDetector). The position of each hit will be the centre of the volume (crystal).
- The final signal (named reconstructed hit) will be provided from the hits taking into account the following:

1. Crystal energy resolution
2. Hits signal will be merged by a crystal block corresponding to the defined PMT: Crystal Anger logic will be used for positioning, and energy will be the sum of the energy of the hit.
3. Paralyzable and non-paralyzable dead time will be taken into account.
4. The hits and the reconstructed hits will be dumped into an ASCII file.
5. If one of the final signals in PMTs has an energy close to the defined SPECT energy, a line will be built joining the detector centre with the

closest collimator centre. This line will be written to an ASCII file.

7.9.2 Inveon SPECT

7.9.2.1 Inveon Detector Properties

The SPECT component of the Inveon system has a dual head detector and can be mounted on a rotating framework. Each detector contains a 68×68 pixelated scintillator array of $2\ mm \times 2\ mm \times 10\ mm$ NaI(Tl) crystals with a $0.2\ mm$ gap. It is combined with a position-sensitive photomultiplier tube readout [357].

7.9.2.2 Geometry

The 5-multi pinhole collimator of pinhole aperture 1mm (5-MWB-1.0) was used for the Inveon SPECT model. The top and bottom views of the actual set up used in this work are shown in Figure 7.10a. Figure 7.10b shows the Inveon geometry I developed in GENAT4. Figure 7.10c and Figure 7.10d show the pyramid pinhole holder associated with the SIEMENS Inveon 5 pinole collimator and a zoomed view of the crystals of the Inveon's detector, respectively.

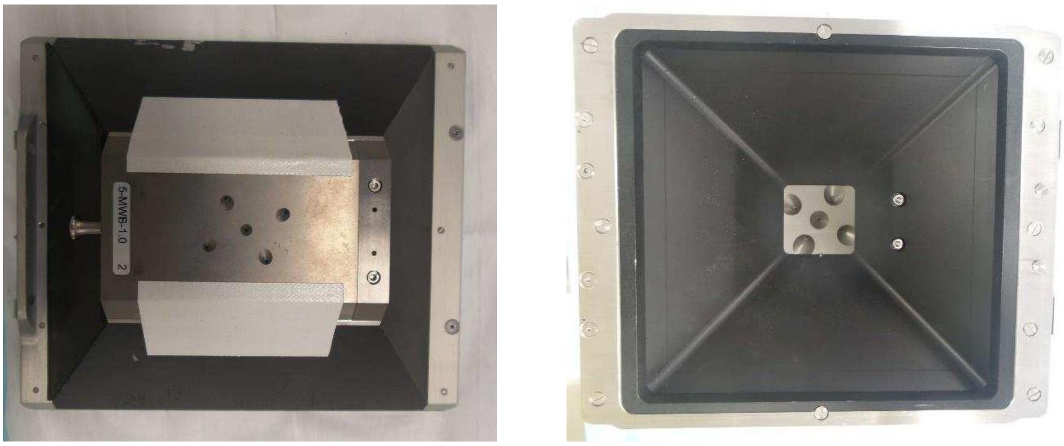

(top) **(bottom)**

(a)

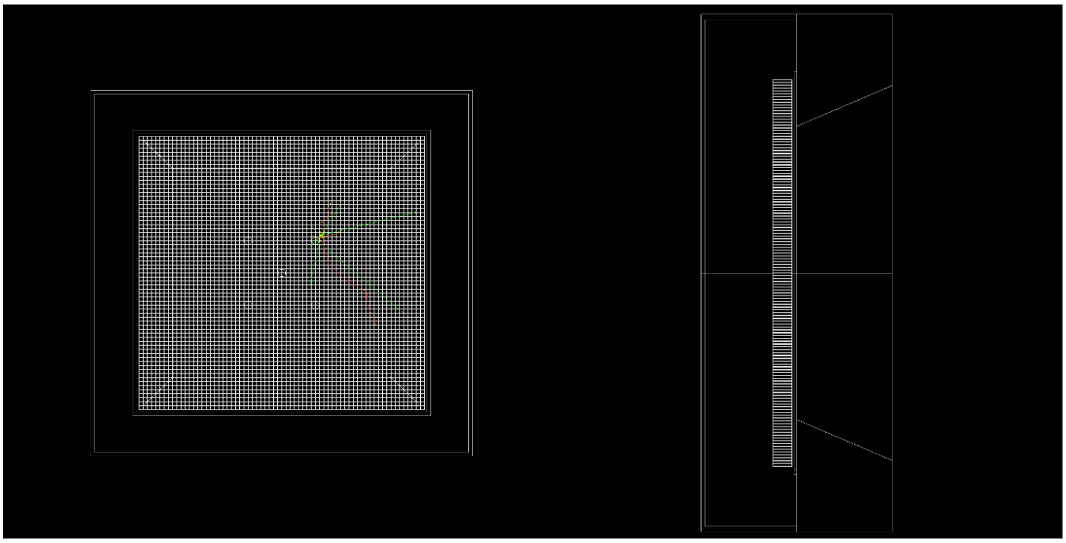

(b)

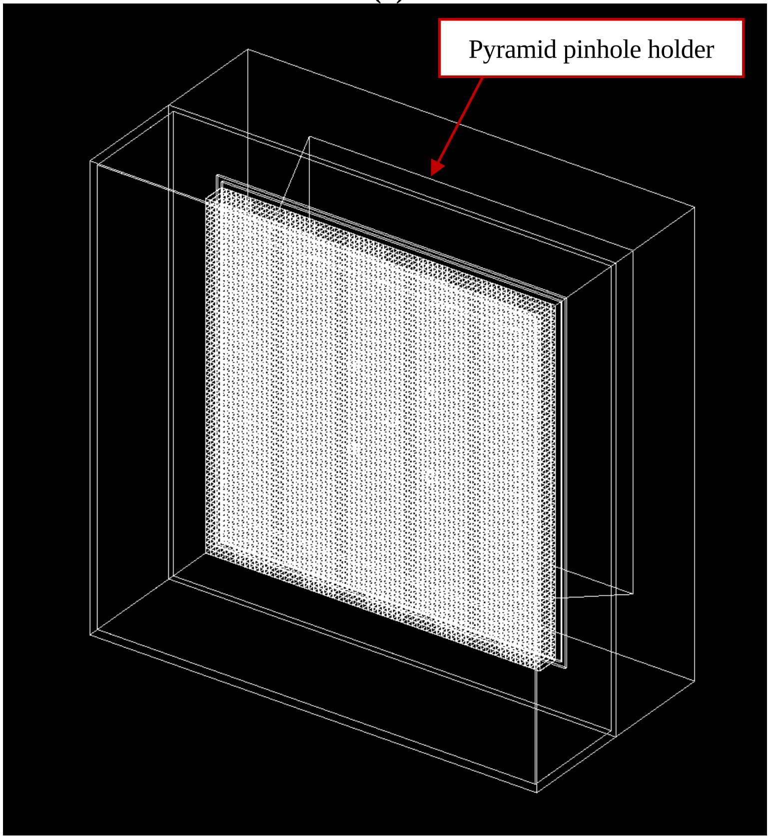

(c)

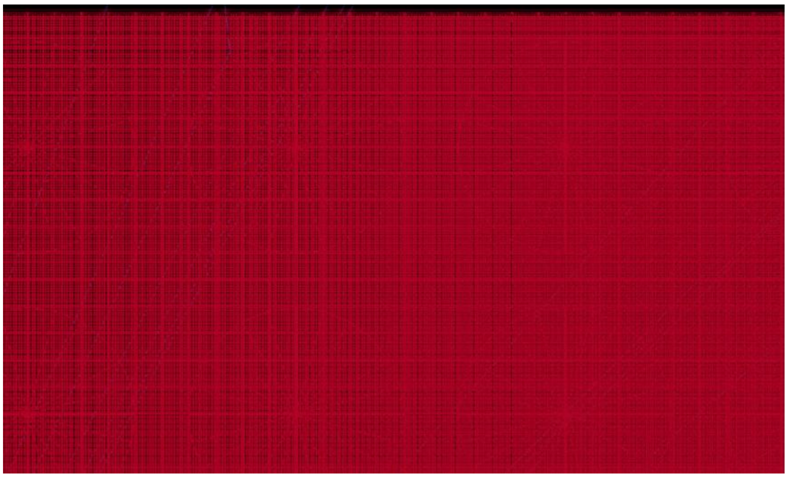

(d)

Figure 7.10 (a) Top and bottom view of the actual set up of the Inveon SPECT 5-MWB-1.0 used in research, (b) The Inveon geometry developed in GEANT4, (c) The pyramid pinhole holder that is associated with the Inveon 5 pinole collimator, (d) Zoomed view for the Inveon's detector's crystals.

7.9.2.3 Deposited Hits Histograms Results

Figure 7.11a shows the energy histogram using NEMA point source. Figure 7.11b and Figure 7.11c show the width R3 of the reconstructed hits in mm and the ***width phi*** angle of the reconstructed hits in deg, respectively.

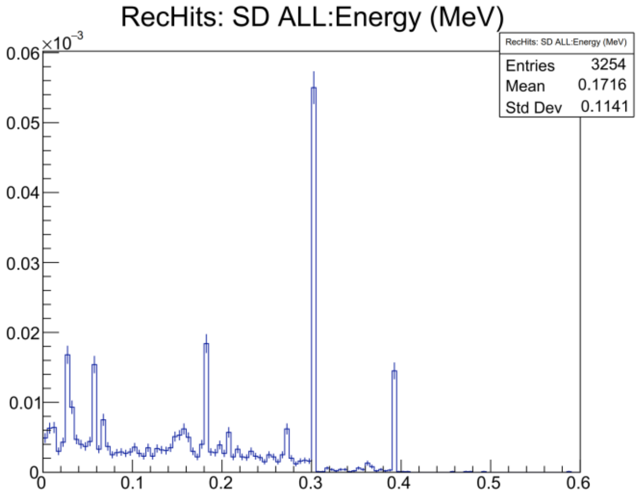

(a)

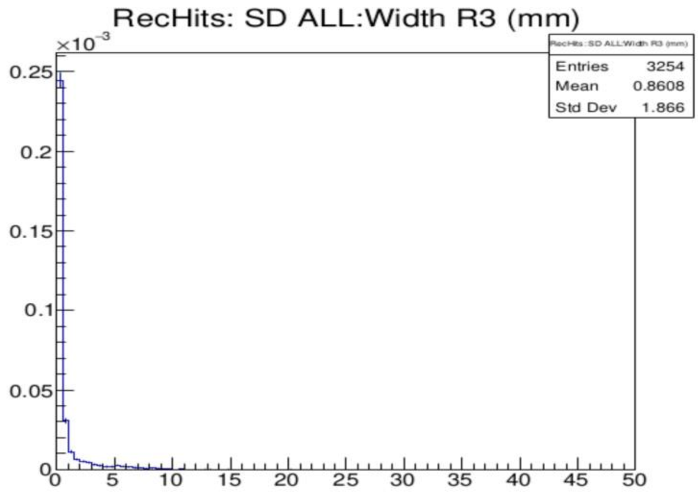

(b)

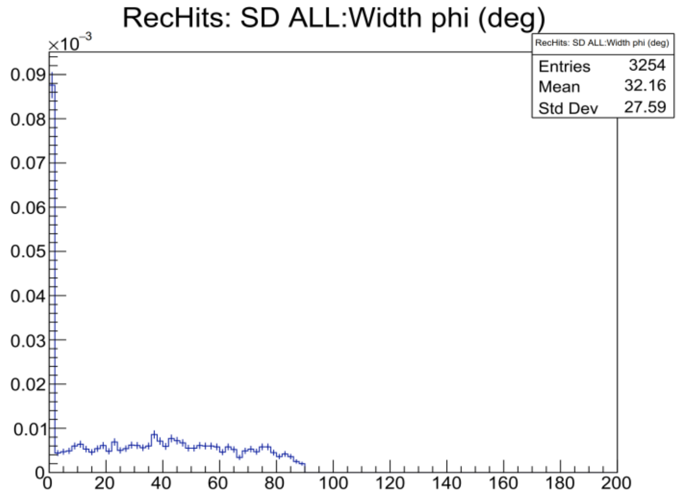

(c)

Figure 7.11 Inveon SPECT (a) Energy histograms of the reconstructed hits, (b) Width R3 of the reconstructed hits, (c) Width of phi angle of the reconstructed hits.

7.9.3 Lens-Based SPECT/Inveon

In this case study, I incorporated the lens-based SPECT configuration with the Inveon set up with identical detector properties mentioned in Section 7.9.2.1.

7.9.3.1 Geometry

Figure 7.12 shows the multi lens-based SPECT and the Laue collimator consisting of nine Laue lenses in a planer plane that I discussed in Chapter 5.

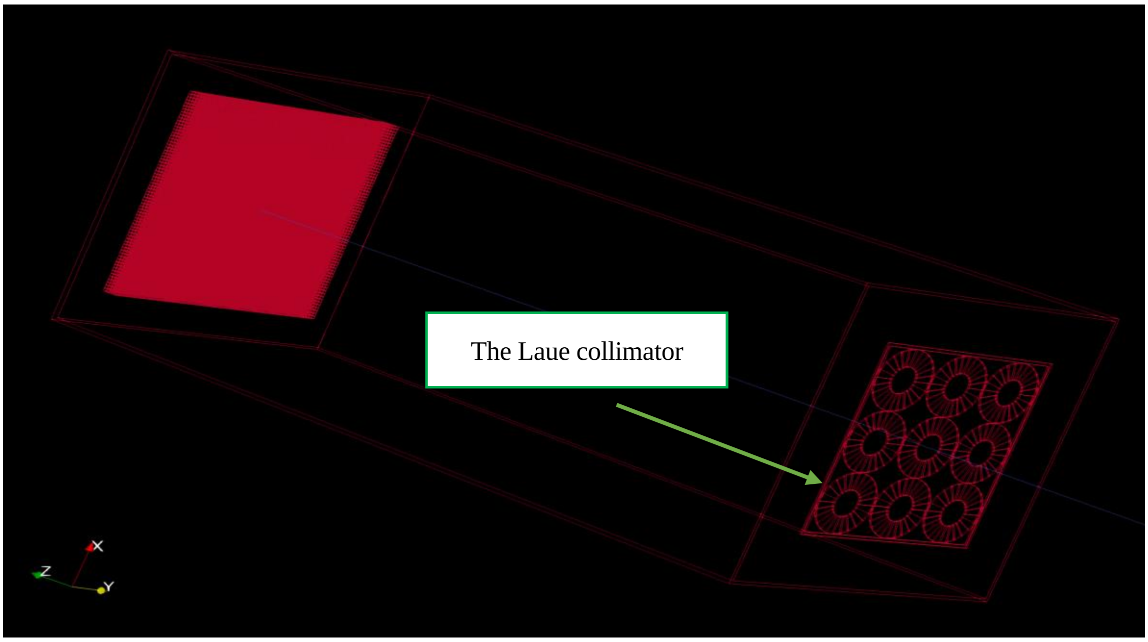

Figure 7.12 Multi lens-based SPECT design with the Laue collimator indicated modelled in GEANT4.

7.9.3.2 Deposited Hits Histograms Results

Figure 7.13a shows the energy histogram using NEMA point source. Figure 7.13b and Figure 7.13c show the width R3 of the reconstructed hits in mm and the ***width phi*** angle of the reconstructed in deg, respectively.

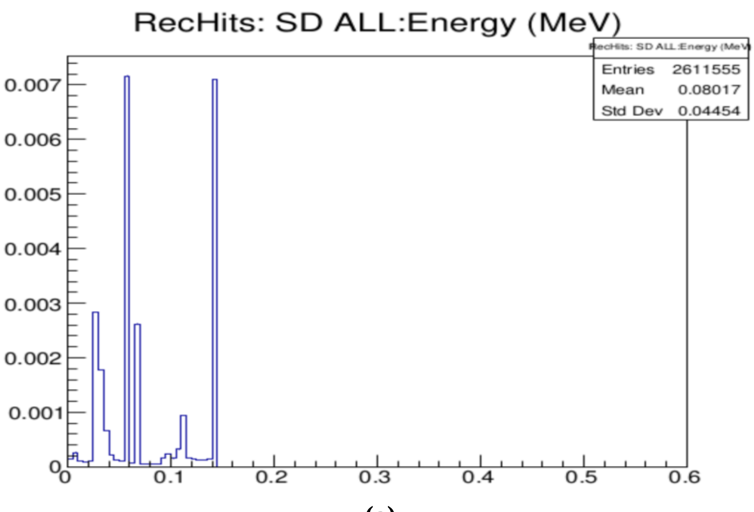

(a)

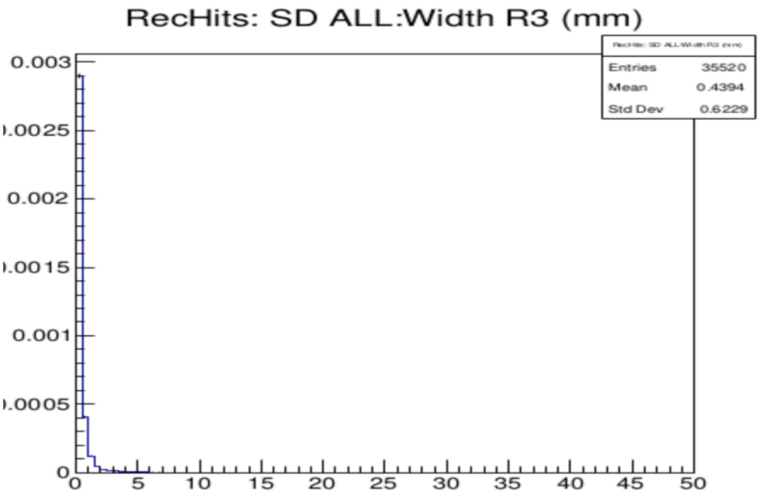

(b)

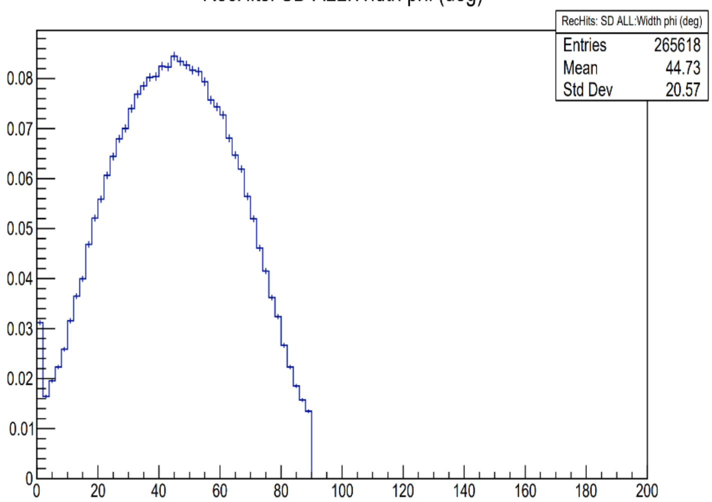

(c)

Figure 7.13 Laue lens/Inveon SPECT (a) Energy histograms of the reconstructed hits, (b) Width of R3 of the reconstructed hits, (c) Width of phi angle of the reconstructed hits.

7.10 Critical Discussion about the Case Studies Results Presented in Sections 7.9.2 and 7.9.3

In these case studies, it is essential to note that significant time was dedicated to developing and designing the geometries and environments from scratch. The process involved multiple iterations to ensure the validity and accuracy of both case studies. As a result, these studies focus primarily on the design and validation of the setups, and no specific analysis is presented regarding the image processing aspect.

Following a similar approach as in Chapter 6, I utilized histograms of the deposited hits to examine the system's functionality. The histograms visually represented the distribution and frequency of deposited hits and reconstructed hits representing the gamma interaction on the scintillator.

Different energy histograms indicate variations in the energy distribution of reconstructed hits. The different number of peaks in the energy histogram indicates variations in the energy between the two systems. In some cases, multiple peaks in the energy histograms may be desirable and indicate the system's capability to resolve different energy levels or distinguish between various radiation sources. By examining Figure 7.11a and Figure 7.13a, it can be noticed that both systems cover different ranges of energies.

The histogram of the width R3 histogram for the reconstructed hits represents a measure of the spread of reconstructed hits along the Z-axis in the coordinate system. It gives a benchmark for the dispersion of the deposited hits. It determines the system's ability to capture detector interactions in the third dimension [304]. Moreover, it indicates the system's resolution along the z-axis; the narrower the graph, the better the ability to distinguish different interactions in the Z coordinate. If the distribution of the R3 width histograms is too wide, adjustments can be made to the system's design to enhance the resolution in the z-axis.

Upon analysing Figure 7.11b and Figure 7.13b, a noticeable observation is that the width of the R3 histogram is larger for the Inveon SPECT compared to the Laue lens/Inveon SPECT. This indicates that incorporating the array of Laue lenses with the Inveon detector resulted in an enhancement of the resolution along the Z coordinate. In simpler terms, the lens-based SPECT system would be capable of distinguishing finer details in the Z direction compared to the Inveon SPECT alone.

The histogram of ***width phi*** (deg) represents a measure of the spread of the reconstructed hits in the azimuthal direction (around the axis perpendicular to the Z-axis). It represents the system's ability to distinguish between closely placed features with different azimuthal angles [304]. The narrower the ***width phi*** distribution, the higher is the resolution. In other words, it suggests the system has better angular precision to map the reconstructed hits in the azimuthal angle direction.

Upon analysing Figure 7.11c and Figure 7.13c, comparing the Inveon SPECT and the Laue lens/Inveon regarding the ***width phi*** histogram, we observe that both systems cover a similar range of angular values as they have almost the same distribution width in the ***width phi*** histograms. However, there is a noticeable difference in the values on the y-axis occurrences. The Laue lens/Inveon system exhibits significantly higher counts or frequencies of detected events per angular range compared to the Inveon SPECT. This indicates that within each angular range, the Laue lens/Inveon system detects a more significant number of events, suggesting that more events are detected within that range compared to other ranges, or in other words, it suggests that the Laue lens/Inveon has higher sensitivity in detecting the different angular ranges compared to Inveon SPECT.

7.11 Chapter Summary

In this chapter, I discussed the first attempt to model the focusing of X-rays and gamma rays based on Laue diffraction in the GEANT4 toolset, utilizing an advanced example and plugin that I developed. The GEANT4 Laue diffraction example was initiated with the goal of developing an open-source simulation software that seamlessly integrates into the GEANT4 Monte-Carlo simulation toolkit. Over time, the project has seen continual growth in its functionality and capabilities, accompanied by ongoing efforts to enhance its performance. Due to the object-oriented approach's adaptability, it is possible to simply integrate external simulation packages into the GEANT4 system as modules of physical processes. However, it is not trivial to focus X-rays with good efficiency, and the modalities of implementation of an X-rays concentrator still represent an open issue. The problem of focusing hard X-rays can be approached via a Laue lens. The designed GEANT4 example tool for diffraction serves as the foundation for this ongoing project. Moreover, it offers a simulation tool for high-energy particle diffraction processes that are vastly superior to those used in conventional engineering.

For the proof of concept, I designed and customized the first experiments for two different configurations in GEANT4 utilizing the developed code. The first one is the commercial Inveon SPECT design, the second one is the Inveon SPECT augmented with a Laue lens. I utilized histograms of the deposited hits to examine the system's functionality. Based on analysing the difference in the width of the R3 histogram and the width of phi angles of the reconstructed hits for both Inveon and Laue lens/Inveon, I made a final conclusion on the results: the narrower width and distinctive properties of the histograms in the Laue lens/Inveon system compared to the Inveon SPECT demonstrate its advantages in improved angular precision and higher sensitivity to different angular ranges. These capabilities are valuable in applications where precise angular mapping and sensitivity to angular variations are essential for accurate imaging.

7.12 Acknowledgement

This chapter articulates and expands on work for which the concepts and basic findings were partially published in:

1. A. Barhoum, M. Tahtali and R. Camattari and Susanna Guatelli. (2022, October). The GEANT4-Gamma Diffraction Code Based on Laue lens Modelling: Design Foundation and Implementation of the First Set of Models in GEANT4. In 2022 Fourth GEANT4 International User Conference at The Physics-Medicine-Biology Frontier.

7.13 Scientific Contributions

- Developed a plugin and an advanced example for GEANT4 implementing the Laue lens diffraction. The extended example is to be approved by Prof. Susanna Guatelli, (Under review).

8. First Set of Models in GAMOS for the Laue Lens Diffraction (Plugin)

Numerous disciplines of physics, such as high-energy physics, medical physics, space physics, etc., have adopted GEANT4 due to its extensive library of physics models and its exceptional geometry and visualisation tools. Nevertheless, using GEANT4 frequently necessitates a lengthy learning curve, which demands a solid understanding of C++ and the GEANT4 code itself. GAMOS makes using GEANT4 easier by eliminating the need for C++ programming and offering a set of user commands instead. One of the unique features of GAMOS compared to other simulation environments is its adaptability, which makes it suitable for simulation in other physics domains [358]. This adaptability is facilitated by a vast array of geometrical configurations, primary generators, physics lists, and a comprehensive set of tools that enable the user to obtain precise information from the simulation via user instructions. The usage of plug-in technology contributes to this adaptability, enabling the framework to be extended to accommodate unanticipated additional functionality [308].

As discussed in Chapter 6, I ran several case studies to examine the detector response due to the focused photos. However, as stated before, the GAMOS study was limited because the diffraction process and the wave-based properties which can be used to simulate gamma diffraction were not implemented yet in any of the available Monte Carlo toolkits. In this chapter, I am extending the GAMOS functionality by developing a GAMOS-based detector simulation example for Laue lens diffraction as a first attempt. In other words, I extended the functionality of the GEANT4-developed example in Chapter 7 and ran it in the GAMOS toolkit. In Chapter 7, I ran case studies by incorporating my design with the commercial Inveon SPECT detector configuration, in which I kept the original Inveon detector properties and design. However, I replaced Inveon's collimator with an array of Laue lense instead of the pinholes.

This chapter is structured as follows: Section 8.1 presents the methodology employed in the study. Subsequently, Section 8.1.1 focuses on studying system characteristics, while Section 8.1.2 shows the proposed detector configuration. Section 8.1.3 defines the radiation source, and Section 8.1.4 discusses the GAMOS generator. The chapter also covers extending the GEANT4 example functionality to GAMOS in Section 8.1.5. The subsequent sections explore specific configurations and case studies, such as Configuration 1: Single Lens Collimator in Section 8.2, with further subdivisions for one-point source and three-point source case studies. Section 8.3 delves into the Multi-Lens Collimator configuration, including one-point source and three-point source case studies. The LEHR SPECT Geometry is addressed in Section 8.4, followed by a chapter summary in Section 8.5, which provides a concise overview of the key points discussed throughout the chapter.

8.1 Methodology

This section describes the methods used to model and characterize the design of the conceptualized lens-based SPECT system in GAMOS. First, I extended the functionality of the GEANT4 example that I developed in Chapter 7 to GAMOS utilizing its plug-in technology. Then, I incorporated the proposed detector design into the lens-based SPECT system. Four geometries were considered and built in GAMOS. The first and second are single lens in a pinhole with one and three-point sources, respectively. The third and fourth case studies were the multi Laue lenses in multi-pinhole arrangements with single and three-point sources, respectively.

In order to assess the accuracy and practicality of the detector design that I developed for the proposed system, I employed the custom 3D reconstruction algorithm described in Chapters 4 and 5 to generate the 3D reconstructed images for each of the various configurations. For comparison purposes, I built the geometry of the conventional SIEMENS Symbia LEHR SPECT collimator and detector in GAMOS to evaluate its performance against the suggested lens-based SPECT with the proposed detector configuration.

8.1.1 Study of System Characteristics

I used the same source properties that were used in MATLAB simulations. This is to ensure accurate comparisons and evaluations of the envisioned system behaviour under various conditions, provide a reliable baseline for comparison, and confirm the reproducibility of the study's findings that I obtained in Chapters 4, 5 and 6. The one-point source is $0.03\ mm$ in radius consists of Tc^{99} sphere filled with air and activity of $10^9\ Bq$, and the three-point phantom with the same content and radioactivity, spaced by $0.1\ mm$. The scans were performed for full 360° rotation at 10° increments.

8.1.2 Proposed Detector Configuration

The scintillator is connected to an array of 100×100 Position Sensitive Photomultiplier Tubes (PSPMTs), $0.48\ mm \times 0.48\ mm$ each. Each detector consists of a $0.48\ mm \times 0.48\ mm\ \times 10\ mm$ pixelated scintillator array of $0.04\ mm \times 0.04\ mm\ \times 10\ mm$ NaI crystals. The detectors are shielded by lead septa with dimensions of $48\ mm \times 48\ mm \times 10\ mm$. The maximum active imaging region is $48\ mm\ x\ 48\ mm$, and the detectable energy range is $20 - 160\ keV$. In this study, I implemented the identical detector design initially proposed by our research team for the L-SPECT geometry (see Figure 2.28) [255]. The detector properties are kept the same for all the case studies presented in this chapter.

8.1.3 Source Definition

When replicated experiments provide identical or consistent results as the original study, the findings gain increased credibility. To this end, I wanted to reproduce the study's findings I obtained in MATLAB, but in a more realistic environment using the code I developed in GEANT4 and the extended one to GAMOS. The source solid and wireframe views are shown in Figure 8.1.

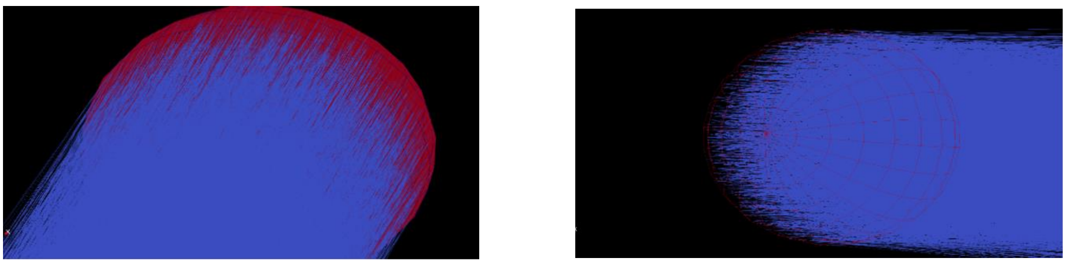

Figure 8.1 The TC^{99} filled with air and activity $10^9\ Bq$. The radius of the spheres is $0.03\ mm$. Solid (left) and wireframe (right) views for the source and the emitted gamma radiations.

8.1.4 GAMOS Generator

The definition of the source and the source distribution based on the tangent of angles is defined in GAMOS itself, not in the *ExLLPrimaryGeneratorAction,* as in the previous chapter, it uses the below command line:

```
/gamos/generator GmGenerator
```

The process is called to GAMOS whenever a Laue lens volume is identified using the below command in *ExLLPhysicsProcess*:

```
if(!MPT)
  return G4VRestDiscreteProcess::PostStepDoIt(aTrack, aStep);
```

8.1.5 Extending the GEANT4 Example Functionality to GAMOS

When I first created the Laue lens geometry in GAMOS using the developed example, I faced one problem with changing the scale factor. The scale factor is only controlled in *ExLLDetectorConstruction*, which is the one that sets the ScaleFactor (see Chapter 7 Section 7.6.1) and defines the command for changing it. So, in the extended GAMOS example, a GEANT4 user command was added to change *ExLLPhysicsProcess.cc* to change the scale factor without writing any extra scripts.

8.2 Configuration 1: Single Lens Collimator

8.2.1 This section introduces the case study of a single lens configuration with one Tc^{99} point source utilising the GAMOS plugin code with the envisioned detector design. Integrating the lens-based SPECT into the detector design provides practical insights into the system's behaviour within a realistic experimental setup. One-Point TC^{99} Source Case Study

8.2.1.1 Geometry

For this case study, I defined one pinhole with a 20.83 mm radius. It is defined as tubes but with attaching the Laue lens material and properties to the defined pinhole volume. The below lines place the pinhole (the Laue lens) at half of the distance between the source and the detector:

```
:P LensFocus 500.
:VOLU pinhole_matrix BOX $pinhole_N*$pinhole_pitch/2.+$pinhole_R
$pinhole_N*$pinhole_pitch/2.+$pinhole_R $LL_Z/2. G4_AIR
:PLACE pinhole_matrix 1 World RM0 0 0 $LensFocus.
```

The geometry of the lens inside a pinhole is shown in Figure 8.2. The geometry of the lens and the detector at different rotation angles is shown in Figure 8.3. The simulation for different rotation angles for single lens SPECT is shown in Figure 8.4.

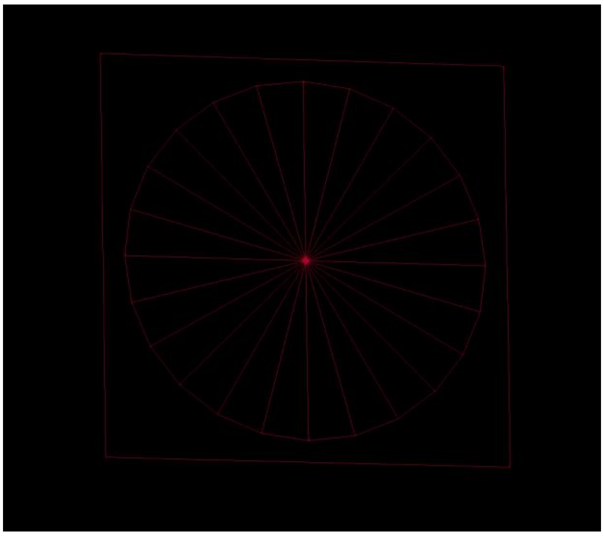

Figure 8.2 Laue lens features attached to pinhole volume.

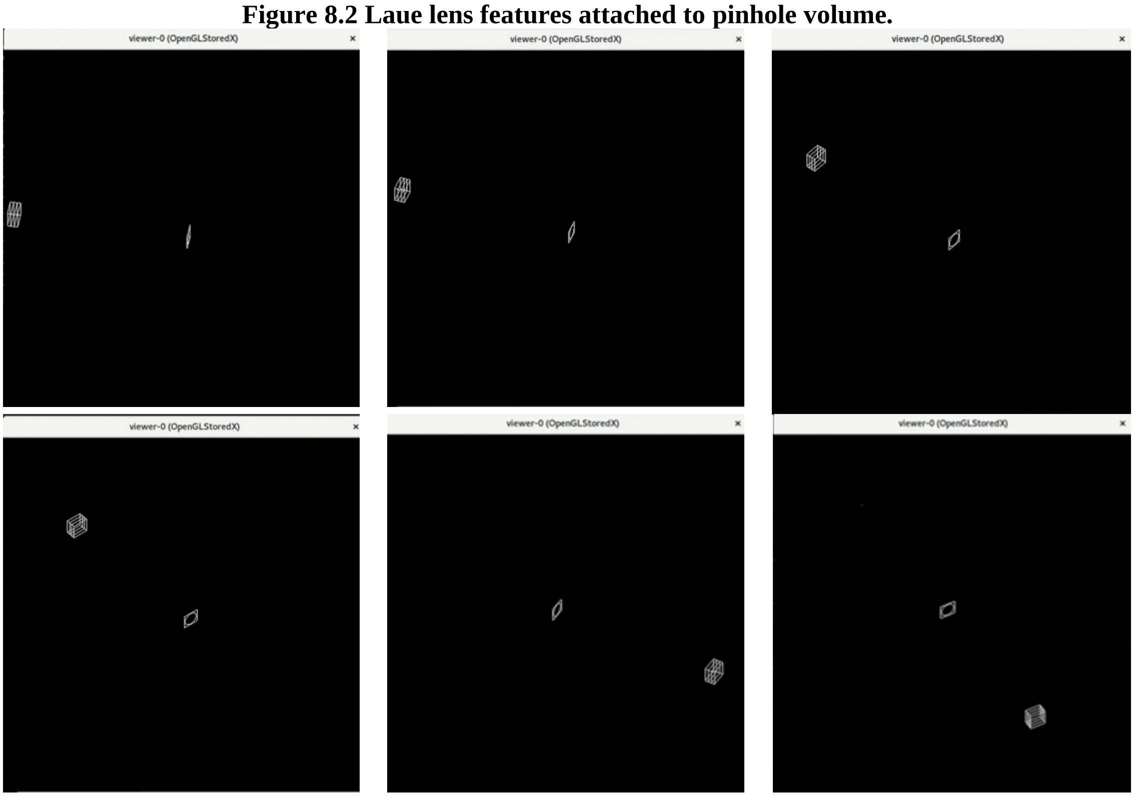

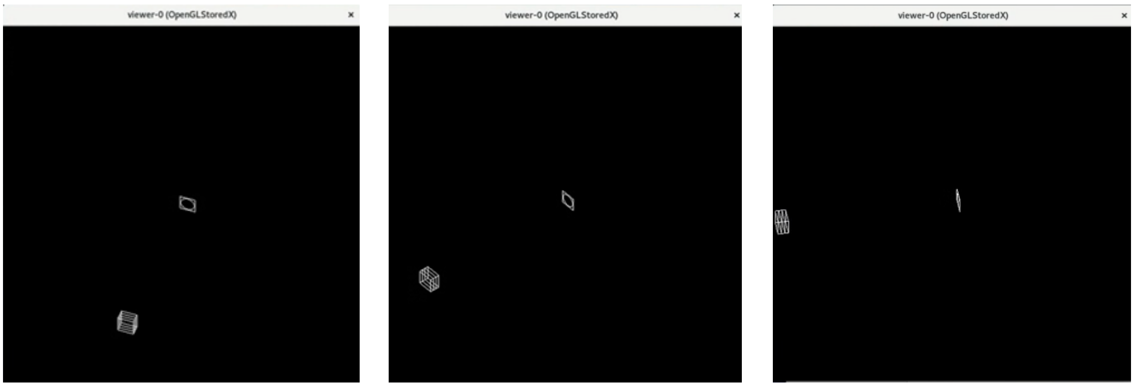

Figure 8.3 Geometry of the single lens-based SPECT at different rotation angles, showing the lens and the detector.

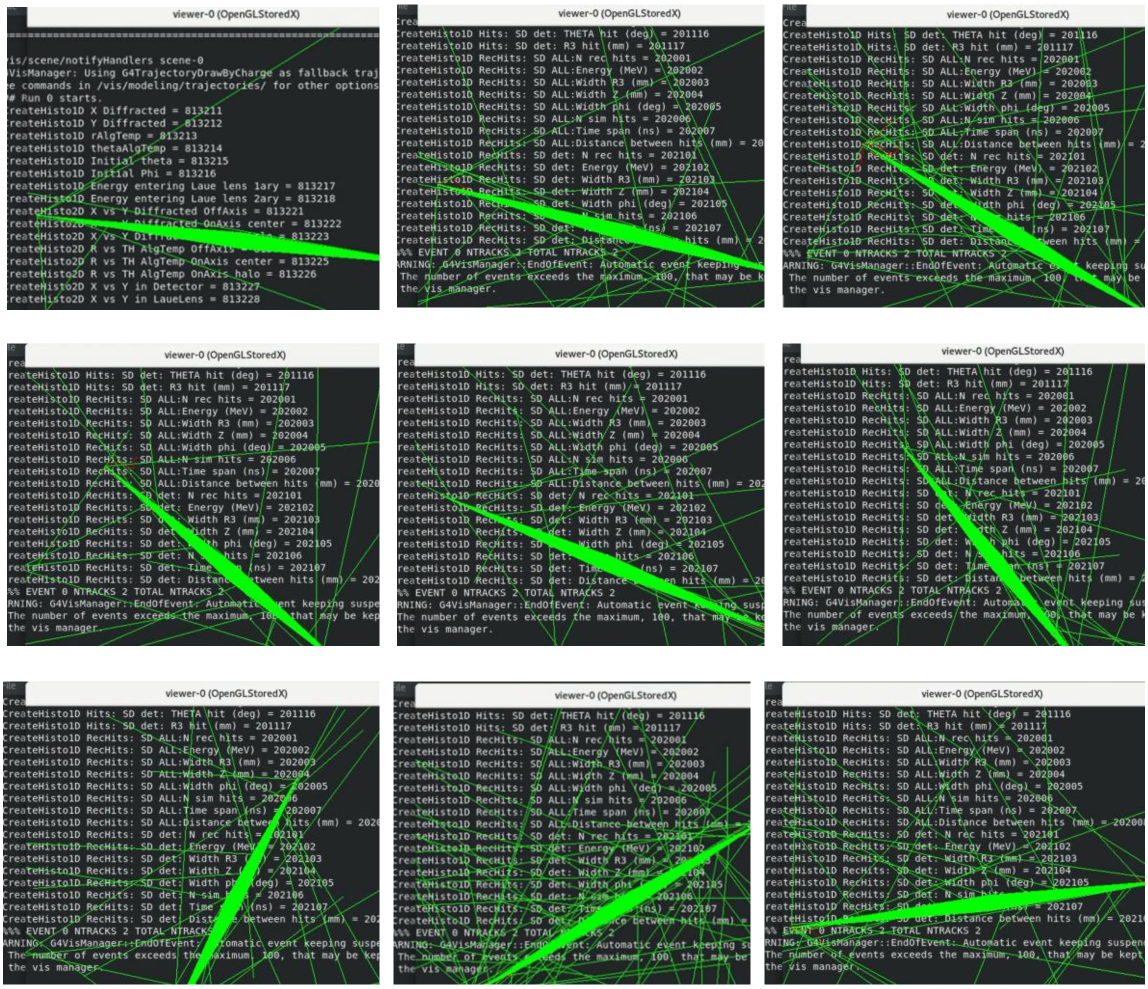

Figure 8.4 GAMOS screen grab showing the focused gamma rays at different rotation angles. For some reason, GAMOS is not windowing this output and displaying it on top of everything.

8.2.1.2 Reconstructed Hits and 3D Image Reconstruction

Figure 8.5a and Figure 8.5b show the hits spot on the detector plane and energy deposition of the X vs Y diffracted point on the pixilated detector plane, respectively.

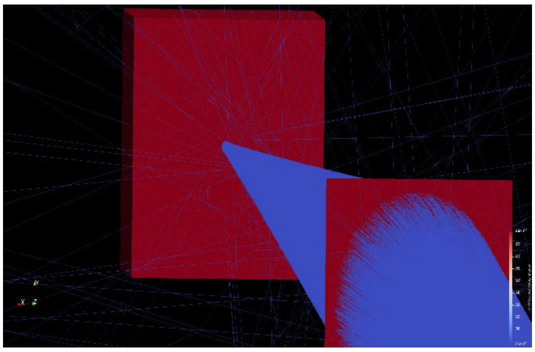

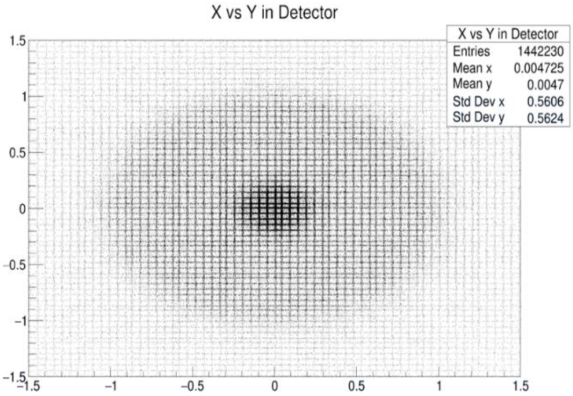

(a) **(b)**

Figure 8.5 (a) Hits spot on the detector plane, (b) Energy deposition of the X vs Y diffracted point on the pixilated detector plane.

The 3D reconstructed images generated from the one Laue lens case study with one point source were reconstructed using the 3D reconstruction algorithm discussed in Chapter 4. Figure 8.6a shows the pixelated image of a point source and one Laue lens. Figure 8.6b and Figure 8.6c show the XY and XZ slices of the 3D reconstructed images, respectively. The results demonstrate a level of consistency with previous case studies conducted under ideal and controlled conditions (Chapters 4 and 5), albeit with some observed distortions; the deviations from the ideal results are attributed to the applied detector effects.

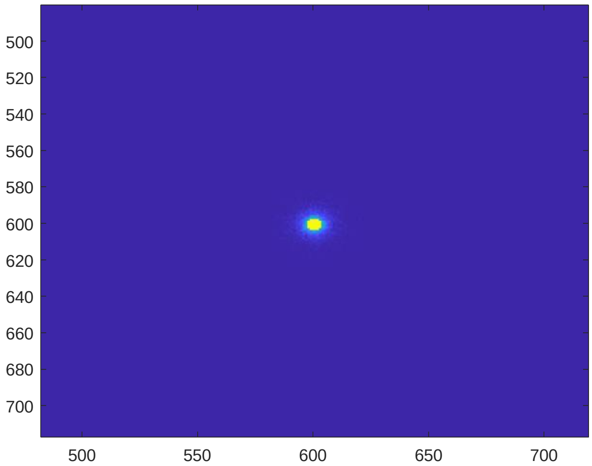

(a)

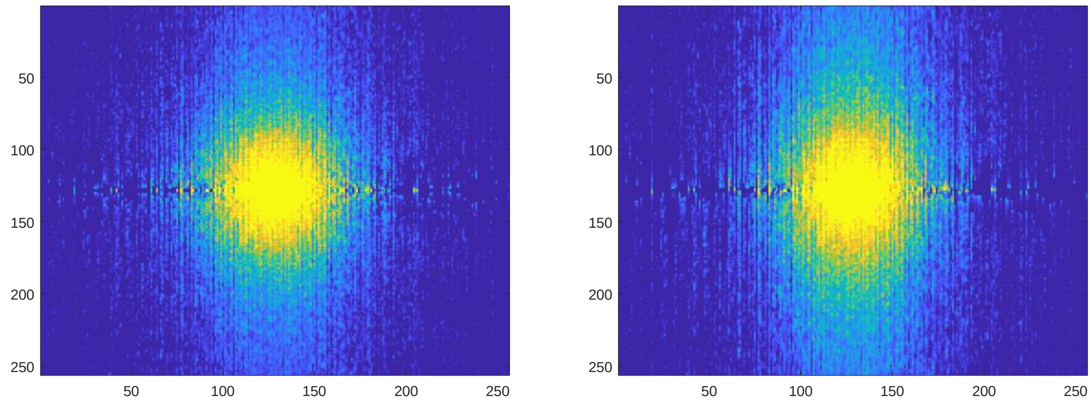

(b) **(c)**

Figure 8.6 (a) Pixelated mage of a TC^{99}point sources and one Laue lens. The x-axis represents the column index, and the y-axis represents the raw index of the pixelated projection image, (b) XY slice of the 3D reconstructed image, (c) XZ slice of the 3D reconstructed image. The X and Y measurements are in mm.

8.2.2 Three-point TC^{99} Source Case Study

This section introduces the case study of a single lens configuration with a three Tc^{99} point source utilising the GAMOS plugin code with the envisioned detector design.

8.2.2.1 Geometry

The sketch of the three-sphere geometry is shown in Figure 8.7a. The defined geometry is exactly the same as the one described for the single lens with TC^{99} one-point source, but with three-point sources instead, as shown in Figure 8.7b.

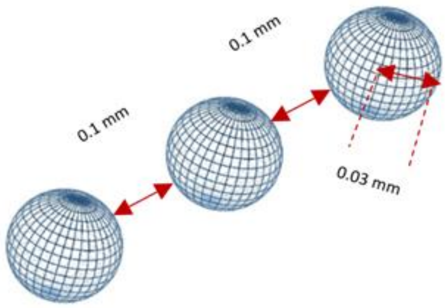

(a)

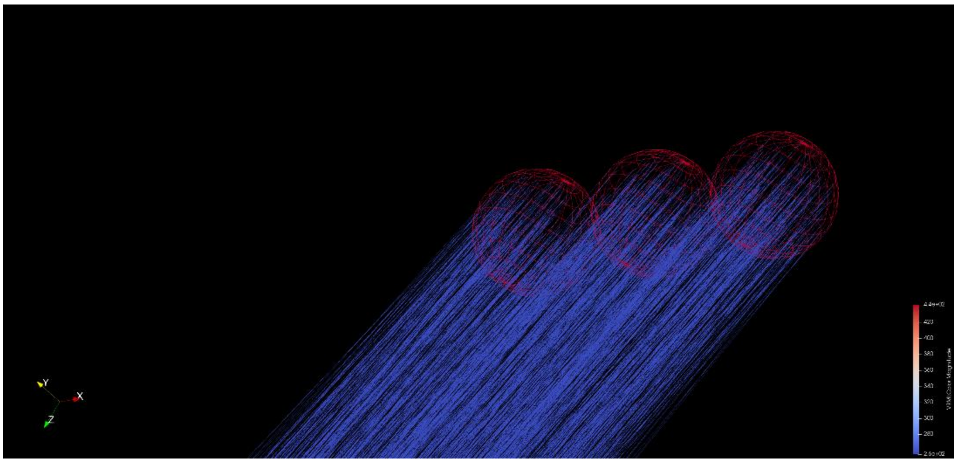

(b)

Figure 8.7 (a) Sketch of the three-sphere phantom, (b) Wireframe view for the three-point source and the radiations of TC^{99} filled with air and activity 10^9 Bq. The radius of the spheres is 0.03 mm, and the distance between the spheres from centre to centre is 0.1 mm.

8.2.2.2 Reconstructed Hits and 3D Image Reconstruction

The zoomed view of the three spot projections on the detector plane is shown in Figure 8.8.

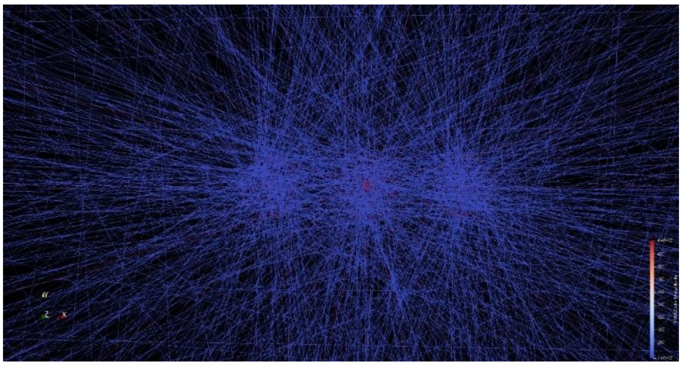

Figure 8.8 Zoomed view of the hits on the detector plane.

Figure 8.9a shows the pixelated image of a TC^{99} three-point source and one Laue lens. Figure 8.9b shows the 3D reconstructed images.

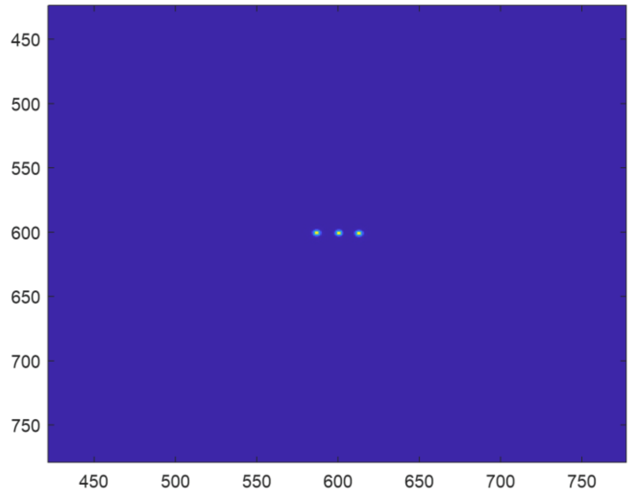

(a)

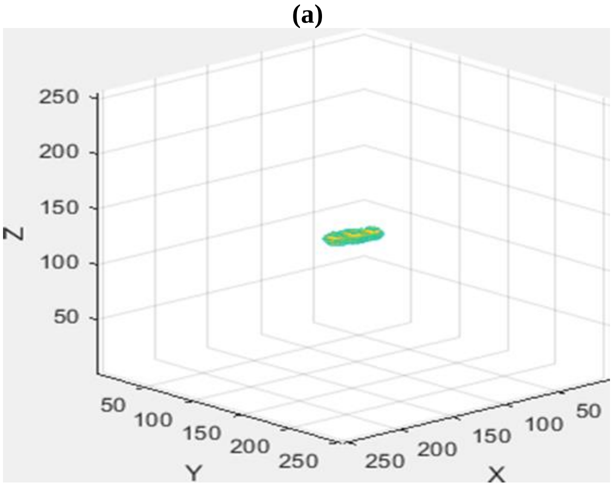

(b)

Figure 8.9 (a) Pixelated image of a TC^{99} three-point sources and one Laue lens. The x-axis represents the column index, and the y-axis represents the raw index of the pixelated projection image, (b) 3D reconstructed image. The X and Y measurements are in mm.

8.3 Multi-Lens Collimator

For this multi-lens case study, I defined nine pinholes with $20.83\ mm$ radius each. And as for the single lens, I set the pinholes as tubes and attached Laue lens material and properties to the defined pinhole volume. The geometry of the Laue collimator with nine Laue lenses is shown in Figure 8.10. The geometry at different rotation angles is shown in Figure 8.11. The simulation for different rotation angles and the different focused rays based on Laue gamma diffraction are shown in Figure 8.12.

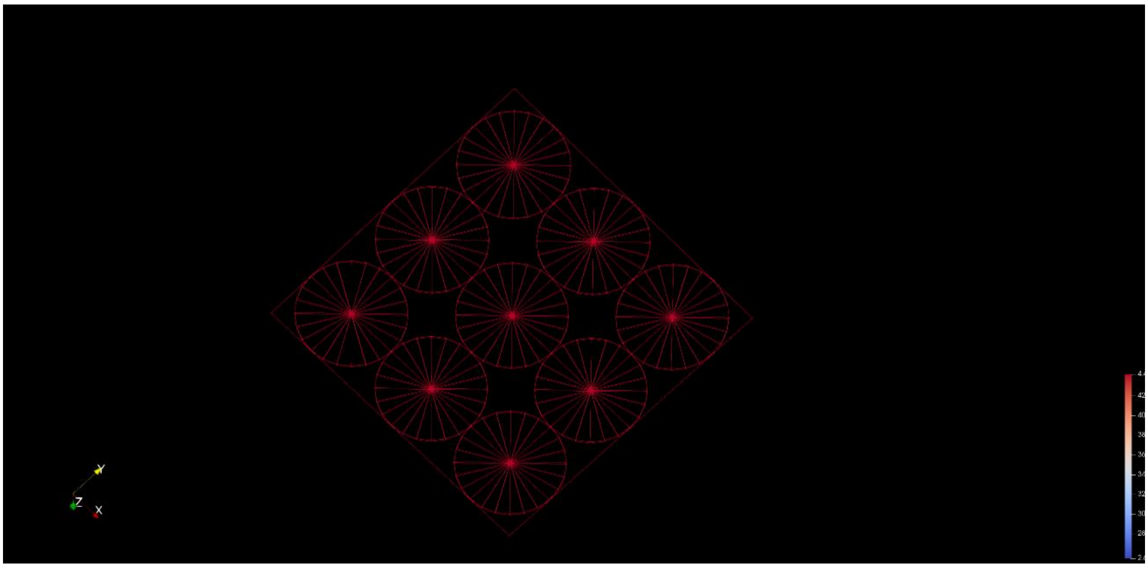

Figure 8.10 Laue collimator geometry with nine Laue lenses.

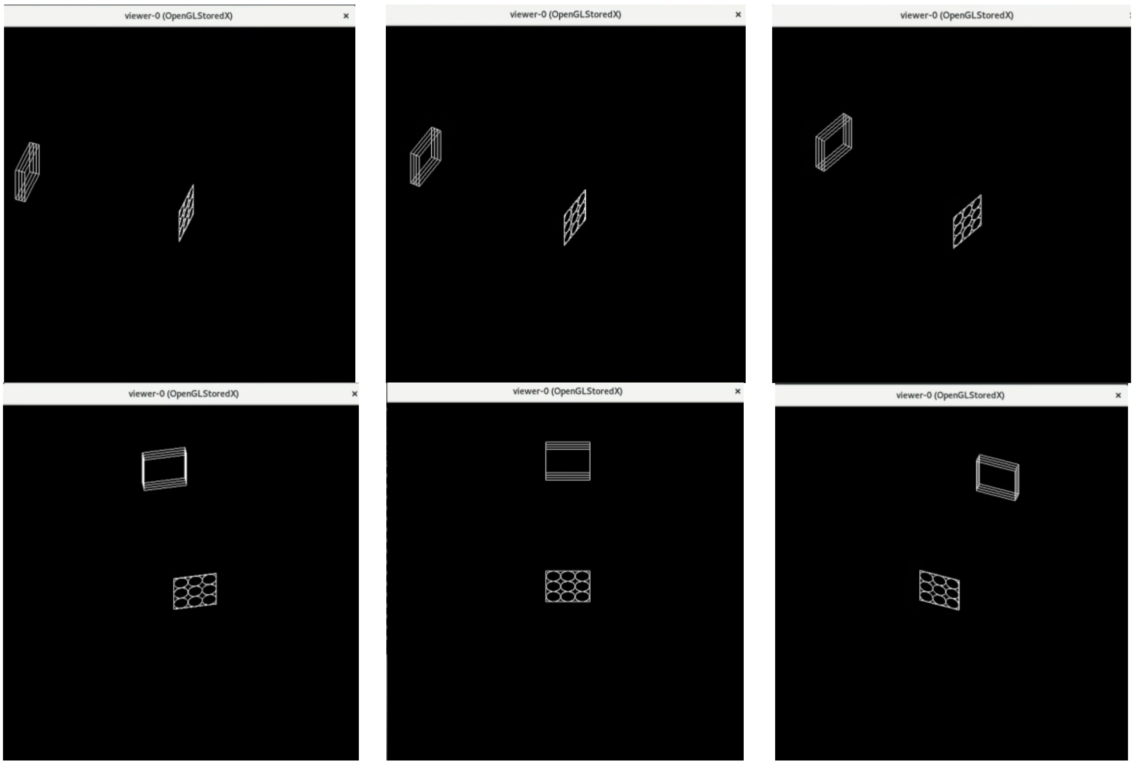

Figure 8.11 Geometry of the multi lens-based SPECT at different rotation angles.

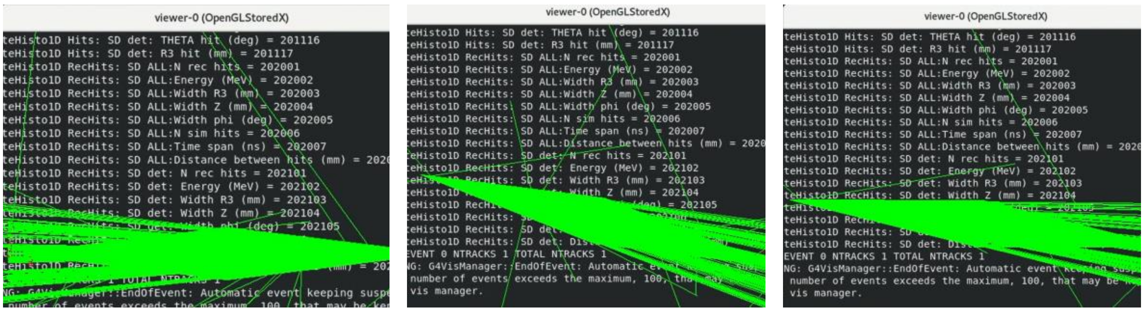

Figure 8.12 Focused gamma rays at different rotation angles show the different focused beam's directions diffracted towards different focal points of different lenses.

8.3.1 One-Point Source Case Study

Figure 8.13 shows the T_c^{99} one-point source radiations directed to the Laue collimator, where the nine lenses are located.

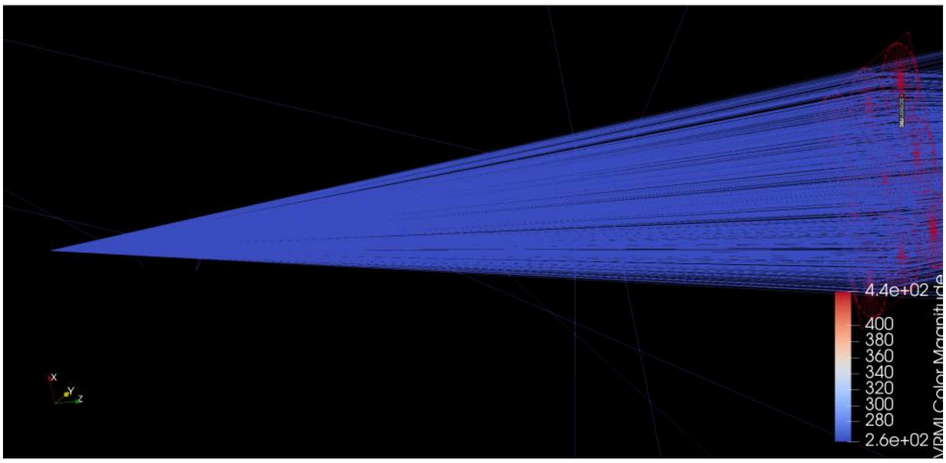

Figure 8.13 TC^{99} one-point source radiations are directed to the nine Laue lenses.

8.3.1.1 3D Image Reconstruction

Figure 8.14a shows the pixelated image of a TC^{99} one-point source for an array of Laue lenses. Figure 8.14b and Figure 8.14c show the XY and XZ slices of the 3D reconstructed images for nine Laue lenses and TC^{99} one point source, respectively. The projection image exhibits nine distinct points on the detector. Despite the non-controlled conditions and the imposed detector effects, the reconstruction process yielded satisfactory results in terms of getting successful at capturing multiple sources, which highlights the capabilities of the Laue lenses in accurately detecting and imaging the targeted object, and it provides compelling evidence of the effectiveness and viability of the detector configuration.

However, by looking at Figure 8.14c, the occurrence of the back rays can be noted; this is attributed to the back projection of the rays during the reconstruction process.

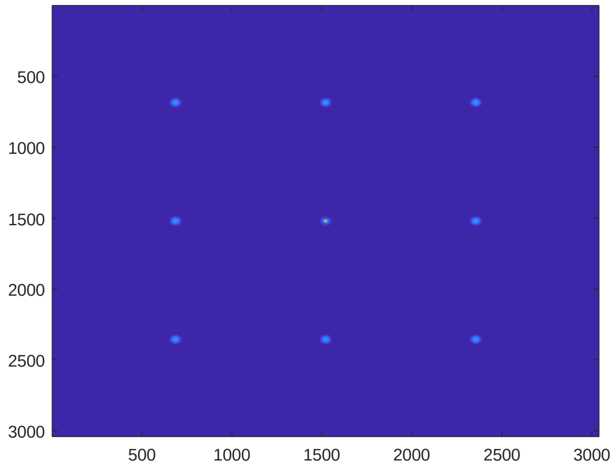

(a)

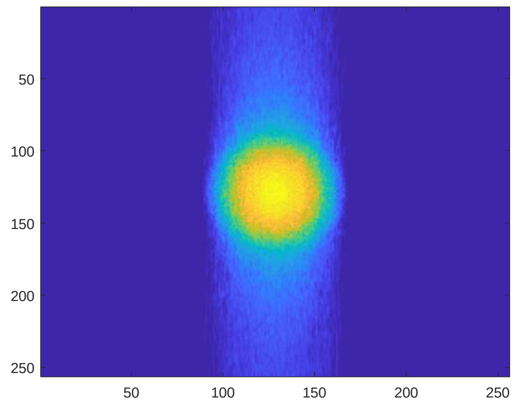

(b)

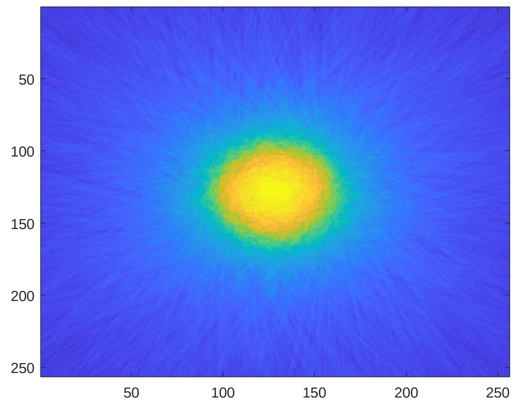

(c)

Figure 8.14 (a) Pixelated image of a TC^{99} one-point source for an array of nine Laue lenses. The x-axis represents the column index, and the y-axis represents the raw index of the pixelated projection image, (b) XY slice of the 3D reconstructed image, (c) XZ slice of the 3D reconstructed image. The X and Y measurements are in mm.

8.3.2 Three-Point Source Case Study

Using the multi-Laue lens geometry presented in Section 8.3, I repeated the case study but with a TC^{99} three-point source.

8.3.2.1 3D Image Reconstruction

Figure 8.15a shows the pixelated image of a TC^{99} three-point source for an array of Laue lenses. Figure 8.15b and Figure 8.15c show the XY and XZ slices of the 3D reconstructed images for nine Laue lenses and a TC^{99} three-point source, respectively. The multi lens-based case study confirmed the successful resolution of the spheres in the 3D reconstructed images under the proposed detector design, accounting for applied detector effects. Furthermore, it is in agreement with the obtained results and the idealized scenario, but with lower resolution. However, when using the GAMOS and GEANT3 simulation frameworks, the addition of detector effects can significantly degrade the image quality. One notable effect is the slight overlap between the reconstructed spheres in the 3D images, which is evident in Figure 8.15b and Figure 8.15c. The projection image shows that the spheres are still resolved, however, these effects align with both the acquired results and the expected idealized scenario; however, they do result in a reduced resolution. Notably, in the utilization of the GAMOS and GEANT3 simulation frameworks, introducing detector effects notably degrades image quality. One significant outcome of this degradation is the slight overlap observed between the reconstructed spheres

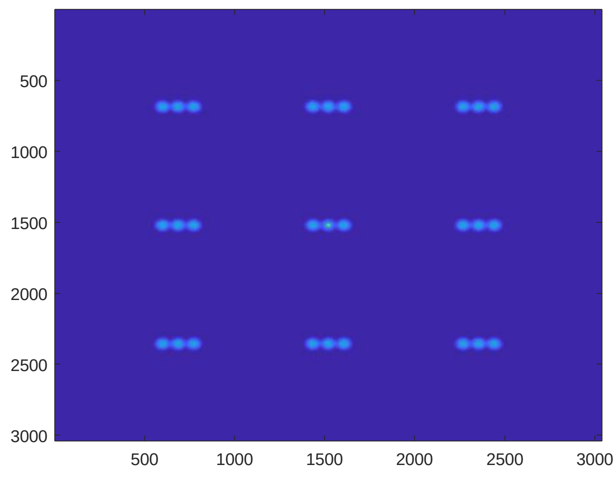

(a)

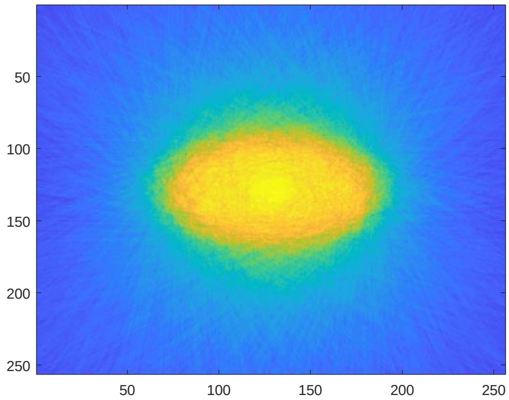

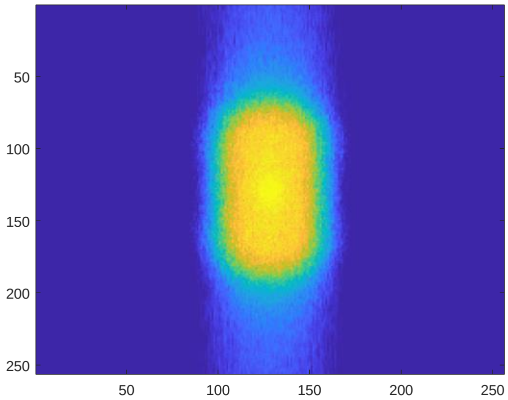

(b) **(c)**

Figure 8.15 (a) Pixelated image of a TC^{99} three-point source for an array of nine Laue lenses. The x-axis represents the column index, and the y-axis represents the raw index of the pixelated projection image, (b) XY slice of the 3D reconstructed image, (c) XZ slice of the 3D reconstructed image. The X and Y measurements are in mm.

8.4 LEHR SPECT Geometry

To establish a comparative study with existing conventional SPECT, SIEMENS' Symbia LEHR SPECT was modelled based on its system specifications and the collimator parameters. The SIEMENS Symbia T camera is a dual-head SPECT camera including a low-energy high-resolution (LEHR) collimator, a scintillation crystal, a light path, and an array of photomultiplier tubes [359]. The low energy high resolution (LEHR) collimator consists of a slab filled with lead material and parallel hexagonal holes with cells measuring $0.111\ cm$ in hole diameter, $0.016\ cm$ in septal thickness, and $2.405\ cm$ in height. The detector is comprised of sodium iodide NaI(TI) scintillation crystals and measures $0.9525\ cm$ in thickness and $53.3\ 38.7\ cm^2$ in area. The crystal dimensions are $59.1\ cm \times\ 44.5\ cm \times\ 0.95\ cm$. Each cell's dimensions in the crystal (pixels) are $0.1\ cm \times\ 0.1\ cm\ \times 0.95\ cm$. The number of pixels inside the detector crystal is $591\ \times 591$.

8.4.1 Geometry

Figure 8.16a shows different views for the LEHR collimator consisting of a slab filled with lead material and parallel hexagonal holes. Figure 8.16b shows the side view for the hexagonal tubes modelled in GAMOS. Figure 8.16c shows the SIEMENS Symbia LEHR camera head modelled in GAMOS. Figure 8.17a and Figure 8.17b show different rotation angles for the Symbia LEHR camera head and the source radiations directed towards the parallel hole, respectively. The radius of the sphere is 0.03 mm, and the distance between the spheres from centre to centre is 0.1 mm.

8.4.2 Reconstructed Hits

Figure 8.18a and Figure 8.18b show the transmitted radiations to the detector plane and the spot of the reconstructed hits on the detector plane, respectively.

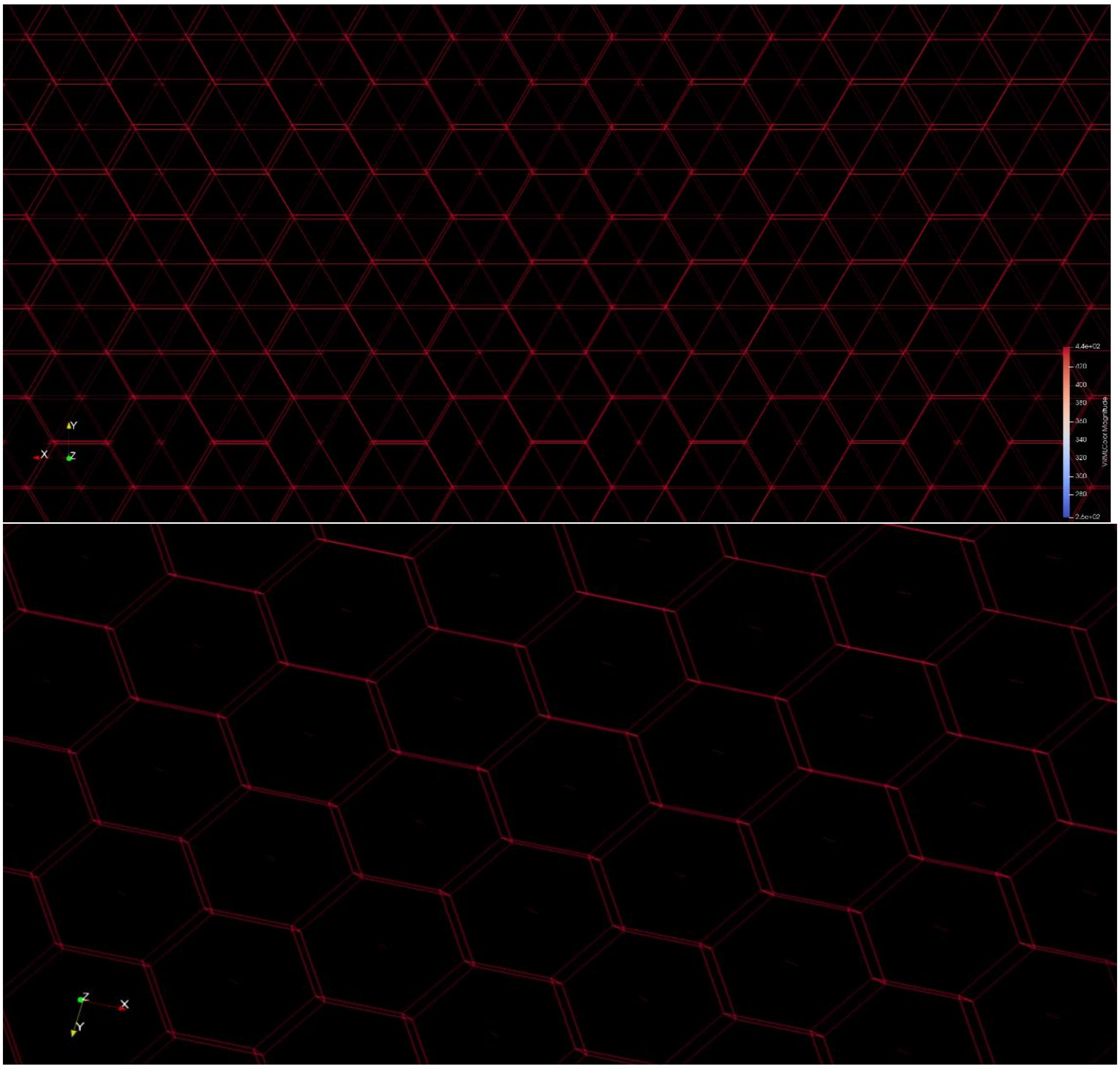

(a)

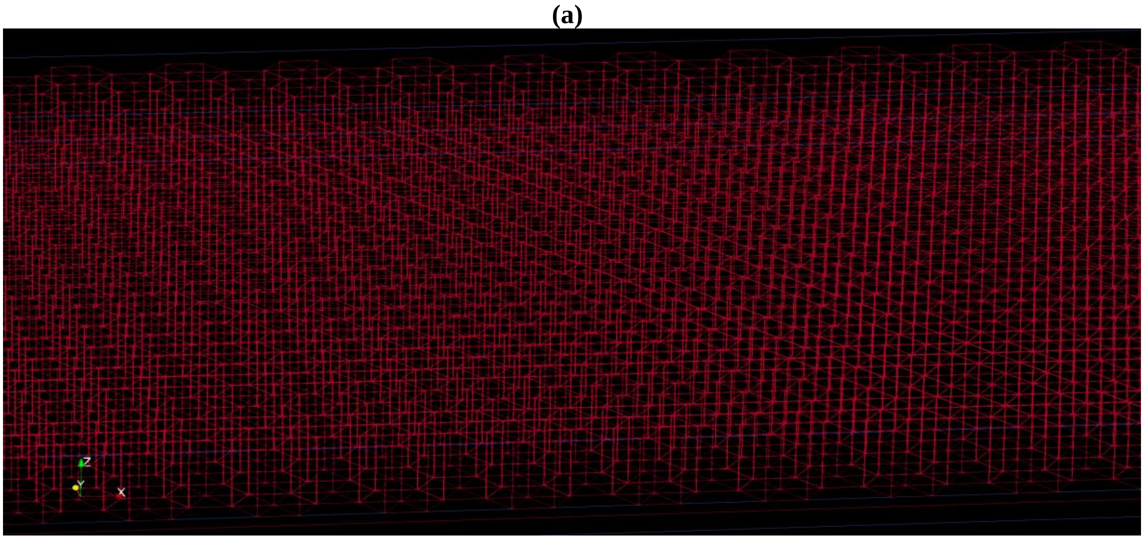

(b)

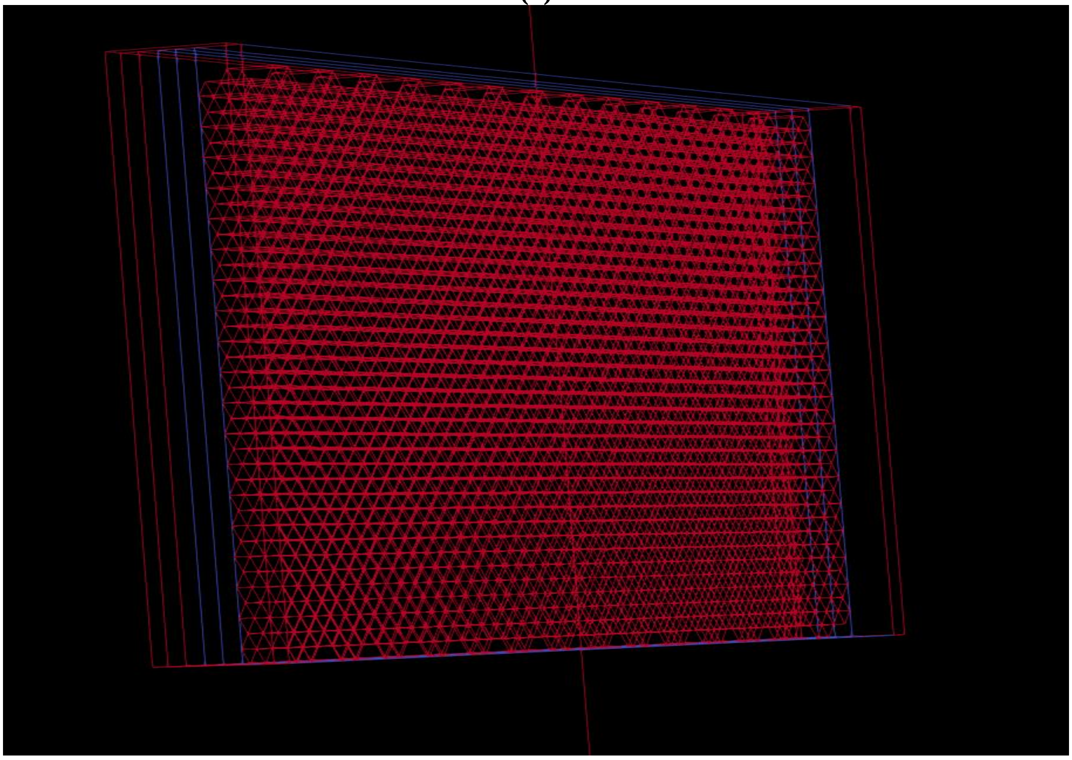

(c)

Figure 8.16 (a) Modelled hexagonal pinholes in the LEHR SPECT collimator, (b) Depth of the hexagonal tubes of pinholes in the LEHR SPECT collimator, (c) Modelled Symbia LEHR camera head.

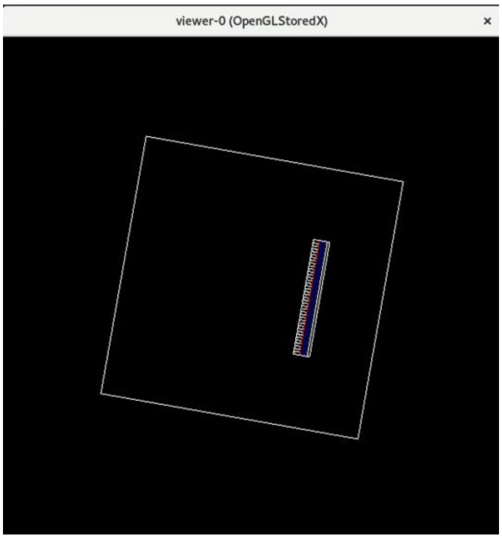

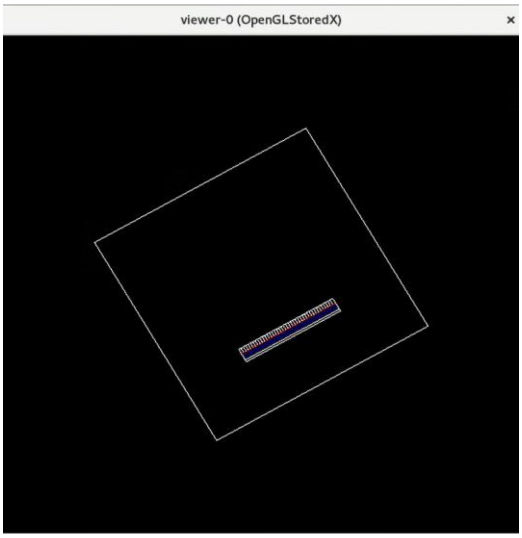

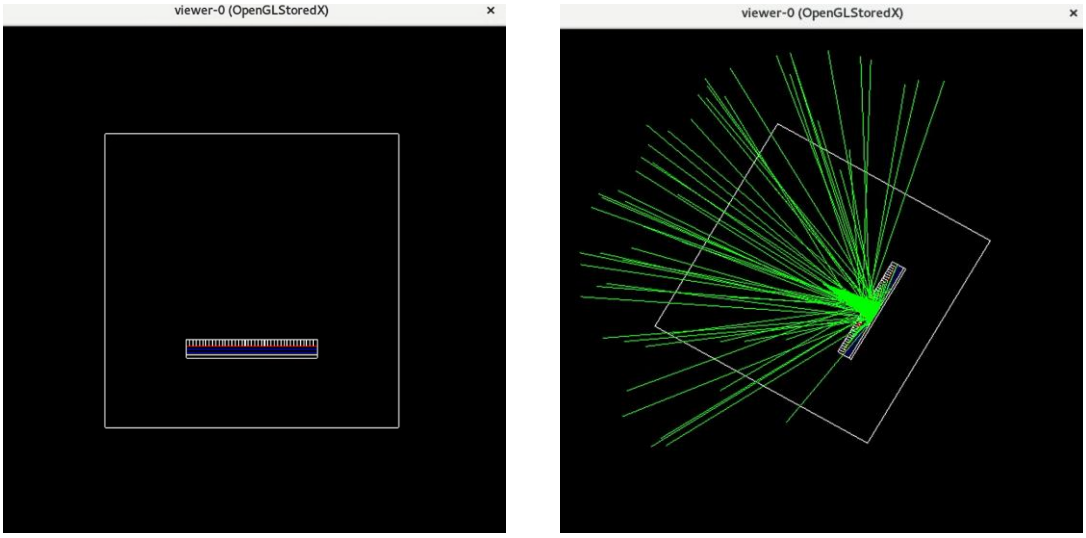

(a)

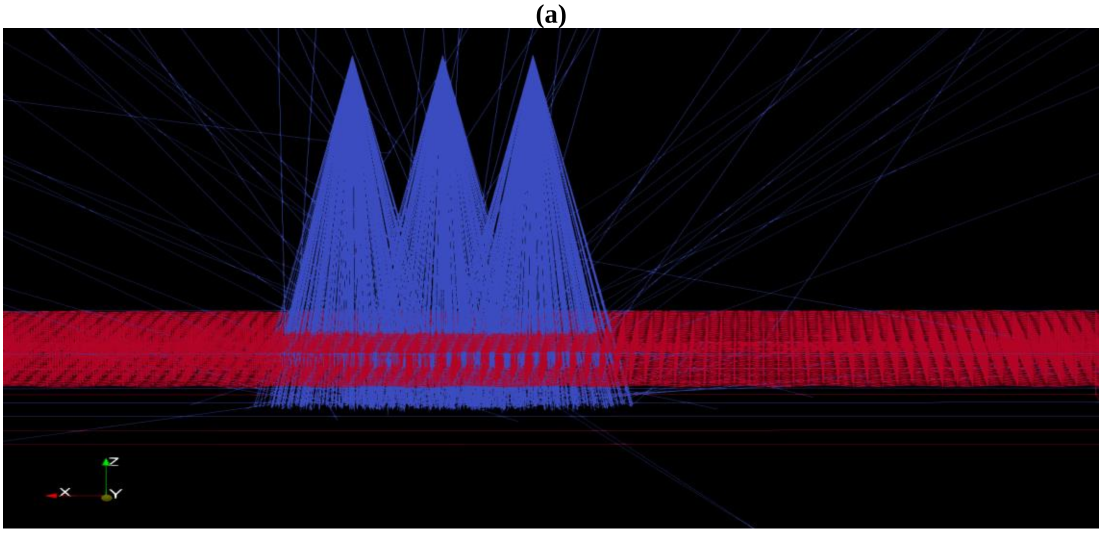

(b)

Figure 8.17 (a) Different rotation angles for the Symbia LEHR camera head, (b) The TC^{99}source radiations directed towards the parallel hole.

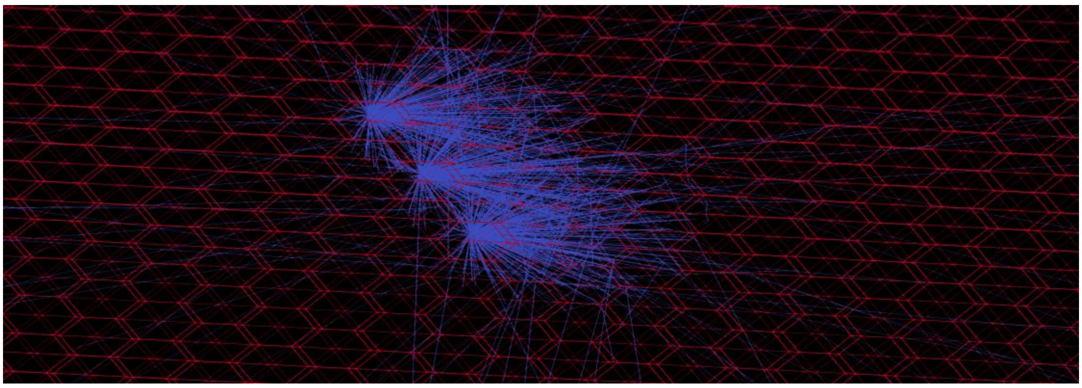

(a)

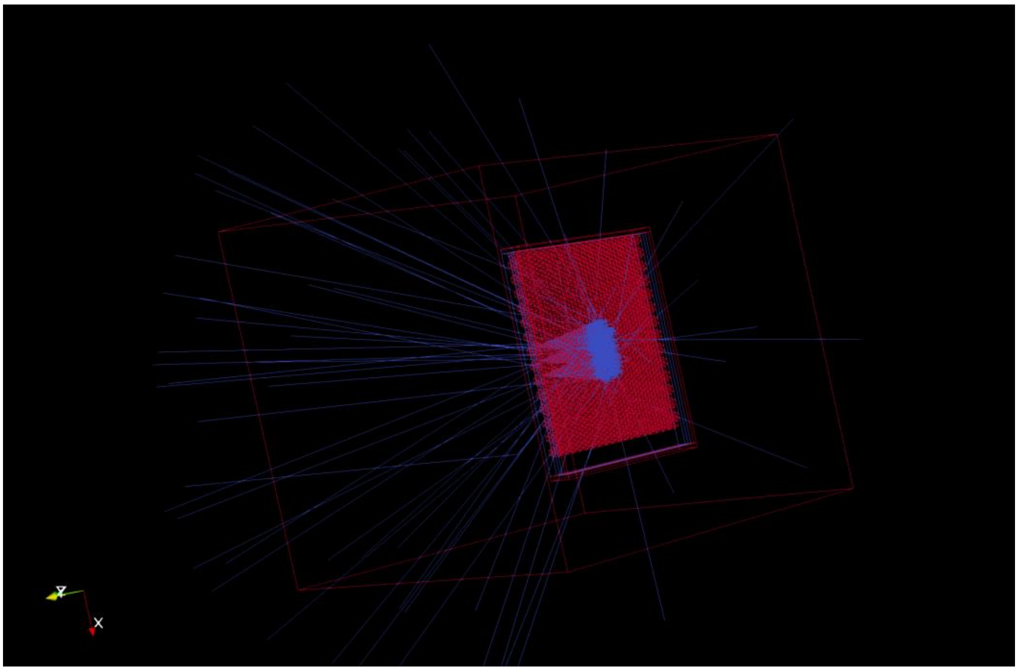

(b)

Figure 8.18 (a) Transmitted radiations to the detector plane, (b) Spot of the reconstructed hits on the detector plane.

8.4.3 3D Image Reconstruction

The pixelated projection image of the LEHR SPECT using a TC^{99} three-point source and collimator thickness $24\ mm$ is shown in Figure 8.19a. It is clear that the three spheres were not resolved using the LEHR collimator. Despite the fact that increasing the LEHR collimator thickness could potentially improve image resolution, several challenges arise that make this approach problematic and it is considered impractical. I ran a second case study with increasing the LEHR collimator thickness from $24\ mm$ to $100\ mm$. Figure 8.19b shows the pixelated projection image of the LEHR SPECT using a TC^{99} three-point source with collimator thickness of $100\ mm$. Figure 8.19c shows the 3D reconstructed image for the 24 mm collimator thickness. The smallest detectable volume that can be resolved by LEHR SPECT typically ranges from approximately $0.1 - 0.2\ mL$ [360]. This level of resolution is achieved through the use of high-resolution collimators and advanced imaging techniques. While LEHR SPECT excels in achieving high-resolution in conventional imaging, its capability to detect minute volumes is limited. LEHR SPECT typically operates within the millilitre range [355]. Consequently, the detection and resolution of volumes smaller than this range, including the $0.113\ nL$ volumes detected by lens-based SPECT, is not feasible using LEHR SPECT, as demonstrated in Figure 8.19b. Therefore, lens-based SPECT stands out for ultra-sensitive applications requiring the detection of extremely small volumes. It is evident that increasing the LEHR thickness to $100\ mm$ was not an effective solution for resolving the spheres, as seen in Figure 8.19b and Figure 8.19c.

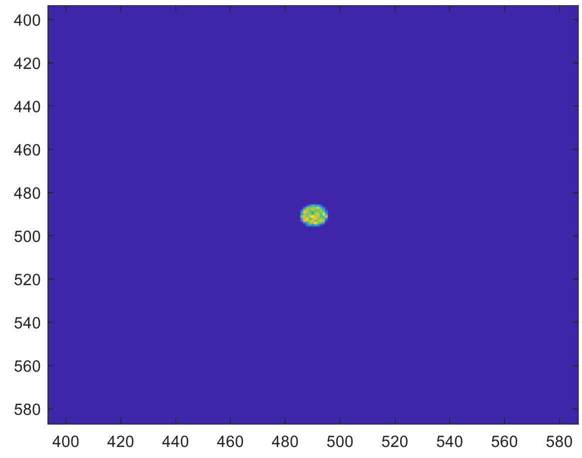

(a)

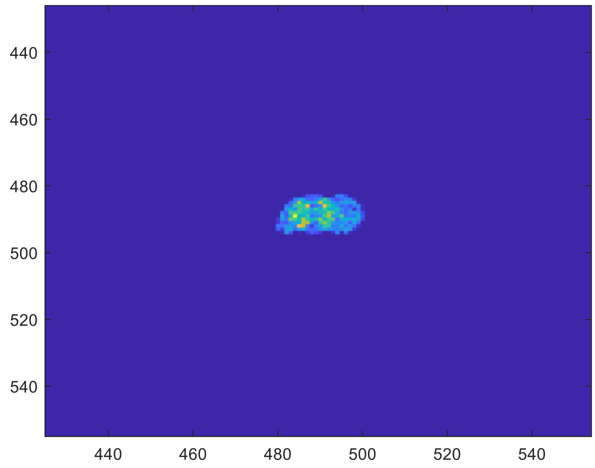

(b)

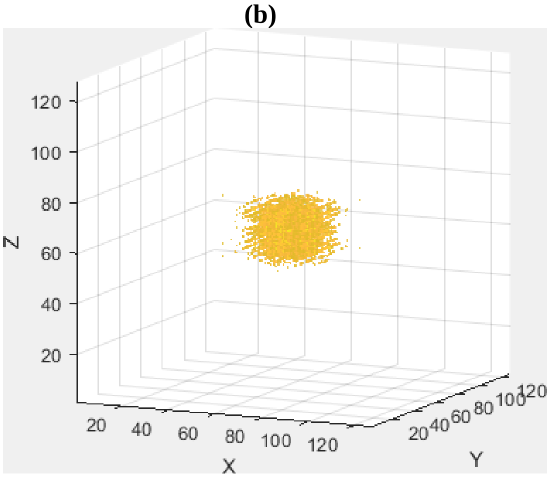

(c)

Figure 8.19 (a) Pixelated projection image of the LEHR SPECT using a TC^{99} three-point source and collimator thickness 24 mm. The x-axis represents the column index, and the y-axis represents the raw index of the pixelated projection image, (b) Pixelated projection image of the LEHR SPECT using a TC^{99} three-point and collimator thickness 100 mm, (c) 3D reconstructed image for the the 24 mm collimator thickness. The X and Y measurements are in mm.

8.5 Chapter Summary

In this chapter, the case studies were conducted using a detector concept designed with parameters specifically tailored for the envisioned lens-based SPECT. I conducted four case studies; the first configuration is a single lens in a pinhole with a single-point source. The second design is the single lens in a pinhole with a three-point sources. The third and fourth case studies concern multi-Laue lenses in multi-pinhole arrangement with single and three-point sources, respectively.

To test the validity and the feasibility of the detector design that I proposed for the envisioned system, the 3D images were generated using the 3D reconstruction algorithm that I developed for each of the different configurations.

In addition, for comparison purposes, I built the conventional LEHR SPECT collimator and detector geometry in GAMOS to evaluate its performance against the suggested lens-based SPECT based on the proposed detector configuration. Based on the visual assessment of the 3D reconstructed images, it can be concluded that the proposed lens-based-SPECT has the ability to detect minute volumes with $0.1\ mm$ resolution. However, the three spheres were not resolved using the model based on the specifications of conventional SIEMENS Symbia LEHR SPECT. Moreover, the 3D reconstruction images presented in this chapter confirm the argument stated throughout the thesis and one of the main thesis objectives, which is the capability of the lens-based SPECT to detect volumes as small as $0.113\ nL$. The lens based SPECT exhibits a substantially smaller volume range of detection or resolution compared to the conventional parallel collimator SPECT.

8.6 Acknowledgement

This chapter articulates and expands on work for which the concepts and basic findings were partially published in:

1. A. Barhoum, M. Tahtali and R. Camattari and Susanna Guatelli. (2022, October). The GEANT4-Gamma Diffraction Code Based on Laue lens Modelling: Design Foundation and Implementation of the First Set of Models in GEANT4. In 2022 the Fourth GEANT4 International User Conference at The Physics-Medicine-Biology Frontier.

8.7 Scientific contribution

- Contributed to extending GAMOS functionality by developing a GAMOS based detector simulation example for Laue lens diffraction as a first attempt. The example has been reviewed by Professor Pedro Arce, CERN, GAMOS 6.3.0

9. Conclusions, Summary and Future Work

This chapter presents a comprehensive summary and reflection on the principal findings and conclusions derived from the extensive research undertaken within this thesis. Moreover, it discusses the broader implications in light of the evidence and experimental results presented in this thesis. The results provide valuable insights into the application of the Laue lens in SPECT imaging and have direct relevance to the research objectives I initially set out to address.

9.1 Introduction

The overarching objective of this thesis was to explore and investigate the development of an innovative lens-based SPECT system augmented with an array of Laue lenses. The aim was to leverage the capabilities of gamma focusing in SPECT medical imaging to attain an unparalleled level of submillimeter resolution without relying on the conventional pinhole concept. Moreover, it discusses the implications of the envisioned system improving a new paradigm in SPECT imaging.

To accomplish this, several toolkits (MATLAB, GAMOS, GEANT4) were utilized to develop dedicated Monte Carlo simulations for the different geometries of the proposed lens-based SPECT system. In order to validate the feasibility of the proposed lens-based system, the obtained projection images in each environment underwent a rigorous calibration process. This calibration was performed to establish a consistent reference point for comparison across different environments. The calibration procedure involved aligning and normalizing the projection images from each environment, ensuring accurate and reliable performance analysis. Furthermore, a comprehensive evaluation of the system's sensitivity and resolution was carried out by comparing the three developed Monte Carlo implementations. These implementations were specifically designed for the proposed lens-based SPECT, enabling an in-depth assessment of its performance characteristics. By quantitatively analysing sensitivity and resolution metrics, I aimed to evaluate the system's capability to accurately detect and resolve target features. This comparative analysis serves as a robust validation of the proposed lens-based SPECT and provides valuable insights for further optimization of the system.

Moreover, in this concluding chapter, I acknowledge the research limitations and challenges encountered throughout the study as a critical step toward fostering future growth and enhancing the quality of subsequent investigations of the lens-based SPECT system. Additionally, I present potential avenues for future work, indicating promising directions for further exploration and advancement.

This chapter is organized as follows: Section 9.2 discusses the main research finding. Section 9.3 discusses the summary of the thesis work for each of the chapters separately. Sections 9.4 and 9.5 critically discuss the research limitations and challenges, and future work, respectively. Section 9.6 presents the final discussions and conclusions.

9.2 Key Research Findings

This thesis's culmination has yielded key findings that contribute to the understanding of the application of the Laue lens in SPECT medical imaging, which shed light on crucial aspects of SPECT imaging and the notion of focusing gamma rays via diffraction.

One of the noteworthy findings of this research entails conceptualising a Laue lens tailored and optimized specifically for SPECT applications. While the design parameters of this envisaged lens bear resemblance to those commonly employed in astrophysics, the design methodology employed in this study differs substantially. Unlike the scenario in astrophysics, where polychromatic radiated hard X-rays from distant celestial sources are presumed to be parallel, nuclear imaging involves the emission of divergent monochromatic photons. In this investigation, the choice of materials for the lens components was predicated by a Monte Carlo simulation encompassing diverse single-crystal materials with favourable lattice plane orientations. Notably, the specific lens design that resulted from this research represents a hitherto unexplored avenue in the existing scholarly discourse.

One of the significant research contributions of this thesis is the development of the initial geometry for a lens-based SPECT system. This achievement involved realizing and understanding a novel geometry for effectively integrating a Laue lens within a SPECT gamma camera setup. I also systematically presented the progressive development and evolution of the lens-based SPECT system across three distinct geometries (single, modular and multi). Throughout this iterative process, I consistently validated and optimized the performance parameters associated with each geometry.

The methodology followed throughout this research was characterized by its adherence to standardized approaches. Furthermore, the utilized toolkits for Monte Carlo simulations are known as stable and reliable environments, ensuring the robustness of the analyses conducted. In this investigation, novel tracking Monte Carlo simulation frameworks were developed in three stable Monte Carlo toolkits. These simulation environments were meticulously tailored to accommodate the parameters of the SPECT gamma camera settings marking a pioneering approach in this research field.

One of the notable findings and contributions of this research is the development of a 3D reconstruction algorithm to demonstrate the feasibility, viability of the design, and functionality of the visualized lens-based SPECT and to produce visual evidence of the system's ability to capture and reconstruct 3D information of the radiotracer accurately. The success in reconstructing the 3D images pushed this research further to benchmark the performance parameters, identify limitations, and explore potential opportunities for enhancement.

One of this research's vital findings pertains to the results of the comparative study. The comparative study aimed to compare the performance of the proposed lens-based SPECT system against existing imaging modalities or approaches, such as SIEMENS LEHR parallel SPECT and multi-pinhole Inveon SPECT. It was found that the sensitivity of the lens-based SPECT is comparable to conventional SPECT imaging techniques. However, the system achieved an unprecedented level of resolution of $0.1\,mm$, surpassing the capabilities of existing systems. The single lens-based SPECT detected one hit per 42 source photons, corresponding to a sensitivity of $790\ cps/\mu Ci$. The modular lens-based SPECT detected three hits per 42 source photons, corresponding to a sensitivity of $2{,}373\ cps/\mu Ci$. The multi lens-based SPECT detected one hit per 20 source photons, comparable to a sensitivity of $1{,}670\ cps/\mu Ci$.

Furthermore, the lens-based SPECT system exhibited superior performance regarding the minimum detectable volume. Its abilities exceeded those of the existing systems, enabling the detection of volumes as low as 0.113 nL with enhanced accuracy and precision. The system's ability to maintain sensitivity while achieving exceptional resolution and improved detectability of smaller volumes positions it as a promising candidate for enhancing the capabilities of medical imaging in terms of early detection of cancer.

Another significant finding was based on the conducted experiments using real detector properties and applied effects to achieve realistic and accurate results. By considering factors such as detector response, dead time, energy resolution, spatial resolution, and other relevant parameters, it was possible to simulate and reproduce the actual conditions encountered in practical scenarios in SPECT imaging detector behaviour and to enhance the realism and fidelity of the obtained results.

The development of a Laue lens diffraction plug-in and an advanced example for the GEANT4 toolkit, which I hope to have it available as open source once I get the GEANT4 developers' approval, are amongst the main contributions. This example has paved the way for setting up realistic experiments and obtaining accurate results for the proposed lens-based SPECT system.

9.2.1 Implications of Research Findings

In this section, I am setting the stage for discussing the broader significance and practical applications of the stated research findings. The implications that I am discussing in this section are closely tied to the stated research questions and problems that kicked off the start of this thesis work. The findings of this thesis have important implications that extend beyond the boundaries of this study and have meaningful contributions to the field of SPECT imaging.

The introduction of a lens-based focusing holds the potential to establish a new SPECT imaging technology that combines elements of tomosynthesis and lightfield imaging. Tomosynthesis is a technique that involves capturing multiple X-ray images from different angles and using them to reconstruct a three-dimensional representation of the imaged object [361]. By applying a similar concept to SPECT imaging with the lens-based system, it becomes possible to acquire multiple projections or views of the radiotracer distribution within the body. Furthermore, lightfield imaging refers to a method that captures both spatial and directional information of incoming light rays, allowing for post-acquisition refocusing and depth estimation [132]. Incorporating this concept into the lens-based SPECT system enables the capture of additional information about the radiotracer distribution, such as the direction and angle of emitted gamma rays. This multidimensional dataset can provide more accurate localization and characterization of the radiotracer distribution, leading to enhanced diagnostic capabilities and more precise treatment planning [133, 309].

The spatial resolution of the conventional LEHR SPECT technique is restricted to $1 - 2\ mm$ [117-119]. Due to the small size of rat subjects, spatial resolutions must be at the submillimeter levels. In addition, the sensitivity must be sufficient to provide an acceptable image. Submillimeter resolution is crucial for studying anatomical structures, physiological processes, and the distribution of radiotracers within small animal models. The outstanding resolution capabilities of a lens-based SPECT system that resulted from employing the focusing effect significantly contribute to both small animal and molecular research. The focusing effect of the lens-based SPECT system also contributes to the reduction of back-scattered radiations, thus increased SNR leading to improved image quality. This enables researchers to improve the accuracy and reliability of image interpretation.

Current imaging systems, such as conventional SPECT, encounter challenges and limitations in detecting cancer at early stages due to restricted resolution, sensitivity, and the inability to detect volumes in the sub mL range. These limitations hinder the identification of small, early-stage tumours when they are most treatable and potentially curable.

Also, these limitations impact the system's ability to distinguish small lesions compared to healthy background tissues. Cancerous cells proliferate and evolve within minute volumes before they become detectable by conventional SPECT or PET imaging techniques. Based on the findings and the visual evidence provided by the 3D reconstructed images, the lens-based SPECT presents a promising and feasible solution to overcome these limitations and improve early-stage cancer detection.

The intention behind using low activity phantoms in the experiments presented throughout this thesis served to answer another specific research problem: whether the lens-based SPECT would be effective in reducing the amount of injected radiotracers substances to the patients and to assess its capability to detect and visualize abnormalities with reduced doses of radiotracer administered to the patient. The experimental results show that the lens-based SPECT can distinguish and differentiate small volumes in the range of $0.113\ nL$ with low activity.

Finally, the development of my own advanced example and plug-in in GEANT4 for the Laue diffraction process presents an important contribution to the existing body of knowledge. Moreover, it would provide researchers with a tool to simulate and study the gamma diffraction phenomena in a controlled and customizable environment for different applications, and it also provides us with a foundation for further exploration and improvement to the lens-based SPECT system design.

9.2.2 Highlights of Chapter 1: Introduction

In Chapter 1, an overview of the conventional medical imaging techniques, namely PET and SPECT, was provided, highlighting their strengths and pitfalls. The identified pitfalls and problems associated with these techniques established the existing gaps which guided this research. Furthermore, the research problems and motivations were presented, outlining the rationale for undertaking this study. Moreover, the research contributions were also clearly identified,

9.2.3 Highlights of Chapter 2: Literature Review

In Chapter 2, I examined in depth the many proposed designs of SPECT collimator and detector design optimization strategies in light of the most recent developments. Presented were studies that provided insights and expert commentary on the path and future of SPECT design research. The literature on the influence of pinhole size, shape, material, and geometry on the performance and resolution of SPECT imaging in determining the ideal collimator design and the effect on the final 3D reconstructed images is reviewed in detail.

In addition, the strategies offered to minimize the effects of multiplexing, system customization, and task-based imaging technologies that gave rise to adaptive SPECT were investigated. The recently shown technologies and geometries for SPECT detectors, as well as the available strategies for increasing light extraction, are investigated. SPECT imaging based on the lightfield is evaluated in light of the most recent technological breakthroughs and emerging trends. The history of Laue lens applications in astronomy and their expanded use in nuclear medicine are thoroughly examined. Moreover, the simulation tools and specific Monte Carlo settings built for the MATLAB, GAMOS, and GEANT4 toolkits are described.

9.2.4 Highlights of Chapter 3: Methodology

The Methodology chapter provided a comprehensive overview of the research approach and a roadmap for the research process. In this chapter, I delved into the specific research methods and procedures employed in this study and the methodology followed in this thesis by describing the simulation tools and the designed environment setups. Additionally, I briefly discussed the potential limitations and challenges associated with the designed methods, including all the limitations I encountered due to the long computation times and the steps taken to mitigate them.

9.2.5 Highlights of Chapter 4: A Novel Ultra High-Resolution Lens-Based SPECT: Insight to Lightfield Imaging: MATLAB Monte Carlo Study

In Chapter 4, I demonstrated a new SPECT system that allows for molecular imaging of small objects with enhanced sensitivity and in high-resolution. The system is integrated with unique tools to boost focusing capabilities and associated sensitivity for imaging the animal's small areas and specific regions. The lens-based SPECT combines a collimator with Laue lenses and a moving detector setup. With the aid of the Laue lens focusing capabilities, the system design incorporates preselection of the field of view, enhancing the sensitivity. The new gamma focusing features significantly improve the proposed system over conventional collimation methods. The characterization of the initial performance of the system based on sensitivity and resolution were evaluated for different phantom experiments. The attained resolution is unmatched by any of the previous conventional SPECT systems. The focused imaging enables studying a specific region of interest with improved sensitivity. The simulation experiments and ideas given in these results presented in this chapter may provide insight for further advancements beyond the existing state-of-the-art in small animal SPECT imaging.

9.2.6 Highlights of Chapter 5: Modular and Multi-Lens-Based SPECT Geometries with Dedicated Reconstruction Algorithms: Monte Carlo Study

In Chapter 5, for the sake of enhancing the sensitivity, I introduced and elaborated upon the proposed system together with an appropriate validation method and evaluated the high-resolution capabilities of improved lens-based SPECT geometries. I started by introducing the modular lens-based SPECT system design and assessed the initial performance parameters. The Laue lenses are placed in tiled planes in a modular fashion and with detector geometry in such a way that their fields of view converge. The feasibility of the proposed system is demonstrated by the Monte Carlo simulation. Given the new geometry and data acquisition protocol for the modular multi lens-based SPECT, the FOV cannot be determined straightforwardly. The overall FOV of the system is the portion of the potential FOV, which can be reconstructed by having enough number of views and with enough disparity between the acquired projection data of the views. Hence, the FOV was determined based on the module width and the lens' focal length. The performance parameters were contrasted against the existing SPECT for system validation purposes. Moreover, the sensitivity mapping over the modules' FOV showed a gradual degradation; however, it still outperformed the parallel LEHR. The lens has two distinguishing features: first, its effectiveness does not diminish when the size of the source decreases, as it is the case with many existing imaging systems. Second, it can locate and identify objects with millimetre resolution. The preliminary evaluation of the system using 3-point sources is presented. By scanning the source with multiple lenses that look at the same volume from different angles, one can generate a three-dimensional image. Monte Carlo simulations were used to accurately model and evaluate the proposed concept and design. Furthermore, a dedicated image reconstruction algorithm was developed and validated for the system.

Then, I moved further and described the development and analysis of a new multi lens-based SPECT in a plane geometry that, through a novel approach to focused gamma rays, would potentially provide improved performance compared to conventional SPECT. Physical principles governing the design of this system are presented, along with a series of measurements analysing various characteristics of the generated projection and 3D reconstructed images.

The multi lens-based SPECT system uses a novel design that enables high resolution image acquisition. The system is aimed to be adapted in the future for use in oncology, thyroid, and breast SPECT imaging to take advantage of its high-resolution feature for early detection of tumours. The proposed system offers an exceptional sensitivity/resolution trade-off and is envisioned to be fitted with a field of view big enough to cover most vital mouse organs. The advantage of the focusing feature is that it allows for acquiring a significant number of projections from a single point of focus. Extending the FOV is feasible by moving the object. This adjusts the Laue lenses to focus on different sections of the animal. Another desirability in using Laue lenses is the capacity to adjust the lens shape with ultra-high spatial resolution and sensitivity to identify sub-μCi sources as an example of the lens system's customization in medical imaging. The Laue lens' achievable resolution and sensitivity are decoupled from the geometry and depend solely on the size and orientation of the crystals, in contrast to the existing parallel SPECT systems that suffer from resolution-sensitivity trade-off. The spatial resolution is boosted by a factor of two by scaling down the lens system by a factor of two, while the lens's sensitivity to a small source is not affected because all angles remain constant [209].

Furthermore, downsizing would lessen the background noise influence caused by residual activity in non-cancerous tissue by four and sixteen times, respectively. As a result, the signal-to-background ratio and the signal-to-noise ratio rise by four and sixteen times, respectively [209, 237], this is in contrast to the LEHR SPECT, where the septa are used to prevent septal penetration at the cost of sensitivity and resolution. However, conventional planar performance metrics may not be applied to the proposed system. The challenging part has been to demonstrate how this concept applies to practical/clinical use. The National Electrical Manufacturers Association (NEMA) has established procedures to standardize the specifications of instrument performance. These, however, apply only to conventional systems and may not apply to systems with an alternative design. Consequently, direct comparisons to conventionally required results acquisition are not always meaningful.

Nonetheless, I aimed to conduct a series of case studies to demonstrate performance. The obtained performance parameters may lay a foundation for future performance metrics suitable for non-traditional instruments, such as the lens-based SPECT. The stated results indicate that, compared to the multi-pinhole Inveon and parallel LEHR collimators, the multi lens-based SPECT offers significantly higher spatial resolution (by a factor of about 10) and comparable sensitivity. In contrast to methods that rely on absorptive collimation like single- or multiple-pinhole cameras, the use of refractive optics decouples spatial resolution from sensitivity and efficiency. The conducted feasibility studies have refined and applied ray-tracing routines to design focusing optics for small animal studies. This study aims to develop a means of performing gamma rays imaging of small animals that would not rely on parallel hole collimators, as a method of offering the best prospect for achieving sub-millimetre spatial resolution. The novel approach relies on the Laue lens as a focusing element. The spatial resolution achievable is decoupled from the sensitivity and depends solely on the mosaicity and orientation of the crystals, in contrast to the existing collimators that suffer from resolution-sensitivity trade-off. However, despite the promising results, the work presented in this thesis bears several limitations. I believe that the multi lens-based SPECT is not performing optimally in its current configuration. While such a system might eventually be technically feasible, it is still uncertain whether it would be practical for biological applications.

Additionally, I understand the limitations of this approach, and the task at handis to expand future work in the following ways: The conducted case studies demonstrate the system's practicality to accurately map 3D images of the scanned small phantoms. However, there are definite limitations for high-resolution imaging of large objects that I will delineate more carefully in forthcoming publications. A future reconstruction algorithm that accounts for the probabilistic distribution behind each Laue lens will be considered. Furthermore, for the sake of reducing the uncertainty in the reconstructed image, I aim to develop a reconstruction algorithm for non-multiplexed projections by placing a slant between the Laue lenses.

9.2.7 Highlights of Chapter 6: Detector Analysis GEANT4/GAMOS: Single and Multi-Lens-Based SPECT

In Chapter 6, I aimed to assess the validity of the claim stated throughout this thesis by expanding on the prior work and analysing the response of an actual detector design to the focused Laue lens gamma rays in a stable Monte Carlo setting specialised for medical physics application. However, none of the available Monte Carlo toolkits provided the simulation of wave-based properties as the diffraction process was not implemented in any of them. To this end, I proposed an alternative method to simulate the effect of focusing the gamma rays at the sensor plane and simulate detector response due to the focused projection in GAMOS/GEANT4, besides the MATLAB Monte Carlo simulations. I developed a customised Monte Carlo model in MATLAB that simulates the Laue lens behaviour placed at the SPECT pinhole, generating the coordinates and the momentums of the diffracted photons. Those coordinates and momentums were then used to setup the TXT files, which were imported to GAMOS as the source generator inputs. The histograms of the deposited and reconstructed hits were generated. Moreover, the histograms of event generator particles may confirm the generated radiations positions were generated. Then, the hits were converted into CSV files and imported to MATLAB. The GAMOS hits were reconstructed to generate the 3D images by utilising the developed LAUE reconstruction algorithm. For a realistic detector response, a number of detector effects were simulated to reflect the real detector design. Then I applied the 3D image reconstruction algorithm to the deposited and generated hits with imposed detector effects.

9.2.8 Highlights of Chapter 7: Design Foundation and Implementation of the First Set of Models in GEANT4 for Laue Lens Diffraction: Laue lens Modelling

In Chapter 7, I discussed the first attempt to model the focusing of X-rays and gamma rays based on Laue diffraction in the GEANT4 toolset, using an advanced example. The GEANT4 Laue diffraction project proposed to produce an open-source simulation software fully integrated into the GEANT4 Monte-Carlo simulation toolkit to simulate the diffraction of the gamma rays based on the Laue lens focusing effect. Its functionality and capabilities carry on expanding at the same time as its performance is being improved. It is written in C++ and exploits advanced software engineering techniques and object-oriented technology to achieve transparency. Due to the object-oriented approach's adaptability, it is possible to simply integrate external simulation packages into the GEANT4 system as modules of physical processes. However, it is not trivial to focus X-rays with good efficiency, and the modalities of implementation of an X-rays concentrator still represent an open issue. The problem of focusing hard X-rays can be approached via a Laue lens. The designed GEANT4 example tool for diffraction serves as the foundation for this ongoing project. Moreover, it offers a simulation tool for high-energy particle diffraction processes that are vastly superior to those used in conventional engineering.

As I mentioned in Chapter 3, at the start of this research, I was inspired by the lightfield-based CT imaging concept proposed by Tahtali [253]. I had the vision to propose a lens based SPECT imaging system using a Laue lens, instead of pinholes. The later proposed L-SPECT system was also based on the concept of lightfield imaging [356] where an array of pinholes was considered.

I aimed to pick up where they left off in the lightfield SPECT experiments and draw upon the experiences I gained in GEANT4 to duplicate the real experiments they had started. The lightfield SPECT and lens-based SPECT both were the product of several attempts to reframe conventional nuclear imaging based on introducing new methods and technologies, such as the lightfield imaging.

However, I understand that the conventional planar performance metrics may not be applied to these theoretical systems. The challenging part has been demonstrating how this concept applies to practical and clinical practice. The National Electrical Manufacturers Association (NEMA) has standardised the procedures for specifying instrument performance. Thus, to demonstrate the performance, I intended to conduct a series of case studies for the previously proposed LSPECT, and the lens-based SPECT incorporated in a well-known SPECT configuration which is the SIEMENS Inveon Multi-Modality System "5-MWB-1.0" and having the NEMA NU-4 as the phantom. Figure 7.9 shows the NEMA NU-4 that I modelled in GEANT4. For the proof of concept, I designed and customised the first experiments for two different configurations in GEANT4 utilising the developed code. [362], and the second is the incorporated Laue lens with Inveon SPECT. Based on analysing the difference in the width of the R3 histogram and the width of phi angles of the reconstructed hits for both Inveon and Laue lens/Inveon, I made a final conclusion on the results. The narrower width and distinctive properties of the histograms in the Laue lens/Inveon system compared to the Inveon SPECT demonstrate its advantages in improved angular precision and higher sensitivity to different angular ranges. These capabilities are valuable in applications where precise angular mapping and sensitivity to angular variations are essential for accurate imaging.

9.2.9 Highlights of Chapter 8: First Set of Models in GAMOS for the Laue Lens Diffraction (Plugin) with detector modelling

In Chapter 8, the case studies were conducted using a detector concept designed with parameters specifically tailored for the envisioned lens-based SPECT, as opposed to putting it into a commercial SPECT configuration. I conducted four case studies; the first configuration is a single lens in a pinhole with a single-point source. The second design is the single lens in a pinhole with a three-point source. The third and fourth case studies concern multi-Laue lenses in multi-pinhole arrangement with single and three-point sources, respectively. In addition, for comparison, I designed the LEHR SPECT geometry in GAMOS to evaluate its performance against the suggested lens-based SPECT based on the proposed detector configuration. It can be concluded that the proposed lens-based-SPECT has the ability to detect nano-litre volumes with 0.1 mm resolution based on the obtained results from the three-point sphere studies. However, the three spheres were not resolved using the modelled conventional SIEMENS Symbia LEHR SPECT.

9.3 Research Limitations and Challenges

The absence of a readily available process for simulating diffraction in any of the existing Monte Carlo toolkits posed a significant challenge at the outset of this thesis. Thus, the initial conducted experiments were run under ideal detector conditions. After several attempts to develop an example for the Laue lens diffraction, I set it up and added its functionality to GEANT4, this marked a significant milestone in the research.

The extensive computation times required for the Monte Carlo experiments, especially the ones in GEANT4 and GAMOS, brought about a significant impediment posed a significant challenge during this thesis work. To overcome this challenge, considerable effort was invested in optimising the computational codes. Several iterations of code optimisation were performed. It is worth noting that code optimisation is an ongoing endeavour, and further improvements could be made beyond the scope of this thesis work. However, optimising the codes significantly contributed to the successful execution of the Monte Carlo simulations and attaining the research objectives within the available resources and time constraints.

The manufacturing of the Laue lens was not accomplished during this thesis work due to the challenges highlighted in Section 7.2. The need for conducting realistic physical experiments to push the boundaries of this research and expand its potential applications is acknowledged.

Fortunately, the need for ablating an amorphous phase to transform it into a crystalline state is not necessary for the Laue lens fabrication. Therefore, the task of fabricating the crystals can be entrusted to experts in the field. Notably, companies like Mateck, Advatech, Epic-crystal, and Saint-Gobain specialize are manufacturing these crystals and offer them commercially. However, fixing all the crystals within a frame poses a considerable challenge. Also, maintaining the crystals at the precise angle and alignment required for X-ray diffraction necessitates a high level of precision, within 10 micro radians. Achieving this level of precision is demanding and requires careful attention to detail and expertise.

9.4 Future Work

As for future work, there are several areas that can be explored to further enhance the capabilities and applications of lens-based SPECT imaging. These directions hold significant promise for improving the system design and addressing the associated limitations.

On the basis of the findings of this study, the following are some potential future directions that could be pursued to expand this research.

9.4.1 Application: Thyroid and Breast Cancer Detection

Aspects of the newly proposed system are discussed, considering their possible clinical application as a tumour detection tool that takes maximum advantage of the unique properties of the Laue lens focusing capability. Based on the achieved resolution and the capacity of the lens-based SPECT to detect nano-litre volumes, future work will be devoted to designing a Laue lens for different applications. One of the applications I have in the plan is to develop a thyroid and breast cancer detection system by optimising the Laue lens for I^{123} radiotracer. This requires optimising the Laue lens parameters to focus gamma rays at the energy range of 159 keV using the developed Monte Carlo environment.

9.4.2 3D Image Reconstruction Algorithm Optimisation

The development of dedicated 3D reconstruction algorithms for lens-based SPECT is of paramount importance. The developed Monte Carlo model will be applied for further case studies on the development and evaluation of the system and effort will be devoted to optimising the methods for image forward projection and 3D reconstruction. Exploring advanced iterative reconstruction techniques, statistical image reconstruction methods, and incorporation of anatomical methods could lead to further improvements in image quality, noise reduction, and quantitative accuracy and overcome the encountered limitations.

Moreover, the application of machine learning and artificial intelligence techniques could be applied to develop 3D reconstruction algorithm dedicated to the lens-based SPECT imaging.

9.4.3 Phantom Studies

To demonstrate the capabilities of the Laue lens for observing small sources with high spatial resolutions it is crucial to expand the scope of future investigations. In the future, it is essential to consider conducting case studies with more complicated source phantoms other than one and three-point sources to investigate the response of the lens and the effects of absorption and scattering that are expected from the body.

9.4.4 Geometry Optimization.

The phantom must be rotated to in order to acquire the projection images or the Laue lenses' plane must be rotated, to enable precise source localisation and achieve submillimetre resolution. By placing the envisioned Laue collimator on a mechanical system/arm that adapts the focal length in response to the desired depth, a submillimetre resolution and precise source localisation could be achieved. Moreover, sensitivity is expected to improve considerably with an array of Laue lenses arranged in modular fashion at angled planes and detector geometry such that the field of view of the Laue lenses placed in various planes converges. By adjusting the angles between the modular planes, it would be feasible to view the phantom from multiple perspectives using projection images from the individual Laue lenses.

9.5 Final Discussion and Conclusions

I aligned the research findings with the research questions, the research problem, and the study's implications to address existing challenges and potentially open new avenues for further exploration and development in lens-based SPECT imaging.

Throughout this thesis work, the progression of the research involved a shift from conducting ideal case studies to studying the system's behaviour in more realistic simulations with real scintillator design using custom GEANT4 example with realistic detector effects.

The initial phase of this research involved modelling the lens-based SPECT in ideal environments using MATLAB (Chapters 4 and 5). This provided a foundation for studying the system's behaviour and assessing its performance under idealised conditions. By creating a mathematical model, various system parameters and characteristics were explored and analysed in a controlled setting. The MATLAB modelling phase was significant in deducing a theoretical framework and understanding the fundamental principles for the lens-based SPECT. It provided proof of concept and the green light to go further with the formulated hypothesis.

However, the next step of conducting physical case studies was hindered by the inability to manufacture the lens within the scope of this thesis. Nevertheless, the boundaries of the research were pushed by exploring new avenues. Initially, simulation case studies were conducted using the GAMOS toolkit (Chapter 6), still, the limitations arose due to the unavailability of wave-based properties implemented as a process in any of the existing Monte Carlo toolkits.

To further advance the research, an example was developed in the GEANT4 toolkit to enable modelling of a real scintillator with applied detector effects, simulating the environment and response of a gamma camera SPECT system (Chapter 7). Once the GEANT4 example was developed, case studies were conducted, encompassing the entire process from source definition to scintillator setup.

In a final attempt to advance the research in this thesis, case studies were conducted in GAMOS using the GENAT4 plugin code that I have developed. One notable distinction in the conducted case studies here (Chapter 8), which sets them apart from previous ones, is the utilization of the envisioned detector design. Combining the Laue lens with the proposed envisioned detector design aimed to explore the system's behaviour in a more practical setting that closely resembled the intended application and to bridge the gap between theoretical considerations and real applicability.

It is worth noting that the results revealed significant differences in the images obtained with the inclusion of real detector effects compared to those obtained in the idealized environment. The observed distortions in the images highlight the influence of the detector's characteristics on the overall image quality. These discrepancies further emphasize the need to account for and address these effects when developing and evaluating imaging systems.

Although the Laue lens manufacturing was not achieved, significant strides were made in exploring and understanding the impact of realistic detector effects on the obtained images from the lens-based SPECT.

References

[1] C. Grupen and I. Buvat, Handbook of particle detection and imaging. Springer Science & Business Media, 2011.

[2] F. A. Mettler Jr and M. J. Guiberteau, Essentials of nuclear medicine imaging: expert consult-online and print. Elsevier Health Sciences, 2012.

[3] R. Cole and A.M. Hespel, "Principles of Computed Tomography and Magnetic Resonance Imaging," in Feline Diagnostic Imaging, 2020, pp. 13-26.

[4] P. Blake, B. Johnson, and J. W. J. VanMeter, "Positron Emission Tomography (PET) and Single Photon Emission Computed Tomography (SPECT): Clinical Applications," J. Nuc. Med., vol. 23, no. 1, pp. 34-41, 2003.

[5] D. L. Bailey, K. P. Willowson, and M. Imaging, "Quantitative SPECT/CT: SPECT Joins PET as a Quantitative Imaging Modality," Journal of Nuclear Medicine, vol. 41, no. 1, pp. 17-25, 2014.

[6] V. I. Mikla and V. V. Mikla, Medical Imaging Technology, Elsevier, 2013.

[7] R. J. Jaszczak, R. E. Coleman, and C. B. Lim, "SPECT: Single Photon Emission Computed Tomography," IEEE Transactions on Nuclear Science, vol. 27, no. 3, pp. 1137-1153, 1980.

[8] A. J. N. Elliott, "Medical Imaging," Nuclear Instruments and Methods in Physics Research Section A: Accelerators, Detectors, and Associated Equipment, vol. 546, no. 1-2, pp. 1-13, 2005.

[9] Y. Seo, C. Mari, and B. H. Hasegawa, "Technological Development and Advances in Single-Photon Emission Computed Tomography/Computed Tomography," Seminars in Nuclear Medicine, vol. 38, no. 3, pp. 177-198, 2008.

[10] R. A. Powsner and E. R. Powsner, Essential Nuclear Medicine Physics, John Wiley & Sons, 2008.

[11] S. R. Cherry, J. A. Sorenson, and M. E. Phelps, Physics in Nuclear Medicine, Elsevier Health Sciences, 2012.

[12] S. C. Vaz, F. Oliveira, K. Herrmann, and P. J. Veit-Haibach, "Nuclear Medicine and Molecular Imaging Advances in the 21st Century," The British Journal of Radiology, vol. 93, no. 1110, p. 20200095, 2020.

[13] R. Zimmerman, "Advances in Nuclear Medicine Imaging Instrumentation," in Medical Radionuclide Imaging, 1977.

[14] L. Bodei, K. Herrmann, H. Schoeder, A. M. Scott, and J. S. Lewis, "Radiotheranostics in Oncology: Current Challenges and Emerging Opportunities," Journal of Nuclear Medicine and Radiology and Radiation Oncology, vol. 19, no. 8, pp. 534-550, 2022.

[15] J.-H. Jung et al., "Recent Advances in Nuclear Medicine Imaging Instrumentation," IEEE Transactions on Nuclear Science, vol. 42, no. 2, pp. 98-111, 2008.

[16] P. F. Sharp, H. G. Gemmell, and A. D. Murray, Practical Nuclear Medicine, Springer, 2005.

[17] J. Van Sluis et al., "Performance Characteristics of the Digital Biograph Vision PET/CT System," Journal of Nuclear Medicine, vol. 60, no. 7, pp. 1031-1036, 2019.

[18] J. Zhang and M. V. Knopp, "Solid-State Digital Photon Counting PET/CT," in Advances in PET, Springer, 2020, pp. 53-69.

[19] P. Lecoq and P. Sciences, "Pushing the Limits in Time-of-Flight PET Imaging," IEEE Transactions on Radiological and Laboratory Medicine, vol. 1, no. 6, pp. 473-485, 2017.

[20] B. Huang, M. W.-M. Law, and P.-L. Khong, "Whole-Body PET/CT Scanning: Estimation of Radiation Dose and Cancer Risk," Radiology, vol. 251, no. 1, p. 166, 2009.

[21] D. L. Miller, B. A. Schueler, and S. J. Balter, "New Recommendations for Occupational Radiation Protection," Journal of the American College of Radiology, vol. 9, no. 5, pp. 366-368, 2012.

[22] J.S. Karp, M.E. Daube-Witherspoon, E.J. Hoffman, T.K. Lewellen, J.M. Links, W.H. Wong, R.D. Hichwa, M.E. Casey, J.G. Colsher, R.E. Hitchens, and G. Muehllehner, "Performance Standards in Positron Emission Tomography," IEEE Transactions on Nuclear Science, vol. 32, no. 12, pp. 2342-2350, 1991.

[23] T. Li, E.C. Ao, B. Lambert, B. Brans, S. Vandenberghe, and G.S. Mok, "Quantitative Imaging for Targeted Radionuclide Therapy Dosimetry - Technical Review," Theranostics, vol. 7, no. 18, p. 4551, 2017.

[24] S.R. Cherry, T. Jones, J.S. Karp, J. Qi, W.W. Moses, and R.D. Badawi, "Total-Body PET: Maximizing Sensitivity to Create New Opportunities for Clinical Research and Patient Care," Journal of Nuclear Medicine, vol. 59, no. 1, pp. 3-12, 2018.

[25] H. Phan, P. Jager, J. Plukker, B. Wolffenbuttel, R. Dierckx, and T. Links, "The Diagnostic Value of 124I-PET in Patients with Differentiated Thyroid Cancer," IEEE Transactions on Nuclear Science, year of publication 2007.

[26] I. Miederer and H. Boecker, "PET: Theoretical Background and Practical Aspects," in Functional Neuroimaging in Exercise and Sport Sciences, pp. 319-331, New York, NY, Springer New York, 2012.

[27] B. Ganguly, N. Mondal, M. Nandy, and F. Roesch, "Some Physical Aspects of Positron Annihilation Tomography: A Critical Review," IEEE Transactions on Nuclear Science, vol. 279, no. 2, pp. 685-698, 2009.

[28] A. M. Alessio, E. Butterworth, J. H. Caldwell, and J. B. Bassingthwaighte, "Quantitative Imaging of Coronary Blood Flow," IEEE Transactions on Medical Imaging, vol. 1, no. 1, p. 5110, 2010.

[29] M. M. Hanasono, L. D. Kunda, G. M. Segall, G. H. Ku, and D. J. Terris, "Uses and Limitations of FDG Positron Emission Tomography in Patients with Head and Neck Cancer," IEEE Transactions on Nuclear Science, vol. 109, no. 6, pp. 880-885, 1999.

[30] G. B. Saha, Basics of PET Imaging: Physics, Chemistry, and Regulations, Springer, 2015.

[31] A. C. Kak and M. Slaney, Principles of Computerized Tomographic Imaging, Society for Industrial and Applied Mathematics, 2001.

[32] G. B. Saha, "Radiation Biology," in IEEE Transactions on Medical Imaging, pp. 226-267, 2006.

[33] I. A. Somlai Schweiger, "Novel High-Resolution Photon Detectors for PET Imaging," Ph.D. dissertation, Technische Universität München, 2015.

[34] M. Bergström, L. Eriksson, C. Bohm, G. Blomqvist, and J. Litton, "Correction for Scattered Radiation in a Ring Detector Positron Camera by Integral Transformation of the Projections," IEEE Transactions on Medical Imaging, vol. 7, no. 1, pp. 42-50, 1983.

[35] J. S. Fowler, N. D. Volkow, G. J. Wang, Y. S. Ding, and S. L. Dewey, "PET and Drug Research and Development," IEEE Transactions on Nuclear Science, vol. 40, no. 7, pp. 1154-1163, 1999.

[36] D. C. MacLaren, T. Toyokuni, S. R. Cherry, J. R. Barrio, M. E. Phelps, H. R. Herschman, and S. S. Gambhir, "PET Imaging of Transgene Expression," IEEE Transactions on Nuclear Science, vol. 48, no. 5, pp. 337-348, 2000.

[37] T. H. A. Arulampalam, D. C. Costa, J. B. Bomanji, and P. J. Ell, "The Clinical Application of Positron Emission Tomography to Colorectal Cancer Management," IEEE Transactions on Medical Imaging, vol. 45, no. 3, p. 215, 2001.

[38] E. Lin, "F-18 Fluorodeoxyglucose Uptake in a Benign Gastric Ulcer," IEEE Transactions on Medical Imaging, vol. 32, no. 6, pp. 462-463, 2007.

[39] H. I. Kornblum, D. M. Araujo, A. J. Annala, K. J. Tatsukawa, M. E. Phelps, and S. R. Cherry, "In Vivo Imaging of Neuronal Activation and Plasticity in the Rat Brain by High-Resolution Positron Emission Tomography (microPET)," IEEE Transactions on Nuclear Science, vol. 18, no. 6, pp. 655-660, 2000.

[40] C. P. Lanting, E. De Kleine, and P. Van Dijk, "Neural Activity Underlying Tinnitus Generation: Results from PET and fMRI," IEEE Transactions on Biomedical Engineering, vol. 255, no. 1-2, pp. 1-13, 2009.

[41] S. Basu, T. C. Kwee, S. Surti, E. A. Akin, D. Yoo, and A. Alavi, "Fundamentals of PET and PET/CT Imaging," IEEE Transactions on Medical Imaging, vol. 1228, no. 1, pp. 1-18, 2011.

[42] A. Mikhno, "Non-Invasive and Cost-Effective Quantification of Positron Emission Tomography Data," Ph.D. dissertation, Columbia University, 2015.

[43] I. A. Somlai Schweiger, "Novel High-Resolution Photon Detectors for PET Imaging," Ph.D. dissertation, Technische Universität München, 2015.

[44] S. R. Cherry, J. A. Sorenson, M. E. Phelps, "Physics in Nuclear Medicine," vol. 3, Saunders, 2003.

[45] M. N. Wernick and J. N. Aarsvold, Emission Tomography: The Fundamentals of PET and SPECT, Elsevier, 2004.

[46] D. W. Townsend, J. P. Carney, J. T. Yap, and N. C. Hall, "PET/CT Today and Tomorrow," IEEE Transactions on Nuclear Science, vol. 45, no. 1 suppl, pp. 4S-14S, 2004.

[47] G. Muehllehner and J. S. Karp, "Positron Emission Tomography," IEEE Transactions on Medical Imaging, vol. 51, no. 13, p. R117, 2006.

[48] F. H. Fahey, "Data Acquisition in PET Imaging," IEEE Transactions on Nuclear Science, vol. 30, no. 2, pp. 39-49, 2002.

[49] F. R. Wrenn Jr, M. L. Good, and P. Handler, "The Use of Positron-Emitting Radioisotopes for the Localization of Brain Tumors," IEEE Transactions on Medical Imaging, vol. 1, no. 1, pp. 525-527, 1951.

[50] W. H. Sweet, "The Uses of Nuclear Disintegration in the Diagnosis and Treatment of Brain Tumor," IEEE Transactions on Medical Imaging, vol. 1, no. 1, pp. 875-878, 1951.

[51] W. H. Sweet and G. L. Brownell, "Localization of Intracranial Lesions by Scanning with Positron-Emitting Arsenic," IEEE Transactions on Medical Imaging, vol. 1, no. 1, pp. 1183-1188, 1955.

[52] S. Rankowitz, J. S. Robertson, W. A. Higinbotham, and M. J. Rosenblum, "Positron Scanner for Locating Brain Tumors," Tech. Rep. BNL-6041, Brookhaven National Lab., Upton, NY, 1961.

[53] Anger, H.O. and Van Dyke, D.C., 1964. Human bone marrow distribution shown in vivo by iron-52 and the positron scintillation camera. Science, 144(3626), pp.1587-1589.
[54] C. A. Burnham, S. Aronow, and G. L. Brownell, "A Hybrid Positron Scanner," IEEE Transactions on Medical Imaging, vol. 15, no. 3, p. 517, 1970.
[55] C.A. Burnham and G.L. Brownell, "A Multi-Crystal Positron Camera," IEEE Transactions on Nuclear Science, vol. 19, no. 3, pp. 201-205, 1972.
[56] Z.H. Cho, J.K. Chan, and L. Eriksson, "Circular Ring Transverse Axial Positron Camera for 3-Dimensional Reconstruction of Radionuclides Distribution," IEEE Transactions on Nuclear Science, vol. 23, no. 1, pp. 613-622, 1976.
[57] J.G. Colsher, "Fully-Three-Dimensional Positron Emission Tomography," IEEE Transactions on Medical Imaging, vol. 25, no. 1, p. 103, 1980.
[58] M.M. Ter-Pogossian, M.E. Phelps, E.J. Hoffman, and N.A. Mullani, "A Positron-Emission Transaxial Tomograph for Nuclear Imaging (PETT)," IEEE Transactions on Medical Imaging, vol. 114, no. 1, pp. 89-98, 1975.
[59] M.E. Phelps, E.J. Hoffman, N.A. Mullani, and M.M. Ter-Pogossian, "Application of Annihilation Coincidence Detection to Transaxial Reconstruction Tomography," IEEE Transactions on Medical Imaging, vol. 16, no. 3, pp. 210-224, 1975.
[60] Y. Jung, L.G. Jordan III, V.J. Lowe, K. Kantarci, J.E. Parisi, D.W. Dickson, M.E. Murray, R.R. Reichard, T.J. Ferman, D.T. Jones, and J. Graff-Radford, "Clinicopathological and 123I-FP-CIT SPECT Correlations in Patients with Dementia," IEEE Transactions on Medical Imaging, vol. 5, no. 3, pp. 376-381, 2018.
[61] T. Miyagawa, S. Przybelski, D. Maltais, H.K. Min, L. Jordan, T. Lesnick, M. Silber, S. McCarter, E.S. Louis, J. Graff-Radford, and D. Jones, "Longitudinal 123I-FP-CIT SPECT Imaging in Isolated REM Sleep Behavior Disorder (S1.004)," IEEE Transactions on Medical Imaging, 2022.
[62] E.E. Van der Wall, "Cost Analysis Favours SPECT Over PET and CTA for Evaluation of Coronary Artery Disease: The SPARC Study," IEEE Transactions on Medical Imaging, vol. 22, no. 6, pp. 257-258, 2014.
[63] K. Peremans, B. Cornelissen, B. Van Den Bossche, K. Audenaert, and C. Van de Wiele, "A Review of Small Animal Imaging Planar and Pinhole SPECT γ Camera Imaging," IEEE Transactions on Medical Imaging, vol. 46, no. 2, pp. 162-170, 2005.
[64] M.V. Narayanan, M.A. King, M.N. Wernick, C.L. Byrne, E.J. Soares, and P.H. Pretorius, "Improved Image Quality and Computation Reduction in 4-D Reconstruction of Cardiac-Gated SPECT Images," IEEE Transactions on Medical Imaging, vol. 19, no. 5, pp. 423-433, 2000.
[65] D.K. Foot, R.P. Lewis, T.A. Pearson, and G.A. Beller, "Demographics and Cardiology, 1950–2050," IEEE Transactions on Medical Imaging, vol. 35, no. 4, pp. 1067-1081, 2000.
[66] D.G. Amen, J.H. Paldi, and R.A. Thisted, "Brain SPECT Imaging," IEEE Transactions on Medical Imaging, 1993.
[67] A. Kazemi and M. Ghorbanpour, "Introduction to Environmental Challenges in All Over the World," IEEE Transactions on Medical Imaging, pp. 25-48, 2017.
[68] S. B. McGrayne, "Nobel Prize Women in Science: Their Lives, Struggles, and Momentous Discoveries," 2001.
[69] G. Hevesy, "The Absorption and Translocation of Lead by Plants: A Contribution to the Application of the Method of Radioactive Indicators in the Investigation of the Change of Substance in Plants," in Source Book in Chemistry, 1900–1950, Harvard University Press, 1968, pp. 48-50.
[70] G. Hevesy and J. Ottesen, "Rate of Formation of Nucleic Acid in the Organs of the Rat," Acta Physiologica Scandinavica, vol. 5, no. 2-3, pp. 237-247, 1943.
[71] E. O. Lawrence, L. W. Alvarez, W. M. Brobeck, D. Cooksey, D. R. Corson, E. M. McMillan, W. W. Salisbury, and R. L. Thornton, "Initial Performance of the 60-Inch Cyclotron of the William H. Crocker Radiation Laboratory, University of California," Physical Review, vol. 56, no. 1, p. 124, 1939.
[72] E. Segrè and G. T. Seaborg, "Nuclear Isomerism in Element 43," Physical Review, vol. 54, no. 9, p. 772, 1938.
[73] Montgomery, C.G. and Montgomery, D.D., 1940. The discharge mechanism of Geiger-Mueller counters. Physical Review, 57(11), p.1030.
[74] R. Hofstadter, "The detection of gamma-rays with thallium-activated sodium iodide crystals," Physical Review, vol. 75, no. 5, p. 796, 1949.
[75] E.K. Plyler, W.S. Benedict, and S. Silverman, "Precise measurements in the infrared spectrum of carbon monoxide," The Journal of Chemical Physics, vol. 20, no. 1, pp. 175-184, 1952.
[76] P. R. Wallace, "Positron annihilation in solids and liquids," in Solid State Physics, vol. 10, pp. 1-69, Academic Press, 1960.

[77] H.C. Allen Jr, R.L. Libby, and B. Cassen, "The scintillation counter in clinical studies of human thyroid physiology using I131," The Journal of Clinical Endocrinology, vol. 11, no. 5, pp. 492-511, 1951.
[78] J.B. Stanbury, K. Ohela, and R. Pitt-Rivers, "The metabolism of iodine in 2 goitrous cretins compared with that in 2 patients receiving methimazole," The Journal of Clinical Endocrinology & Metabolism, vol. 15, no. 1, pp. 54-72, 1955.
[79] B.F. Hutton, "The contribution of Medical Physics to Nuclear Medicine: looking back-a physicist's perspective," EJNMMI physics, vol. 1, no. 1, pp. 1-7, 2014.
[80] R.J. Jaszczak, "The early years of single photon emission computed tomography (SPECT): an anthology of selected reminiscences," Physics in Medicine & Biology, vol. 51, no. 13, p. R99, 2006.
[81] B.L. Shulkin, D.M. Wieland, M. Schwaiger, N.W. Thompson, I.R. Francis, M.S. Haka, K.C. Rosenspire, B. Shapiro, J.C. Sisson, and D.E. Kuhl, "PET scanning with hydroxyephedrine: an approach to the localization of pheochromocytoma," Journal of Nuclear Medicine, vol. 33, no. 6, pp. 1125-1131, 1992.
[82] M.W. Groch and W.D. Erwin, "SPECT in the year 2000: basic principles," Journal of Nuclear Medicine Technology, vol. 28, no. 4, pp. 233-244, 2000.
[83] I.O. Umeda, K. Tani, K. Tsuda, M. Kobayashi, M. Ogata, S. Kimura, M. Yoshimoto, S. Kojima, K. Moribe, K. Yamamoto, and N. Moriyama, "High resolution SPECT imaging for visualization of intratumoral heterogeneity using a SPECT/CT scanner dedicated for small animal imaging," Annals of Nuclear Medicine, vol. 26, pp. 67-76, 2012.
[84] L. Livieratos, "Basic principles of SPECT and PET imaging," in Radionuclide and Hybrid Bone Imaging, Berlin, Heidelberg: Springer Berlin Heidelberg, 2012, pp. 345-359.
[85] M. Pfützner, M. Karny, L.V. Grigorenko, and K. Riisager, "Radioactive decays at limits of nuclear stability," Reviews of Modern Physics, vol. 84, no. 2, p. 567, 2012.
[86] S. Mairinger, T. Erker, M. Muller, and O. Langer, "PET and SPECT radiotracers to assess function and expression of ABC transporters in vivo," Current Drug Metabolism, vol. 12, no. 8, pp. 774-792, 2011.
[87] B.F. Hutton, "The origins of SPECT and SPECT/CT," European Journal of Nuclear Medicine and Molecular Imaging, vol. 41, pp. 3-16, 2014.
[88] K. Van Audenhaege, R. Van Holen, S. Vandenberghe, C. Vanhove, S.D. Metzler, and S.C. Moore, "Review of SPECT collimator selection, optimization, and fabrication for clinical and preclinical imaging," Medical Physics, vol. 42, no. 8, pp. 4796-4813, 2015.
[89] R.J. Jaszczak, R.E. Coleman, and F.R. Whitehead, "Physical factors affecting quantitative measurements using camera-based single photon emission computed tomography (SPECT)," IEEE Transactions on Nuclear Science, vol. 28, no. 1, pp. 69-80, 1981.
[90] T.S. Caldwell Jr, "Searching for dark matter with single phase liquid argon," University of Pennsylvania, 2015.
[91] Genster, C., Schever, M., Ludhova, L., Soiron, M., Stahl, A. and Wiebusch, C., 2018. Muon reconstruction with a geometrical model in JUNO. Journal of Instrumentation, 13(03), p.T03003.
[92] R.G. Wells, A. Celler, and R. Harrop, "Analytical calculation of photon distributions in SPECT projections," IEEE Transactions on Nuclear Science, vol. 45, no. 6, pp. 3202-3214, 1998.
[93] T.E. Peterson and L.R. Furenlid, "SPECT detectors: the Anger Camera and beyond," Physics in Medicine & Biology, vol. 56, no. 17, p. R145, 2011.
[94] R. Accorsi, "Brain single-photon emission CT physics principles," American Journal of Neuroradiology, vol. 29, no. 7, pp. 1247-1256, 2008.
[95] M. B. Tomas, P. V. Pugliese, G. G. Tronco, C. Love, C. J. Palestro, and K. J. Nichols, "Pinhole versus parallel-hole collimators for parathyroid imaging: an intraindividual comparison," Journal of Nuclear Medicine Technology, vol. 36, no. 4, pp. 189-194, 2008.
[96] J. G. Park, S. H. Jung, J. B. Kim, J. Moon, M. C. Han, and C. H. Kim, "Development of advanced industrial SPECT system with 12-gonal diverging-collimator," Applied Radiation and Isotopes, vol. 89, pp. 159-166, 2014.
[97] F. A. Mettler and M. J. Guiberteau, "Essentials of Nuclear Medicine and Molecular Imaging," Elsevier Health Sciences, 2018.
[98] R. J. Jaszczak, J. Li, H. Wang, M. R. Zalutsky, and R. E. Coleman, "Pinhole collimation for ultra-high-resolution, small-field-of-view SPECT," Physics in Medicine & Biology, vol. 39, no. 3, p. 425, 1994.
[99] D. A. Weber, M. Ivanovic, D. Franceschi, S. E. Strand, K. Erlandsson, M. Franceschi, H. L. Atkins, J. A. Coderre, H. Susskind, T. Button, and K. Ljunggren, "Pinhole SPECT: an approach to in vivo high-resolution SPECT imaging in small laboratory animals," in Journal of Nuclear Medicine, vol. 35, no. 2, pp. 342-348, 1994.

[100] D. R. Gilland, E. L. Johnson, T. G. Turkington, R. E. Coleman, and R. J. Jaszczak, "Evaluation of a pinhole collimator for I-131 SPECT head imaging," IEEE Transactions on Nuclear Science, vol. 43, no. 4, pp. 2230-2238, 1996.

[101] M. P. Sandler, Ed., "Diagnostic Nuclear Medicine," Lippincott Williams & Wilkins, 2003.

[102] N. U. Schramm, G. Ebel, U. Engeland, T. Schurrat, M. Behe, and T. M. Behr, "High-resolution SPECT using multipinhole collimation," IEEE Transactions on Nuclear Science, vol. 50, no. 3, pp. 315-320, 2003.

[103] N. U. Schramm, M. Schipper, T. Schurrat, M. Behe, H. Alfke, U. Engeland, G. Ebel, and T. M. Behr, "Performance of a multi-pinhole animal SPECT," in 2003 IEEE Nuclear Science Symposium. Conference Record (IEEE Cat. No. 03CH37515), vol. 3, pp. 2077-2079, IEEE, October 2003.

[104] L. S. Graham, "Quality control for SPECT systems," Radiographics, vol. 15, no. 6, pp. 1471-1481, 1995.

[105] Y. Shao, R. W. Silverman, R. Farrell, L. Cirignano, R. Grazioso, K. S. Shah, G. Vissel, M. Clajus, T. O. Tumer, and S. R. Cherry, "Design studies of a high-resolution PET detector using APD arrays," IEEE Transactions on Nuclear Science, vol. 47, no. 3, pp. 1051-1057, 2000.

[106] A. Wirrwar, N. Schramm, H. Vosberg, and H. W. Müller-Gärtner, "High resolution SPECT in small animal research," Reviews in the Neurosciences, vol. 12, no. 2, pp. 187-193, 2001.

[107] S. V. Smith, M. Jones, and V. Holmes, "Production and selection of metal PET radioisotopes for molecular imaging," in Radioisotopes-Applications in Bio-Medical Science, pp. 200-224, 2011.

[108] Z. Liu, G. A. Kastis, G. D. Stevenson, H. H. Barrett, L. R. Furenlid, M. A. Kupinski, D. D. Patton, and D. W. Wilson, "Quantitative analysis of acute myocardial infarct in rat hearts with ischemia-reperfusion using a high-resolution stationary SPECT system," Journal of Nuclear Medicine, vol. 43, no. 7, pp. 933-939, 2002.

[109] L. R. MacDonald, B. E. Patt, J. S. Iwanczyk, B. M. Tsui, Y. Wang, E. C. Frey, D. E. Wessell, P. D. Acton, and H. F. Kung, "Pinhole SPECT of mice using the LumaGEM gamma camera," IEEE Transactions on Nuclear Science, vol. 48, no. 3, pp. 830-836, 2001.

[110] M. C. Wu, D. W. Gao, R. E. Sievers, R. J. Lee, B. H. Hasegawa, and M. W. Dae, "Pinhole single-photon emission computed tomography for myocardial perfusion imaging of mice," Journal of the American College of Cardiology, vol. 42, no. 3, pp. 576-582, 2003.

[111] D. A. Weber and M. Ivanovic, "Ultra-high-resolution imaging of small animals: implications for preclinical and research studies," Journal of Nuclear Cardiology, vol. 6, no. 3, p. 332, 1999.

[112] W. A. Weber, J. Czernin, C. J. Anderson, R. D. Badawi, H. Barthel, F. Bengel, L. Bodei, I. Buvat, M. DiCarli, M. M. Graham, and J. Grimm, "The future of nuclear medicine, molecular imaging, and theranostics," Journal of Nuclear Medicine, vol. 61, no. Supplement 2, pp. 263S-272S, 2020.

[113] B. L. Franc, P. D. Acton, C. Mari, and B. H. Hasegawa, "Small-animal SPECT and SPECT/CT: Important Tools for Preclinical Investigation," Journal of Nuclear Medicine, vol. 49, no. 10, pp. 1651-1663, 2008.

[114] A. Marusyk and J. DeGregori, "Building a Better Model of Cancer," Cell Division, vol. 1, no. 1, pp. 1-6, 2006.

[115] B.S. Carver and P.P. Pandolfi, "Mouse Modeling in Oncologic Preclinical and Translational Research," Clinical Cancer Research, vol. 12, no. 18, pp. 5305-5311, 2006.

[116] S. Lee, J. Xie, and X. Chen, "Peptide-Based Probes for Targeted Molecular Imaging," Biochemistry, vol. 49, no. 7, pp. 1364-1376, 2010.

[117] M. J. Pivovaroff, T. Funk, W. C. Barber, B. D. Ramsey, and B. H. Hasegawa, "Progress of Focusing X-ray and Gamma-ray Optics for Small Animal Imaging," in Penetrating Radiation Systems and Applications VII, vol. 5923, pp. 65-78, SPIE, September 2005.

[118] M.J. Pivovaroff, W.B. Barber, F.E. Christensen, W.W. Craig, T. Decker, M. Epstein, T. Funk, C.J. Hailey, B.H. Hasegawa, R. Hill, and J.G. Jernigan, "Small-Animal Radionuclide Imaging with Focusing Gamma-Ray Optics," in Penetrating Radiation Systems and Applications V, vol. 5199, pp. 147-161, SPIE, December 2003.

[119] L.R. Furenlid, H.H. Barrett, H.B. Barber, E.W. Clarkson, M.A. Kupinski, Z. Liu, G.D. Stevenson, and J.M. Woolfenden, "Molecular Imaging in the College of Optical Sciences: An Overview of Two Decades of Instrumentation Development," Fifty Years of Optical Sciences at The University of Arizona, vol. 9186, pp. 188-203, 2014.

[120] S.P. Mueller, J.F. Polak, M.F. Kijewski, and B.L. Holman, "Collimator Selection for SPECT Brain Imaging: The Advantage of High Resolution," Journal of Nuclear Medicine, vol. 27, no. 11, pp. 1729-1738, 1986.

[121] S. Genna and A.P. Smith, "The Development of ASPECT, an Annular Single Crystal Brain Camera for High Efficiency SPECT," IEEE Transactions on Nuclear Science, vol. 35, no. 1, pp. 654-658, 1988.

[122] W.L. Rogers, N.H. Clinthorne, L. Shao, P. Chiao, Y. Ding, J.A. Stamos, and K.F. Koral, "SPRINT II: A Second Generation Single Photon Ring Tomograph," IEEE Transactions on Medical Imaging, vol. 7, no. 4, pp. 291-297, 1988.
[123] B.M. Tsui, Y. Wang, and S.P. Mok, "Molecular SPECT Imaging Instrumentation and Techniques," in M.G. Pomper and J. Gelovani (Eds.), Molecular Imaging in Oncology, New York: Informa Healthcare, 2008, pp. 93-108.
[124] M.M. Rogulski, H.B. Barber, H.H. Barrett, R.L. Shoemaker, and J.M. Woolfenden, "Ultra-High-Resolution Brain SPECT Imaging: Simulation Results," IEEE Transactions on Nuclear Science, vol. 40, no. 4, pp. 1123-1129, 1993.
[125] M.C. Goorden, M.C.M. Rentmeester, and F.J. Beekman, "Theoretical Analysis of Full-Ring Multi-Pinhole Brain SPECT," Physics in Medicine & Biology, vol. 54, no. 21, p. 6593, 2009.
[126] R. Van Holen, B. Vandeghinste, K. Deprez, and S. Vandenberghe, "Design and Performance of a Compact and Stationary MicroSPECT System," Medical Physics, vol. 40, no. 11, p. 112501, 2013.
[127] A. Authier, "Dynamical Theory of X-ray Diffraction," in International Tables for Crystallography, pp. 534-551, 2006.
[128] P. Gorenstein, "Grazing Incidence Telescopes for X-ray Astronomy," Optical Engineering, vol. 51, no. 1, pp. 011010-011010, 2012.
[129] C. Hahne, A. Aggoun, S. Haxha, V. Velisavljevic, and J. C. J. Fernández, "Light Field Geometry of a Standard Plenoptic Camera," in Optics Express, vol. 22, no. 22, pp. 26659-26673, 2014.
[130] M. Levoy, "Light Fields and Computational Imaging," Computer, vol. 39, no. 8, pp. 46-55, 2006.
[131] E.H. Adelson and J.R. Bergen, "The Plenoptic Function and the Elements of Early Vision," Computational Models of Visual Processing, vol. 1, no. 2, pp. 3-20, 1991.
[132] I. Ihrke, J. Restrepo, and L. Mignard-Debise, "Principles of Light Field Imaging: Briefly Revisiting 25 Years of Research," IEEE Signal Processing Magazine, vol. 33, no. 5, pp. 59-69, 2016.
[133] A. Barhoum, M. Francis, R. Camattari, and M. Tahtali, "Design and Evaluation of a Novel Ultra High-Resolution Lens-Based SPECT: Insight to Light Field Imaging," in 2021 IEEE International Conference on Systems, Man, and Cybernetics (SMC), pp. 1436-1442, October 2021.
[134] S. Shokouhi, S. D. Metzler, D. W. Wilson, and T. E. Peterson, "Multi-pinhole collimator design for small-object imaging with SiliSPECT: a high-resolution SPECT," in Physics in Medicine & Biology, vol. 54, no. 2, p. 207, 2008.
[135] T. Y. Song, Y. Choi, Y. H. Chung, J. H. Jung, Y. S. Choe, K. H. Lee, S. E. Kim, and B. T. Kim, "Optimization of pinhole collimator for small animal SPECT using Monte Carlo simulation," in IEEE Transactions on Nuclear Science, vol. 50, no. 3, pp. 327-332, 2003.
[136] A. Könik, B. Auer, J. De Beenhouwer, K. Kalluri, N. Zeraatkar, L. R. Furenlid, and M. A. King, "Primary, scatter, and penetration characterizations of parallel-hole and pinhole collimators for I-123 SPECT," in Physics in Medicine & Biology, vol. 64, no. 24, p. 245001, 2019.
[137] H. Akbari-Lalimi and S. A. Shafiei, "Design feasibility of gamma camera without collimator based on specific arrangement of the detectors," in Nuclear Science and Techniques, vol. 27, pp. 1-7, 2016.
[138] J. Van Roosmalen, F. J. Beekman, and M. C. Goorden, "Comparison of fan beam, slit-slat and multi-pinhole collimators for molecular breast tomosynthesis," in Physics in Medicine & Biology, vol. 63, no. 10, p. 105009, 2018.
[139] J.A. Case and T.M. Bateman, "Taking the perfect nuclear image: quality control, acquisition, and processing techniques for cardiac SPECT, PET, and hybrid imaging," Journal of Nuclear Cardiology, vol. 20, pp. 891-907, 2013.
[140] N. Fuin, A. Bousse, S. Pedemonte, S. Arridge, S. Ourselin, and B. Hutton, "Collimator design in SPECT, an optimization tool," in 2010 IEEE Nuclear Science Symposium and Medical Imaging Conference (NSS/MIC), 2010
[141] S. R. Cherry, J. A. Sorenson, M. E. Phelps, and ScienceDirect (Online service), "Physics in Nuclear Medicine," vol. 3, Saunders, 2003.
[143] O. Ivashchenko, F. van der Have, M.C. Goorden, R.M. Ramakers, and F.J. Beekman, "Ultra-High-Sensitivity Submillimeter Mouse SPECT," Journal of Nuclear Medicine, vol. 56, no. 3, pp. 470-475, 2015.
[144] Z. Telikani and A. Sadremomtaz, "A Monte Carlo Simulation Study of Optimization for Collimator in a Pixelated SPECT Camera," Journal of Medical Imaging and Radiation Sciences, vol. 50, no. 1, pp. 163-170, 2019.
[145] Siman, W. and Kappadath, S.C., 2011. Performance characteristics of a new pixelated portable gamma camera. Journal of Medical Imaging, vol. 49, no. 1, pp. 163-170, 2011.
[146] Kubota, H., Motomura, N., and Ogawa, K., "Simulation Study on a Stationary SPECT System With Multi-pinhole Collimators," in 2017 IEEE Nuclear Science Symposium and Medical Imaging Conference (NSS/MIC), pp. 1-3, October 2017.

[147] J.Y. Hesterman, M.A. Kupinski, L.R. Furenlid, D.W. Wilson, and H.H. Barrett, "The multi-module, multi-resolution system: A novel small-animal SPECT system," Medical Physics, vol. 34, no. 3, pp. 987-993, 2007.

[148] M. Freed, M.A. Kupinski, L.R. Furenlid, D.W. Wilson, and H.H. Barrett, "A prototype instrument for single pinhole small animal adaptive SPECT imaging," Medical Physics, vol. 35, no. 5, pp. 1912-1925, 2008.

[149] N. Ghanbari, "One-Step Optimization of Adaptive SPECT Systems," Doctoral dissertation, The University of Arizona, 2018.

[150] S. Bae, J. Chun, H. Cha, J.Y. Yeom, K. Lee, and H. Lee, "Simulation study of a novel target oriented SPECT design using a variable pinhole collimator," Medical physics, vol. 44, no. 2, pp. 470-478, 2017.

[151] H.H. Barrett, L.R. Furenlid, M. Freed, J.Y. Hesterman, M.A. Kupinski, E. Clarkson, and M.K. Whitaker, "Adaptive SPECT," IEEE Transactions on Medical Imaging, vol. 27, no. 6, pp. 775-788, 2008.

[152] H.L. Durko, H.H. Barrett, and L.R. Furenlid, "High-Resolution Anamorphic SPECT Imaging," IEEE Transactions on Nuclear Science, vol. 61, no. 3, pp. 1126-1135, 2014.

[153] B. Auer, K. Kalluri, J. De Beenhouwer, N. Zeraatkar, N. Momsen, P. Kuo, L. Furenlid, and M. King, "Keel-Edge Height Selection for Improved Multi-Pinhole 123I Brain SPECT Imaging," Journal of Nuclear Medicine, vol. 61, supplement 1, p. 573, 2020.

[154] N. C. Momsen, G. Richards, M. A. King, N. Zeraatkar, and L. R. Furenlid, "Design of a Selectable Pinhole Module for Use in Adaptive SPECT Collimators," in 2018 IEEE Nuclear Science Symposium and Medical Imaging Conference Proceedings (NSS/MIC), pp. 1-3, November 2018.

[155] D. Volterrani, P. A. Erba, I. Carrió, H. W. Strauss, and G. Mariani, Eds., "Nuclear Medicine Textbook: Methodology and Clinical Applications," Springer International Publishing, 2019.

[156] M. May, N. C. Momsen, R. G. Richards, K. S. Kalluri, N. Zeraatkar, B. Auer, M. A. King, P. H. Kuo, and L. R. Furenlid, "Design of Adaptive Pinhole SPECT Collimators for Improved Spatial Resolution and Sensitivity," in 2020 IEEE Nuclear Science Symposium and Medical Imaging Conference (NSS/MIC), 2020.

[157] G. S. Mok, Y. Wang, and B. M. Tsui, "Quantification of the Multiplexing Effects in Multi-Pinhole Small Animal SPECT: A Simulation Study," in IEEE Transactions on Nuclear Science, vol. 56, no. 5, pp. 2636-2643, 2009.

[158] Z. Cao, G. Bal, R. Accorsi, and P. D. Acton, "Optimal Number of Pinholes in Multi-Pinhole SPECT for Mouse Brain Imaging—A Simulation Study," in Physics in Medicine & Biology, vol. 50, no. 19, p. 4609, 2005.

[159] Mahmood, S.T., Erlandsson, K., Cullum, I. and Hutton, B.F., 2010. The potential for mixed multiplexed and non-multiplexed data to improve the reconstruction quality of a multi-slit–slat collimator SPECT system. Physics in Medicine & Biology, 55(8), p.2247.

[160] Mok, G.S., Tsui, B.M. and Beekman, F.J., 2011. The effects of object activity distribution on multiplexing multi-pinhole SPECT. Physics in Medicine & Biology, 56(8), p.2635.

[161] V. Ilisie, L. Moliner, S. Oliver, F. Sánchez, A. J. González, M. Seimetz, M. J. Rodríguez-Álvarez, and J. M. Benlloch, "High Resolution and Sensitivity Gamma Camera with Active Septa: A First Monte Carlo Study," in Scientific Reports, vol. 9, no. 1, p. 18431, 2019.

[162] A. Schwarz, A. Shemer, Y. Danan, R. Bar-Shalom, H. Avraham, A. Zlotnik, and Z. Zalevsky, "Gamma Radiation Imaging System via Variable and Time-Multiplexed Pinhole Arrays," in Sensors, vol. 20, no. 11, p. 3013, 2020.

[163] V. Ilisie, L. Moliner, C. Morera, J. Nuyts, and J. M. Benlloch, "Gamma Camera Imaging with Rotating Multi-Pinhole Collimator: A Monte Carlo Feasibility Study," in Sensors, vol. 21, no. 10, p. 3367, 2021.

[164] D. W. Wilson, H. H. Barrett, and E. W. Clarkson, "Reconstruction of Two-and Three-Dimensional Images from Synthetic-Collimator Data," in IEEE Transactions on Medical Imaging, vol. 19, no. 5, pp. 412-422, 2000.

[165] A. Lin, M. A. Kupinski, T. E. Peterson, S. Shokouhi, and L. C. Johnson, "Task-Based Design of a Synthetic-Collimator SPECT System Used for Small Animal Imaging," in Medical Physics, vol. 45, no. 7, pp. 2952-2963, 2018.

[166] L. Chen, B. M. Tsui, and G. S. Mok, "Design and Evaluation of Two Multi-Pinhole Collimators for Brain SPECT," in Annals of Nuclear Medicine, vol. 31, pp. 636-648, 2017.

[167] C. Si, G. S. Mok, L. Chen, and B. M. Tsui, "Design and Evaluation of an Adaptive Multipinhole Collimator for High-Performance Clinical and Preclinical Imaging," in Nuclear Medicine Communications, vol. 37, no. 3, pp. 313-321, 2016

[168] L. R. Pato, S. Vandenberghe, T. Zedda, and R. Van Holen, "Parallel-Hole Collimator Concept for Stationary SPECT Imaging," in Physics in Medicine & Biology, vol. 60, no. 22, p. 8791, 2015.

[169] D. U. Ozsahin, L. Bläckberg, G. El Fakhri, and H. Sabet, "GATE Simulation of a New Design of Pinhole SPECT System for Small Animal Brain Imaging," in Journal of Instrumentation, vol. 12, no. 01, p. C01085, 2017.
[170] F. Weng, S. Bagchi, Y. Zan, Q. Huang, and Y. Seo, "An Energy-Optimized Collimator Design for a CZT-Based SPECT Camera," in Nuclear Instruments and Methods in Physics Research Section A: Accelerators, Spectrometers, Detectors and Associated Equipment, vol. 806, pp. 330-339, 2016.
[171] R. Massari, A. D'elia, and A. Soluri, "Preliminary Results on a Small Animal SPECT System Based on H13700 PMT Coupled with CRY018 Array," in Nuclear Instruments and Methods in Physics Research Section A: Accelerators, Spectrometers, Detectors and Associated Equipment, vol. 940, pp. 296-301, 2019.
[172] R. Massari, D. Caputo, S. Ronchi, and A. Soluri, "Low-Power Charge Division Circuits for Wireless Applications Based on Silicon Photomultipliers," in IEEE Sensors Journal, vol. 16, no. 23, pp. 8214-8219, 2016.
[173] R. Massari, A. Ucci, C. Campisi, F. Scopinaro, and A. Soluri, "A Novel Fully Integrated Handheld Gamma Camera," in Nuclear Instruments and Methods in Physics Research Section A: Accelerators, Spectrometers, Detectors and Associated Equipment, vol. 832, pp. 271-278, 2016.
[174] W. W. Moses, V. Gayshan, and A. Gektin, "The Evolution of SPECT–From Anger to Today and Beyond," in Radiation Detectors for Medical Applications, pp. 37-80, Springer Netherlands, 2006.
[175] R. Massari, A. D'Elia, A. Soluri, and A. Soluri, "Super Spatial Resolution (SSR) Method for Small Animal SPECT Imaging: A Monte Carlo Study," Nuclear Instruments and Methods in Physics Research Section A: Accelerators, Spectrometers, Detectors and Associated Equipment, vol. 982, p. 164584, 2020.
[176] K. S. Kalluri, N. Zeraatkar, B. Auer, P. H. Kuo, L. R. Furenlid, and M. A. King, "Preliminary Investigation of AdaptiSPECT-C Designs with Square or Square and Hexagonal Detectors Employing Direct and Oblique Apertures," in 15th International Meeting on Fully Three-Dimensional Image Reconstruction in Radiology and Nuclear Medicine, vol. 11072, pp. 191-195, SPIE, May 2019.
[177] K. S. Kalluri, N. Zeraatkar, B. Auer, T. J. Fromme, P. H. Kuo, L. R. Furenlid, and M. A. King, "Preliminary Investigation of an AdaptiSPECT-C Design with Rotated Square and Hexagonal Detectors," in 2019 IEEE Nuclear Science Symposium and Medical Imaging Conference (NSS/MIC), pp. 1-3, IEEE, October 2019.
[178] E. Goshen, L. Beilin, E. Stern, T. Kenig, R. Goldkorn, and S. Ben-Haim, "Feasibility Study of a Novel General Purpose CZT-Based Digital SPECT Camera: Initial Clinical Results," EJNMMI Physics, vol. 5, no. 1, pp. 1-12, 2018.
[179] K. Erlandsson, K. Kacperski, D. Van Gramberg, and B. F. Hutton, "Performance Evaluation of D-SPECT: A Novel SPECT System for Nuclear Cardiology," Physics in Medicine & Biology, vol. 54, no. 9, p. 2635, 2009.
[180] T.H. Seo, K.J. Lee, A.H. Park, C.H. Hong, E.K. Suh, S.J. Chae, Y.H. Lee, T.V. Cuong, V.H. Pham, J.S. Chung, and E.J. Kim, "Enhanced Light Output Power of Near UV Light Emitting Diodes with Graphene/Indium Tin Oxide Nanodot Nodes for Transparent and Current Spreading Electrode," Optics Express, vol. 19, no. 23, pp. 23111-23117, 2011.
[181] B. Kesanli, K. Hong, K. Meyer, H.J. Im, and S. Dai, "Highly Efficient Solid-State Neutron Scintillators Based on Hybrid Sol-Gel Nanocomposite Materials," Applied Physics Letters, vol. 89, no. 21, 2006.
[182] B. Liu, Z. Zhu, Q. Wu, C. Cheng, M. Gu, J. Xu, H. Chen, J. Liu, L. Chen, and X. Ouyang, "Plasmonic Lattice Resonance-Enhanced Light Emission from Plastic Scintillators by Periodical Ag Nanoparticle Arrays," Applied Physics Letters, vol. 110, no. 18, 2017.
[183] B. Liu, Z. Zhu, J. Zhu, S. Wu, H. Chen, M. Gu, Q. Cheng, C. Cheng, Z. Wang, Y. Zhao, and Q. Zhang, "An approach to achieve significantly faster luminescence decay of thin-film scintillator by surface plasmons," Appl. Phys. Lett., vol. 104, no. 6, 2014.
[184] A.I. Zhmakin, "Enhancement of light extraction from light emitting diodes," Physics Reports, vol. 498, no. 4-5, pp. 189-241, 2011.
[185] X. Chen, B. Liu, Q. Wu, Z. Zhu, J. Zhu, M. Gu, H. Chen, J. Liu, L. Chen, and X. Ouyang, "Enhanced light extraction of plastic scintillator using large-area photonic crystal structures fabricated by hot embossing," Optics Express, vol. 26, no. 9, pp. 11438-11446, 2018.
[186] D. Yuan, B. Liu, Z. Zhu, Y. Guo, C. Cheng, H. Chen, M. Gu, M. Xu, L. Chen, J. Liu, and X. Ouyang, "Directional control and enhancement of light output of scintillators by using microlens arrays," ACS Applied Materials & Interfaces, vol. 12, no. 26, pp. 29473-29480, 2020.
[187] X. Chen, B. Liu, J. Zhu, M. Gu, H. Chen, J. Liu, L. Chen, and X. Ouyang, "Light extraction enhancement and directional control of scintillator by using microlens arrays," Optics Express, vol. 26, no. 18, pp. 23132-23141, 2018. [188]Y. Huh et al., "Evaluation of a variable-aperture full-ring SPECT

system using large-area pixelated CZT modules: A simulation study for brain SPECT applications," vol. 48, no. 5, pp. 2301-2314, 2021.
[189] H.H. Barrett, "Fresnel zone plate imaging in nuclear medicine," Journal of Nuclear Medicine, vol. 13, no. 6, pp. 382-385, 1972.
[190] E.E. Fenimore and T.M. Cannon, "Uniformly redundant arrays: digital reconstruction methods," Applied Optics, vol. 20, no. 10, pp. 1858-1864, 1981.
[191] G.R. Gindi, J. Arendt, H.H. Barrett, M.Y. Chiu, A. Ervin, C.L. Giles, M.A. Kujoory, E.L. Miller, and R.G. Simpson, "Imaging with rotating slit apertures and rotating collimators," *Medical Physics*, vol. 9, no. 3, pp. 324-339, 1982.
[192] O. Gal, M. Gmar, O. P. Ivanov, F. Lainé, F. Lamadie, C. Le Goaller, C. Mahé, E. Manach, and V. E. Stepanov, "Development of a portable gamma camera with coded aperture," Nuclear Instruments and Methods in Physics Research Section A: Accelerators, Spectrometers, Detectors and Associated Equipment, vol. 563, no. 1, pp. 233-237, 2006.
[193] R. Accorsi, F. Gasparini, and R. C. Lanza, "A coded aperture for high-resolution nuclear medicine planar imaging with a conventional Anger camera: experimental results," IEEE Transactions on Nuclear Science, vol. 48, no. 6, pp. 2411-2417, 2001.
[194] H. Fujii, J.D. Idoine, S. Gioux, R. Accorsi, D.R. Slochower, R.C. Lanza, and J.V. Frangioni, "Optimization of coded aperture radioscintigraphy for sentinel lymph node mapping," Molecular Imaging and Biology, vol. 14, pp. 173-182, 2012.
[195] R. Accorsi, F. Gasparini, and R. C. Lanza, "Optimal coded aperture patterns for improved SNR in nuclear medicine imaging," Nuclear Instruments and Methods in Physics Research Section A: Accelerators, Spectrometers, Detectors and Associated Equipment, vol. 474, no. 3, pp. 273-284, 2001.
[196] R. Accorsi and R. C. Lanza, "Near-field artifact reduction in planar coded aperture imaging," Applied Optics, vol. 40, no. 26, pp. 4697-4705, 2001.
[197] Z. Mu, L.W. Dobrucki, and Y.H. Liu, "SPECT imaging of 2-D and 3-D distributed sources with near-field coded aperture collimation: computer simulation and real data validation," Journal of Medical and Biological Engineering, vol. 36, pp. 32-43, 2016.
[198] V. Rozhkov, I. Hernández, O. Ivanov, D. Kozhevnikov, A. Leyva, A. Perera, D. Rastorguev, P. Smolyanskiy, L. Torres, and A. Zhemchugov, "Visualization of radiotracers for SPECT imaging using a Timepix detector with a coded aperture," Journal of Instrumentation, vol. 15, no. 06, p. P06028, 2020.
[199] E. Caroli, J.B. Stephen, A. Spizzichino, G. Di Cocco, and L. Natalucci, "Coded Aperture Imaging," in Data Analysis in Astronomy II, pp. 77-86, Springer US, Boston, MA, 1986.
[200] J.B. Ding, K.T. Takasaki, and B.L. Sabatini, "Supraresolution imaging in brain slices using stimulated-emission depletion two-photon laser scanning microscopy," Neuron, vol. 63, no. 4, pp. 429-437, 2009.
[201] N. Lund, "A study of focusing telescopes for soft gamma rays," Experimental Astronomy, vol. 2, no. 5, pp. 259-273, 1992.
[202] R. Giacconi, W.P. Reidy, G.S. Vaiana, L.P. Van Speybroeck, and T.F. Zehnpfennig, "Grazing-incidence telescopes for x-ray astronomy," Space Science Reviews, vol. 9, no. 1, pp. 3-57, 1969.
[203] E. Caroli, J.B. Stephen, G. Di Cocco, L. Natalucci, and A. Spizzichino, "Coded aperture imaging in X- and gamma-ray astronomy," Space Science Reviews, vol. 45, no. 3-4, pp. 349-403, 1987.
[204] F.A. Harrison, F.E. Christensen, W. Craig, C. Hailey, W. Baumgartner, C.M.H. Chen, J. Chonko, W.R. Cook, J. Koglin, K.K. Madsen, and M. Pivavoroff, "Development of the HEFT and NuSTAR focusing telescopes," in Focusing Telescopes in Nuclear Astrophysics, pp. 131-137, 2006.
[205] F. Frontera, E. Virgilli, V. Valsan, V. Liccardo, V. Carassiti, E. Caroli, F. Cassese, C. Ferrari, V. Guidi, S. Mottini, and M. Pecora, "Scientific prospects in soft gamma-ray astronomy enabled by the LAUE project," in Optics for EUV, X-Ray, and Gamma-Ray Astronomy VI, vol. 8861, pp. 47-63, SPIE, September 2013.
[206] E. Virgilli, F. Frontera, V. Valsan, V. Liccardo, E. Caroli, J.B. Stephen, F. Cassese, L. Recanatesi, M. Pecora, P. Attiná, and S. Mottini, "The LAUE project for broadband gamma-ray focusing lenses," in International Journal of Modern Physics: Conference Series, vol. 23, pp. 43-47, World Scientific Publishing Company, 2013.
[207] B.S. Acharya and CTA Consortium, "Science with the Cherenkov Telescope Array," WSP, 2018. [Online]. Available: arXiv:1709.07997.
[208] R.K. Smither, "Invited Review Article: Development of crystal lenses for energetic photons," Review of Scientific Instruments, vol. 85, no. 8, 2014.
[209] R.K. Smither, "Development of crystal lenses for energetic photons," Review of Scientific Instruments, vol. 85, no. 8, 2014.
[210] H. Halloin, P. von Ballmoos, J. Evrard, G.K. Skinner, M. Hernanz, N.V. Abrosimov, P. Bastie, B. Hamelin, V. Lonjou, J.M. Alvarez, and A. Laurens, "CLAIRE gamma-ray lens: flight and long-

distance test results," in Optics for EUV, X-Ray, and Gamma-Ray Astronomy, vol. 5168, pp. 471-481, SPIE, January 2004.
[211] P. Ubertini, F. Lebrun, G. Di Cocco, A. Bazzano, A.J. Bird, K.E. Broenstad, A. Goldwurm, G. La Rosa, C. Labanti, P. Laurent, and I.F. Mirabel, "IBIS: The Imager on-board INTEGRAL," Astronomy & Astrophysics, vol. 411, no. 1, pp. L131-L139, 2003.
[212] N. Barrière, P. Von Ballmoos, H. Halloin, N. Abrosimov, J.M. Alvarez, K. Andersen, P. Bastie, S. Boggs, P. Courtois, T. Courvoisier, and M. Harris, "MAX, a Laue diffraction lens for nuclear astrophysics," in Focusing Telescopes in Nuclear Astrophysics, pp. 269-278, 2006.
[213] C.B. Wunderer, S.E. Boggs, J. Kurfess, J.M. Ryan, E. Aprile, N. Gehrels, R.M. Kippen, M. Leising, U. Oberlack, A. Zych, and M. Baring, "The Advanced Compton Telescope Mission," in *The Obscured Universe. Proceedings of the VI INTEGRAL Workshop*, ESA Publication Division, July 2006.
[214] M. Feroci, E. Costa, P. Soffitta, E. Del Monte, G. Di Persio, I. Donnarumma, Y. Evangelista, M. Frutti, I. Lapshov, F. Lazzarotto, and M. Mastropietro, "SuperAGILE: The hard X-ray imager for the AGILE space mission," Nuclear Instruments and Methods in Physics Research Section A: Accelerators, Spectrometers, Detectors and Associated Equipment, vol. 581, no. 3, pp. 728-754, 2007.
[215] H. Awaki, H. Kunieda, M. Ishida, H. Matsumoto, Y. Babazaki, T. Demoto, A. Furuzawa, Y. Haba, T. Hayashi, R. Iizuka, and K. Ishibashi, "Hard x-ray telescopes to be onboard ASTRO-H," Applied Optics, vol. 53, no. 32, pp. 7664-7676, 2014.
[216] R. Giacconi, G. Branduardi, U. Briel, A. Epstein, D. Fabricant, E. Feigelson, W. Forman, P. Gorenstein, J. Grindlay, H. Gursky, and F.R. Harnden, "The Einstein/HEAO 2/x-ray observatory," Astrophysical Journal, Part 1, vol. 230, pp. 540-550, June 1, 1979.
[217] R. Giacconi and H. Tananbaum, "The Einstein observatory: New perspectives in astronomy," Science, vol. 209, no. 4459, pp. 865-876, 1980.
[218] H. Tananbaum, "'Netherlands Foundation for Radio Astronomy': X-Ray Astronomy with the Einstein Observatory," Journal of the Washington Academy of Sciences, vol. 71, no. 1, pp. 44-67, 1981.
[219] R.K. Smither, "A new method for focusing and imaging X-rays and gamma-rays with diffraction crystals," NASA Technical Memorandum, TM-83843, pp. 477-495, 1981.
[220] R.K. Smither, "New method for focusing x rays and gamma rays," *Review of Scientific Instruments*, vol. 53, no. 2, pp. 131-141, 1982.
[221] R.K. Smither, "Gamma-ray and X-ray telescope using variable-metric diffraction crystals," Annals of the New York Academy of Sciences, vol. 422, no. 1, pp. 384, 1984.
[222] R.K. Smither, "Instrument and method for focusing x-rays, gamma rays, and neutrons," U.S. Patent No. A255974, Historical Energy Database (United States), 1981.
[223] N. Lund and R.K. Smither, "A Bragg crystal flux concentrator for annihilation radiation," in Proceedings from the 18th International Cosmic Ray Conference, held in Bangalore, India, 22 August-3 September, 1983, vol. 9, p. 339, 1983.
[224] R.K. Smither, "Crystal diffraction lenses for imaging gamma-ray telescope," Argonne National Lab., IL (USA), Technical Report No. CONF-8612112-1, 1987.
[225] R.K. Smither, L.R. Greenwood, and C.T. Roche, "Crystal diffraction telescope for discrete line sources, recent experimental results," Proceedings of the Gamma Ray Observation Science Workshop, GSFC, 1989.
[226] S. Melone, O. Francescangeli, and R. Caciuffo, "Gamma-ray focusing concentrators for astrophysical observations by crystal diffraction in Laue geometry," Review of Scientific Instruments, vol. 64, no. 12, pp. 3467-3473, 1993.
[227] H. Halloin, P. Von Ballmoos, J. Evrard, G.K. Skinner, N. Abrosimov, P. Bastie, G. Di Cocco, M. George, B. Hamelin, P. Jean, and J. Knödleseder, "Performance of CLAIRE, the first balloon-borne γ-ray lens telescope," Nuclear Instruments and Methods in Physics Research Section A: Accelerators, Spectrometers, Detectors, and Associated Equipment, vol. 504, no. 1-3, pp. 120-125, 2003.
[228] P. von Ballmoos, "Instruments for Nuclear Astrophysics," in High Energy Spectroscopic Astrophysics, p. 83, 2005.
[229] E.V. Garcia, "Physical attributes, limitations, and future potential for PET and SPECT," Journal of Nuclear Cardiology, vol. 19, pp. 19-29, 2012.
[230] H. Wolter, "Spiegelsysteme streifenden Einfalls als abbildende Optiken für Röntgenstrahlen," Annalen der Physik, vol. 445, no. 1-2, pp. 94-114, 1952.
[231] G. Pareschi, D. Spiga, and C. Pelliciari, "X-ray Telescopes Based on Wolter-I Optics," in The WSPC Handbook of Astronomical Instrumentation: Volume 4: X-Ray Astronomical Instrumentation, pp. 3-31, 2021.
[232] M.J. Pivovaroff, W.B. Barber, F.E. Christensen, W.W. Craig, T. Decker, M. Epstein, T. Funk, C.J. Hailey, B.H. Hasegawa, R. Hill, and J.G. Jernigan, "Small-animal radionuclide imaging with focusing

gamma-ray optics," in Penetrating Radiation Systems and Applications V, vol. 5199, pp. 147-161, SPIE, December 2003.

[233] M. Pivovaroff, W. Barber, T. Funk, B. Hasegawa, C. Taylor, W. Craig, and K. Ziock, "High-Resolution Radionuclide Imaging Using Focusing Gamma-Ray Optics," in Small-Animal SPECT Imaging, pp. 267-271, 2005.

[234] M.J. Pivovaroff, W.C. Barber, W.W. Craig, B.H. Hasegawa, B.D. Ramsey, and C. Taylor, "Gamma-Ray Focusing Optics for Small Animal Imaging," presented at the IEEE Rome 2004 Medical Imaging Conference, January 2004.

[235] G.K. Skinner, "Diffractive-refractive optics for high energy astronomy-II. Variations on the theme," Astronomy & Astrophysics, vol. 383, no. 1, pp. 352-359, 2002.

[236] I. Neri, R. Camattari, V. Bellucci, V. Guidi, and P. Bastie, "Stack of curved crystals as an optical component for hard x-and gamma-ray focusing through a Laue lens," in Space Telescopes and Instrumentation 2012: Ultraviolet to Gamma Ray, vol. 8443, pp. 903-912, SPIE, September 2012.

[237] D.E. Roa, R.K. Smither, X. Zhang, K. Nie, Y.Y. Shieh, N.S. Ramsinghani, N. Milne, J.V. Kuo, J.L. Redpath, M.S.A.L. Al-Ghazi, and P. Caligiuri, "Development of a new photon diffraction imaging system for diagnostic nuclear medicine," in Focusing Telescopes in Nuclear Astrophysics, pp. 229-239, 2006.

[238] R.K. Smither, K.A. Saleem, D.E. Roa, M.A. Beno, P.V. Ballmoos, and G.K. Skinner, "High diffraction efficiency, broadband, diffraction crystals for use in crystal diffraction lenses," Experimental Astronomy, vol. 20, pp. 201-210, 2005.

[239] R. Atun, L.O.M. De Andrade, G. Almeida, D. Cotlear, T. Dmytraczenko, P. Frenz, P. Garcia, O. Gómez-Dantés, F.M. Knaul, C. Muntaner, and J.B. De Paula, "Health-system reform and universal health coverage in Latin America," The Lancet, vol. 385, no. 9974, pp. 1230-1247, 2015.

[240] O. Desouky, N. Ding, and G. Zhou, "Targeted and non-targeted effects of ionizing radiation," Journal of Radiation Research and Applied Sciences, vol. 8, no. 2, pp. 247-254, 2015.

[241] S. Demaria, N. Kawashima, A.M. Yang, M.L. Devitt, J.S. Babb, J.P. Allison, and S.C. Formenti, "Immune-mediated inhibition of metastases after treatment with local radiation and CTLA-4 blockade in a mouse model of breast cancer," Clinical Cancer Research, vol. 11, no. 2, pp. 728-734, 2005.

[242] J. Overgaard, "Simultaneous and sequential hyperthermia and radiation treatment of an experimental tumor and its surrounding normal tissue in vivo," International Journal of Radiation Oncology* Biology Physics, vol. 6, no. 11, pp. 1507-1517, 1980.

[243] E. Ron, J.H. Lubin, R.E. Shore, K. Mabuchi, B. Modan, L.M. Pottern, A.B. Schneider, M.A. Tucker, and J.D. Boice Jr, "Thyroid cancer after exposure to external radiation: a pooled analysis of seven studies," Radiation Research, vol. 141, no. 3, pp. 259-277, 1995.

[244] B.J. Gerbi, A.S. Meigooni, and F.M. Khan, "Dose buildup for obliquely incident photon beams," Medical Physics, vol. 14, no. 3, pp. 393-399, 1987.

[245] G. Paterno, M. Marziani, R. Camattari, V. Bellucci, A. Mazzolari, M. Gambaccini, and V. Guidi, "Laue lens to focus an X-ray beam for radiation therapy," Journal of Applied Crystallography, vol. 49, no. 2, pp. 468-478, 2016.

[246] C.A. MacDonald and J.C. Petruccelli, "Polycapillary optics for medical applications," in Journal of Physics: Conference Series, vol. 776, no. 1, p. 012001, IOP Publishing, November 2016.

[247] C.A. MacDonald, "Focusing polycapillary optics and their applications," X-ray Optics and Instrumentation, 2010.

[248] V. Bellucci, G. Paterno, R. Camattari, V. Guidi, M. Jentschel, and P. Bastie, "High-efficiency diffraction and focusing of X-rays through asymmetric bent crystalline planes," Journal of Applied Crystallography, vol. 48, no. 1, pp. 297-300, 2015.

[249] R. Camattari, "Laue lens for radiotherapy applications through a focused hard x-ray beam: a feasibility study on requirements and tolerances," Physics in Medicine & Biology, vol. 62, no. 18, p. 7249, 2017.

[250] D.Y. Breitkreutz, "Design and evaluation of a Monte Carlo model of a low-cost kilovoltage x-ray arc therapy system" (Doctoral dissertation), 2019.

[251] D.A. Bartkoski, A. Bar-David, M. Kleckner, D. Mirkovic, R. Tailor, J. Moradi-Kurdestany, S. Borukhin, Z.E. Harel, Z. Burshtein, A. Zuck, and M. Salehpour, "Analysis of a novel X-ray lens for converging beam radiotherapy," Scientific Reports, vol. 11, no. 1, p. 19180, 2021.

[252] R.S. Overbeck, D. Erickson, D. Evangelakos, M. Pharr, and P. Debevec, "A system for acquiring, processing, and rendering panoramic light field stills for virtual reality," ACM Transactions on Graphics (TOG), vol. 37, no. 6, pp. 1-15, 2018.

[253] M. Tahtali, S.K. Saha, A.J. Lambert, and M.R. Pickering, "A new imaging method for real-time 3D x-ray reconstruction," in Medical Imaging 2013: Physics of Medical Imaging, vol. 8668, pp. 1425-1433, SPIE, March 2013.

[254] S.K. Saha, M. Tahtali, A. Lambert, and M. Pickering, "CT reconstruction from simultaneous projections: a step towards capturing CT in One Go," Computer Methods in Biomechanics and Biomedical Engineering: Imaging & Visualization, vol. 5, no. 2, pp. 87-99, 2017.
[255] TT. Rahman, M. Tahtali, and M.R. Pickering, "Performance evaluation of a newly proposed novel L-SPECT system for SPECT imaging," in 2015 International Conference on Digital Image Computing: Techniques and Applications (DICTA), pp. 1-6, IEEE, November 2015.
[256] D.L. Gunter, "Collimator design for nuclear medicine," in *Emission Tomography*, pp. 153-168, Academic Press, 2004.
[257] G. Paterno, V. Bellucci, R. Camattari, and V. Guidi, "Design study of a Laue lens for nuclear medicine," Journal of Applied Crystallography, vol. 48, no. 1, pp. 125-137, 2015.
[258] M.M. Ter-Pogossian, "Basic principles of computed axial tomography," in Seminars in Nuclear Medicine, vol. 7, no. 2, pp. 109-127, WB Saunders, April 1977.
[259] X. Pan, E.Y. Sidky, and M. Vannier, "Why do commercial CT scanners still employ traditional, filtered back-projection for image reconstruction?," Inverse Problems, vol. 25, no. 12, p. 123009, 2009.
[260] R. Khilar, S. Chitrakala, and S. SelvamParvathy, "3D image reconstruction: Techniques, applications and challenges," in 2013 International Conference on Optical Imaging Sensor and Security (ICOSS), pp. 1-6, IEEE, July 2013.
[261] W.A. Kalender, "Computed Tomography: Fundamentals, System Technology, Image Quality, Applications," John Wiley & Sons, 2011.
[262] P.P. Bruyant, "Analytic and iterative reconstruction algorithms in SPECT," Journal of Nuclear Medicine, vol. 43, no. 10, pp. 1343-1358, 2002.
[263] M. King and T. Farncombe, "An overview of attenuation and scatter correction of planar and SPECT data for dosimetry studies," Cancer Biotherapy and Radiopharmaceuticals, vol. 18, no. 2, pp. 181-190, 2003.
[264] RT.R. Miller and K.S. Sampathkumaran, "Digital filtering in nuclear medicine," Journal of Nuclear Medicine, vol. 23, no. 1, pp. 66-72, 1982.
[265] N. Zeraatkar, A. Rahmim, S. Sarkar, and M.R. Ay, "Development and Evaluation of Image Reconstruction Algorithms for a Novel Desktop SPECT System," Asia Oceania Journal of Nuclear Medicine and Biology, vol. 5, no. 2, p. 120, 2017.
[266] H.M., "Accelerated image reconstruction using ordered subsets of projection data," IEEE Transactions on Medical Imaging, vol. 13, no. 4, pp. 594-600, 1994.
[267] J.A. Fessler and W.L. Rogers, "Spatial resolution properties of penalized-likelihood image reconstruction: space-invariant tomographs," IEEE Transactions on Image Processing, vol. 5, no. 9, pp. 1346-1358, 1996.
[268] K. Li, J. Garrett, Y. Ge, and G.H. Chen, "Statistical model based iterative reconstruction (MBIR) in clinical CT systems. Part II. Experimental assessment of spatial resolution performance," Medical Physics, vol. 41, no. 7, p. 071911, 2014.
[269] L. Yu, T.J. Vrieze, S. Leng, J.G. Fletcher, and C.H. McCollough, "Measuring contrast-and noise-dependent spatial resolution of an iterative reconstruction method in CT using ensemble averaging," Medical Physics, vol. 42, no. 5, pp. 2261-2267, 2015.
[270] E.C. Ehman, L. Yu, A. Manduca, A.K. Hara, M.M. Shiung, D. Jondal, D.S. Lake, R.G. Paden, D.J. Blezek, M.R. Bruesewitz, and C.H. McCollough, "Methods for clinical evaluation of noise reduction techniques in abdominopelvic CT," Radiographics, vol. 34, no. 4, pp. 849-862, 2014.
[271] S.T. Schindera, D. Odedra, S.A. Raza, T.K. Kim, H.J. Jang, Z. Szucs-Farkas, and P. Rogalla, "Iterative reconstruction algorithm for CT: can radiation dose be decreased while low-contrast detectability is preserved?," Radiology, vol. 269, no. 2, pp. 511-518, 2013.
[272] A.H. Goenka, B.R. Herts, N.A. Obuchowski, A.N. Primak, F. Dong, W. Karim, and M.E. Baker, "Effect of reduced radiation exposure and iterative reconstruction on detection of low-contrast low-attenuation lesions in an anthropomorphic liver phantom: an 18-reader study," Radiology, vol. 272, no. 1, pp. 154-163, 2014.
[273] C.H. McCollough, L. Yu, J.M. Kofler, S. Leng, Y. Zhang, Z. Li, and R.E. Carter, "Degradation of CT low-contrast spatial resolution due to the use of iterative reconstruction and reduced dose levels," Radiology, vol. 276, no. 2, pp. 499-506, 2015.
[274] A. Winklehner, C. Karlo, G. Puippe, B. Schmidt, T. Flohr, R. Goetti, T. Pfammatter, T. Frauenfelder, and H. Alkadhi, "Raw data-based iterative reconstruction in body CTA: evaluation of radiation dose saving potential," European radiology, vol. 21, pp. 2521-2526, 2011.
[275] J.G. Fletcher, L. Yu, Z. Li, A. Manduca, D.J. Blezek, D.M. Hough, S.K. Venkatesh, G.C. Brickner, J.C. Cernigliaro, A.K. Hara, and J.L. Fidler, "Observer performance in the detection and classification of malignant hepatic nodules and masses with CT image-space denoising and iterative reconstruction," Radiology, vol. 276, no. 2, pp. 465-478, 2015.

[276] L. Yu, S. Leng, L. Chen, J.M. Kofler, R.E. Carter, and C.H. McCollough, "Prediction of human observer performance in a 2-alternative forced choice low-contrast detection task using channelized Hotelling observer: Impact of radiation dose and reconstruction algorithms," Medical physics, vol. 40, no. 4, p. 041908, 2013.

[277] E. Samei and S. Richard, "Assessment of the dose reduction potential of a model-based iterative reconstruction algorithm using a task-based performance metrology," Medical physics, vol. 42, no. 1, pp. 314-323, 2015.

[278] V. Israel-Jost, P. Choquet, S. Salmon, C. Blondet, E. Sonnendrucker, and A. Constantinesco, "Pinhole SPECT imaging: compact projection/backprojection operator for efficient algebraic reconstruction," IEEE transactions on medical imaging, vol. 25, no. 2, pp. 158-167, 2006.

[279] A.H. Vija, E.G. Hawman, and J.C. Engdahl, "Analysis of a SPECT OSEM reconstruction method with 3D beam modeling and optional attenuation correction: phantom studies," in 2003 IEEE Nuclear Science Symposium. Conference Record (IEEE Cat. No. 03CH37515), vol. 4, pp. 2662-2666, October 2003.

[280] G.L. Zeng, "Medical Image Reconstruction," vol. 530, Heidelberg: Springer, 2010.

[281] P. Després, M. Sun, B.H. Hasegawa, and S. Prevrhal, "FFT and cone-beam CT reconstruction on graphics hardware," in Medical Imaging 2007: Physics of Medical Imaging, vol. 6510, pp. 1807-1813, March 2007.

[282] G. L. Zeng, Y. J. I. t. o. r. Li, and p. m. sciences, "Fourier-domain analysis of the iterative Landweber algorithm," vol. 1, no. 6, pp. 511-516, 2017.

[283] Lyra, M. and Ploussi, A., 2011. Filtering in SPECT image reconstruction. Journal of Biomedical Imaging, 2011.

[284] T. Vijayakumar, "Posed inverse problem rectification using novel deep convolutional neural network," Journal of Innovative Image Processing (JIIP), vol. 2, no. 03, pp. 121-127, 2020.

[285] G.T. Herman and A. Lent, "Iterative reconstruction algorithms," Computers in Biology and Medicine, vol. 6, no. 4, pp. 273-294, 1976.

[286] G.J. Ramírez-Nava, C.L. Santos-Cuevas, I. Chairez, and L. Aranda-Lara, "Multimodal molecular 3D imaging for the tumoral volumetric distribution assessment of folate-based biosensors," Medical & Biological Engineering & Computing, vol. 56, pp. 1135-1148, 2018.

[287] D. C. Clark, "The Localization of TECHNETIUM-99 (M)-LABELED Lymphocytes at Tumor Site and Detection by Gamma Camera Imaging," Ph.D. dissertation, University of California, Irvine, 1977.

[288] J. Seco and F. Verhaegen, Eds., "Monte Carlo Techniques in Radiation Therapy," CRC Press, 2013.

[289] J. Apostolakis, M. Bandieramonte, S. Banerjee, N. Bartosik, G. Corti, G. Cosmo, V. D. Elvira, T. Evans, A. Gheata, S. Pagan Griso, V. Ivantchenko, "Detector Simulation Challenges for Future Accelerator Experiments," Frontiers in Physics, vol. 10, p. 913510, 2022.

[290] H. Zaidi and P. Andreo, "Monte Carlo Techniques in Nuclear Medicine Dosimetry," in Monte Carlo Calculations in Nuclear Medicine (Second Edition) Therapeutic Applications, Bristol, UK: IOP Publishing, 2022.

[291] Liu, T. Zhao, and M. Baradaran-Ghahfarokhi, "Monte Carlo Techniques in Medical Physics," in Radiation Therapy Dosimetry: A Practical Handbook, CRC Press, 2021.

[292] D. Sarrut, A. Etxebeste, E. Muñoz, N. Krah, and J. M. Létang, "Artificial intelligence for Monte Carlo simulation in medical physics," Frontiers in Physics, vol. 9, p. 738112, 2021.

[293] N. Chatzisavvas, G. Priniotakis, M. Papoutsidakis, D. Nikolopoulos, I. Valais, and G. Karpetas, "Monte Carlo Computational Software and Methods in Radiation Dosimetry," Annals of Emerging Technologies in Computing (AETiC), vol. 5, no. 3, pp. 36-50, 2021.

[294] Kawrakow, "The EGSnrc Code System, Monte Carlo Simulation of Electron and Photon Transport," NRCC Report PIRS-701, 2001.

[295] A. Kling, F.J. Barao, M. Nakagawa, L. Tavora, and P. Vaz, Eds., "Advanced Monte Carlo for Radiation Physics, Particle Transport Simulation and Applications: Proceedings of the Monte Carlo 2000 Conference, Lisbon, 23–26 October 2000," Springer Science & Business Media, 2014.

[296] F. Salvat, J. M. Fernández-Varea, and J. Sempau, "PENELOPE-2006: A code system for Monte Carlo simulation of electron and photon transport," Workshop proceedings, vol. 4, no. 6222, pp. 7, Nuclear Energy Agency, Organization for Economic Co-operation and Development, Barcelona, Spain, July 2006.

[297] T. T. Böhlen, F. Cerutti, M. P. W. Chin, A. Fassò, A. Ferrari, P. G. Ortega, A. Mairani, P. R. Sala, G. Smirnov, and V. Vlachoudis, "The FLUKA code: developments and challenges for high energy and medical applications," Nuclear Data Sheets, vol. 120, pp. 211-214, 2014.

[298] J. Allison, "Facilities and methods: Geant4–a simulation toolkit," Nuclear Physics News, vol. 17, no. 2, pp. 20-24, 2007.

[299] J. Allison et al., "Recent developments in Geant4," Nuclear Instruments and Methods in Physics Research Section A: Accelerators, Spectrometers, Detectors and Associated Equipment, vol. 835, pp. 186-225, 2016.
[300] S. Jan et al., "GATE V6: a major enhancement of the GATE simulation platform enabling modelling of CT and radiotherapy," Physics in Medicine & Biology, vol. 56, no. 4, p. 881, 2011.
[301] D. Sarrut et al., "Advanced Monte Carlo simulations of emission tomography imaging systems with GATE," Physics in Medicine & Biology, vol. 66, no. 10, p. 10TR03, 2021.
[302] D. Sarrut et al., "A review of the use and potential of the GATE Monte Carlo simulation code for radiation therapy and dosimetry applications," Medical physics, vol. 41, no. 6Part1, p. 064301, 2014.
[303] S. Staelens and I. Buvat, "Monte Carlo simulations in nuclear medicine imaging," in Advances in Biomedical Engineering, pp. 177-209, Elsevier, 2009.
[304] E. Cuevas, A. Luque, and H. Escobar, "Graphing with MATLAB," in Computational Methods with MATLAB®, Springer Nature Switzerland, 2023, pp. 19-56.
[305] S. Agostinelli et al., "GEANT4—a simulation toolkit," Nuclear Instruments and Methods in Physics Research Section A: Accelerators, Spectrometers, Detectors and Associated Equipment, vol. 506, no. 3, pp. 250-303, 2003.
[306] J. Allison et al., "Geant4 developments and applications," IEEE Transactions on Nuclear Science, vol. 53, pp. 270-278, 2006.
[307] P. Arce, P. Rato, M. Canadas, and J.I. Lagares, "GAMOS: A Geant4-based easy and flexible framework for nuclear medicine applications," in 2008 IEEE Nuclear Science Symposium Conference Record, pp. 3162-3168, October 2008.
[308] A.K. Glaser, S.C. Kanick, R. Zhang, P. Arce, and B.W. Pogue, "A GAMOS plug-in for GEANT4 based Monte Carlo simulation of radiation-induced light transport in biological media," Biomedical Optics Express, vol. 4, no. 5, pp. 741-759, 2013.
[309] A. Barhoum, M. Tahtali, and R. Camattari, "Feasibility Study of a Lens-Based SPECT With a Tiled Lens and Detector Geometry for Animal Research: Simulation Results," 2022 IEEE International Conference on Systems, Man, and Cybernetics (SMC), pp. 3143-3149, October 2022.
[310] A. Klöckner, N. Pinto, Y. Lee, B. Catanzaro, P. Ivanov, and A. Fasih, "PyCUDA and PyOpenCL: A scripting-based approach to GPU run-time code generation," Parallel Computing, vol. 38, no. 3, pp. 157-174, 2012.
[311] P. Luszczek, "Parallel programming in MATLAB," The International Journal of High Performance Computing Applications, vol. 23, no. 3, pp. 277-283, 2009.
[312] V. Ivanchenko et al., "Recent improvements in Geant4 electromagnetic physics models and interfaces," Progress in Nuclear Science and Technology, vol. 2, pp. 898-903, 2011.
[313] M. Assalmi and N. Mansour, "Validation of Monte Carlo Geant4 multithreading code for a 6 MV photon beam of Varian Linac on the Grid Computing," Reports of Practical Oncology and Radiotherapy, vol. 25, no. 6, pp. 1001-1010, 2020.
[314] B.M.W. Tsui and G.T. Gullberg, "The geometric transfer function for cone and fan beam collimators," Physics in Medicine & Biology, vol. 35, no. 1, p. 81, 1990.
[315] L. Zhou and G. Gindi, "Collimator optimization in SPECT based on a joint detection and localization task," Physics in Medicine & Biology, vol. 54, no. 14, p. 4423, 2009.
[316] D.P. McElroy, L.R. MacDonald, F.J. Beekman, Y. Wang, B.E. Patt, J.S. Iwanczyk, B.M. Tsui, and E.J. Hoffman, "Performance evaluation of A-SPECT: a high resolution desktop pinhole SPECT system for imaging small animals," IEEE Transactions on Nuclear Science, vol. 49, no. 5, pp. 2139-2147, 2002.
[317] H. Zaidi, "Relevance of accurate Monte Carlo modeling in nuclear medical imaging," Medical Physics, vol. 26, no. 4, pp. 574-608, 1999.
[318] N. Lanconelli, "The importance of Monte Carlo simulations in modeling detectors for Nuclear Medicine," Mathematics and Computers in Simulation, vol. 80, no. 10, pp. 2109-2114, 2010.
[319] N. Balram and I. Tošić, "Light-field imaging and display systems," Information Display, vol. 32, no. 4, pp. 6-13, 2016.
[320] J.C. Yang, M. Everett, C. Buehler, and L. McMillan, "A real-time distributed light field camera," in Rendering Techniques, 2002.
[321] G. Wu, B. Masia, A. Jarabo, Y. Zhang, L. Wang, Q. Dai, T. Chai, and Y. Liu, "Light field image processing: An overview," in IEEE Journal of Selected Topics in Signal Processing, vol. 11, no. 7, pp. 926-954, 2017.
[322] R. J. Motta, "The future of photography," in Digital Photography VI, vol. 7537, pp. 11-17, January 2010.

[323] R. Camattari and V. Guidi, "Genetic algorithm to design Laue lenses with optimal performance for focusing hard X- and γ-rays," Astronomy & Astrophysics, vol. 570, p. A17, 2014.
[324] E. Nazaretski, J. Kim, H. Yan, K. Lauer, D. Eom, D. Shu, J. Maser, Z. Pešić, U. Wagner, C. Rau, and Y. S. Chu, "Performance and characterization of the prototype nm-scale spatial resolution scanning multilayer Laue lenses microscope," Review of Scientific Instruments, vol. 84, no. 3, 2013.
[325] F. Frontera and P. Von Ballmoos, "Laue gamma-ray lenses for space astrophysics: status and prospects," X-ray Optics and Instrumentation, 2010.
[326] V.K. Pecharsky and P.Y. Zavalij, "Fundamentals of diffraction," Springer US, 2003.
[327] A. Authier and C. Malgrange, "Diffraction physics," Acta Crystallographica Section A: Foundations of Crystallography, vol. 54, no. 6, pp. 806-819, 1998.
[328] K. Kozlovskaya, E. Ovchinnikova, J. Kokubun, A. Rogalev, F. Wilhelm, F. Guillou, F. de Bergevin, A. F. Konstantinova, and V. E. Dmitrienko, "Determination of absolute structure of chiral crystals using three-wave x-ray diffraction," Crystals, vol. 11, no. 11, p. 1389, 2021.
[329] D. E. Roa and R. K. Smither, "Copper crystal lens for medical imaging: first results," in Medical Imaging 2001: Physics of Medical Imaging, vol. 4320, pp. 435-446, June 2001.
[330] R. Camattari, V. Guidi, V. Bellucci, and A. Mazzolari, "The 'quasi-mosaic' effect in crystals and its applications in modern physics," Journal of Applied Crystallography, vol. 48, no. 4, pp. 977-989, 2015.
[331] D. E. Roa, R. K. Smither, X. Zhang, K. Nie, Y. Y. Shieh, N. S. Ramsinghani, N. Milne, J. V. Kuo, J. L. Redpath, M. S. A. L. Al-Ghazi, and P. Caligiuri, "Development of a new photon diffraction imaging system for diagnostic nuclear medicine," in Focusing Telescopes in Nuclear Astrophysics, pp. 229-239, 2006.
[332] K. J. Lee and D. C. Barber, "Use of forward projection to correct patient motion during SPECT imaging," Physics in Medicine & Biology, vol. 43, no. 1, p. 171, 1998.
[333] C. Y. Chou, Y. Y. Chuo, Y. Hung, and W. Wang, "A fast forward projection using multithreads for multirays on GPUs in medical image reconstruction," Medical Physics, vol. 38, no. 7, pp. 4052-4065, 2011.
[334] P. Aguiar, M. Rafecas, J. E. Ortuño, G. Kontaxakis, A. Santos, J. Pavía, and D. Ros, "Geometrical and Monte Carlo projectors in 3D PET reconstruction," Medical Physics, vol. 37, no. 11, pp. 5691-5702, 2010.
[335] F. Tamburini, G. Anzolin, G. Umbriaco, A. Bianchini, and C. Barbieri, "Overcoming the Rayleigh criterion limit with optical vortices," Physical Review Letters, vol. 97, no. 16, p. 163903, 2006.
[336] Y. J. Lee, H. J. Ryu, S. W. Lee, S. J. Park, and H. J. Kim, "Comparison of ultra-high-resolution parallel-hole collimator materials based on the CdTe pixelated semiconductor SPECT system," Nuclear Instruments and Methods in Physics Research Section A: Accelerators, Spectrometers, Detectors and Associated Equipment, vol. 713, pp. 33-39, 2013.
[337] R. K. Smither and D. E. Roa, "Physics of medical imaging with crystal diffraction lenses," in Medical Imaging 2001: Physics of Medical Imaging, vol. 4320, pp. 447-458, SPIE, June 2001.
[338] N. Zeraatkar, K. S. Kalluri, B. Auer, A. Könik, T. J. Fromme, L. R. Furenlid, P. H. Kuo, and M. A. King, "Investigation of axial and angular sampling in multi-detector pinhole-SPECT brain imaging," in IEEE Transactions on Medical Imaging, vol. 39, no. 12, pp. 4209-4224, 2020.
[339] M. A. King, J. M. Mukherjee, A. Könik, I. G. Zubal, J. Dey, and R. J. I. t. o. n. s. Licho, "Design of a multi-pinhole collimator for I-123 DaTscan imaging on dual-headed SPECT systems in combination with a fan-beam collimator," vol. 63, no. 1, pp. 90-97, 2016.
[340] T. Krüwel, D. Nevoltris, J. Bode, C. Dullin, D. Baty, P. Chames, and F. Alves, "In vivo detection of small tumor lesions by multi-pinhole SPECT applying a 99mTc-labelled nanobody targeting the Epidermal Growth Factor Receptor," in Scientific Reports, vol. 6, no. 1, p. 21834, 2016.
[341] S. Abbaspour, K. Tanha, B. Mahmoudian, M. Assadi, and J. P. Islamian, "A Monte Carlo study on the performance evaluation of a parallel hole collimator for a HiReSPECT: A dedicated small-animal SPECT," in Applied Radiation and Isotopes, vol. 139, pp. 53-60, 2018.
[342] F. Boisson, D. Zahra, A. Parmar, M.C. Gregoire, S.R. Meikle, H. Hamse, and A. Reilhac, "Imaging capabilities of the Inveon SPECT system using single- and multipinhole collimators," in Journal of Nuclear Medicine, vol. 54, no. 10, pp. 1833-1840, 2013.
[343] GAMOS Collaboration, "GAMOS 5.1.0 User's Guide," 2017.
[344] R. P. Drake, "Introduction to High-Energy-Density Physics," in High-Energy-Density Physics: Foundation of Inertial Fusion and Experimental Astrophysics, 2018, pp. 1-20.
[345] D. P. Landau, S. H. Tsai, and M. Exler, "A New Approach to Monte Carlo Simulations in Statistical Physics: Wang-Landau Sampling," American Journal of Physics, vol. 72, no. 10, pp. 1294-1302, 2004.
[346] A. Authier, "Early Days of X-ray Crystallography," OUP Oxford, 2013.
[347] C.B. Wunderer, P. von Ballmoos, N. Barriere, A. Bazzano, S.E. Boggs, F. Christensen, F. Frontera, M. Hernanz, J. Knodlseder, and A. Zoglauer, "Gamma-Ray Lenses for Astrophysics—and the

Gamma-Ray Imager Mission GRI," in IEEE Transactions on Nuclear Science, vol. 56, no. 3, pp. 1242-1249, 2009.
[348] A. De Angelis, V. Tatischeff, A. Argan, S. Brandt, A. Bulgarelli, A. Bykov, E. Costantini, R. C. Silva, I. A. Grenier, L. Hanlon, D. Hartmann, et al., "Gamma-ray astrophysics in the MeV range: The ASTROGAM concept and beyond," Experimental Astronomy, vol. 51, pp. 1225-1254, 2021.
[349] P. M. De Freitas and H. Videau, "Detector simulation with MOKKA/GEANT4: Present and future," pp. 623-627, LC-TOOL-2003-010, 2002.
[350] Geant4 Collaboration, "Introduction to Geant4," 2010.
[351] C.P. Gloster, "Comment on 'Gamma-ray spectroscopy using angular distribution of Compton scattering' [Nucl. Instr. and Meth. A 1031 (2022) 166502]," Nuclear Instruments and Methods in Physics Research Section A: Accelerators, Spectrometers, Detectors and Associated Equipment, vol. 1049, p. 167923, 2023.
[352] M.G. Pia, "The GEANT4 Object Oriented Simulation Toolkit," INFN-AE-99-22, 1999.
[353] I. G. Evseev, H. R. Schelin, S. A. Paschuk, E. Milhoretto, J. A. Setti, O. Yevseyeva, J. T. de Assis, J. M. Hormaza, K. S. Díaz, and R. T. Lopes, "Comparison of SRIM, MCNPX, and GEANT simulations with experimental data for thick Al absorbers," Applied Radiation and Isotopes, vol. 68, no. 4-5, pp. 948-950, 2010.
[354] M. Asai, K. Amako, J. Apostolakis, H. Kurasige, T. Sasaki, and J. P. Wellisch, "Design of tracking and generic processes in GEANT4," in Advanced Monte Carlo for Radiation Physics, Particle Transport Simulation and Applications: Proceedings of the Monte Carlo 2000 Conference, Lisbon, 23–26 October 2000, pp. 1117-1122, Springer Berlin Heidelberg, 2001.
[355] G. Collaboration, "Geant4 User's Guide for Application Developers," Version geant4, 9, 2012.
[356] T. Rahman, "Design and evaluation of the newly proposed L-SPECT system based on light field imaging," Ph.D. dissertation, UNSW Sydney, 2017.
[357] S. Lee, J. Gregor, and D. Osborne, "Development and validation of a complete GATE model of the Siemens Inveon trimodal imaging platform," Molecular Imaging, vol. 12, no. 7, pp. 7290-2013, 2013.
[358] P. Arce, J. I. Lagares, L. Harkness, L. Desorgher, G. De Lorenzo, Y. Abreu, and Z. Wang, "GAMOS: an easy and flexible way to use GEANT4," in 2011 IEEE Nuclear Science Symposium Conference Record, October 2011.
[359] X. Dong, M.I. Saripan, R. Mahmud, S. Mashohor, and A. Wang, "Characterization of SIEMENS Symbia T SPECT camera in Monte Carlo simulation environment," Pakistan Journal of Nuclear Medicine, vol. 8, no. 1, pp. 18-26, 2019.
[360] P.B. Zanzonico, "Radionuclide Imaging," CRC Press, Boca Raton, Florida, USA, 2015.
[361] J.T. Dobbins III and D.J. Godfrey, "Digital X-Ray Tomosynthesis: Current State of the Art and Clinical Potential," Physics in Medicine & Biology, vol. 48, no. 19, p. R65, 2003.
[362] T. Rahman, M. Tahtali, and M.R. Pickering, "Quantitative Analysis of L-SPECT System for Small Animal Brain Imaging," in Medical Imaging 2016: Physics of Medical Imaging, vol. 9783, pp. 1425-1435, March 2016.